Characterising Protective Corrosion Product Development in Demanding CO_2 Environments

Robert Anthony Jacklin

Submitted in accordance with the requirements for the degree of
Doctor of Philosophy

The University of Leeds
Institute of Functional Surfaces
School of Mechanical Engineering

February 2023

Publication Statement

The candidate confirms that the work submitted is his/her own, except where work which has formed part of jointly-authored publications has been included. The contribution of the candidate and the other authors to this work has been explicitly indicated below. The candidate confirms that appropriate credit has been given within the thesis where reference has been made to the work of others.

In all papers listed below, the primary author completed all experimental studies, evaluation of data and preparation of publications. All authors contributed to proof reading of the articles prior to publication.

Jacklin, R., Owen, J., Burkle, D., Neville, A., Woollam, R., Barker, R. Iron Calcium Carbonate Formation in CO_2 Environments – Effects of A/V Ratio in Autoclave Experiments. In: *AMPP Annual Conference + Expo,* 6-10 March 2022, San Antonio, Texas. AMPP, 2022, Paper No. AMPP-2022-17622.

Acknowledgements

I would like to first thank the whole team at the University of Leeds Institute of Functional Surfaces, both past and present, for all of the support, guidance and knowledge that made this project possible, even in the midst of a global pandemic!

A special thanks to my supervisor throughout the project Prof. Richard Barker, for you leadership, support, guidance, and encyclopaedic knowledge of corrosion (and The Simpsons). A massive thanks also to Dr Joshua Owen for stepping in as a supervisor and providing incredible support on experimental set up and technical assistance whenever needed. Another huge thanks to the fountain of knowledge that is Richard Woollam, again joining the project at a late stage and quickly helping to squeeze every last bit of information from my results. I would also like to thank my industrial sponsor LBBC Baskerville and my mentor Dr Danny Burkle for support and equipment throughout the project.

I'd like to thank the iFS technicians Jordan Thomas, Mick Huggan and Paul Kilburn for all of their hard work to maintain the labs and provide equipment, materials, and light entertainment. Thanks also to Zabeada Aslam and Stuart Micklethwaite from LEMAS for their brilliant work on surface analysis, FIB and diffraction. Special thanks also to Harry Bullock for his support on the chemistry model validation and for his impeccable polishing skills. Thanks to Dr. Amir Shamsa for training me to use autoclaves and to the rest of my friends in iFS (special mention to the dungeon office: Mari, Dan, Raeesa, Ana, Mo, Kabir, Jonas, Wenlong, Alex).

Thanks to my Dad, Trevor Jacklin for inspiring me to become an engineer and the rest of my family (Anna, Sarah, Katie and Ali and all of the family). Thanks especially to Audrey for your immense support and our four legged family members (Eddy, Leo and Jaya) for keeping me sane throughout. Thank you also to Geoff and Danie for supporting us and the great memories over lockdown.

Finally I want to dedicate this thesis to two inspirational women that left us too soon, my mum Hilary Jacklin and my supervisor Prof. Anne Neville. Thank you both for everything.

Abstract

Carbon Dioxide (CO_2) corrosion has implications for carbon steel asset integrity across a range of current and emerging energy markets. Such environments are becoming increasingly severe as exploration moves to deeper wells and more aggressive forms of recovery to meet current and future energy demands. A long proposed economical and environmentally sustainable solution for extending the life of carbon steel in these environments is to exploit the corrosion products that form on the steel surface, namely iron carbonate ($FeCO_3$). Research has shown that the level of protection offered by $FeCO_3$ is heavily dependent on the environment in which it forms, in particular influenced by pressure, temperature, pH and presence of brine ions such as Ca^{2+}.

The current study aims at exploring the formation of $FeCO_3$ in more demanding environments, using autoclaves to simulate the effects of elevated CO_2 partial pressure (5.5 bar) and low brine pH (~3.6) as well as the consequence of calcium incorporation on corrosion product performance. The study also highlights the impact that solution evolution rates in such aggressive environments can have on the perceived performance of the corrosion product layer, as assessed by variation of the steel surface area to solution volume (A/V) ratio.

Experiments were conducted at 80 °C using a combination of *ex situ* analytical techniques and *in situ* electrochemical measurements, the research suggests that the $FeCO_3$ formation process occurs in four distinct phases, with the resultant layer properties dependent on the A/V ratio of the system. At low A/V the layer grows almost entirely within an iron carbide (Fe_3C) network remaining at the steel surface after ferrite depletion while at high A/V the layer is able to extend out of and cover the Fe_3C network creating a more effective diffusion barrier.

The presence of calcium in the brine is also shown to affect localised corrosion by promoting morphological changes in the corrosion layer during formation. This effect appears most pronounced when the cationic constituents (Ca^{2+} and Fe^{2+}) are evenly balanced within the layer with an average composition of $Fe_{0.5}Ca_{0.5}CO_3$.

Table of Contents

List of Tables

List of Figures

Nomenclature

Symbol	Definition	Units
a	Activity	
A	Area	cm^2
AAS	Atomic Absorption Spectroscopy	
Ag/AgCl	Silver/Silver Chloride	
API	American Petroleum Institute	
ASTM	American Society for Testing and Materials	
A/V	Area-to-volume	$cm^2 \cdot L^{-1}$
AWG	American Wire Gauge	
B	Stearn-Geary coefficient	Volts, V
BDM	Bockris-Devanthan-Müller	
BPR	Back Pressure Regulator	
BSE	Back Scattered Electron	
c	Species concentration	$mol \cdot L^{-1}$
C	Capacitance	$F \cdot cm^{-2}$
Ca	Calcium	
Ca^{2+}	Calcium ion	
$CaCl_2$	Calcium chloride	
$CaCO_3$	Calcium carbonate	
CCS	Carbon Capture and Storage	
C_{dl}	Double Layer Capacitance	$F \cdot cm^{-2}$
CE	Counter Electrode	
CO_2	Carbon dioxide	
CO_3^{2-}	Carbonate ion	
CPE	Constant Phase Element	
CPM	Corrosion Product Mass	grams, g
CSTR	Continuously Stirred Tank Reactor	
d	Inter-planar d-spacing	
D	Diffusion coefficient	$cm^2 \cdot s^{-1}$
E	Potential	Volts, V
E^0	Standard Electrode Potential	Volts, V
e^-	Electron	

EBSD	Electron Back-Scattered Diffraction	
EDL	Electrical Double Layer	
EDX/EDS	Energy Dispersive X-ray Spectroscopy	
EEC	Equivalent Electrical Circuit	
EELS	Electron Energy Loss Spectroscopy	
EIS	Electrochemical Impedance Spectroscopy	
EMF	Electromotive Force	
EMP	Electron microprobe	
EOR	Enhanced Oil Recovery	
EXAFS	Extended X-ray Absorption Fine Structure	
F	Faraday's constant	$C \cdot mol^{-1}$
Fe	Iron	
Fe^{2+}	Ferrous ion	
Fe^{3+}	Ferric iron	
Fe_3C	Iron carbide (Cementite)	
Fe_3O_4	Magnetite	
$FeCO_3$	Iron carbonate (Siderite)	
FEP	Fluorinated Ethylene Propylene	
$Fe_xCa_yCO_3$	Iron calcium carbonate	
FTIR	Fourier Transform Infrared	
G	Gibbs free energy	Joules, J
H^+	Hydrogen ion (Proton)	
H_2	Hydrogen gas	
H_2O	Water	
H_2CO_3	Carbonic acid	
H_3O^+	Hydronium ion	
HCl	Hydrochloric acid	
H_{CO2}	Henry's constant for CO_2	
HCO_3^-	Bicarbonate ion	
i	Current density	$A \cdot cm^{-2}$
I	Current	Ampere, A
I	Ionic strength	$mol \cdot L^{-1}$
ICDD	International Centre for Diffraction Data	
i_{corr}	Corrosion current density	$A \cdot cm^{-2}$

ICP	Inductively Coupled Plasma Spectroscopy	
i_0	Exchange (free) current density	$A \cdot cm^{-2}$
IHP	Inner Helmholtz Plane	
ISE	Ion Selective Electrode	
j	Imaginary number	
K_{bi}	Bicarbonate ion dissociation constant	
K_{ca}	Carbonic acid dissociation constant	
KCl	Potassium chloride	
K_{hy}	CO_2 hydration constant	
K_{sol}	CO_2 solubility constant	
K_{sp}	Solubility product constant	
K_u	Unit conversion factor	
K_{wa}	Water dissociation constant	
L	Inductance	Henry, H
L_{ads}	Adsorption inductor	Henry, H
LPR	Linear Polarisation Resistance	
M	Metal ion	
m_0	Original specimen mass	grams, g
m_{cp}	Mass with corrosion products	grams, g
m_f	Final mass	grams, g
Mg	Magnesium	
Mg^{2+}	Magnesium ion	
$MgCO_3$	Magnesium carbonate (Magnesite)	
M_L	Mass (metal) loss	grams, g
Mr	Molar mass	$g \cdot mol^{-1}$
n	Charge number (valency)	
N_2	Nitrogen gas	
NaCl	Sodium chloride	
$NaHCO_3$	Sodium bicarbonate	
NaOH	Sodium hydroxide	
n_{aq}	Moles of aqueous CO_2	mole
n_t	Total moles of CO_2	mole
n_v	Moles of vapour phase CO_2	mole
O_2	Oxygen	

OCP	Open Circuit Potential	
OHP	Outer Helmholtz Plane	
pCO_2	CO_2 partial pressure	bar
ppb	Parts per billion	
ppm	Parts per million	
PLF	Pit-like Feature	
PR	Precipitation rate	
PTFE	Polytetrafluoroethylene	
Q	Effective capacitance	$(F \cdot cm^{-2})^{\alpha}$
Qdl	Effective double layer capacitance	$(F \cdot cm^{-2})^{\alpha}$
R	Universal gas constant	$J \cdot mol^{-1}K^{-1}$
R_{ads}	Adsorption resistor	$\Omega \cdot cm^2$
R_{ct}	Charge transfer resistance	$\Omega \cdot cm^2$
R_e	Electrolyte resistance	$\Omega \cdot cm^2$
RE	Reference Electrode	
R_p	Polarisation resistance	$\Omega \cdot cm^2$
R_W	Warburg resistance	$\Omega \cdot cm^2$
S_a	Active surface area	%
SE	Secondary Electron	
SEM	Scanning Electron Microscopy	
SHE	Standard Hydrogen Electrode	
SR	Saturation Ratio	
STEM	Scanning Transmission Electron Microscopy	
t	Time	Seconds, s
T_c	Temperature	Celsius, °C
TEM	Transmission Electron Microscopy	
TDS	Total Dissolved Salts	
T_f	Temperature	Fahrenheit, °F
T_k	Absolute temperature	Kelvin, K
U	Measured electrode potential	Volts, V
UV-Vis	Ultraviolet-visible	
V	Volume	Litres, L
WDXRF	Wavelength Dispersive X-ray Fluorescence	

WE	Working Electrode	
XANES	X-ray Absorption Near Edge Structure	
XPS	X-ray Photoelectron Spectroscopy	
XRD	X-ray Diffraction	
Z	Impedance	$\Omega \cdot cm^2$
Z_O	Warburg impedance	
α	Dimensionless coefficient between 0 and 1	
β_a	Anodic Tafel constant	$V \cdot decade^{-1}$
β_c	Cathodic Tafel constant	$V \cdot decade^{-1}$
δ	Film thickness	
ε	Permittivity	$F \cdot cm^{-1}$
ρ	Density	$g \cdot cm^{-3}$
η	Overpotential	Volts, V
τ	Time constant	Seconds, s
τ_D	Diffusion time constant	Seconds, s
Φ	Intermediate cell potential	Volts, V
Φ_{CO2}	CO_2 fugacity coefficient	
Φ_W	Warburg dispersion coefficient	
ω	Angular frequency	$rad \cdot s^{-1}$
ω_c	Characteristic frequency	$rad \cdot s^{-1}$

Chapter 1
Introduction

1.1 Background

In 2016, The National Association of Corrosion Engineers (NACE) International released the International Measures of Prevention, Application and Economics of Corrosion Technology Study (IMPACT). In this comprehensive analysis, the global cost of corrosion was estimated at around 2.5 trillion USD annually. This equated to 3.4% of global Gross Domestic Product (GDP). The IMPACT study suggested that up to 35% of this cost could have been saved by implementing existing control practices, such as monitoring techniques and maintenance procedures [1].

The capital-intensive industry of hydrocarbon recovery is a major driver for improved corrosion control. Operating facilities are heavily affected by corrosion, predominantly in aqueous environments, with costs amounting to as much as 27 billion USD for the USA oil and gas sector alone [2]. Further to cost, a number of high profile corrosion based incidents such as the Prudhoe Bay oil spill have seen the sector face unprecedented scrutiny both publicly and regulatory in relation to the environmental impact of failures [2, 3]. Carbon Dioxide (CO_2) corrosion has often been cited as the number one cause of corrosion failures in the industry, accounting for as much as 25% of all safety incidents [4]. Despite high susceptibility to CO_2 corrosion, carbon steel is the preferred choice of material for the vast majority of infrastructure in CO_2 environments due to its low cost, ease of manufacture and availability [4]. To combat failures and enhance the longevity of carbon steel components, operators typically employ a combination of pre-emptive strategies such as predictive modelling of the corrosion phenomena to inform material selection, coating requirements and cathodic protection, and routine monitoring to determine chemical inhibition schedules and maintenance [2].

A potential low-cost and environmentally sustainable alternative to chemical inhibition and coatings is to harness the protective nature of carbonate minerals that naturally form on carbon steels as part of the CO_2 corrosion process.

Where detailed studies have been performed on the performance of carbonate mineral deposits such as iron carbonate ($FeCO_3$) and ($CaCO_3$) as protective coatings on carbon steels, they have typically focused on near neural pH and atmospheric pressure where *in situ* characterisation and control over laboratory scale experiments is simplified. A detailed understanding of how these layers form over a wide range of conditions is necessary to fully optimise their performance as naturally formed protective coatings, not just in hydrocarbon recovery but the wider energy sector as highlighted in the following section.

1.2 Pertinent Applications in CO_2 Environments

Aside from typical hydrocarbon applications, demanding CO_2 environments are becoming increasingly prevalent across the energy sector. Remaining fuel supplies are becoming harder to extract, resulting in deeper wells and dependency on processes such as Enhanced Oil Recovery to meet future energy demands [1, 2, 5]. Geothermal applications and carbon capture solutions are perhaps even more critical as the world aims to reduce its carbon footprint and move towards cleaner energy sources [6, 7].

1.2.1 Carbon Capture and Storage (CCS)

Carbon Capture and Storage (CCS) categorises a number of new and developing technologies aimed at capture, purification, transport and sequestration of CO_2. This process is gaining recognition as a viable means to reduce CO_2 emissions from industrial processes. CCS can also provide a source of CO_2 for other applications such as Enhanced Oil Recovery (EOR) and has many uses within the food industry [8]. To achieve cost-effective, safe and efficient transportation, CO_2 is typically compressed into a supercritical ‘dense’ phase [9] above its critical point (31.1 °C and 7.38 MPa). In a pure form, CO_2 poses minimal corrosive threat. When coupled with impurities, and particularly water in the flow stream, the result can be an aggressive aqueous phase [10, 11]. CO_2 impurities can also impact EOR operations, causing unwanted reactions with hydrocarbons in the reservoir. Therefore, strict limits on allowable water and impurity content need to be imposed when utilising sequestered anthropogenic CO_2. Operating temperatures in CCS can typically range from 5 °C to 85 °C and pressures from 7.3 MPa to 30.0 MPa [9].

A study by Johnsen et al. [12] compiled reports of CO_2 pipeline failures recorded by the Pipeline and Hazardous Materials Safety Administration (PHMSA) in the US between 1986 and 2008 (Figure 1.1). The data collated likely omits many of the minor failures which did not directly lead to gas releases and were therefore not officially reported. Regardless, of the 29 failures documented, 45% were attributed to corrosion, making it the foremost contributor to CO_2 pipeline failures.

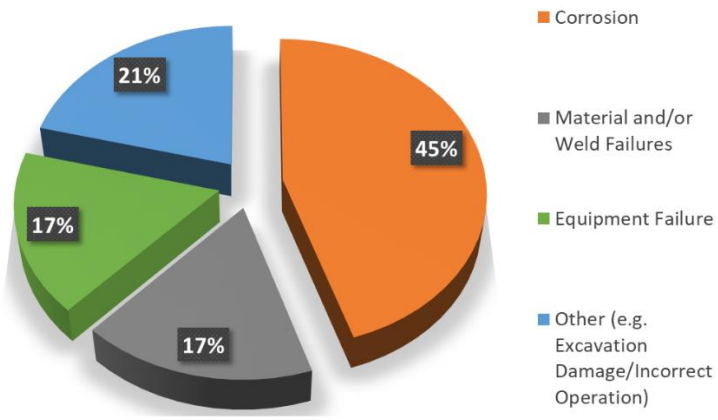

Figure 1.1: Failure modes of CO_2 pipelines in the US - adapted from [12]

Aside from transportation, the safe deposition of excess anthropogenic CO_2 into stable underground storage is a complex challenge. Studies such as those from the Research Centre for Gas Innovation in Brazil have driven the development of salt layer storage caverns for CO_2 and CH_4 in caverns up to 3km in depth. [13]. Other more convenient storage solutions exploit depleted oil and gas fields. However, Choi et al. [14] highlighted that wellbore integrity will be a concern. High pressure CO_2 can lead to corrosion rates of up to 20 $mm \cdot year^{-1}$ on carbon steel casing if cement integrity is poor and iron carbonate fails to form.

1.2.2 Enhanced Oil Recovery (EOR)

Enhanced Oil Recovery (EOR) refers to a third or 'Tertiary' phase of crude oil recovery. The precursors to this are primary recovery, which yields around 10 % of the original oil, and secondary recovery which extends this to between 20-40 %. In primary recovery the natural pressure of the reservoir is sufficient to drive oil into the wellbore where it is brought to the surface using pumps. In secondary recovery oil is driven in to the well bore through displacement by injected water or gas.

EOR is a more recent addition to the process, which has the potential to increase oil recovery to as much as 60% or more of the original oil content of a field [15, 16]. EOR processes are unique in that they also increase the mobility of the oil by reducing its viscosity or by increasing the permittivity of the well. The three major categories of EOR are as follows:

Chemical injection – Either uses long-chained polymers to improve waterflood efficiency, or detergent-like surfactants to lower the surface tension that can prevent oil droplets from passing through a reservoir. Chemical techniques account for around 1% of US EOR.

Thermal recovery - Uses heat, often from steam injection, to reduce the viscosity of heavy oils, improving their ability to flow through the reservoir. This technique accounts for over 40% of EOR production in the US.

Gas injection – This includes the use of gases such as CO_2 that expand in a reservoir to force additional oil into a production wellbore. Another method of gas injection is the use of gases that dissolve in the oil to reduce its viscosity and improve its flow rate. Gas injection accounts for almost 60% of EOR production in the US.

EOR is still a developing technique, and as such can often be costly and unreliable. This hasn't prevented the technique being heavily adopted in the US. According to a special report on CO_2-EOR [17], in 2010 there were over 114 active CO_2 injection projects. Combined, these projects injected over 2 billion cubic feet of CO_2 to recover over 280,000 Barrels of Oil per day (BOPD). The most promising area of EOR is certainly through the use of CO_2, in particular when it is combined with carbon capture techniques to offset CO_2 emissions into the atmosphere.

A 2010 report prepared for the British Governments Department of Energy & Climate Change (DECC) Office of Carbon Capture & Storage, highlighted that the economic viability of both CO_2-EOR and CCS is dependent on their combined usage. Global shortages in high purity CO_2 from natural sources is driving the need for CCS to supplement EOR. Meanwhile CO_2-EOR is seen as a facilitator for CCS in areas where financial incentives for sequestering CO_2 are limited and CCS is therefore un-economical.

Storing CO_2 concurrently with EOR can minimise the overall costs associated with CCS, encouraging oil producers to invest to increase hydrocarbon recovery. In developing countries, it is anticipated that the availability of CO_2-EOR opportunities may be a prerequisite for the initiation of CCS projects. Aside from facilitating CCS, another environmental advantage of EOR is that increasing reservoir life may result in a decrease in demand for new drill sites each year, reducing disruption to ecological systems. An example where CCS and EOR are being successfully applied is the Dakota Gasification Company's plant in Beulah, North Dakota. The plant sequesters anthropogenic CO_2 and delivers it by a 204-mile pipeline to the Weyburn oil field in Saskatchewan, Canada. The CO_2 supplied is expected to aid the retrieval of up to 130 million barrels of oil, extending the reservoir life by as much as 25 years [18].

In 1994 a report by Kapusta and Canter [19] assessed corrosion and corrosion control at the Little Creek Field (MS) CO_2-EOR project. Wells there started producing in 1986 with down-hole conditions of 24.1 MPa and 115 °C. The produced water had very high total dissolved solids (TDS), and a relatively high $CaCO_3$ scaling tendency due to 15200 $mg \cdot L^{-1}$ of Ca^{2+}. Other ions included 96,700 $mg \cdot L^{-1}$ Cl^-, 79 $mg \cdot L^{-1}$ SO_4^{2-}, 473 $mg \cdot L^{-1}$ HCO_3^-, 243 $mg \cdot L^{-1}$ Mg^{2+} and 14 $mg \cdot L^{-1}$ Ba^{2+}, as well as Na^+. Corrosion rates on N-80 steel casing was as high as 6.35 $mm \cdot year^{-1}$ after 10 months.

1.2.3 Geothermal

Geothermal energy is stored beneath the Earth’s surface in the form of heat and has been harnessed throughout human existence. Its early application was the natural heating of groundwater which produces hot springs and steam geysers useful for bathing and agriculture. In 1904 geothermal energy was first used to generate electricity and now deep systems are in operation in over 24 countries [20]. The heat energy comes from three main sources: residual heat from the accretion and formation of the planet; frictional heat produced as dense material sinks towards the planets core and heat from the decay of radioactive elements, primarily potassium, uranium and thorium [21]. According to the British Geological Survey [20] 99.9% of the Earth is at a temperature above 100 °C, making geothermal energy a substantial renewable resource.

Geothermal energy plants, as depicted in Figure 1.2, are typically located in areas of volcanic activity, such as in Iceland where it is the primary source of energy for heating and electricity.

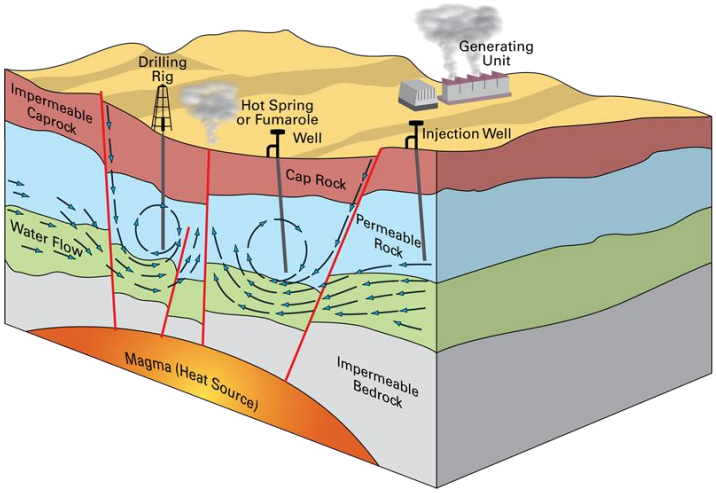

Figure 1.2: Geothermal Power Generation [20]

Nogara and Zarrouk [22] created a harmonized classification system (Table 1.1) for the corrosivity of fluids found in geothermal fields across the world. Geothermal brines are typically high in TDS and salinity whilst acidified by dissolved gases such as CO_2.

Table 1.1: Harmonized geothermal corrosivity classification

Class	Resource Type	Total Key Species (TKS), ppm	Chloride in TKS %	pH unflashed/ flashed	Resource temp/plant inlet temp, °C	$CaCO_3$, ppm
I	Liquid-dominated	>100,000	99	<5/5-6	326/199	
II-A	Liquid-dominated – acid sulfate (chloride)	1000-60,000	15-99	>3/<5	Not established	
II-B	Liquid-dominated – acid chlorine (sulfate)	500-40,000	20-99	<3	Not established	
III	Liquid-dominated	10,000-20,000	45-99	5-6/>6	178-300/149-191	
IV	Liquid-dominated	500-10,000	45-99	≥5/>6	137-280/121-199	
V-A	Liquid-dominated	<5000	3-72	6.7-7.6/NA	49-96/49-96	207-1239
V-B	Liquid-dominated	<5000	3-72	7.8-9.85/NA	120-205/120-205	<210
VI-A	Vapour-dominated	<1	-	NA	160-182/177-250	
VI-B	Vapour-dominated (High NCG)					
VI-C	Vapour-dominated (HCl gas production)					

1.2.4 Typical Brine Compositions

As evidenced, CO_2 saturated brines with high TDS are commonly encountered across the energy sector. Originating in deep underground reservoirs alongside gaseous phases, oils and organic acids, brines are also used for reinjection for enhanced oil recovery (EOR). The hydrostatic force in these environments means the brine is generally at elevated pressure and temperature [5]. Example brine compositions from a range of application are presented in Table 1.2.

Table 1.2: Example brine compositions from various CO_2 environments

Application	Ion Concentration /mg·L^{-1}								
	Cl^-	Na^+	K^+	Ca^{2+}	Mg^{2+}	Ba^{2+}	Sr^{2+}	SO_4^{2-}	HCO_3^-
1	96700	N/S	N/S	15200	243	14	N/S	79	473
2	39007	22115	32	2198	360	52	112	N/S	695
3	59000	27500	3250	6900	125	10	450	59	N/S
4	75200	38100	2200	7740	434	4	324	387	N/S
5	50000	40000		1500	500	N/S	N/S	1500	800

1 – Little Creek Field, Mississippi, CO2-EOR project [19]

2 – Average values from United States Geological Survey (USGS) database for deep water wells in the Gulf of Mexico based on ~11,000 data points [5]

3 – Soultz geothermal site in the Upper Rhine Graben (URG) [23]

4 – Bruchsal geothermal site in the Upper Rhine Graben (URG) [23]

5 – Tarim oilfield, Northwest China, ultra-deep oil well [24]

1.3 Utilisation of Corrosion Products as Protective Coatings

It has been well established that CO_2 environments can be conducive to the formation of $FeCO_3$ corrosion products on the surface of carbon steels, enabling them to withstand much harsher environments than would otherwise be expected [4, 25-27]. The mechanisms of $FeCO_3$ formation have been extensively studied in literature using laboratory experiments to determine ideal conditions for protective morphologies to form [28, 29]. Most studies typically focus on simple NaCl brines at atmospheric pressures, however the complex brine chemistry in real applications such as those in Table 1.2 have been shown to influence the physico-chemical properties of the corrosion product, subsequently altering its protective characteristics [11, 25, 30, 31].

There is potential for corrosion products to become an integral part of corrosion mitigation strategies, offering a low-cost, self-maintaining alternative to synthetic coatings and chemical inhibition with reduced environmental impact [32]. To achieve this objective relies on a much deeper understanding of their formation kinetics, how this is influenced by environmental factors and consequences this has on protectiveness.

1.4 Statement of Research Question

The research question is: What are the limitations of current laboratory scale corrosion test methodologies at elevated pressures and temperatures both in terms of maintenance of the bulk chemical environment, and the type of *in situ* characterisation that can be performed, and what is the consequence of this on our perception of corrosion layer formation and performance. In this study, the question is applied to carbonate formation on carbon steels in CO_2 environments in order to extend our knowledge of this process across a wider range of industry relevant conditions.

As Francis LaQue once said in his seminal work on corrosion testing:

"…sooner or later one's judgement may be questioned if continued use of an unreliable test in place of the exercise of good judgement in some other way should lead to a series of poor decisions" [33].

1.5 Research Objectives

In alignment with the research question, the objectives of the project are divided into fundamental scientific tasks and secondary objectives related to the practicalities of conducting experiments necessary to answer the primary research question.

1.5.1 Scientific Objectives

S1. Implement a CO_2 chemistry model to assess the influence of the corrosion process on the bulk chemical environment and identify a set of industry relevant conditions conducive to the formation of significant corrosion product layers

S2. Investigate the role of a common brine ion (Ca^{2+}) on the formation, morphology and performance of carbonate corrosion product layers using *ex situ* surface, elemental and gravimetric analysis techniques.

S3. Evaluate the electrochemical response of substrate steel as corrosion layers form using a combination of direct and alternating current techniques. Use this to determine the properties of the corrosion layer and identify key stages in corrosion layer formation.

S4. Corroborate *in situ* electrochemical and *ex situ* analysis techniques to establish the mechanism for substrate protection as well as causes of compromised layer integrity in demanding CO_2 environments

1.5.2 Methodological Objectives

M1. Establish a suitable methodology for preparation of CO_2 brines for experiments at elevated pressures and temperatures

M2. Investigate the effect that brine chemistry evolution due to the corrosion process has on the rate of corrosion product accumulation and relate this to observations from *ex situ* gravimetric analysis

M3. Perform electrochemical measurements and crystallographic analysis to investigate the long-term consequences of different rates of bulk chemistry evolution on corrosion layer properties.

M4. Corroborate *in situ* electrochemical and *ex situ* analysis techniques to establish the impact of an evolving system chemistry on corrosion product formation and the subsequent role this has on substrate protection and corrosion layer integrity.

A breakdown of how the results chapters of the thesis meet the research objectives is provided in Figure 1.3.

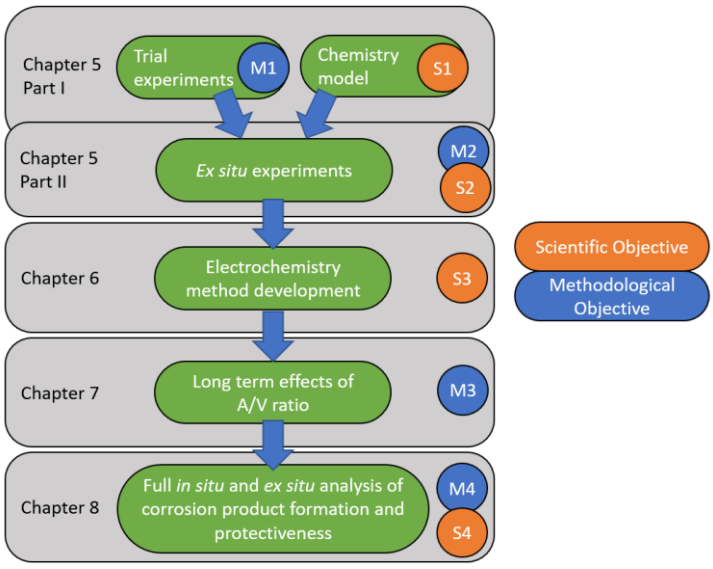

Figure 1.3: Structure of thesis results chapters in relation to research objectives

1.6 Thesis Outline

The thesis is broken down into ten chapters.

Chapter 1 is the introduction and justification for the project.

Chapter 2 introduces essential theoretical concepts relevant to aqueous corrosion, electrochemical techniques and the basic principles of the CO_2 corrosion mechanism and corrosion product nucleation and growth.

Chapter 3 is a review of literature on the formation of $FeCO_3$, followed by a comprehensive review specifically focused on mixed carbonate $Fe_xCa_yCO_3$ and electrochemical techniques used to evaluate such carbonate layers.

Chapter 4 covers the full experimental methodology employed in the research project, including a description of all apparatus, electrochemical and analytical techniques used.

Chapter 5 is the first of four results chapters. The first part introduces preliminary experiments and a parametric study by numerical modelling used to establish the operating conditions used for the remainder of the project. In the second part, a series of 3-day autoclave experiments are conducted using the experimental conditions derived from part 1.
Tests are conducted in the presence and absence of Ca^{2+} ions at two different solution volume to specimen area (A/V) ratios to investigate the effects of calcium incorporation into the corrosion product at different rates of bulk chemistry evolution. Corrosion performance is quantified by gravimetric analysis while corrosion layers are assessed through the use of microscopy, spectroscopy, and powder diffraction.

Chapter 6 builds on the findings of Chapter 5 to establish an appropriate method for *in situ* electrochemical characterisation of layers that formed previously, with a focus on $FeCO_3$ formed in the absence of Ca^{2+} over longer periods at a low A/V ratio.

Chapter 7 extends the analysis performed in Chapter 6 to $FeCO_3$ formed at a high A/V to establish the long-term impact of initial bulk solution evolution rates on the structure and electrochemical properties of the corrosion product layer.

Chapter 8 revisits the full experimental matrix of Chapter 5 part 2 coupled with the electrochemical analysis developed in Chapter 6 and executed over longer periods of up to 7 days. Electrochemical measurements are compared with gravimetric analysis as well as profilometry to assess localised corrosion.
A detailed look at the build-up of competing corrosion and scale components within the layers is also performed using Selected Area Electron Diffraction (SAED) and Scanning Transmission Electron Microscopy (STEM). This provides a detailed picture of the effects of bulk solution evolution rates and calcium incorporation on the formation, structure, performance and integrity of corrosion scales formed in demanding CO_2 environments.

Chapter 9 is the discussion section which pulls together all of the results chapters and compares and contrasts this with the currently available literature.

Chapter 10 is the final conclusions of the project and also includes recommendations for future work.

Chapter 2

Theory of Aqueous CO_2 Corrosion and Electrochemistry

2.1 Introduction

This section provides an overview of the key concepts of corrosion in an aqueous environment as well as relevant electrochemical techniques for corrosion analysis. This information will serve as the foundations for later literature review and experimental methodology.

2.2 Definition of Corrosion

A generalised definition of corrosion is the destruction or deterioration of a material by reaction with its environment [34]. For the purpose of this work the definition will only apply to metallic materials under chemical or electrochemical attack. Degradation of metallic components can also be the result of mechanical processes. Fracture and fatigue occur due to applied or cyclic stresses. Erosion and wear are a result of relative motion between contacting solid surfaces or at a solid to liquid interface. A combination of one or more of these degradation processes with a corrosion mechanism is known as mechanically assisted corrosion and can often lead to rapid and catastrophic failures [34].

2.3 Electrochemical Corrosion

In most cases, corrosion is an electrochemical process whereby the metal reacts with its environment through a series of coupled half-cell reactions [34]. These half-cell reactions induce a continuous movement of charged particles in the system i.e. an electrical current. In aqueous corrosion the fundamental features which allow current flow are the molecular nature of the metal, an electrolytic solution and the chemical reactions that take place at the interface between them. The Fermi sea of electrons in a metal allow negative charge to be transferred easily within the material. An electrolytic solution can transfer charge through diffusion of ions such as dissolved salts in water. The movement of electrons, whilst detrimental to the material, also enables the measurement of electrical potential and current which can be used to infer corrosion mechanisms and rates.

2.3.1 Half Cell Reactions

Half-reactions are a means to display both components of an overall reaction in which electron transfer takes place. When metal ions pass into solution they leave behind freely moving valence electrons which remain in the metal lattice. This is termed an Anodic or Oxidation reaction since the release of negative charge carriers (electrons) results in an increased net charge on the ion. The excess electrons are consumed in a Cathodic or Reduction reaction. The overall reaction is also termed a REDOX reaction. By convention, anodic reactions are written with the electron appearing on the right hand side of the reaction as a product while electrons appear on the left as reactants in cathodic reactions [34]. For a corroding metal M, the anodic reaction is:

$$\mathrm{M} \rightarrow \mathrm{M}^{n+} + \mathrm{ne}^{-} \tag{2.1}$$

Where n is equivalence or moles of electrons e^{-} transferred per mole of metal species M.

2.3.2 Coupled Electrochemical Reactions

In the simple analogy for a galvanic cell, anodic reactions take place at an anode while cathodic reactions take place at a cathode. These are represented by fixed components of dissimilar potentials in Figure 2.1(a). On a corroding metal surface this is better visualised as anodic and cathodic sites which can change position over time [35] as illustrated in Figure 2.1 (b). These sites are made possible by the heterogeneous nature of the metal surface.

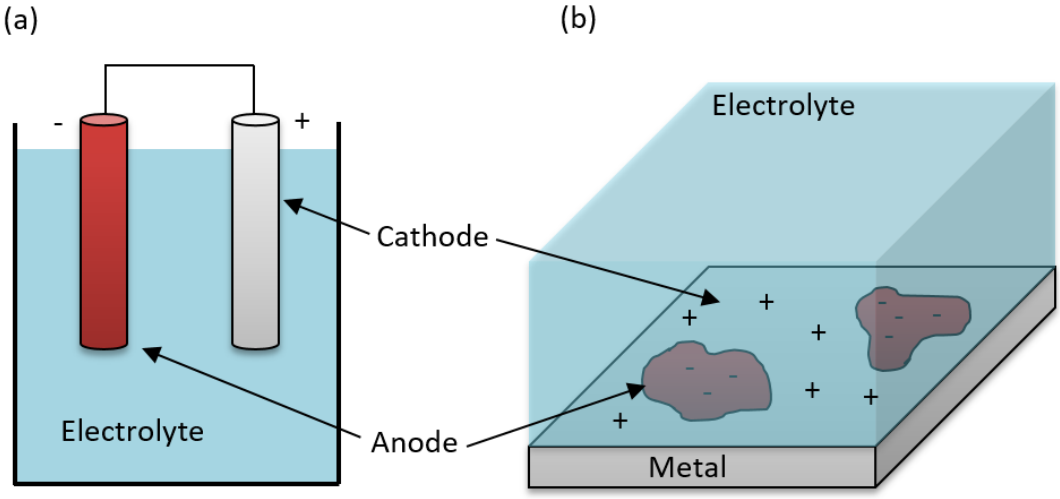

Figure 2.1: (a) Depiction of simple galvanic cell and (b) schematic of local corrosion cells on a metal surface

Dissimilar crystal faces and grain boundaries present varying site energies in polycrystalline metals. In addition, defects, impurities and adsorbed ions from the electrolyte can also change the surface energy of the local metal ions [34]. These sites may change position frequently, reaching a dynamic equilibrium whereby the entire surface will corrode uniformally. In the case of localised corrosion, the sites remain relatively fixed and disparities in surface energy increase, accelerating the corrosion mechanism. A Scanning Electrochemical Microscope (SECM) can be used to visualise these areas as shown in Figure 2.2.

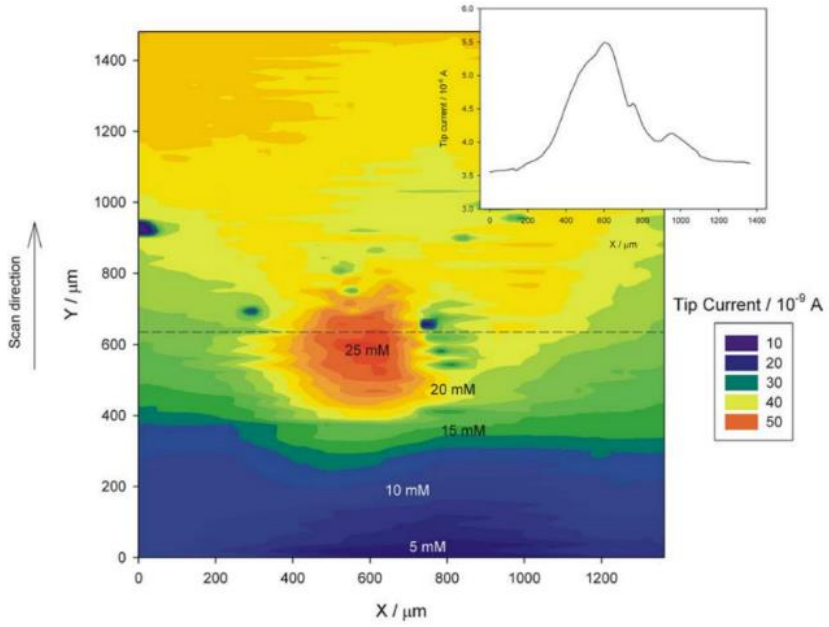

Figure 2.2: SECM contour plot showing anodic region (red) due to defect on tin plate immersed in 10mM H_2SO_4 [36]

2.4 Faraday's Law

As discussed, corrosion is a multi-step chemical process on an atomic scale, dictated by the transport of atomic, molecular or ionic species. The exact stages of the process are impossible to visualise at this scale and are typically extrapolated from indirect measurements such as mass loss or surface changes [37]. In the early nineteenth century, Michael Faraday identified a quantifiable link between the current flowing in an electrochemical cell and the rate at which matter was deposited or released in the system [35]. It is therefore stated that current, which is the coulombic flowrate of charge carriers, is proportional to the equivalent mass of material reacting per second. As expressed in equation (2.2).

$$M_L = \frac{I \cdot t \cdot Mr_m}{n \cdot F} \quad (2.2)$$

Where M_L is metal loss in grams, t is time in seconds, I is the faradaic current in Ampere and Mr_m is the molar mass of the metal. F denotes the Faraday constant which is approximately 96485 Coulombs per mole. The method of obtaining the current I in a corroding system first requires the introduction of some important concepts and thermodynamic principles.

2.5 The Electrical Double Layer

In aqueous corrosion the electrical double layer (EDL) refers to the arrangement of charged species at the interface between the metal and solution. Solution ions near the interface will orient themselves in a way that balances the charge on the metal surface. In doing so, there becomes a net charge difference between the interface layer and neutrally charged bulk solution [34]. According to the Bockris-Devanthan-Müller (BDM) model there are multiple stages to a water-based electrolyte layer. The first stage, known as the Inner Helmholtz Plane (IHP), consists of competing adsorbed ions and orientated water molecules. The adsorbed ions are closely followed by hydrated counter ions in the Outer Helmholtz Plane (OHP). After this is the Guoy-Chapman diffuse layer which balances the charge on the inner layers. The ions here are more randomly distributed and freely moving [38].

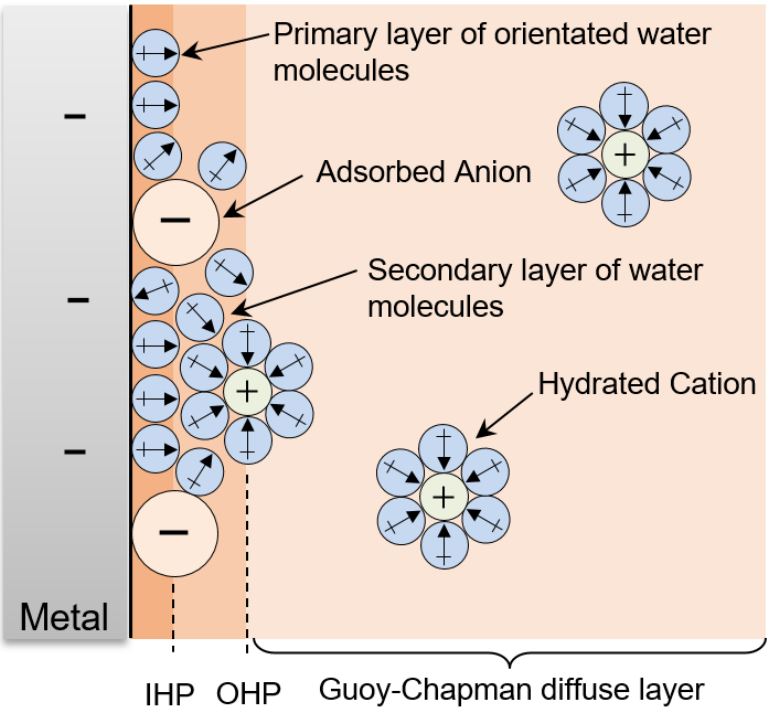

Figure 2.3: BDM model of the Electrical Double Layer [38]

The importance of the double layer is that it creates a potential barrier through which ions must cross to move between the metal surface and the bulk solution. The double layer effectively acts like a parallel plate capacitor as shown in Figure 2.4. The magnitude of the potential difference across the EDL can be measured against a reference electrode which will be discussed later.

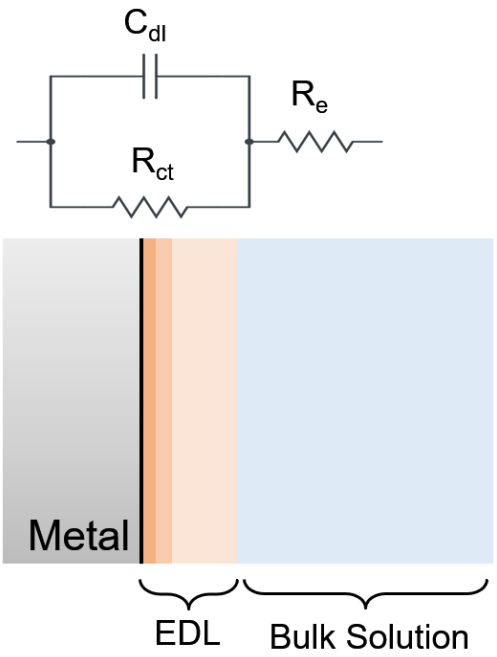

Figure 2.4: Equivalent capacitive circuit of EDL and bulk solution

2.6 Overview of Thermodynamics

It has been established in the previous section that an electromotive force (EMF) drives the corrosion process, under freely corroding conditions this force or potential, is provided by the energy transfer that occurs in the half cell reactions [35]. The link can be made between potential and energy change using the following equation:

$$\Delta G = -nFE \tag{2.3}$$

Where ΔG is the change in Gibbs free energy in Joules and E is the EMF in volts. ΔG is also an indicator for which direction a reaction is likely to proceed. A reaction is spontaneous if the change in free energy is negative. This is referred to as an exergonic reaction, indicating a release of energy. The negative sign in (2.3) means that the reverse is true when discussing potentials. Under standard conditions, denoted by °, equation (2.3) becomes:

$$\Delta G^\circ = -nFE^\circ \tag{2.4}$$

E° is known as the Standard Electrode Potential which is tabulated for metals in various texts as the EMF series.

E° is typically quoted as the reduction potential therefore a greater positive potential indicates a less reactive material.

2.6.1 The Nernst Equation

Building on equations (2.3) and (2.4), the change in free energy can be expressed using thermodynamic properties and a known free energy at standard conditions:

$$\Delta G - \Delta G° = RT_k \ln \frac{[a_p]}{[a_r]} \tag{2.5}$$

Where R is the universal gas constant (8.314 $J \cdot mol^{-1}K^{-1}$) and T_k is temperature in Kelvin, $[a_p]$ and $[a_r]$ are calculated using the activities of the reactants and products respectively. An example is given below:

$$\text{if} \quad xX \rightarrow yY + zZ \quad \text{then} \quad \frac{[a_p]}{[a_r]} = \frac{{a_Y}^y \cdot {a_Z}^z}{{a_X}^x} \tag{2.6}$$

Where x, y and z represent the moles of species X, Y and Z with activities of a_X, a_Y and a_Z respectively. Activity is a measure of the effective concentration of a species under non-ideal conditions. For a gas, this would be replaced with its fugacity, a measure of effective partial pressure. An activity or fugacity of one indicates an ideal solution or gas. For dilute solutions, activities can be replaced by the corresponding concentrations [37]. Combining equations (2.3), (2.4) and (2.5) gives an expression for electrode potential at non-standard conditions as a function of activities:

$$E = E° - \frac{RT_k}{nF} \ln \frac{[a_p]}{[a_r]} \tag{2.7}$$

This is known as the Nernst equation. The importance of this equation is it defines the potential of a given reaction from which other unknown potentials can be measured against. Reference and pH electrodes are designed on the principles of the Nernst equation, these electrodes can be coupled with another of unknown potential in an electrochemical cell. The two electrode or half-cell potentials can be summed using the following equation:

$$E_{cell} = E_{cathode} - E_{anode} \tag{2.8}$$

Where E_{cell} is the cell potential. $E_{cathode}$ and E_{anode} are cathodic and anodic reduction potentials. As described previously, a positive potential indicates a negative Gibbs free energy, therefore reactions will spontaneously occur if E_{cell} is positive.

2.6.2 Drivers for Corrosion Reactions

Corrosion rate is a multi-faceted phenomenon ultimately driven by how favourable the reactions are and the rate at which these reactions can be facilitated at the material-solution interface. Increasing temperature can increase the kinetics of a reaction and make the reaction more favourable within the EDL but it can also alter the equilibrium concentration of species in the bulk solution. This is particularly complex with multiphase systems. In terms of facilitating reactions this can be divided into three modes of mass transport.

- Migration, which is the motion of charged particles due to electrical potential gradients.
- Diffusion, the motion of species due to chemical potential i.e. concentration gradients.
- Convection, due to hydrodynamic effects, this can be a forced convection in a flowing or stirred system or a natural convection such as in the presence of density gradients [39].

These transport systems can be hindered by the formation of natural protective films on the metal surface or by the presence of inhibitors. Potential gradients can be overcome by an external voltage source while sacrificial materials can be used to protect the material by preferentially corroding. Understanding mass transport mechanisms is essential for interpreting electrochemical measurements, particularly in complex CO_2 environments.

2.7 The CO_2 Corrosion Mechanism

The actual mechanisms of corrosion in brines containing carbonic acid and or other weak acids have been the subject of much discussion in recent years [40]. By definition, a weak acid such as carbonic or acetic does not fully dissociate into its component ions when dissolved in water. This implies that the acid can act as a reservoir for hydrogen ions when H^+ is consumed at the cathodic site in a corrosion process. The full process of uniform attack of carbon steel by CO_2 corrosion is illustrated in Figure 2.5. The process starts by the slow dissolution of CO_2 into its aqueous form. A fraction of the aqueous CO_2 is then reversibly hydrated to form carbonic acid H_2CO_3. As a weak diprotic acid, part of the H_2CO_3 quickly disassociates, releasing a single proton (H^+) to the surrounding water molecules.

This forms a hydronium ion H_3O^+ and bicarbonate ion HCO_3^-. The bicarbonate ion also partially and reversibly disassociates into a proton and carbonate ion CO_3^{2-}. For simplicity, the remainder of this report will refer to hydrogen ions (H^+), in place of hydronium (H_3O^+) as the net reactions are thermodynamically equal. These reversible reactions will progress or recede at different rates depending on the thermodynamics and kinetics of the reaction and the activities of each species.

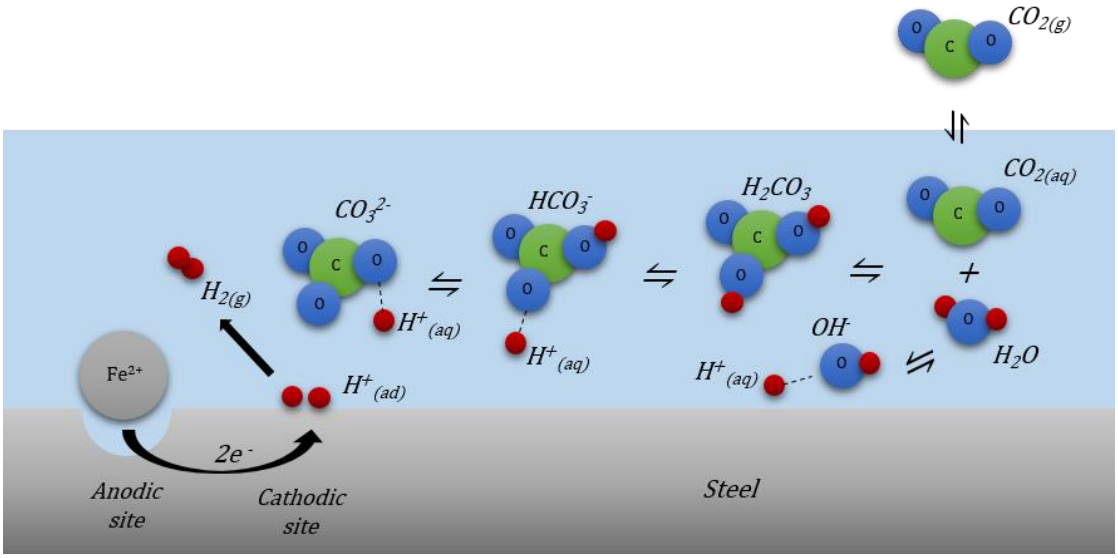

Figure 2.5: Simplified CO_2 Corrosion Mechanism in Aqueous Solution

In a static system, both forward and backward reactions will eventually reach a dynamic equilibrium. The hydration reaction which forms carbonic acid is kinetically much slower than dissociation reactions thereafter and is therefore the rate determining step in the process [25]. Further detail on the consequences of these reactions is presented in Chapter 5.

2.7.1 Cathodic Reactions

For a basic CO_2 saturated brine, the primary cathodic reaction which occurs at the steel surface is the direct reduction of hydrogen ions to form hydrogen gas. The mechanism for this is electrochemical adsorption of the hydrogen ion on to the metal surface (2.9) followed by electrochemical (2.10) or chemical desorption (2.11).

$$H^+_{(aq)} + e^- \rightarrow H_{ads} \quad (2.9)$$

$$H_{ads} + H^+_{(aq)} + e^- \rightarrow H_{2(g)} \quad (2.10)$$

$$H_{ads} + H_{ads} \rightarrow H_{ads} \quad (2.11)$$

Over the years many other reactions and pathways have been proposed as summarised by Dugstad in 2006 [26] and Barker et al. in 2018 [25]. These include the direct reduction of H_2CO_3 and at low pCO_2 and high pH, the direct reduction of water molecules as well as the bicarbonate ions.

$$2H^+_{(aq)} + 2e^- \rightarrow H_{2(g)} \quad (2.12)$$

$$2H_2CO_{3(aq)} + 2e^- \rightarrow H_{2(g)} + 2HCO^-_{3(aq)} \quad (2.13)$$

$$2HCO^-_{3(aq)} + 2e^- \rightarrow H_{2(g)} + 2CO^{2-}_{3(aq)} \quad (2.14)$$

$$2H_2O_{(l)} + 2e^- \rightarrow H_{2(g)} + 2OH^-_{(aq)} \quad (2.15)$$

De Waard and Milliams [41] were amongst the first to investigate the mechanisms of CO_2 corrosion of pipeline steel. Their model, published in 1975 and still used today, postulates that direct reduction of carbonic acid is the primary cathodic reaction. Later studies by Kahyarian and Nešić [40] have since concluded that the direct reduction of carbonic acid is negligible under typical oil and gas conditions used in their experiments. Using a mechanistic approach, they were able to obtain a good agreement between their mathematical models and laboratory experiments using reduction of protons as the sole cathodic reaction in their calculations. The test parameters included a pH range of 4-5, pCO_2 of 0-5 bar and temperatures of 30 °C and 10 °C. The low temperature allowed for a decrease in the charge transfer reactions with a lesser effect on the limiting currents, giving a clearer observation of the charge transfer controlled regions of the anodic and cathodic polarisation curves. The experiments showed that as CO_2 partial pressure increased, and thus carbonic acid concentration, there was an insignificant change in the charge transfer response of the cathodic branch of the polarisation curve. The authors claimed that these findings prove that direct reduction of H_2CO_3 has no effect on the corrosion mechanism under the conditions tested.

2.7.2 Anodic Reactions

The anodic process can be described by a single overall reaction which is the release of a ferrous ion (Fe^{2+}) into the solution:

$$Fe_{(s)} \rightarrow Fe^{2+}_{(aq)} + 2e^- \quad (2.16)$$

Bockris et al. [42] described the mechanism for this process in strong acids:

$$\begin{gathered} \mathrm{Fe_{(s)} + H_2O_{(l)} \rightleftharpoons (FeOH)_{ads} + H^+_{(aq)} + e^-} \\ \mathrm{(FeOH)_{ads} \rightarrow FeOH^+_{(aq)} + e^-} \\ \mathrm{FeOH^+_{(aq)} + H^+_{(aq)} \rightleftharpoons Fe^{2+}_{(aq)} + H_2O_{(l)}} \end{gathered} \tag{2.17}$$

Since publication in 1961 this 'consecutive' mechanism has been widely adopted to describe the dissolution of iron in a CO_2 environment, much to the criticism of some researchers [27]. A more recent study by Nešić et al. in 1996 [43] reported that CO_2 has a role in the dissolution process. Based on the observation that iron dissolution has different kinetics in CO_2 compared to strong acids, they inferred that carbonic species must act as chemical ligands and catalyse the dissolution of iron, an effect independent of pH. Noting that H_2CO_3 and dissolved CO_2 are the only carbonic species independent of pH and with CO_2 present in much higher concentrations than H_2CO_3 the following mechanism was proposed:

$$\begin{gathered} \mathrm{Fe + CO_2 \rightleftharpoons Fe_L} \\ \mathrm{Fe_L + H_2O \rightleftharpoons Fe_LOH_{ad} + H^+ + e^-} \\ \mathrm{Fe_LOH_{ad} \rightarrow Fe_LOH^+_{ad} + e^-} \\ \mathrm{Fe_LOH^+_{ad} + H_2O \rightleftharpoons Fe_L(OH)_{2ad} + H^+} \\ \mathrm{Fe_L(OH)_{2ad} \rightleftharpoons Fe_L(OH)_{2sol}} \\ \mathrm{Fe_L(OH)_{2sol} + 2H^+ \rightleftharpoons Fe^{2+} + CO_2 + 2H_2O} \end{gathered} \tag{2.18}$$

Where Fe_L = Fe-CO_2 is the chemical ligand formed as an adsorbed species at the metal surface.

2.7.3 Corrosion Product and Scale Formation in CO_2 Environments

When conditions are favourable, iron dissolution in a CO_2 saturated brine leads to the precipitation and formation of corrosion products, the most common of which is iron carbonate ($FeCO_3$) [4, 26, 27]. Magnetite (Fe_3O_4) is also commonly observed within the corrosion product layers at higher temperatures (>100 °C) or high pH while $Fe_2(OH)_2CO_3$, $Fe_6(OH)_{12}CO_3$, $Fe_6(OH)_{12}CO_3{\cdot}H_2O$ and $Fe_2O_2CO_3$, have also been proposed to form on mild steel at temperatures between 20 and 40 °C [44, 45]. The presence of alkaline earth metals in the aqueous media such as calcium (Ca) and magnesium (Mg) also leads to the precipitation of scales. Like Fe, Ca and Mg are commonly observed divalent cations in CO_2 systems and can bond with CO_3^{2-} ions to form calcium carbonate ($CaCO_3$) and magnesium carbonate ($MgCO_3$).

The isostructurality of these carbonate scales means that Ca^{2+} and Mg^{2+} can substitute Fe^{2+} in the $FeCO_3$ lattice and/or co-precipitate to form complex corrosion scales with unique characteristics. Calcium in particular has a high affinity to co-precipitation with Fe to form $Fe_xCa_yCO_3$ and is the primary focus of the current work. Table 2.1 provides a summary of the chemical and morphological properties of $FeCO_3$, Fe_3O_4 and the polymorphs of $CaCO_3$.

Table 2.1: Common CO_2 corrosion products and scales

Corrosion Products			
Mineral	Siderite	Magnetite	
Category	Carbonate	Iron Oxide	
Composition	$FeCO_3$	Fe_3O_4	
Crystal System	Trigonal	Cubic	
Morphology	Rhombohedral	Octahedral	
Density (kg/cm^3)	3.96	5.1	
Mohs Hardness	5.5-6	3.5	
Calcium Carbonate Polymorphs			
Mineral	Calcite	Aragonite	Vaterite
Category	Carbonate	Carbonate	Carbonate
Composition	$CaCO_3$	$CaCO_3$	$CaCO_3$
Crystal System	Trigonal	Orthorhombic	Hexagonal
Morphology	Rhombohedral	Prismatic	Spherulitic
Density (kg/cm^3)	2.71	2.93	2.54
Mohs Hardness	3	3.5-4	3

Mineral property data taken from [46], [47], [48] and [49]

2.7.3.1 Iron Carbonate ($FeCO_3$) Corrosion Product

Iron carbonate ($FeCO_3$) in its mineral form is known as siderite, a member of the trigonal crystal system. When formed as a corrosion product, $FeCO_3$ typically appears as large rounded rhombohedral crystals as depicted in Figure 2.6. $FeCO_3$ will precipitate when the product of the activities of Fe^{2+} ($a_{Fe^{2+}}$) and CO_3^{2-} ($a_{CO_3^{2+}}$) exceed the solubility limit (K_{sp}) for $FeCO_3$. The saturation ratio (SR) gives a measure of the supersaturation and likelihood of precipitation:

$$SR_{FeCO_3} = \frac{a_{Fe^{2+}} \cdot a_{CO_3^{2+}}}{K_{sp}} \tag{2.19}$$

Where $FeCO_3$ formation is generally reported as a one step process:

$$Fe^{2+} + CO_3^{2-} \rightleftharpoons FeCO_3 \tag{2.20}$$

The relatively slow kinetics of $FeCO_3$ precipitation compared with $CaCO_3$ means that a high supersaturation at the steel surface is required to form a protective layer [25]. These crystals can form densely packed layers that block active sites on the metal surface and act as diffusion barriers to slow down the corrosion process. Conversely, if a less tenacious layer forms it can be prone to breakdown and or poor coverage which can results in localised attack on the substrate [25].

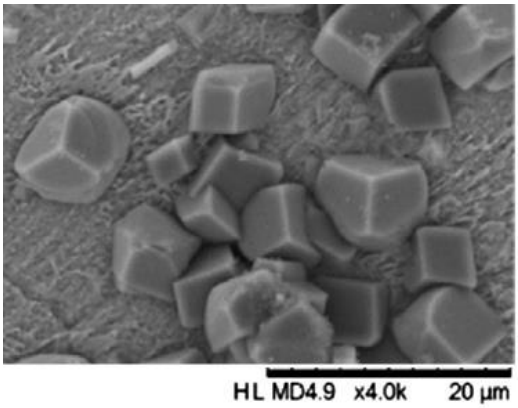

Figure 2.6: Typical morphology of $FeCO_3$ formed on a steel surface from [47]

2.7.3.2 Iron Oxide Fe_3O_4 Corrosion Product

Fe_3O_4 occurs naturally as the mineral magnetite, one of the most abundant forms of iron ore and the first material discovered to exhibit magnetism. Magnetite belongs to the Hexoctahedral class of the Isometric (Cubic) crystal system and contains both ferrous (Fe^{2+}) and ferric (Fe^{3+}) cations. The crystal morphology is most commonly fine and octahedral but can be modified by cation substitution or the presence of organic compounds in the aqueous solution [46, 50]. Fe_3O_4 has been observed to form in anaerobic CO_2 environments [50, 51], particularly at temperatures above 100 °C [52, 53].

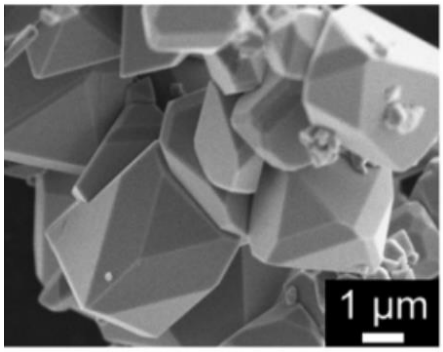

Figure 2.7: Synthesised Fe_3O_4 crystals with quasi-octahedral structure [46]

Schikorr proposed that Fe_3O_4 forms from iron(II) hydroxide in anaerobic conditions according to the following reaction [54]:

$$3Fe(OH)_2 \rightarrow Fe_3O_4 + H_2 + 2H_2O \quad (2.21)$$

2.7.3.3 Calcium Carbonate $CaCO_3$ Scale

$CaCO_3$ is a naturally occurring substance found in mineral form as one of three polymorphs. Calcite is the most stable form and just like siderite, belongs to the Hexagonal Scalenohedral class of the Trigonal crystal system in its natural mineral form. Aragonite is a less stable form of $CaCO_3$ with a needle like structure and will eventually transition to calcite at ambient conditions. Vaterite is the least stable polymorph and will transition to calcite or aragonite at low or high temperatures respectively.

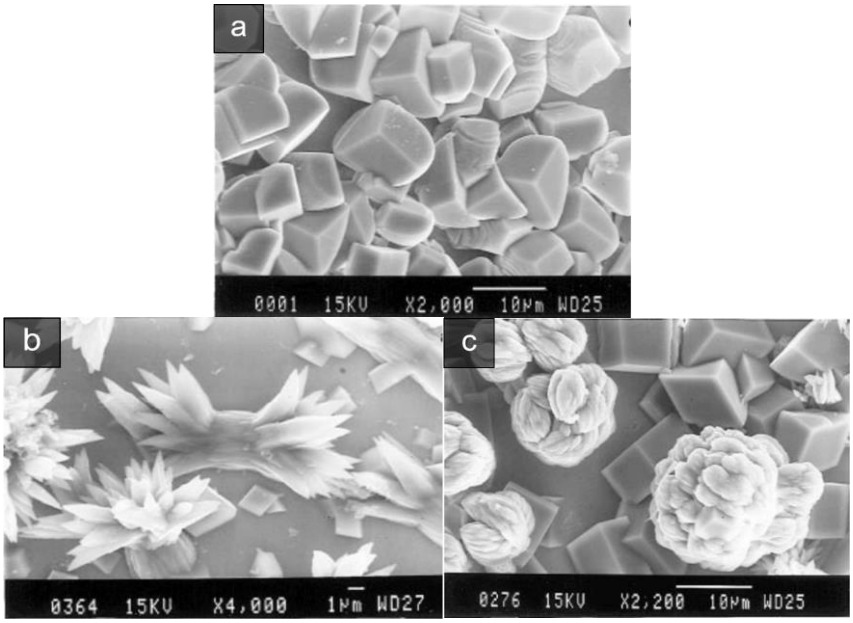

Figure 2.8: Polymorphs of $CaCO_3$ from [48] (a) Calcite (b) Aragonite (c) Vaterite

2.8 Introduction to Electrochemical Measurements for Corrosion

2.8.1 The Electrochemical Cell

Before discussing measurement techniques it is important to introduce the key components of an electrochemical cell and their typical configurations. Aside from the solution, the most important elements of an electrochemical cell are the electrodes. Electrodes can be categorised as current carrying (which includes working and counter electrodes) or sensing elements (reference electrodes). A working electrode is the material that is under investigation i.e. corroding in the case of corrosion experiments.

A Counter or Auxiliary electrode is used to complete the electrochemical circuit. While transferring current, reactions at the counter electrode interface should not interfere with the working electrode. This means that the counter electrode has to be made from a highly stable material, typically platinum [37].

2.8.1.1 Reference Electrodes

A reference electrode is used as a sensing element from which other potentials in the system can be measured. A reference therefore requires a stable reduction potential regardless of the external environment. The benchmark for this is the Standard Hydrogen Electrode (SHE) which is arbitrarily given the potential of 0 V across all temperatures. This is achieved when the fugacity of H_2 and activity of H^+ ions are both unity in a saturated hydrogen solution. Where an electrode potential is expressed in terms of SHE it is said to be on the Standard Hydrogen scale [35]. For practical applications particularly in corrosion testing, the SHE is often substituted for a more convenient design. The two most common approaches are the Calomel electrode and the Silver-Silver Chloride electrode.

Calomel Reaction:

$$\mathrm{Hg_2Cl_2 + 2e^- \rightarrow 2Hg + 2Cl^-} \qquad (\mathrm{E° = 0.268V\ vs\ SHE}) \tag{2.22}$$

Silver-Silver Chloride Reaction:

$$\mathrm{AgCl + e^- \rightarrow Ag + Cl^-} \qquad (\mathrm{E° = 0.222V\ vs\ SHE}) \tag{2.23}$$

Both electrodes can be designed using a potassium chloride filler solution which is separated from the main test cell solution. Charge transfer is made possible through a porous junction such as a glass frit. The junction provides a source of potential difference between the two solutions and has to be accounted for in test measurements if appreciable.

In high pressure applications, conventional glass bodied reference probes are unsuitable. The most common approach to navigate this problem is the use of an external pressure balanced electrode. This type of probe has its electroactive elements outside of the pressure envelope which allows them to be kept at ambient conditions. Connection to the test environment is made through a cooled electrolyte bridge. This means commercial products such as Ag/AgCl electrodes can be used. The disadvantage of external electrodes is that the non-isothermal nature of the electrolyte bridge results in large junction potentials induced by the temperature gradient.

Contamination of the reference electrolyte can also occur due to large pressure gradients drawing test solution across the junction [6, 55]. Internal probes may offer a more precise alternative; however, few electroactive materials are capable of resisting thermal hydrolysis at temperatures above 200 °C and are prone to potential drift over prolonged test periods.

2.8.1.2 Electrode Configuration

Electrochemical measurements utilise a two, three or four electrode configuration to measure potential differences and to pass current during polarisation. Figure 2.9 provides a simplistic map of potential drops in an electrochemical cell with points A and E representing connections to the working and counter electrodes respectively. Points B and D represent the potential at the outer edge of the EDL just inside the electrically neutral diffusion layer. Point C describes the potential within the solution. A two electrode setup comprises a working and counter electrode which pass current between them whilst also acting as sensing elements. In a two electrode setup the net potential drop across the entire cell is what is measured i.e., between points A and E as described in equation (2.8). The most commonly adopted configuration is the three electrode cell in which an additional reference electrode is placed near to the working electrode but still within the bulk solution (Point C). This allows more accurate measurement of the half-cell potential independent of changes occurring at the counter. The measured electrode potential (U) with respect to the reference is:

$$\mathrm{U} = (\Phi_{\mathrm{A}} - \Phi_{\mathrm{C}}) \equiv (\Phi_{\mathrm{WE}} - \Phi_{\mathrm{RE}}) \tag{2.24}$$

The measured potential can be written in terms of the potential adjacent to the working electrode at the outer edge of the EDL, Φ_0 (i.e., Point B):

$$\mathrm{U} = (\Phi_{\mathrm{A}} - \Phi_{\mathrm{B}}) + (\Phi_{\mathrm{B}} - \Phi_{\mathrm{C}}) \equiv (\Phi_{\mathrm{WE}} - \Phi_{0}) + (\Phi_{0} - \Phi_{\mathrm{RE}}) \tag{2.25}$$

Where $(\Phi_{\mathrm{WE}} - \Phi_0)$ represents the interfacial potential E and $(\Phi_0 - \Phi_{\mathrm{RE}})$ represents the ohmic potential drop due to electrolyte resistance, R_e.

Equation (2.25) can therefore be expressed as:

$$\mathrm{U} = \mathrm{E} + \mathrm{i}R_e \tag{2.26}$$

In most cases an ideal setup would place the RE close to point B to minimise ohmic potential drop.

For some specialised applications a four-electrode cell is employed which measures potential changes across the electrolyte itself as opposed to the electrodes. This involves placing reference electrodes close to points B and D, an example would be to measure impedance across membrane or liquid-liquid junctions.

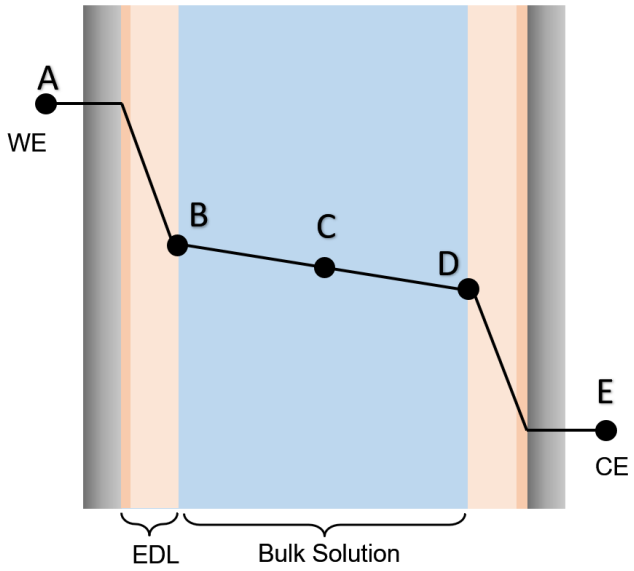

Figure 2.9: Schematic of potential drop across an electrochemical cell reproduced from [56]

2.8.2 Polarisation

Electrochemical polarisation is the change in electrode potential due to the flow of current [34]. This can be categorized into the following:

- Activation (charge transfer) polarisation – caused by slow reaction kinetics
- Concentration polarisation – caused by concentration changes in the EDL
- Ohmic polarisation – caused by IR drops in the solution or across surface films

An important example of polarisation is the electrolysis of water. When polarized to its reduction potential, water will break down to form O_2 and H_2 gases. The mode for this depends on the pH of the system as highlighted by Figure 2.10.

The degree of polarisation is termed overpotential, η which is defined as:

$$\eta = E - E_o \tag{2.27}$$

Where E_o is the interfacial potential when the net current flow from anodic and cathodic reactions is zero, known as the open-circuit potential or corrosion potential.

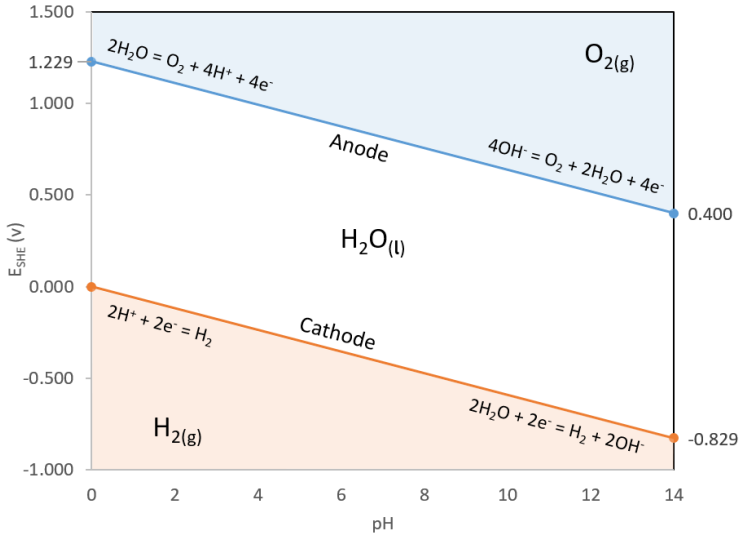

Figure 2.10: Pourbaix Diagram for electrolysis of water at standard conditions (25 °C and unity partial pressure of H_2) measured against Standard Hydrogen Electrode

Whilst it is possible to measure open circuit potential from a reference potential, it is not possible to directly measure the reaction rate in either direction at this condition, known as the exchange current density, i_o. To achieve this, the system needs to be perturbed from equilibrium using experimental techniques. Figure 2.11 illustrates the response of X65 mild steel to both anodic and cathodic polarisation.

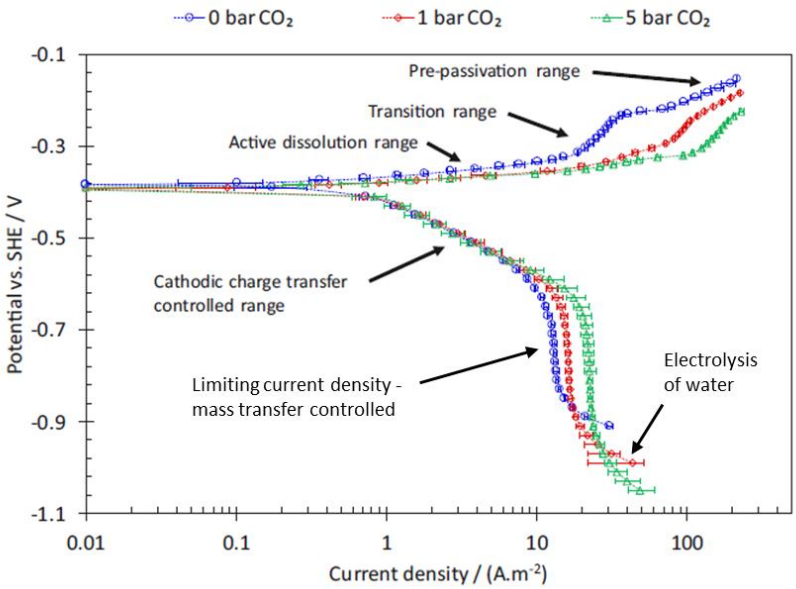

Figure 2.11: Anodic and cathodic polarisation behaviour of X65 mild steel in acidic solutions, at 10C, 12.9ms^{-1} flow velocity, 0.1 M NaCl, pH 4 and varying pCO_2 [40]

Regions of each curve display different correlations between overpotential and current density which indicate the mode of polarisation and also give an insight into what changes are occurring at the electrode surface.

For a system such as Figure 2.1(a) with only one cathodic and one anodic reaction taking place, the Butler-Volmer equation (2.28) has been experimentally derived which gives the measured corrosion current density as a function of applied overpotential and free current density i_o.

$$i = i_o\left[e^{\alpha nF\eta/RT} - e^{-(1-\alpha)nF\eta/RT}\right] \qquad (2.28)$$

Where i is the current density in A/cm^2 due to applied overpotential η in Volts. α is a dimensionless parameter between 0 and 1 that measures the symmetry of the free energy barrier change due to η.

2.8.3 Mixed Potentials and Tafel Slopes

In most cases a corroding metal has an irreversible potential meaning that the Nernst equation cannot be used to find the corrosion potential. Likewise, the metal is not in a solution of its own ions, meaning that the Wagner and Traud theory of mixed potentials is necessary to obtain the corrosion current density. This theory states that any electrochemical reaction can be separated into two or more partial oxidation and reduction reactions. In addition, the sum of anodic and cathodic reaction rates is equal to zero at equilibrium. The effect of mixed potentials is illustrated in the Evans diagram in Figure 2.12.

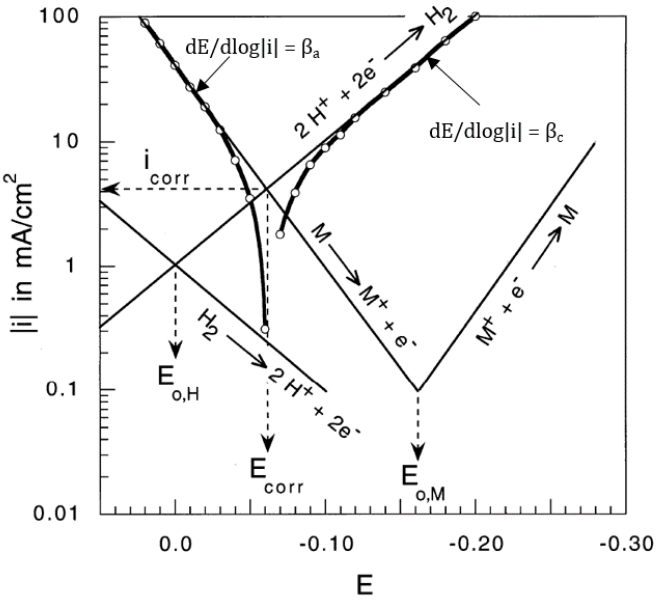

Figure 2.12: Evans diagram plotting $\log_{10}|i|$ vs E for half-cell reactions $M^+ + e^- \leftrightharpoons M$ and $2H^+ + 2\,e^- \leftrightharpoons H_2$ from [34]

It can be seen in the Evans plot in Figure 2.12 that near the corrosion potential the curves are non-linear. This is the combined effect of both half-cell reactions. By applying sufficient overpotential, anodic or cathodic reactions can become insignificant and a linear relationship between potential and $\log_{10}|i|$ can be observed, this is known as a Tafel region. The slope of these curves can be expressed as:

$$\beta_a = \frac{dE}{d\log i} = \frac{2.303RT}{\alpha_a nF} \tag{2.29}$$

$$\beta_c = \frac{dE}{d\log|i|} = -\frac{2.303RT}{(1-\alpha_c)nF} \tag{2.30}$$

The anodic and cathodic overpotentials in this region can be simplified to:

$$\eta_a = \beta_a \log\frac{i}{i_{corr}} \tag{2.31}$$

$$\eta_c = \beta_c \log\frac{i}{i_{corr}} \tag{2.32}$$

From this, the Butler-Volmer equation can be modified, with i_o replaced with $i_{corr.}$ Thermodynamically dependent E_o in (2.28) is replaced with E_{corr} which is dependent on system kinetics. Finally, incorporating (2.29) and (2.30) gives:

$$i = i_{corr}\left[e^{2.303\eta/\beta_a} - e^{-2.303\eta/\beta_c}\right] \tag{2.33}$$

Since $i = i_{corr}$ when $\eta = 0$, equation (2.33) can be extrapolated back to corrosion potential E_{corr} to give the corrosion current density which can subsequently be used to obtain corrosion rate as per equation (2.2).

2.8.4 Linear Polarisation Resistance (LPR)

Tafel polarisation requires large overpotentials which can be detrimental to the test material, particularly under anodic polarisation. The Linear Polarisation Resistance (LPR) method developed by Stern and Geary enables i_{corr} to be identified at much lower overpotentials [57]. The method is based on the observed linearity of E against i close to the corrosion potential E_{corr} in a charge transfer controlled system, such that:

$$R_p = \left(\frac{d\eta}{di}\right)_{\eta\to 0} \tag{2.34}$$

Where R_p is the polarisation resistance in $\Omega\cdot cm^2$.

Corrosion current can be mathematically derived for small overpotentials by MacLaurin series expansion of the mixed potential equation (2.33). A Maclaurin series expansion up to order n takes the form:

$$f(x) = f(0) + f'(0)x + \frac{f''(0)}{2!}x^2 + \frac{f^{(3)}(0)}{3!}x^3 + \cdots + \frac{f^{(n)}(0)}{n!}x^n \tag{2.35}$$

In this case the approximation is linear so the expansion is taken to the order 1 which for e^x gives:

$$e^x = 1 + x \tag{2.36}$$

By applying (2.36) to (2.33) the equation becomes:

$$i = i_{corr}[(1 + 2.303\eta/\beta_a) - (1 - 2.303\eta/\beta_c)] = i_{corr}2.303\eta\left(\frac{1}{\beta_a} + \frac{1}{\beta_c}\right)$$

Rearranging in terms of i_{corr} and substituting (2.34):

$$i_{corr} = \frac{i}{\eta}\left(\frac{\beta_a\beta_c}{2.303(\beta_a + \beta_c)}\right) = \frac{B}{R_p} \tag{2.37}$$

Where B is known as the Stearn-Geary coefficient:

$$B = \frac{\beta_a\beta_c}{2.303(\beta_a + \beta_c)} \tag{2.38}$$

The measured value of R_p also includes an electrolyte resistance R_e which is subtracted to give a true value of R_p.

$$R_p = R_{p_{measured}} - R_e \tag{2.39}$$

The low level of polarisation in LPR means that tests can be repeated multiple times without incurring significant sample damage. It can however be seen from equation (2.37) that Tafel gradients are still required for calculation of i_{corr} and thus for accurate measurement LPR does not omit the need for Tafel polarisation.

2.8.5 Electrochemical Impedance Spectroscopy (EIS)

The following section provides a general overview of the basics of Electrochemical Impedance Spectroscopy (EIS) interpreted from well-established texts [58, 59]. A more extensive treatment of the particular aspects of EIS relevant to this project are presented with the impedance models developed in Chapter 6. Unlike linear polarisation, EIS employs an alternating or sinusoidal input signal and is often referred to as Alternating Current (AC) Impedance. This method gives an insight into the non-faradaic behaviour of the electrode/electrolyte interface and diffusivity characteristics of porous surface layers which LPR does not measure as effectively. The technique is particularly useful for the study of substrate protection such as inhibitors, oxide layers or organic films and has been used extensively in the development of porous electrodes. By applying low amplitude (± 5 to 20mV) sinusoidal voltage perturbations across a series of frequencies the output signal (current) response can be measured.

The exhibited response current is a combination of transient and steady state components due to the cyclic nature of the AC voltage which induces a constant reorientation of polar molecules in response to the electrical field changes. The delay in response to this variation is termed relaxation and is a function of the capacitance and ohmic resistance of particular components of the system, expressed as a time constant (τ):

$$\tau = RC \tag{2.40}$$

The multifaceted structure of a corrosion cell interface can lead to the presence of multiple relaxation processes. At the EDL the response will be rapid and is therefore associated with the high frequency response signal. Diffusion processes are typically much slower and associated with low frequency behaviour with large time constants [58]. The relationship between an input voltage and output current is known as admittance. It is more common however to refer to the inverse of admittance known as impedance (Z) – a measure of the opposition to current flow.

Impedance from relaxation processes creates an offset between the sinusoidal input voltage and the measured output current signal, this is known as the phase shift or phase angle. To account for steady state and transient components of the current response, it is common to express the equations that describe the response as phasors (vectors with real and imaginary components).

In a general form, impedance can be calculated by application of Ohms law:

$$Z(\omega) = \frac{\tilde{U}(\omega)}{\tilde{\imath}(\omega)} \tag{2.41}$$

Where ~ denotes a sinusoidal signal.

2.8.5.1 Passive Element Analogues

The impedance behaviours of many physical features of a corrosion cell, such as the EDL and electrolyte, are analogous to common ‘passive’ circuit elements such as capacitors, and resistors. Adsorbed species on a substrate can also behave like inductors while more complex diffusion elements can be represented by more extensive models. It is important to therefore introduce some of the most commonly referenced passive elements applied in corrosion research, these are listed in Table 2.2.

Table 2.2: Common types of passive circuit element used in EIS analysis

Element	Common Symbol(s)	Impedance	
Resistor		$Z_R = R$	(2.42)
Capacitor		$Z_C = \frac{1}{j\omega C}$	(2.43)
Inductor		$Z_L = j\omega L$	(2.44)
Constant phase element		$Z_{CPE} = \frac{1}{(j\omega)^{\alpha} Q}$	(2.45)

Z = impedance (ohms / Ω), R = resistance (ohms / Ω), C = capacitance (farads / F), L = inductance (henrys / H)

The constant phase element (CPE) represented by equation (2.45) is used to model the effects of a time constant dispersion with α representing a dimensionless parameter between 0 and 1. When α is 1 the CPE becomes an ideal capacitor giving Q the value of capacitance.

2.8.5.2 Time Constant Dispersion of Constant Phase Elements

The Constant Phase Element (CPE) is often ascribed to real systems due to heterogeneity of the reacting (active) surface giving rise to a dispersion of time constants over the interface.

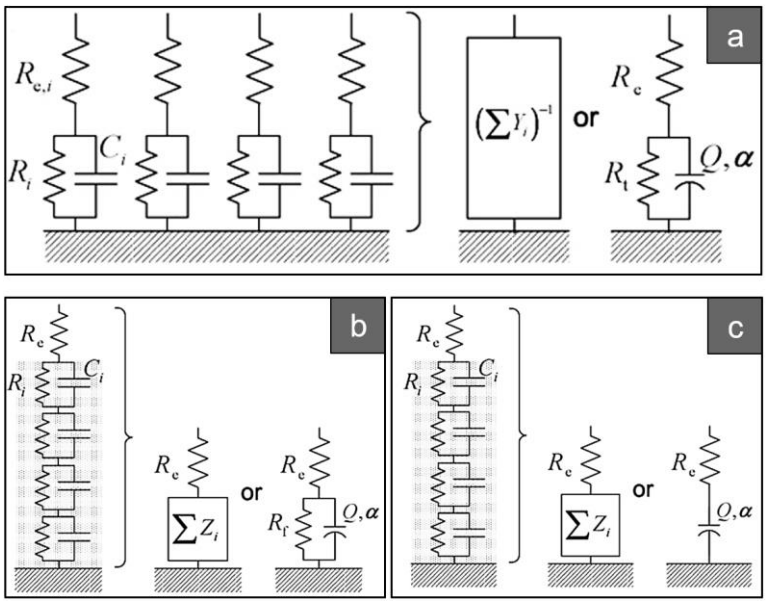

Figure 2.13: Forms of time constant distribution applicable to CPE's (a) surface distribution (b) normal distribution (c) power law distribution [58, 60]

A true CPE has a well-defined time constant distribution, the type of which is important to identify in order to extract physically meaningful parameters from the model. Orazem and Tribollet [58] highlighted three of the main types of distribution that have been derived, surface distributed, normally distributed and power law distributed as shown in Figure 2.13. A true CPE can be identified by the behaviour in the high frequency range of impedance spectra. In a plot of ohmic-resistance corrected phase angle if the phase reaches -90° at high frequency and becomes independent of frequency then a CPE is not needed. If however, the angle approaches a constant value of -90α° (where 0 < α < 1) the application of a CPE is valid.

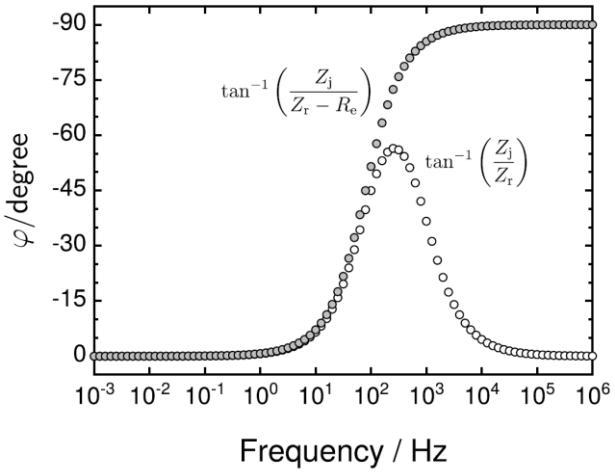

Figure 2.14 - Phase angle bode plot with (grey circles) and without (white circles) ohmic resistance correction from [61]

2.8.5.3 Equivalent Circuit Examples

The equivalent circuit in Figure 2.15(a) represents a simple interfacial impedance response that comprises the parallel combination of a double layer capacitance and a faradaic reaction in series with a solution resistance, commonly referred to as the simplified Randle's circuit [62]. The impedance as a function of perturbation frequency can be expressed as:

$$Z(\omega) = Z' + jZ'' = \underbrace{R_e + \frac{R_{ct}}{1 + (\omega R_{ct} C_{dl})^2}}_{Z} + j\underbrace{\frac{-\omega {R_{ct}}^2 C_{dl}}{1 + (\omega R_{ct} C_{dl})^2}}_{Z''} \qquad (2.46)$$

Where Z' and Z'' are the real and imaginary components of Z respectively. R_e is the electrolyte or solution resistance, C_{dl} is the double layer capacitance of the EDL and ω is the frequency.

The expression plots a perfect semi-circle on a Nyquist diagram which can be used to extract values of R_e, R_{ct} and C_{dl} as discussed later.

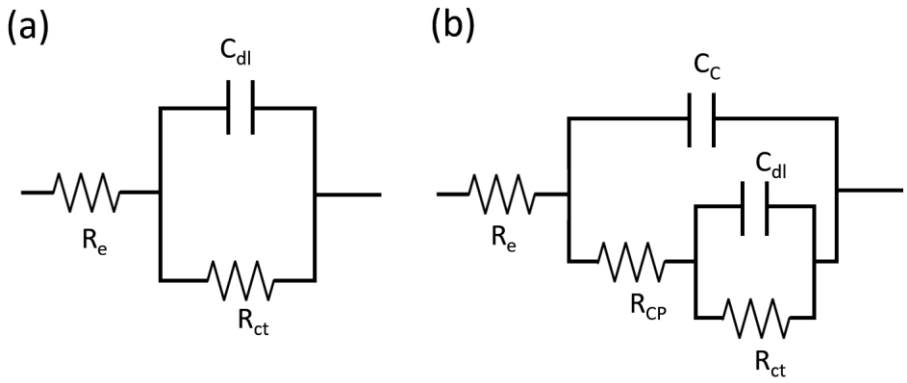

Figure 2.15: Capacitive circuit models of corrosion systems: (a) Simple Randle's circuit. (b) Organically coated metal substrate model where R_{CP} and C_C are coating resistance and capacitance respectively

For more complex systems such as those with organic coatings or porous layers there can be multiple relaxation processes and thus multiple time constants present. To obtain the maximum amount of information on the frequency response of these systems it is often necessary to plot both Nyquist and Bode diagrams. The process of fitting frequency response data to a specific circuit model requires a good understanding of the real system in order to draw meaningful quantitative estimates of physical properties from the fitted parameters.

2.8.5.4 Measurement Error Analysis

A crucial part of impedance data analysis is to differentiate measurement errors from true features of the system. Figure 2.16 illustrates the approach to measurement analysis proposed by Orazem and Tribollet [63].

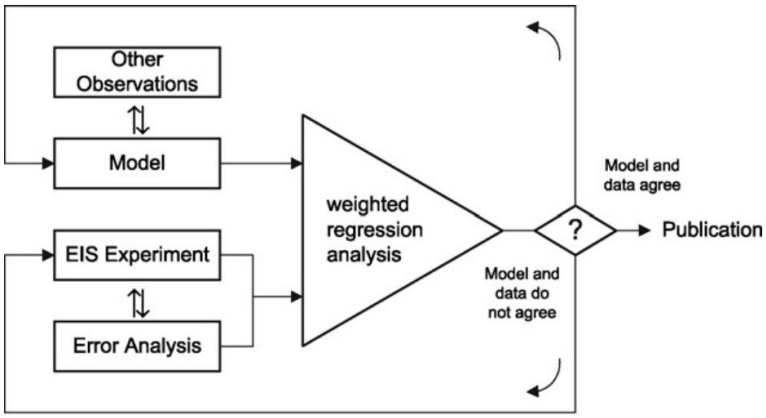

Figure 2.16: Flowchart for assessing and fitting impedance data [63]

Figure 2.16 accounts for both systematic development of a representative equivalent circuit model in tandem with some form of error analysis. One method for assessing the validity of an EIS measurement is to perform a Kramer-Kronig (KK) test. KK relations are generalised constraints that connect real and imaginary components of a complex function and can be applied to systems or frequency domain measurements that conform to the conditions of linearity, causality and stability [58].

- Linearity – The system responds linearly to perturbation
- Causality – A response to a perturbation cannot precede the perturbation
- Stability – Perturbations to the system do not grow

Bode extended the use of these relations to impedance measurements as a means to identify errors in impedance spectra. Errors can include instrumental artefacts and time-dependent phenomena [58]. To obtain a true fit of impedance data to KK relations would require integration between 0 and infinite frequency so for practical purposes the data is typically fitted to a known circuit that always satisfies the KK relations.

Chapter 3
Literature Review – $FeCO_3$ and $Fe_xCa_yCO_3$ Formation in CO_2 Environments

3.1 Chapter Outline

Due to the vast amount of research that has already been undertaken on iron carbonate ($FeCO_3$) formation the first section of the review is focused on the most influential parameters surrounding its formation. The second part of the review attempts to collate all of the existing literature relevant to the interactions between Fe and Ca in mixed carbonate precipitation based on geochemistry and corrosion studies. This is followed by an assessment of electrochemical studies for characterisation of CO_2 corrosion products, and a brief encapsulation of methodologies for modelling and controlling CO_2 system chemistries.

3.2 Iron Carbonate ($FeCO_3$) Precipitation

3.2.1 Effects of Temperature

In a CO_2 saturated solution, the equilibrium concentrations of carbonic species vary with temperature. In addition, higher temperatures increase kinetics and thin, dense and generally protective films can form [29]. The solubility product (K_{sp}) of iron carbonate is also a function of temperature, exhibiting inverse solubility. Barker et al. [25] reviewed the various mathematical models that have been created to describe this relationship and plotted them as shown in Figure 3.1. The model of Sun and Nešić [64] is perhaps one of the more comprehensive models given that it integrates the effects of ionic strength on ion activities in the solubility formula:

$$\log(K_{sp}) = -59.3498 - 0.041377(T_k) - \frac{2.1963}{T_k} + 24.5724\log(T_k) + 2.518(\mathbf{I}^{0.5}) - 0.657(\mathbf{I}) \quad (3.1)$$

Where T_k is absolute temperature in kelvin and $\mathbf{I}$ is ionic strength:

$$\mathbf{I} = \frac{1}{2}\sum_i c_i n_i^2 \quad (3.2)$$

Where c_i is the concentration of the i^{th} species and n_i is its corresponding charge.

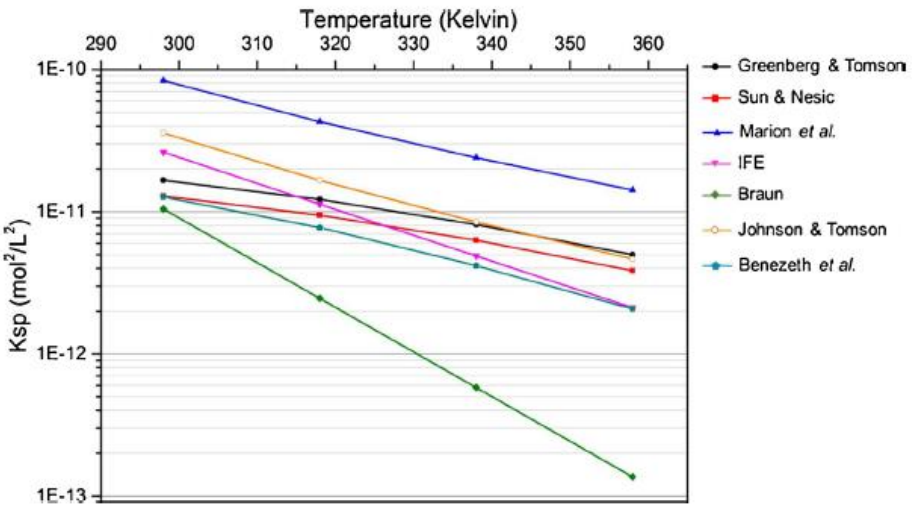

Figure 3.1: $FeCO_3$ solubility models as a function of temperature [25]

The possibility of $FeCO_3$ precipitation across a range of conditions can be interpreted from a Pourbaix diagram. A Pourbaix diagram is a plot of potential against pH which uses the Nernst equation to display regions of thermodynamic stability for different phases in an aqueous system. Tanupabrungsun et al. [45] constructed Pourbaix diagrams for Fe-CO_2-H_2O systems up to temperatures of 250 °C. The results at 25 °C and 250 °C are shown in Figure 3.2. The dotted lines at 25 °C indicate that metastable forms of $Fe(OH)_2$ and Fe_3O_4 can coexist with the more thermodynamically stable $FeCO_3$ on a temporary basis before transforming into $FeCO_3$. At 250 °C Fe_3O_4 becomes the more stable product in neutral and alkaline conditions.

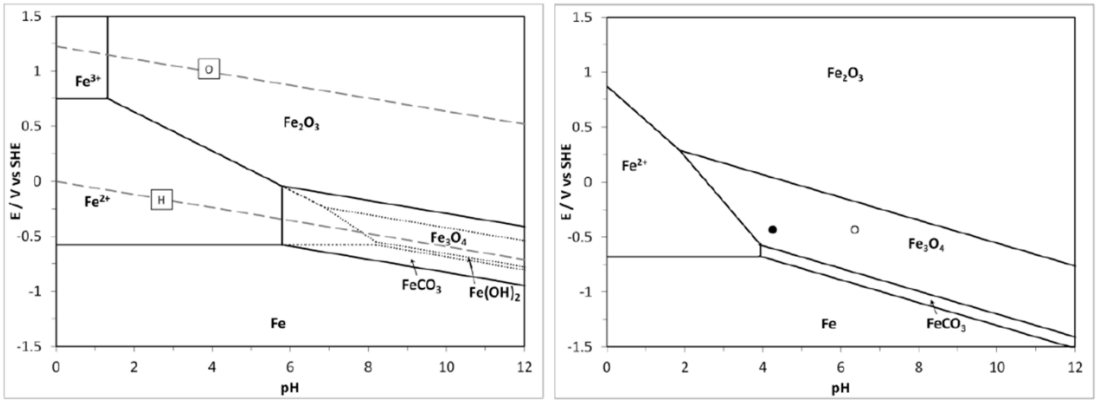

Figure 3.2: Pourbaix diagrams for Fe-CO_2-H_2O systems at 25 °C (left) and 250 °C (right) [45]

3.2.2 Effects of CO_2 Partial Pressure (pCO_2)

Increasing CO_2 partial pressure increases the concentration of dissolved CO_2 as a consequence of Henry's Law. This results in greater concentrations of H_2CO_3, HCO_3^- and H^+ ions and a decrease in CO_3^{2-}. The effect on pH was illustrated by Dugstad [26] as shown in Figure 3.3.

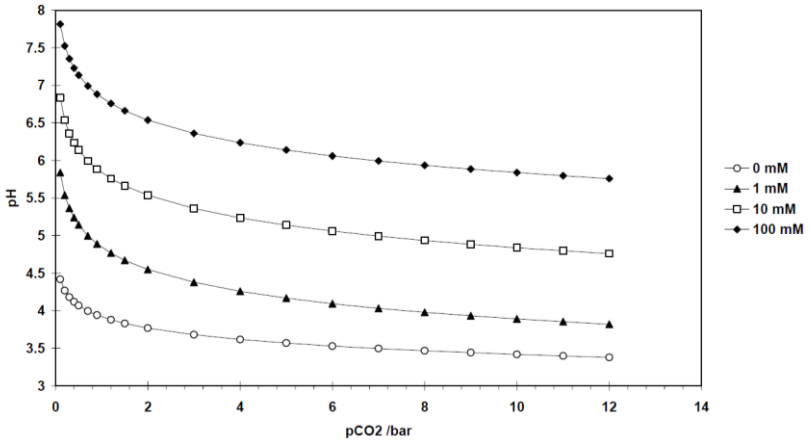

Figure 3.3: pH as a function of CO_2 partial pressure and various concentrations of $NaHCO_3$ at 60 °C and 1wt% NaCl [26]

Despite lowering brine pH, faster corrosion kinetics can encourage faster precipitation of $FeCO_3$ by offsetting the initial decrease in CO_3^{2-}. Videm et al. [65] noted that increasing pCO_2 in an 80 °C brine at pH 5 from 1 to 10 bar resulted in faster film formation on carbon steel. Figure 3.4 from Dugstad [26] shows that the relationship between Fe^{2+} required for saturation exhibits a complex relationship with pCO_2 depending on the pH.

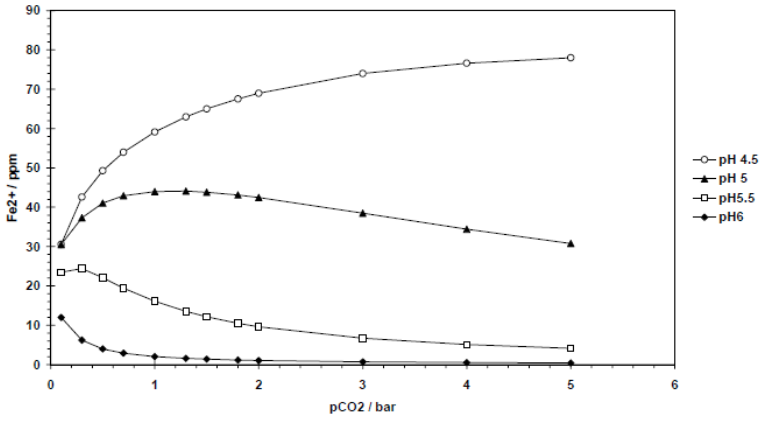

Figure 3.4: Amount of Fe^{2+} required to reach $FeCO_3$ saturation as a function of pCO_2 for various initial brine pH's. 60 °C and 3.5wt% NaCl [26]

3.2.3 Effects of pH

3.2.3.1 Bulk pH

pH is a highly influential parameter for $FeCO_3$ formation because it is directly related to the concentration of CO_3^{2-} ions. Higher pH solutions require less Fe^{2+} to reach $FeCO_3$ supersaturation. Dugstad et al. [26] showed that the required Fe^{2+} can increase by over 100 times when reducing the pH from 6 to 5 in a 1wt% NaCl brine. Tanupabrungsun et al. [66] investigated the effects of pH on CO_2 corrosion of mild steel at elevated temperatures. Tests were conducted in an autoclave with in-situ LPR and EIS at temperatures between 80-200 °C. The solutions contained 1wt% NaCl saturated with CO_2 at pH of 4 and 6. The results indicated that at pH 4 protective corrosion films did not form within the 20 hour tests unless temperature exceeded 150 °C.

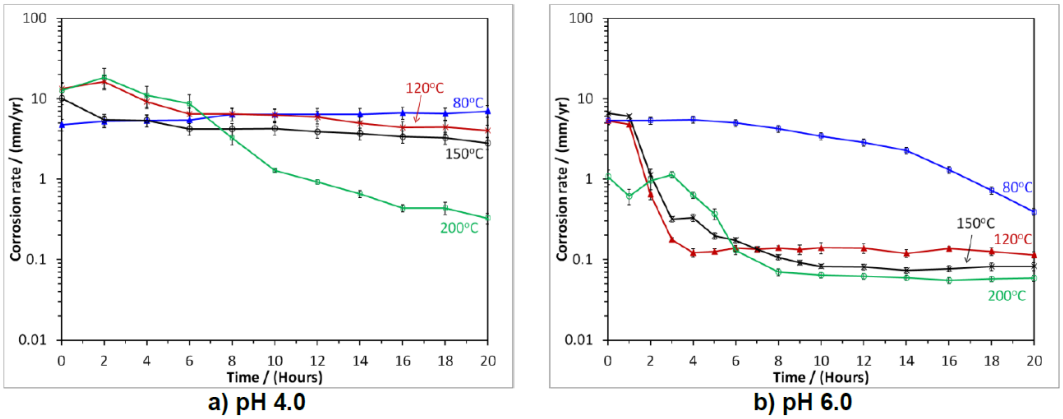

Figure 3.5: Corrosion rates over time based on LPR measurements for various test temperatures and $[CO_2]_{aq}$ = 0.030M (a) pH 4 (b) pH 6 [66]

At pH 6 and above 80 °C corrosion rates dropped substantially within the first 4 hours, indicating the formation of a protective film. These results were confirmed by Scanning Electron Microscopy (SEM) as shown in Figure 3.6. Figure 3.6(a) shows that no film is present on the metal surface at pH 4 and 80 °C while Figure 3.6(c) shows a combination of $FeCO_3$ with a thin underlying layer of Fe_3O_4 at pH 4 and 200 °C. It is important to note that the pH quoted is from the bulk solution and surface pH will likely be higher.

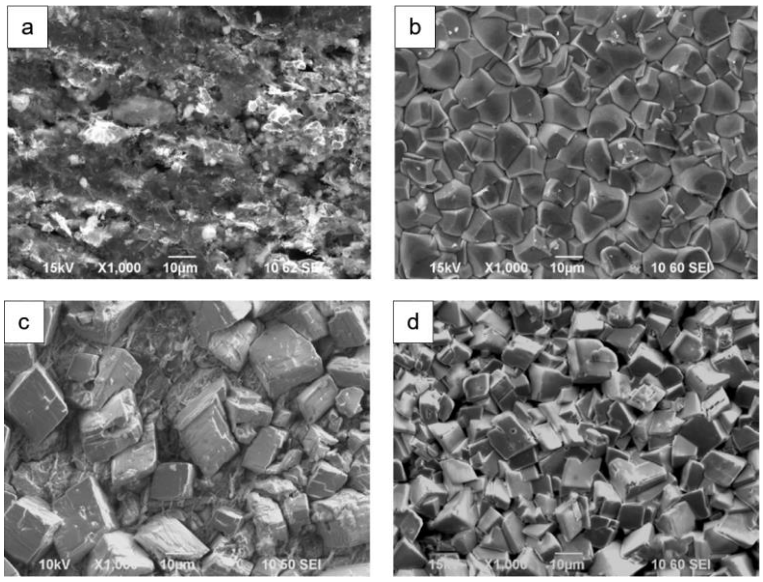

Figure 3.6: SEM images from [66] at (a) 80 °C pH 4 (b) 80 °C pH 6 (c) 200 °C pH 4 (d) 200 °C pH 6

3.2.3.2 Surface pH

A further observation is that of the solution chemistry close to the steel surface. While most studies consider corrosion mechanisms of mild steel as a function of the bulk solution chemistry and pH, the anodic dissolution of iron within the confines of a boundary layer can result in contrasting conditions at and close to the surface of the electrode even in agitated and flowing systems. De Motte et al. [67] used flat glass pH probes to measure discrepancies in surface and bulk pH. The surface probe was mounted in close proximity to a carbon steel mesh as shown in Figure 3.7.

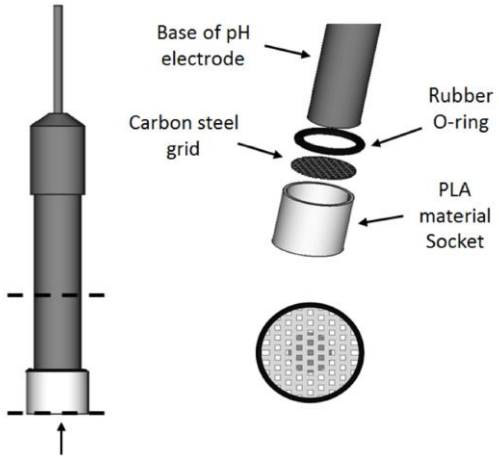

Figure 3.7: Mesh capped pH probe designed by De Motte et al. to measure near surface pH [67]

Experiments were conducted at 80 °C in stagnant 1 and 0.2wt% NaCl CO_2 saturated solutions at ambient pressure. The solutions were buffered with $NaHCO_3$ to bulk pH values of 6 and 6.6. At the end of 12 days of testing the pH 6 solution was observed to have increased to pH 6.3±0.1 at the surface while the pH 6.6 test eventually settled at a surface pH of 7.0±0.1. The results may however have been affected by the design of the local probe, with the solution becoming artificially trapped by the mesh design.

3.2.4 Area-to-Volume Ratio

System chemistry and the resulting pH is a function of many interdependent variables such as temperature, fugacity and activity of species. One of the greatest difficulties in laboratory experiments is maintaining these conditions over time. In a closed vessel, the corrosion process will gradually affect local and bulk conditions as metal ions begin entering the solution and interacting with the various species present. In some instances, this process may be indicative of the field conditions, such as trapped or quiescent media exposed to large areas of active material. In conditions where transport rates are high, this evolution process may be unrealistic. ASTM G31 [68] sets the standard for immersion corrosion testing and highlights the potentially undesirable effects of solution contamination during the corrosion process. This specifically applies when important minor constituents of the solution become consumed or when corrosion products enhance or reduce the corrosion process. To acknowledge this, ASTM G31 limits the ratio between the exposed surface area of the test specimen and the volume of solution. For test durations up to 30 days this is limited to 0.20 $mL \cdot mm^{-2}$ this equates to an A/V ratio of 50 $cm^2 \cdot L^{-1}$ [68]. ASTM G111, the standard for corrosion testing at elevated pressures and temperatures further limits this value to an A/V ratio of 33.3 $cm^2 \cdot L^{-1}$ [69]. This suggests acknowledgement of the greater difficulties of solution control at elevated conditions due to instrumental complexity and increased corrosion kinetics.

The A/V ratio is also used is in precipitation kinetic models to account for the physical limitations of the system when predicting the growth rates of crystals. The existing models [29, 70, 71] for $FeCO_3$ precipitation kinetics take the general form of equation (3.3).

$$PR = k_r \cdot \frac{A}{V} \cdot \sigma(SR) \tag{3.3}$$

Where PR is precipitation rate, k_r is a temperature dependent rate constant, A is surface area of the seed crystal or corroding metal, V is the solution volume and σ is the driving force for the reaction as a function of saturation ratio (SR). Using a bulk precipitation methodology, Tomson and Johnson [29] fitted equation (3.4) to their kinetic model using seed crystal surface area (A_{seed}) expressed here in molar units to give:

$$\frac{d[Fe^{2+}]}{dt} = k_r \cdot \frac{A_{seed}}{V} \cdot \left\{ \left(a_{Fe^{2+}} \cdot a_{CO_3^{2-}} \right)^{0.5} - {K_{sp}}^{0.5} \right\}^2 \tag{3.4}$$

Sun and Nešić [70] extended equation (3.3) to their kinetic model of $FeCO_3$ precipitation on a steel surface, replacing A_{seed} with the surface area of exposed metal (A) when deriving their expression.

Barker et al. [25] and Nešić et al. [72] both highlight the limitations of using the steel surface area in predicting $FeCO_3$ precipitation as this will change over time as material is removed and a porous layer starts to form, significantly affecting the rate of $FeCO_3$ growth.

3.2.5 Effects of Metallurgy - the Role of Cementite (Fe_3C)

An often-cited effect of metallurgy on corrosion and corrosion product formation on carbon steels in CO_2 environments is the role of iron carbide (Fe_3C) also known as cementite. In ferritic-pearlitic carbon steels, Fe_3C is revealed after preferential dissolution of the ferrite phase. Fe_3C has been credited for enhancing the cathodic reaction in a CO_2 systems [73] and facilitating localised corrosion by galvanic coupling due to its conductivity, as well as by local acidification [28, 73]. In contrast, Fe_3C has also been credited as helping to encourage $FeCO_3$ nucleation which can occur directly on the Fe_3C surface [28]. A study by Farelas et al. [74] demonstrated how $FeCO_3$ crystals are able to nucleate within the exposed Fe_3C matrix even in flowing systems at pH 6 that are not normally conducive to $FeCO_3$ precipitation as shown in Figure 3.8. The reasoning for this phenomenon was the diffusion barrier created by the tortuous Fe_3C matrix limiting the flow of ferrous irons (Fe^{2+}) from the surface resulting in a higher surface pH.

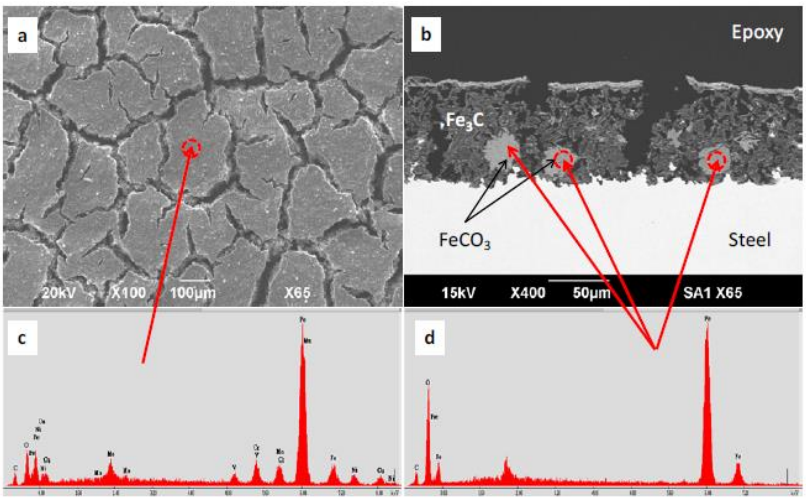

Figure 3.8: $FeCO_3$ growth within exposed Fe_3C matrix on X65 steel sample after 41h of exposure to 3wt% NaCl brine, 80C, 0.5m/s, pH 6 (a) Top view SEM (b) Cross-section SEM (c) Top view EDX (d) Cross-section EDX. [74]

Ieamsupapong et al. [75] made similar observations at pH 5.4 to 6 in which Fe_3C was again credited with create the necessary diffusion barrier to increase local pH. Ueda et al. [76] suggested that Fe_3C also helps to anchor the $FeCO_3$ to the steel substrate.

3.2.6 Effects of Brine Ions

Brines found in deep geological wells are typically high in dissolved salts [19, 22]. Salts can influence the transport of electroactive species and increase the ionic strength of a solution. At constant CO_2 partial pressure, increasing NaCl has been observed to increase corrosion rate initially, before causing a non-linear decrease, attributed to its effect on lowering CO_2 solubility [25].

Han et al. [77] investigated the effects of NaCl concentration on corrosion rates of mild steel in de-aerated CO_2 saturated brines. Maintaining a test temperature of 25 °C and pH of 4, tests were carried out with 0.5,1, 5 and 20wt% NaCl in a glass cell with stirrer speeds varying from 100 to 800 RPM. The results showed that corrosion rate dropped as salt concentration increased while at high salt levels (>20wt% NaCl) corrosion rate became independent of flow rate. Surface imaging with SEM indicated that at 20 wt% NaCl a porous corrosion scale with embedded crystals resembling magnetite was present with no signs of $FeCO_3$. They attributed the flow independence to the diffusion barrier created by the Fe_3O_4 layer.

3.3 Review of Iron and Calcium Interactions and Co-precipitation

Outside of corrosion applications the geochemistry of rhombohedral carbonates such as Calcite and Siderite has been well studied in literature. Romanek et al. summarised much of the work as shown in Figure 3.9 for deposits formed below 100 °C [78]. The figure illustrates the pure end members Calcite ($CaCO_3$) + Rhodochrosite ($MnCO_3$), Siderite ($FeCO_3$) and Magnesite ($MgCO_3$) as well as the combined formations Dolomite ($CaMg(CO_3)_2$) and Ankerite ($(Fe^{2+},Mg,Mn)(CO_3)_2$) which in its pure form is also referred to as ferro-dolomite ($CaFe(CO_3)_2$). The symbols and fields within the figure represent the compositions that have been observed in geological studies and formed below 100 °C.

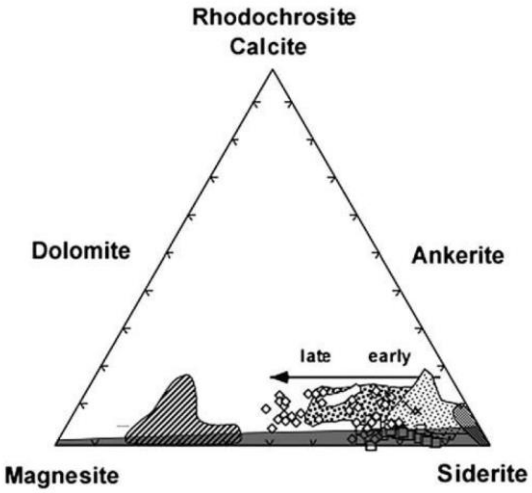

Figure 3.9: Geochemistry of Siderite, Magnesite and Calcite reported in the literature for deposits known to form at <100 °C. Taken from [78]

$CaFe(CO_3)_2$ has not been observed to form naturally and it is believed that Davidson et al. [79] were the first to synthesise a disordered form of the mineral using extremely high temperatures and pressures. Starting materials of Fe-substituted $CaCO_3$ and Ca-substituted $FeCO_3$ were created using mixtures of Fe-oxalate and $CaCO_3$ with 1 wt.% Li_2CO_3 flux that were sealed in gold tubes and pre-reacted in cold-seal pressure vessels at 400 or 450 °C and 2 kbar. The compounds formed were then moved into another piston-cylinder assembly and tested for 2 days (830 °C) to 5 days (722 °C). Phase composition was analysed by Electron microprobe (EMP). Both backscattered electron images and Transmission Electron Microscopy (TEM) analysis suggested compositional and structural homogeneity in the samples with occasional dislocations.

Calcium was found to stabilise $FeCO_3$ to much higher temperatures preventing decarbonation and production of Fe_3O_4. Pressures of up to 30 kbar were required to stabilise $FeCO_3$ sufficiently for disordered $CaFe(CO_3)_2$ to form.

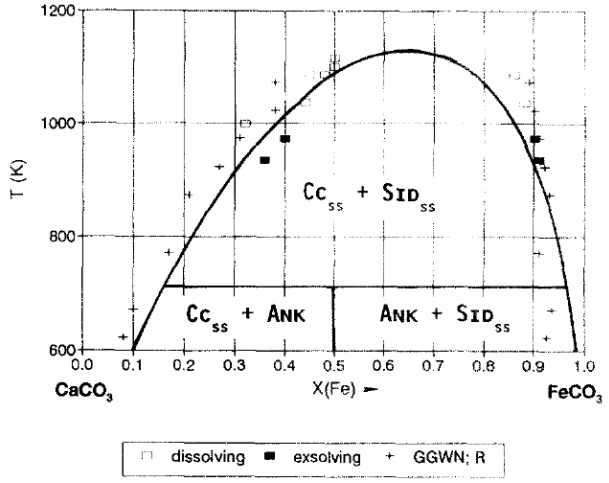

Figure 3.10:T-X section for the join $CaCO_3$-$FeCO_3$. Products from dissolving experiments shown as open squares; those from exsolving experiments shown as filled squares. [79]

Another attempt to synthesise $CaFe(CO_3)_2$ was made by Chai and Navrotsky in 1996 across a range of solid solutions along the dolomite-ankerite join [80]. $FeCO_3$ was synthesised using Fe-oxalate in a cold-seal pressure vessel before being added to precipitated $CaCO_3$ in a piston-cylinder assembly and tested for typically 24 hours at 18 kbar and 850± 50 °C due to difficulty in maintaining temperature. Samples were analysed using XRD while the energetics of ordered and disordered ankerite solid solutions were estimated using data from calorimetry, lattice-energy calculations, and phase equilibria. The enthalpy of formation of ordered ankerite appeared to become more endothermic with increasing Fe content. The enthalpy of disordering in dolomite was shown to be much larger than that in pure ankerite $CaFe(CO_3)_2$. This implied that there is insufficient energy gain on ordering of $CaFe(CO_3)_2$ to stabilise it relative to a two-phase mixture of siderite and calcite. This potentially explains the absence of naturally occurring ordered $CaFe(CO_3)_2$.

3.3.1 $FeCO_3$ and $CaCO_3$ Growth Kinetics

Despite higher solubility than $FeCO_3$, $CaCO_3$ has been shown to have much faster precipitation kinetics.

Tomson and Johnson [29] noted that this can help to explain why in the field, waters saturated with respect to $CaCO_3$ are often greatly supersaturated with respect to $FeCO_3$. Figure 3.11 illustrates how both $FeCO_3$ and $CaCO_3$ growth rates vary as a function of temperature.

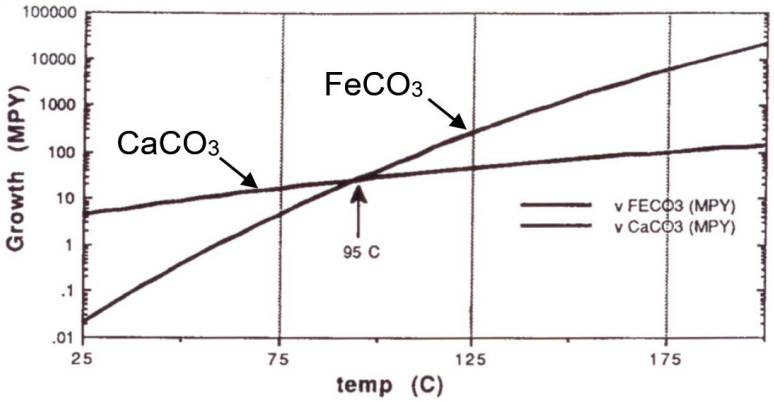

Figure 3.11: Comparison of $CaCO_3$ and $FeCO_3$ growth rates as a function of temperature from [29]

3.3.2 Iron as an Impurity in $CaCO_3$ Growth

Early studies on the interaction between iron and calcium were largely mineralogical, investigating iron as an impurity in calcite growth.

In 1984 Meyer [81] investigated the effects of 34 organic and inorganic impurities on the growth rate of calcite. Using a pH control circuit, calcite saturation was estimated from the difference in actual pH and pH of saturation. The differential pH was maintained to control crystal growth rate before additives were dosed into premade solution containing $CaCl_2$ and $NaHCO_3$.

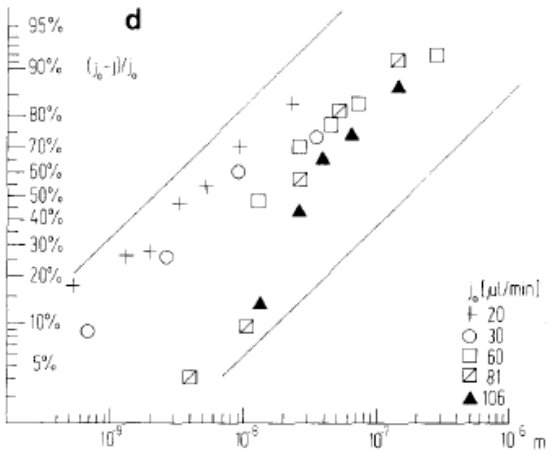

Figure 3.12: Reduction of Calcite crystal growth rate as a function of Fe^{2+} concentration [81]

Fe^{2+} was found to have the greatest inhibitory effect on calcite crystal growth with up to 80% crystal growth reduction from $6x10^{-8}$ $mol \cdot L^{-1}$ Fe^{2+}. For comparison, Mg^{2+} could only inhibit by 20 % at a concentration of $5x10^{-5}$ $mol \cdot L^{-1}$. Further investigation showed that the amount of Fe^{2+} required to halve the initial calcite growth rate would only cover around 0.06 % of the crystal surface (terrace) sites. This excluded the possibility of inhibition by terrace site 'blocking' and suggested blocking of growth steps due to adsorbed Fe^{2+} ions.
In 1989 Herzog et al. [82] investigated the role of Fe^{2+} and Fe^{3+} on the inhibition of $CaCO_3$ nucleation and growth in magnetic water treatment. Solutions were comprised of between 0 and 56 ppm of Fe^{2+}, added as $FeSO_4$, $NaHCO_3$ and $CaCl_2$ to supersaturate for $CaCO_3$ before calcite or aragonite seed crystals were added. A Ca^{2+} selective electrode and Ag/AgCl RE were used to monitor Ca^{2+} consumption from the bulk to quantify crystal growth.
At 5.6 ppm and above Fe^{2+} was found to significantly inhibit calcite growth by precipitating $FeCO_3$ on the calcite surface and blocking growth sites. TEM revealed a partial coating of iron rich material on the calcite seed crystals. Lower Fe^{2+} concentrations reduced the rate at which Ca^{2+} reached an equilibrium in the bulk but had little effect on initial growth rates.
Over time, regardless of Fe^{2+} concentration, Ca^{2+} reached a value close to its equilibrium, suggesting that $CaCO_3$ controls the solubility of the system while Fe^{2+} only affects the kinetics. The effect on aragonite was different, where even 56 ppm of Fe^{2+} had a limited inhibitory effect on aragonite crystal growth. A further test conducted at 53 °C showed that Fe^{2+} strongly inhibited the transformation of aragonite to calcite.

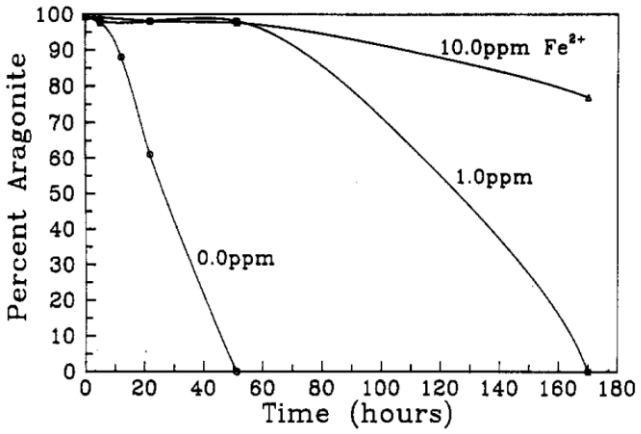

Figure 3.13: Effects of Fe^{2+} on the rate of recrystallization of aragonite into calcite at 53 °C from [82]

Wada et al. [83] made similar observations in a study on the effects of 7 divalent cations (Fe^{2+} Mg^{2+} Ni^{2+} Co^{2+} Zn^{2+} Cu^{2+} Cd^{2+}) on the nucleation, growth and transformation of $CaCO_3$ polymorphs. Tests conducted in a 0.3% agar solution at 15 °C showed that Fe^{2+} favoured the precipitation of aragonite and caused co-precipitation of solid solution $Fe_xCa_{1-x}CO_3$. Aragonite and calcite precipitated as spherulites and distorted rhombohedra respectively.

The conclusion was that aragonite became a stable phase relative to $Fe_xCa_{1-x}CO_3$ which formed through transformation of aragonite and hence the dominance over calcite. In addition, impurities also reduced the growth rate of aragonite nuclei by adsorption.

Langerak et al. [84] tested the inhibitory effects of Fe^{2+} as a means to prevent $CaCO_3$ build up during anaerobic digestion in waste water treatment. They found that iron did not significantly reduce the amount of precipitated $CaCO_3$ unless 500 $mg \cdot L^{-1}$ of Fe^{2+} was added. Unlike Meyer [81], they attributed the inhibition simply to the removal of carbonate in the precipitation of $FeCO_3$, lowering the saturation of $CaCO_3$. Observation of mineral fraction did however show 85-95% aragonite with only 5-15% calcite.

Using molecular dynamic simulations, de Leeuw [85] made similar observations to Meyer [81], which illustrated how Fe^{2+} can inhibit calcite crystal growth. The model demonstrated that impurity carbonate growth on calcite steps was initially an energetically favourable process allowing effective competition with pure calcite. Further incorporation however gradually became more endothermic until the entire growth step was decorated with impurity ions that inhibited further crystal growth.

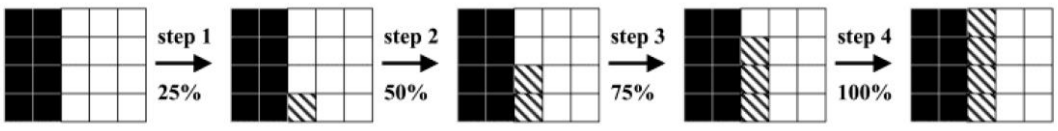

		step 1	step 2	step 3	step 4
Acute	Mg	- 19	- 82	-123	-154
	Fe	- 80	-145	-188	-191
	Cd	+41	- 70	- 41	-109
	Sr	- 48	- 84	-125	-162
Obtuse	Mg	- 65	- 51	-118	-135
	Fe	-166	- 53	-147	-248
	Cd	- 10	+10	- 7	- 92
	Sr	- 92	- 51	- 48	- 92

Figure 3.14: Schematic diagram listing the energies of successive additions of MCO_3 units (M = Mg, Fe, Cd, Sr) at acute and obtuse calcite steps. [85]

A later study by Mejri et al. [86] assessed the individual effects of Fe^{2+} and Fe^{3+} on the early stage nucleation and growth kinetics and microstructure of $CaCO_3$ using a CO_2 out gassing technique in a 1 L stainless steel cell. Calcocarbonic ($Ca(HCO_3)_2$) pure waters were prepared by dissolving 0.2-0.4 $g{\cdot}L^{-1}$ of $CaCO_3$ in deionised water bubbled with CO_2. Fe^{2+} was added as $FeSO_4$ and bubbled with pure N_2 while for Fe^{3+} the solution was bubbled with air. Oxygen content was monitored using a CellOx 325 O_2 sensor and solution samples were analysed using Atomic Adsorption Spectroscopy (AAS). Post-test precipitate was analysed by Fourier Transform Infrared (FTIR) Spectroscopy and XRD as well as SEM. The authors found at high Ca^{2+} concentrations total iron ion concentration had little effect on induction time of $CaCO_3$ precipitation. In fact, at lower Ca^{2+} concentrations of 2 mM the presence of iron actually accelerated $CaCO_3$ nucleation. Fe^{2+} was shown to increase the nucleation step from 36 to 70 mins in 0 and 20 $mg{\cdot}L^{-1}$ of Fe while nucleation pH was not affected. XRD showed that $CaCO_3$ transformed from almost entirely calcite to predominately aragonite in the presence of Fe^{2+} and vaterite in the presence of Fe^{3+}.

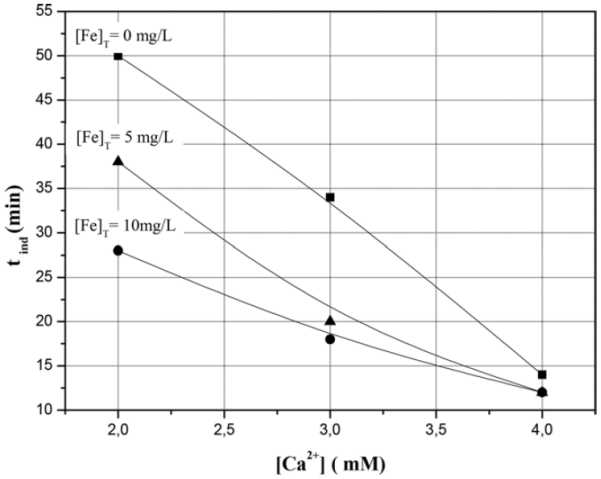

Figure 3.15: Effect of iron ions on $CaCO_3$ nucleation rate in different $Ca(HCO_3)_2$ solutions at 30 °C [86].

In 2017, Di Lorenzo et al. [87] performed a comprehensive study on the effects of Fe^{2+} on $CaCO_3$ precipitation using both constant pH nucleation experiments and constant composition growth experiments as well as molecular dynamic simulations. Solutions were prepared using $CaCl_2$ and $FeCl_2.4H_2O$, Na_2CO_3 $NaHCO_3$ and $CaCO_3$.

Synthetic $CaCO_3$ crystals were homogenised to below 66 µm diameter determined by N_2 adsorption. The solutions were then deoxygenated by boiling while under a continuous flow of nitrogen before rapid cooling with liquid nitrogen. Nucleation experiments used a continuous flux of 10 mM $CaCl_2$ solution into 100mL of sodium carbonate solution.

Conductivity was continuously measured as was Ca^{2+} using an ion selective electrode (ISE). Solid products were analysed using SEM, XRD, TEM, Electron Energy Loss (EELS) and EMP. Solution composition was analysed using Inductively Coupled Plasma Spectrometry (ICP). For growth experiments 100mL of supersaturated $CaCO_3$ solution was placed in a reactor at 25 °C and pH 8.5. pH and SR were controlled by separate titrants of $CaCl_2$ and bicarbonate and the effect of Fe^{2+} on calcite spiral growth was analysed by Atomic Force Microscopy (AFM) in a continuous flow liquid cell. Nucleation results indicated that increasing Fe^{2+} increased the SR_{CaCO3} required before nucleation occurred. In the absence of Fe, XRD showed the main crystalline products to be calcite and vaterite while at high Fe (Ca/Fe <5) aragonite was the most abundant phase. Growth rates of $CaCO_3$ were also reduced in presence of Fe^{2+}.

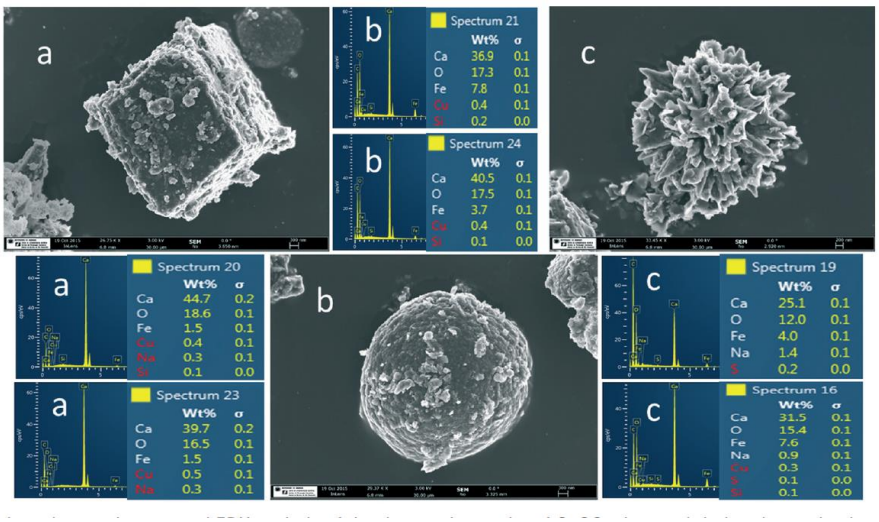

Figure 3.16: SEM secondary electron images and EDX analysis of the three polymorphs of $CaCO_3$ detected during nucleation experiments by [87]

ISE data showed that bound Ca over time was not influenced by Fe in the pre nucleation stage, confirming that the inhibitory effect of Fe was not attributed to a shift in the equilibrium speciation of the solution as was suggested earlier by Langerak et al. [84].

Notably, modelling and experimental work also showed that greater Fe incorporation was possible in aragonite compared to calcite due to the difference in ideal distribution coefficient for the solid solutions.

The most recent study on the effects of ferrous iron on the growth and polymorphism of $CaCO_3$ was conducted by Korchef [88] using a CO_2 degasification technique conducted at 28 °C. $CaCO_3$ was precipitated using the dissolved CO_2 degasification technique in a 1L PVC cell bubbled with air during the test to remove dissolved CO_2. The initial pH of 5.3 was adjusted to 6 with the addition of NaOH while Fe was added as $FeCl_2.4H_2O$. Samples of solution were analysed for hardness and Ca concentration using an EDTA titrimetric method and AAS. Alkalinity was determined by titration with sulfuric acid. In addition, precipitate was filtered, dried and analysed by FTIR, SEM and XRD. SEM analysis indicated that the addition of iron stabilised Vaterite crystals at the expense of Aragonite. $FeCO_3$ was also only observed at low supersaturation. The Author suggested that $FeCO_3$ causes heterogenous precipitation in the bulk which is why an inhibitory effect was observed. At low supersaturations and past the point of nucleation, iron ions were also found to accelerate $CaCO_3$ growth rate. The applicability of this work is limited by the introduction of oxygen likely leading to more precursor iron hydroxides. Despite this, no FeOOH due to air degasification was observed.

3.3.3 Effects of Calcium on $FeCO_3$ Growth

As with the impurity studies on $CaCO_3$, a number of similar investigations have been performed that look at the role of impurity ions on $FeCO_3$ formation. A study in 1985 by Wajon et al. [89] looked at the precipitation of iron from iron sulphate containing wastewater by aragonite, calcite and various lime sands and limestones after it was observed that precipitation of $FeCO_3$ was much lower than expected in waste water sites. XRD detected that iron(II) carbonates, in particular calcium-siderite, were the main if only products of Fe^{2+} and natural carbonate materials. Siderite was precipitated most readily in the presence of aragonite and was completely inhibited in the presence of calcite despite high supersaturation. This suggested that ion exchange between Ca and Fe as well as dissolution of calcite was inhibited. The authors proposed that this could be due to presence of phosphates and other species which inhibit calcite dissolution.

In solutions where $FeCO_3$ precipitated, the precipitation rate was found to be proportional to the square of relative supersaturation. A much later study by Romanek et al. in 2009 [78] investigated the influence of calcium and magnesium on siderite formation at 25 °C and 70 °C.

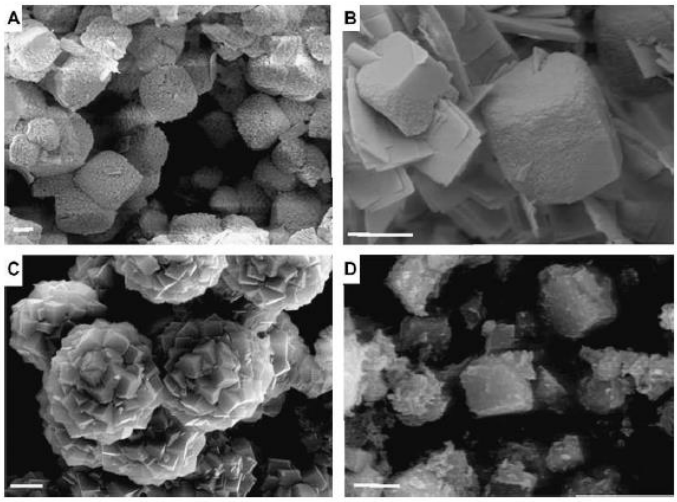

Figure 3.17: SEM images of the effects of impurity ions on $FeCO_3$ morphology from [78]

A range of 21 experimental solutions comprising different concentrations of Ca Fe Mg and $NaHCO_3$ were created using $Fe(ClO_4)_2$, $Ca(ClO_4)_2$, and $Mg(ClO_4)_2$ in deaerated deionised water. Solutions were bottled and stored for up to 6 months before solution and precipitate were analysed using ICP and XRD. At 20 °C, despite being present in most of the solutions, Mg was only found in the precipitate crystals at very high concentrations and did not cause any roughening the siderite crystals. Ca was found to inhibit siderite precipitation and a linear trend was observed between the molar fraction of calcium in the bulk and precipitate. The lower uptake of Mg was attributed to higher energy of dehydration of Mg ions.

Perhaps the most comprehensive body of work related to the interactions between Fe and Ca in carbonate co-precipitation is that of Alsaiari and Tomson at Rice University [90-95]. In 2008 they assessed the influence of Fe^{2+} and Ca^{2+} on the solubility of $FeCO_3$ and $CaCO_3$ at temperatures between 55 and 65 °C in a supersaturated alkaline solution. The investigation considered hydrodynamics by comparing both batch and Continuous Stirred Tank Reactor (CSTR) systems. Test solutions were sparged with CO_2 until oxygen content was below 5 ppb.

For batch tests, NaCl was maintained at 0.01 M while pH varied from 7.55 to 7.31 for Ca concentrations of 0 mM to 95 mM, added in the form of $CaCl_2$. This resulted in a rise in ionic strength from 0.02 M to 0.275 M. 1.9 mM of Fe^{2+} was supplied by $FeSO_4.7H_2O$.

For CSTR tests, NaCl content was increased to 0.5 M to minimise ionic strength drift while a continuous supply of calcium, iron and bicarbonate were pumped independently at a consistent rate. The solution was sampled periodically using spectrophotometry, ICP and titration to measure Fe^{2+}, Ca^{2+} and HCO_3^- respectively. By monitoring the reduction of Fe^{2+} and Ca^{2+} it was possible to quantify the precipitation of siderite and $CaCO_3$. Final bulk precipitate was analysed using XRD and SEM. They found that calcium significantly increased the solubility of siderite. At high saturation levels, $CaCO_3$ formation was thought to strongly impair the affinity of Fe^{2+} with CO_3^{2-}. During CSTR tests siderite formed first before the precipitation of aragonite at an SR for aragonite of ~2. The presence of aragonite appeared to inhibit further precipitation of siderite until higher supersaturation >3 was achieved. At this point both aragonite and siderite were observed to precipitate concomitantly. XRD analysis showed that in the absence of iron, $CaCO_3$ formed as calcite, when iron was present only aragonite formed. SEM imaging revealed that the morphology of the crystals was strongly dependent on the molar ratios of calcium and iron, with siderite forming as highly disorganised plate-like structures and aragonite exhibiting trigonal-hexagonal shape. Mixed crystals that formed through concomitant precipitation exhibited morphology closer to either aragonite of siderite depending on the mole ratio of Ca/Fe. The fraction ratio of iron to calcium in the final crystal structure of these mixed carbonates was also strongly dependent on the quantity of siderite that formed initially before aragonite precipitation.

In their next study [95] they compared bulk calcium and ferrous iron content with the composition of precipitated iron/calcium carbonate. As with the previous experiments the molar ratio of Ca and Fe in the precipitate was calculated based on the measured amount of both ions remaining in the bulk solution based on ICP and titration measurements. The pH range for these experiments was 6.2-7.8 and a temperature of 55 °C. Due to its lower solubility, $FeCO_3$ precipitated first but at high concentrations of calcium $FeCO_3$ formation was fully inhibited.

The molar ratio of Ca to Fe was variant and proportional to the respective ion concentration in the bulk. $CaCO_3$ was likely to precipitate more than $FeCO_3$ in a solution supersaturated with respect to both. The hypothesis for this was that Ca^{2+} has a higher water loss rate constant that Fe^{2+} meaning that Ca^{2+} can more easily lose water molecules to then attach to carbonate ligands.

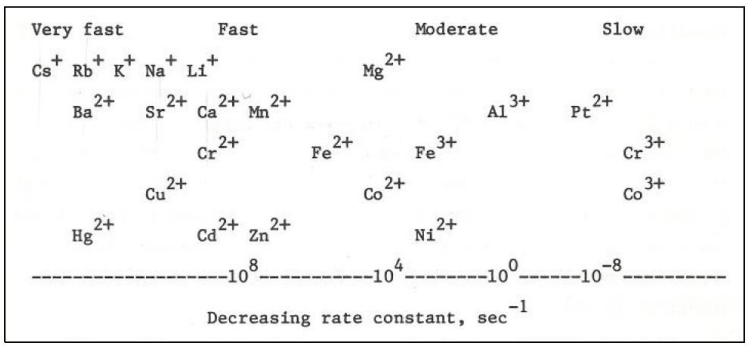

Figure 3.18: Water loss rates of metal ions [95]

In another study from the same group [94], $Fe_xCa_yCO_3$ carbonate crystal growth kinetics were studied under constant bulk composition using refined experimental approach. Seed crystals of iron calcium carbonate were added to 600 ml solutions of water saturated with CO_2 and mixed with NaCl, $NaHCO_3$, $FeSO_4$ and $CaCl_2$ and ionic strength of 0.5 M at temperatures of 31 and 48 °C. pH and ion drop from crystal growth was counteracted by a dual titrant control loop. Successful experiments were conducted with 65 mM Ca^{2+}, 0.42 mM Fe^{2+} and 3.4 mM HCO_3 and constant pH of 7.15±0.05. From EDX analysis, $Fe_{0.013}Ca_{0.987}CO_3$ was found at 31 °C, ionic strength of 0.5M and saturation index (SI) for $CaCO_3$ and $FeCO_3$ of 0.97 and 0.68 respectively. A constant mass flux was shown for crystal growth throughout the experiment.

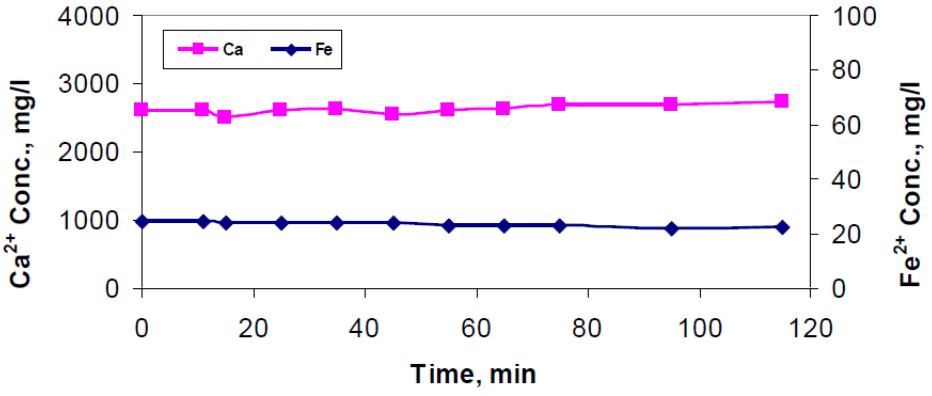

Figure 3.19: Concentrations of calcium and ferrous ions in the reaction solution with time in a representative experiment, x = 0.013 [94]

The authors followed up their initial constant composition study with further results at 55 °C and a range of calcium concentrations with solution pH between 6.2 and 7.8 [93].

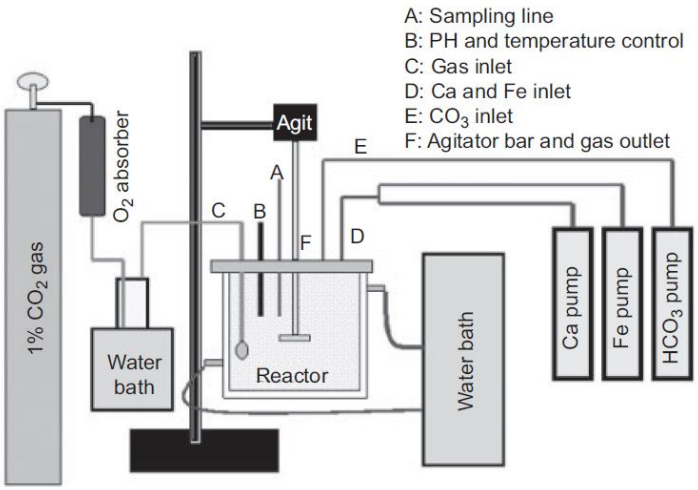

Figure 3.20: Schematic of experimental apparatus from constant composition experiments for $Fe_xCa_{1-x}CO_3$ from [93]

They again concluded that high concentrations of calcium strongly inhibited the Fe^{2+} to CO_3 bond with solution sampling suggesting that high calcium even caused dissolution of $FeCO_3$ in preference for calcium. There was a greater fraction of Ca in the precipitate when compared to the fraction in the bulk. This again supported the finding that $CaCO_3$ is more likely to precipitate when the solution is supersaturated with respect to both calcite and siderite.

Alsaiari et al. concluded the work with a paper in 2012 which claimed to have established a correlation to predict the stoichiometry of mixed iron-calcium carbonate [91]. By conducting a series of experiments at 55 °C and pH 7.3 precipitating mixed iron/calcium carbonates from iron rich to calcium rich they established a correlation between bulk and precipitate composition. The study used a similar methodology to their previous work with the addition of magnetite powder for seed crystals while Fe was added as ferrous chloride 4-hydrate $FeCl_2.4H_2O$. A trial and error approach was used to find titrant rates that maintained a constant composition of Fe^{2+}, Ca^{2+} and HCO_3^- in the bulk, thereby defining the crystal growth rate and composition. After low levels of magnetite were detected in XRD peaks due to magnetite seed crystals this was replaced with zero iron powder and pre-prepared $Fe_{0.99}Ca_{0.01}CO_3$. A logistic correlation was subsequently developed to predict the precipitate composition with an R^2 of 0.97 for all test cases.

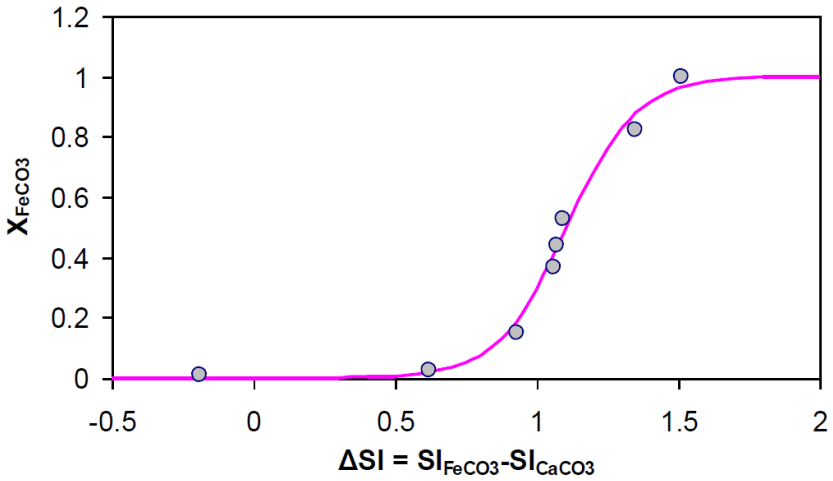

Figure 3.21: Molar concentration of solid solution, $Fe_xCa_{1-x}CO_3$ as a function of the difference in the supersaturation with respect to pure end members at 55 °C. Pink line shows model prediction while grey circles indicate test results. [91]

3.3.4 Iron Calcium Carbonate Formation in Corrosion Studies

Eriksrud and Sontvedt [96] performed one of the earliest corrosion studies that observed incorporation of Ca into $FeCO_3$ during immersion tests in which exposed X52 carbon steel to a variety of real and synthetic formation waters. Tests were conducted in stagnant and flowing conditions at 20 and 60 °C with different oil-salt-water mixtures and CO_2 partial pressures from 1 to 2 bar. The brines contained Ca^{2+}, Mg^{2+}, Ba^{2+} Na^+ Cl^- and SO_4^{2-} ions, with pH ranging from 3.8 in basic NaCl solution to 6.2 with high TDS. Results showed a drop in corrosion rates as Ca^{2+} concentration increased from 0 to 1200 ppm while the effects of Mg^{2+} and SO_4^{2-} were negligible. To investigate further, an additional 20-hour experiment was conducted in an NaCl brine containing 400ppm of Ca^{2+} at 20 °C. Auger Electron Spectroscopy confirmed the presence of Ca within the $FeCO_3$ layer.

Another study by Ueda and Takabe in 1999 [76] investigated the effects of HCO_3^- CH_3COO^- and Ca^{2+} ions and microstructure on the morphology of corrosion products in CO_2 corrosion of J55 and N80 steel. They performed immersion tests in a titanium lined autoclave with 5% NaCl at pH 3.7, 5% NaCl + $NaHCO_3$ at pH 4.7 and 4.7% $CaCl_2$ at pH 4.7. Three 15 x 40 x 2 mm specimens were mounted in a titanium holder. After experiments cross sections of the specimens were analysed with SEM and EMP.

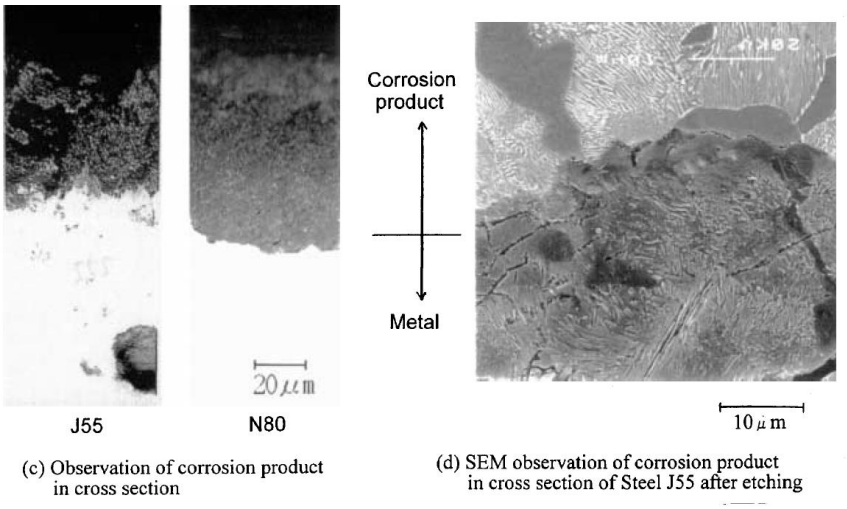

Figure 3.22: Cross section of corrosion scale formed on J55 and N80 steel in presence of calcium at 3 bar and 80 °C from [76]

Results indicated a two phase growth of $FeCO_3$ with 5% NaCl tests due to recrystallization and growth within cementite lamellar left behind during Fe dissolution. In the presence of calcium, corrosion products appeared thicker while general corrosion rates appeared lower. Despite this, localised corrosion increased. Corrosion product was assumed to be a combination of $FeCO_3$ and $CaCO_3$. $FeCO_3$ was suggested to grow inside the cementite lamellar which became enriched with Fe^{2+} while $CaCO_3$ grows in the former ferrite phase.

In 2001, Sridhar et al. used modelling and experimental studies to assess the effects of scale forming species magnesium and calcium, in the corrosion of wet gas pipelines containing H_2S and CO_2. Cylindrical specimens of 1018 carbon steel with exposed area of 9.1 cm^2 were either partially or fully immersed in various stagnant aqueous solutions saturated with combinations of H_2S, CO_2 and O_2. Brine composition was also varied using $CaCl_2$, $MgCl_2$ and NaOH. The tests were completed in 3L 316L autoclaves over 14 days at 15.5 °C. pH was predicted using OLI software and by measurement prior to acid gas addition and immediately after test. No significant correlation between Ca and Mg scaling tendency was observed, which was possibly due to the lack of protective layer formation with the porosity of the layer that formed allowing electrolyte to still reach the substrate steel. Corrosion rate of partially immersed specimens was higher than fully immersed which the authors attributed to higher O_2 exposure or enhanced cathodic reaction kinetics from corrosion products such as greigite.

A study by Wu et al. [97] in 2004 characterised corrosion products formed on N80 steel in CO_2 corrosion from stratum water containing Ca^{2+}. Tests were conducted over 72 hours at 80 °C and 5 bar CO_2 pressure in a rotary autoclave with a flow velocity of 1 $m \cdot s^{-1}$. Surface films were analysed by X-ray Photoelectron Spectroscopy (XPS), EDX, XRD and SEM. SEM showed a well adhered corrosion film with no cracks. EDX showed the film to mainly comprise Fe C and O with additional Ca and Mn. XRD showed the presence of a complex carbonate shifted away from the $FeCO_3$ main peak and $MnCO_3$. Pure $CaCO_3$ was not detected however trace α-FeOOH was detected. XPS analysis confirmed the XRD findings with regards α-FeOOH and $Fe_xCa_{1-x}CO_3$ however no Mn signal was detected. The presence of α-FeOOH was thought to be a consequence of $FeCO_3$ decomposition due to prolonged desiccation and exposure to air.

Cui et al. [98] also tested various steels in simulated produced waters bearing calcium. Test solutions were a mixture of crude oil from Sheng Li oil field and simulated stratum water with Ca^{2+} content of 5405 $mg \cdot L^{-1}$. Solutions were heated and pressurised in a rotary autoclave to 82.74 bar and 60, 90, 120 and 150 °C, flow velocity was 1 $m \cdot s^{-1}$. Corrosion rates of J55, N80 and P110 pipe steels were assessed by mass loss. Corrosion product was analysed by SEM.

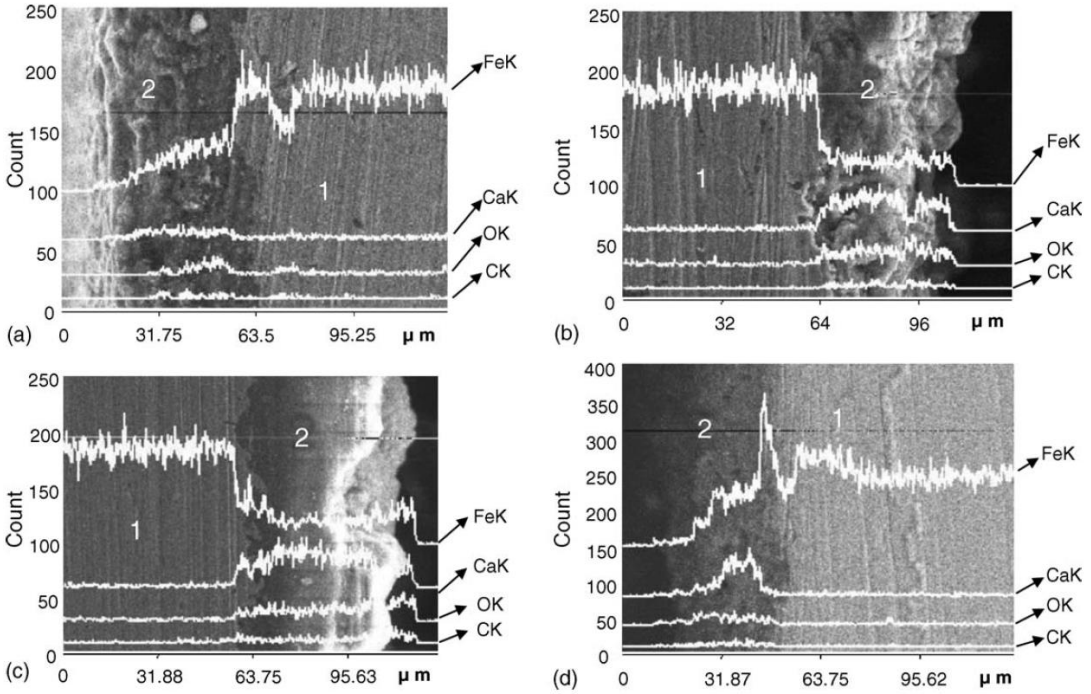

Figure 3.23: EDX line scans through films formed on J55 steel in static CO_2 saturated stratum water (a) 60 °C (b) 90 °C (c) 120 °C (d) 150 °C [98]

In 100% brine tests with no oil, corrosion rates initially dropped from around 30 to 12 mm·year^{-1} after 48 hours then dropped again after 72 hours due to the formation of protective scale. XPS confirmed the presence of (Fe,Ca)CO_3 across the full temperature range but appeared more stable at the lower temperatures. EDX line scans through the layer revealed that the layer became more iron rich close to the surface.

Another case study performed by Zhu et al. [24] employed various microscopic, spectroscopic and electrochemical techniques to investigate a P110 steel piping failure in the presence of $FeCO_3$, Fe_3O_4 and $CaCO_3$. In addition to visual examination, XRD and SEM of failed tubing from the field an autoclave test was performed using 5 samples immersed in sample brine.

This was purged with N_2 and then 3 bar CO_2 before heating to 110 °C and 470 bar pressure for 168 hours. Mass loss, LPR and EIS were performed to assess corrosion rates using saturated calomel reference and graphite counter. XRD of failed tubing showed the presence of $FeCO_3$ and Fe_3O_4 as corrosion products while a mineral scaling layer mainly comprised of $CaCO_3$ with fractions of $FeCO_3$ and Fe_3O_4 also present. At least 89 other mainly non-polar substances, components of the crude oil, made up the bulk of scale products. From autoclave tests, only $FeCO_3$ was detected as the primary corrosion product. This author inferred that Fe_3O_4 was only present on the field material as a result of prolonged exposure in air. The tubing suffered severe localised corrosion likely due to the porosity of the bulky corrosion/scaling layers.

Zhang et al. [99] explored the effects of HCO_3^- concentration on carbonate scales that form during CO_2 corrosion of X65 steel in the presence of Ca^{2+} and Mg^{2+} ions with pH ranging between 4.5 and 7. Tests were conducted at 65 °C and ~0.75 bar and 3 bar pCO_2 in a 10 L autoclave for 144 hours. XRD analysis indicated that at low HCO_3^- and pH only $FeCO_3$ formed while at higher pH a mixed $(Ca,Fe,Mg)(CO_3)_2$ was evident. At low pH the scales were more compact under static conditions compared to flowing while at high pH the film was independent of flow.

Gao et al. [100] observed mixed carbonate formation when assessing the mechanical properties of corrosion scales formed on X65 carbon steel in synthetic brines containing Ca^{2+}, Na^+ SO_4^{2-} and Mg^{2+}. Tests were conducted at 65 °C and 1, 3 and 10 bar pressure for 240 hours.

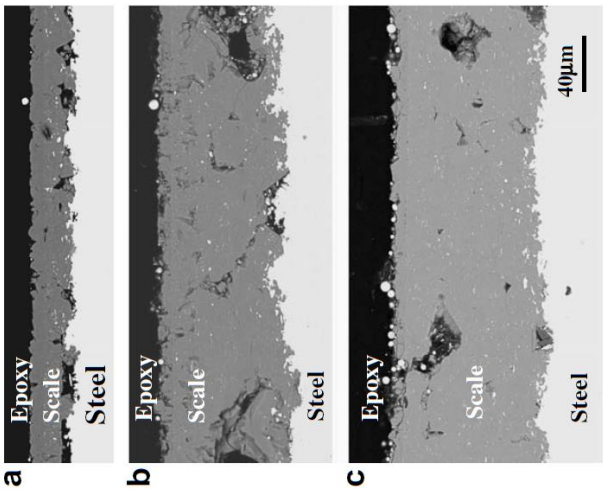

Figure 3.24: Cross section of scale formed on X65 steel at flow rates of (a) 0, (b) 0.5 and (c) 1 $m \cdot s^{-1}$ from [100]

XRD indicated presence of $FeCO_3$ while no peak was observed for $CaCO_3$ despite EDX detecting Ca and Mg in corrosion scale under static conditions and Ca in flowing conditions. This result inferred precipitation of complex carbonates $(Fe,Ca)CO_3$ and $(Fe,Ca,Mg)CO_3$ under flowing and static conditions respectively. Only at the lower pCO_2 of 1 bar were diffraction peaks for $CaCO_3$ and $MgCO_3$ present. The quantity of Ca in the scale decreased with pCO_2 while corrosion product thickness increased. Both general and localized corrosion increased with flowrate and pCO_2.

In 2018, Bai et al. [101] observed formation of $Fe_xCa_yCO_3$ on J55 steel in high pressure CO_2 corrosion studies up to 150 bar in a 30% crude oil brine. XRD and EDX indicated mixed $Fe_xCa_yCO_3$ corrosion products with higher Ca^{2+} at lower pressures of 15bar and 90 bar.

In a study by Rizzo et al. [102] the effects of $CaCO_3$ precipitation on 1Cr carbon steel pre covered with protective $FeCO_3$ was analysed. The experimental procedure involved pre corrosion of the steel at 80 °C and pH 6.5 until protective $FeCO_3$ was formed based on electrochemical measurements and left to stabilise further for 15 hours. A premade solution of $CaCl_2$ was then syringed into the cell. Solution was sampled between phases using Ultraviolet-visible (UV-vis) spectrophotometry and ICP while pH was measured in-situ. Benchmark tests without Ca addition and with simulated pH reduction via HCl were also performed.

At low Ca^{2+} addition pH remained stable but reduced to 5.4 with addition of 10000 ppm this corresponded to an increase in corrosion rate. Adding NaCl to simulate the additional Cl^- showed no effect on increasing the general corrosion rate after $FeCO_3$ has formed. Water analysis showed that the initially high concentrations of Fe decreased to less than 1 ppm during the $FeCO_3$ precipitation and growth stage. During Ca addition, bulk Fe^{2+} increased with increasing Ca^{2+} apart from at low Ca^{2+} of 100 ppm where it was unchanged. XRD showed presence of a $CaCO_3$ layer only at 10000 ppm Ca. Cross section SEM of high Ca^{2+} concentration tests revealed inner layer dissolution with loose $CaCO_3$ precipitated on the surface. Similar results were observed with HCl addition, but with re-precipitated $FeCO_3$ as the outer layer. These observations were consistent with increased localised attack of the substrate. Mixed $Fe_xCa_{1-x}CO_3$ was not observed throughout the study.

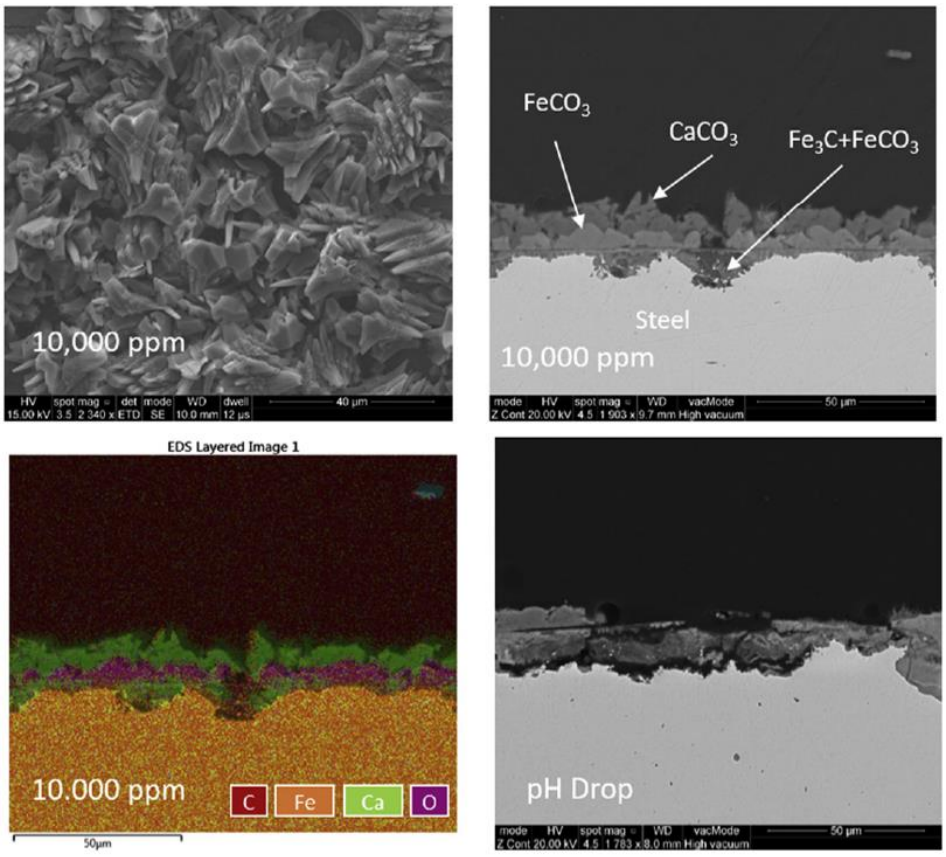

Figure 3.25: Surface morphology and cross section of 1 Cr steel samples after addition of 10,000 ppm of Ca^{2+} to experiments conducted after initial $FeCO_3$ formation.[102]

Matamoros-Veloza et al. [103] also performed experiments to assess the structure and stability of $(Fe,Ca)CO_3$ layers in comparison to $FeCO_3$.

Corrosion products were formed on X65 carbon steel in an autoclave at 80 °C and 30 bar pCO_2 for 72 hours. The brine solutions were 1 wt% NaCl solution with and without 220 $mg \cdot L^{-1}$ of Ca^{2+} added as $CaCl_2.H_2O$. pH was adjusted to 7 with addition of $NaHCO_3$. After film formation the specimens were transferred to a low pressure flow cell which was circulated with a 1 wt% NaCl solution again at 80 °C and pH of 3.6 and 7. Corrosion products were analysed by SEM, XRD, X-ray Absorption Near Edge Structure (XANES) and Extended X-ray Absorption Fine Structure (EXAFS). Initial observations of the corrosion products showed that incorporation of Ca^{2+} produced a more rounded morphology and evidenced a growth mode in kink sites along steps causing spiral dislocations which have been previously reported in calcite [104]. The growth behaviour suggested large anisotropy in bonding with different growth rates in each direction compared to pure $FeCO_3$.

In particular, enlarging the step along the *c*-axis due to the increased atomic radii of Ca compared to Fe. The increased inhomogeneity created by calcium incorporation was considered to promote localised corrosion due to inefficient packing of crystallite structures that formed on the steel surface. The authors also noted that the enlarged structure of $Fe_xCa_yCO_3$ allowed fast hydration of Ca into the solution increasing the solubility of the film and weakening its mechanical integrity.

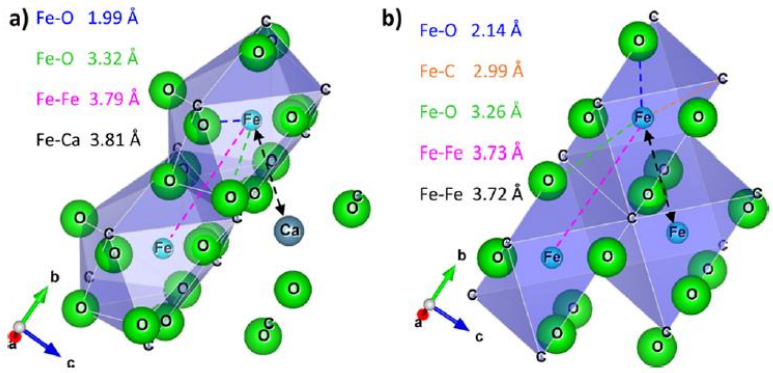

Figure 3.26: (a) Structure of $Fe_xCa_yCO_3$ showing potential modifications when Ca replaces Fe in $FeCO_3$ lattice and (b) $FeCO_3$ structure. Atomic distances found by EXAFS [103]

In 2021, Prieto et al. [105] analysed the mechanical properties of $FeCO_3$ and $Fe_xCa_yCO_3$ layers through the application of scratch testing. Corrosion products were formed in a bubble cell at atmospheric pressure and 80 °C.

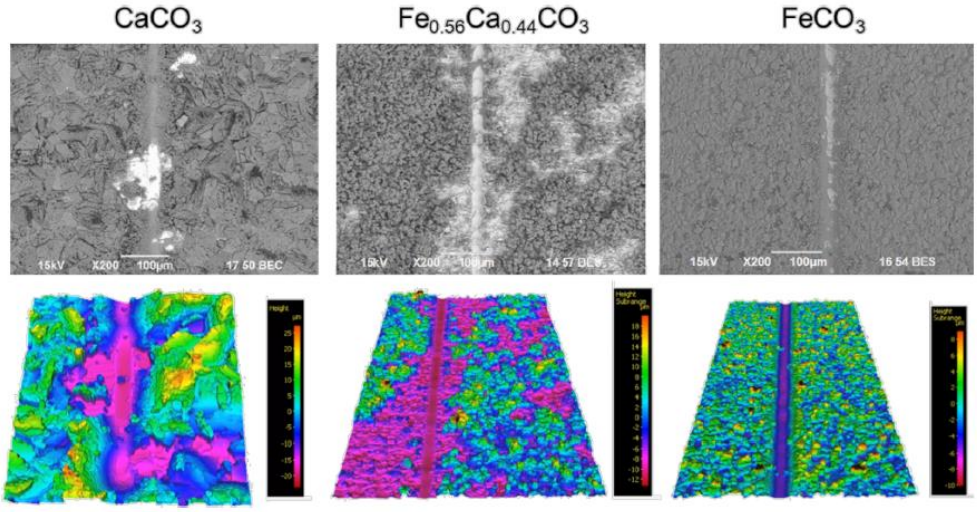

Figure 3.27: SEM (top) and profilometry (bottom) images illustrating failure modes of different types of Fe/Ca carbonate corrosion scales [105]

For $FeCO_3$ layers the pH was adjusted to 6.6 and experiments were left for 3 days. To form pure $CaCO_3$ the duration was 1 day at pH 6.2. For $Fe_xCa_yCO_3$ initial pH was initially highly alkaline at pH 10.5 due to addition of $Ca(OH)_2$ before reducing to pH 6.2 as the surface layer precipitated. The experimental duration for $Fe_xCa_yCO_3$ formation was varied to produce varying stoichiometries ranging from 0.56 to 0.88 mole fraction x of iron.

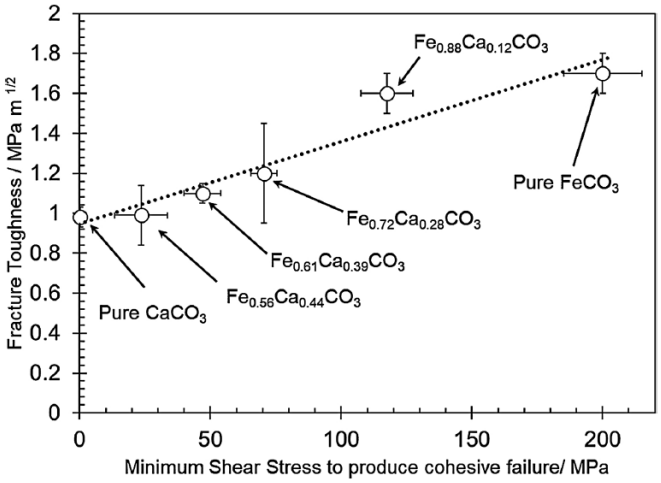

Figure 3.28: Correlations between fracture toughness and minimum shear stress to produce superficial damage as a function of calcium incorporation in $FeCO_3$ [105]

The authors concluded that calcium substitution in to $FeCO_3$ decreased fracture toughness but did not appear to have a detrimental effect on corrosion performance nor were the stresses required for layer removal proximate to those induced by typical pipe flows.

3.3.5 Effects of Calcium Incorporation on General Corrosion Behaviour

Experiments by Zhao et al. [106] using simulated oil field brines showed how Ca^{2+} and Mg^{2+} ions can influence the corrosion rates and morphology of corrosion products on P110 tube steel. Using mass loss and electrochemical techniques they performed autoclave tests at 90 °C and 25 bar. Addition of 6000 ppm of Ca^{2+} and 1000 ppm of Mg^{2+} was shown to initially decrease corrosion rate in comparison to brines without these ions, though over long term (10 days) the corrosion rates were almost indistinguishable. Morphologically, crystalline $FeCO_3$ was replaced by amorphous $Fe(Ca,Mg)(CO_3)_2$ which had inferior adhesion.

A potentiodynamic sweep at the end of the tests showed a simultaneous increase in anodic and decrease in cathodic currents due to the presence of Ca and Mg in the corrosion scale. Further, EIS revealed that layer capacitive and diffusion resistance were decreased while charge transfer resistance increased.

Ding et al. [107] analysed the effects of Ca^{2+} on X65 steel in simulated stratum water at 75 °C and 10 bar pressure. X65 specimens were immersed in simulated solution for 10 days with 64, 128, 256 and 512 $mg \cdot L^{-1}$ of Ca^{2+} added as $CaCl_2$.

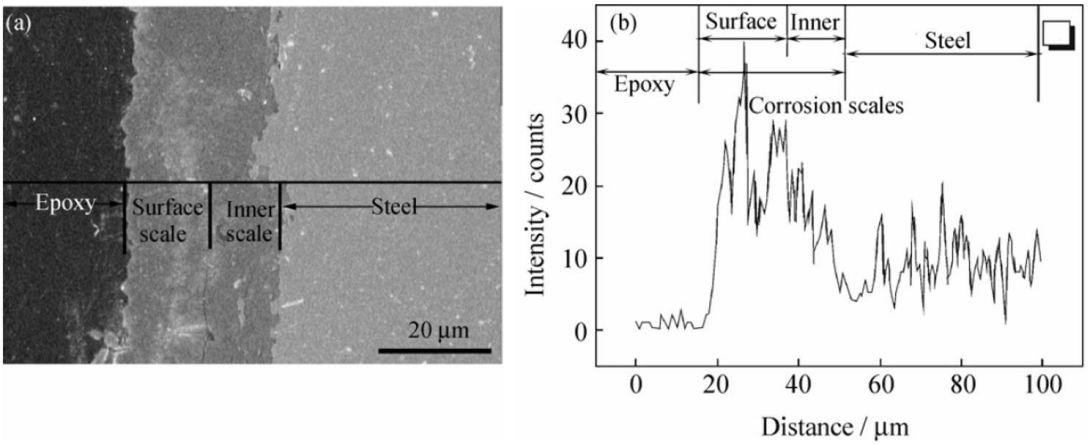

Figure 3.29: EDX analysis of calcium concentration through a corrosion scale layer [107]

Results indicated that corrosion rate increased with calcium concentration due to poor adhesion and larger crystal size resulting in greater porosity. However pH was allowed to drift due to addition of $CaCl_2$. Increasing Ca^{2+} caused a shift in XRD diffraction peaks for $FeCO_3$ to lower values.

Pure $CaCO_3$ or $MgCO_3$ peaks were not observed. Cross section EDS indicated a duplex surface scale rich in calcium on the outside and much lower in the inner scale formed inside the Fe_3C matrix.

In 2011, Jia et al. [108] used electrochemical techniques to evaluate the effects of Ca^{2+} on general and localised corrosion behaviour of 3Cr low alloy steel. Solutions were 0.5M NaCl, 0.15M NaCl + 0.15M $CaCl_2$ and 0.8M NaCl. The authors found addition of Ca^{2+} was found to have minimal effect on corrosion rate. EDS analysis revealed incorporation of Ca into the corrosion product along with Fe and Cr. The author suggested the presence of $Cr(OH)_3$.

Esmaeely et al. [109] focused on the effects of Ca^{2+} in various concentrations on corrosion mechanisms on AISI 1018 steel in simulated saline aquifer environments. In a 2 L glass cell AISI 1018 mild steel samples with exposed area of 5.4 cm^2 were immersed in 1 wt% NaCl CO_2 solution. pH was adjusted to 6.6 by addition of 1 M of NaOH. OCP and LPR were monitored while SEM, EDX and XRD used for analysis as well as Infinite Focus Microscopy (IFM). Ca and Fe concentrations were analysed using ICP and UV-vis respectively. Clarke's solution was used to remove the corrosion on one sample per test. At low Ca^{2+} concentrations (≤100 ppm) $FeCO_3$ was able to form and corrosion rates dropped. This was not the case at higher concentrations suggesting a lack of protective corrosion product formation due to acidification from $CaCO_3$ precipitation. Crystal coverage and morphology was shown to dramatically change due to increased Ca^{2+} concentration. At 1000 ppm and above a uniform scale formed as opposed to distinct crystals. XRD peak shifts indicated a solid solution of $Fe_xCa_{1-x}CO_3$ while higher [Ca^{2+}] resulted in addition of $CaCO_3$ crystals. Cross section SEM and EDX revealed a bilayer of iron rich scale adjacent to the substrate which gradually transitions to a calcium rich outer layer.

Tavares et al. [110] performed long term tests to evaluate the influence of $CaCO_3$ on the corrosion of X65 steel in high pressure and highly saline solution. 6.4 M of NaCl was added to test solution to achieve saturation while $CaCO_3$ powder was dosed at a concentration 10 times its mineral saturation limit. Addition of $CaCO_3$ raised system pH from 2.71 to 4.72. Tests were conducted in a 1l Ti alloy autoclave using LPR and mass loss techniques.

Test periods of 4, 14 and 28 days were selected to verify the stability of the corrosion scales over time. Surface films were characterised using SEM, EDS and XRD. Linear sweep voltammetry was employed post-test by submerging samples in the same brine composition but at 25C and atmospheric pressure to obtain electrochemical properties of the corrosion products. Corrosion rates were on average half the value with addition of $CaCO_3$ however this could be attributed to the pH difference. XRD and EDS indicated an $Fe_{0.79}Ca_{0.21}CO_3$ solid solution corrosion product compared to $FeCO_3$ in the absence of $CaCO_3$ and was noticeably easier to remove during the mass loss procedure. Average crystal size and layer thickness were both reduced in the presence of calcium (layer thickness reduced from 30 to 20 μm after 28 days).

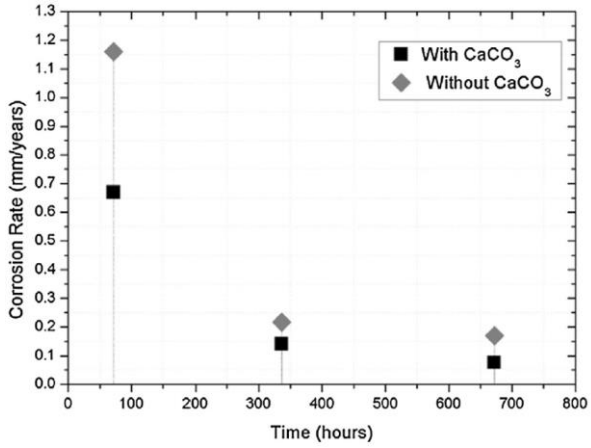

Figure 3.30: Corrosion rate determined by mass loss as a function of exposure time for brines with and without $CaCO_3$ from [110]

In 2018, Hua et al. [11] investigated the protectiveness of corrosion products in the presence of Cl^-, Ca^{2+} and Mg^{2+}. Tests were conducted at 60 °C and 100 bar supercritical CO_2. Samples of X65 steel were placed in an autoclave with a total a/v ratio of 93 $cm^2 \cdot L^{-1}$. Ca^{2+} was added using $CaCl_2.2H_2O$ and Mg^{2+} added using $MgCl_2.6H_2O$. Corrosion rates were analysed using mass loss method, with mass weighed before and after corrosion product removal. Analysis of corrosion product mass and corrosion rate allowed prediction of bulk Fe concentration with pH values predicted using Multiscale software. Corrosion products were analysed using SEM, XRD, EDX and Focused Ion beam (FIB). Localised corrosion was assessed using profilometry. For all tests, pH estimations indicated that corrosion product precipitation restricted pH increase in the bulk to no more than 0.25 units from pH 3, with the solutions becoming stable after 24 hours.

Initially, Ca^{2+} addition decreased corrosion rates while Mg^{2+} had the opposite effect. As with Cl^- content, all conditions converged to a similar corrosion rate by the end of 96 hours with the exception of 10000 ppm Mg^{2+} which remained high. XRD peak shifts indicated gradual Ca substitution into the $FeCO_3$ lattice with increasing Ca^{2+} concentration while morphologically crystals became finer and more globular. This change also corresponded to an increase in apparent porosity of the outer layer that did not appear to affect general corrosion rates. This suggested the properties of an inner layer had greater control over the corrosion process. Close observation of XRD data from Mg^{2+} tests showed a peak broadening and shift to higher 2θ consistent with substitution of Mg in to the $FeCO_3$ lattice. Although less noticeable than Ca due to the comparative sizes of Mg and Fe EDX analysis confirmed much less Mg was present in the layer compared to Ca for a given bulk concentration indicating that Ca has a greater affinity for $FeCO_3$ substitution despite its larger atomic radius.

A recent study by Shamsa et al. [52] explored the corrosion behaviour of carbon steel in CO_2 saturated environments in the presence of Ca^{2+} ions at temperatures of 80 °C and 150 °C. The test solutions were composed of distilled water with 0 and 1.83 wt% $CaCl_2{\cdot}2H_2O$ salt added in conjunction with a corresponding amount of NaCl to maintain a total chloride concentration of 1.83wt%. Mass-loss experiments were performed in an autoclave for 6, 24, 48 and 96 hours. The resulting corrosion products were qualitatively evaluated under SEM while the film composition was quantitatively measured using XRD. Further analysis of the film composition as a function of depth from the surface was performed using Focused Ion Beam (FIB) and EDX line scans.

The results showed that the addition of Ca^{2+} ions produced a mixed carbonate scale of the form $Fe_xCa_yCO_3$. The values of x and y (stoichiometry) could be predicted by the shift in peak position in the XRD results. EDX line scans revealed that the ratio of x:y in $Fe_xCa_yCO_3$ varied across the film depth. Interestingly, at 80 °C calcium content was found to be higher close to the steel surface while the opposite was true at 150 °C.

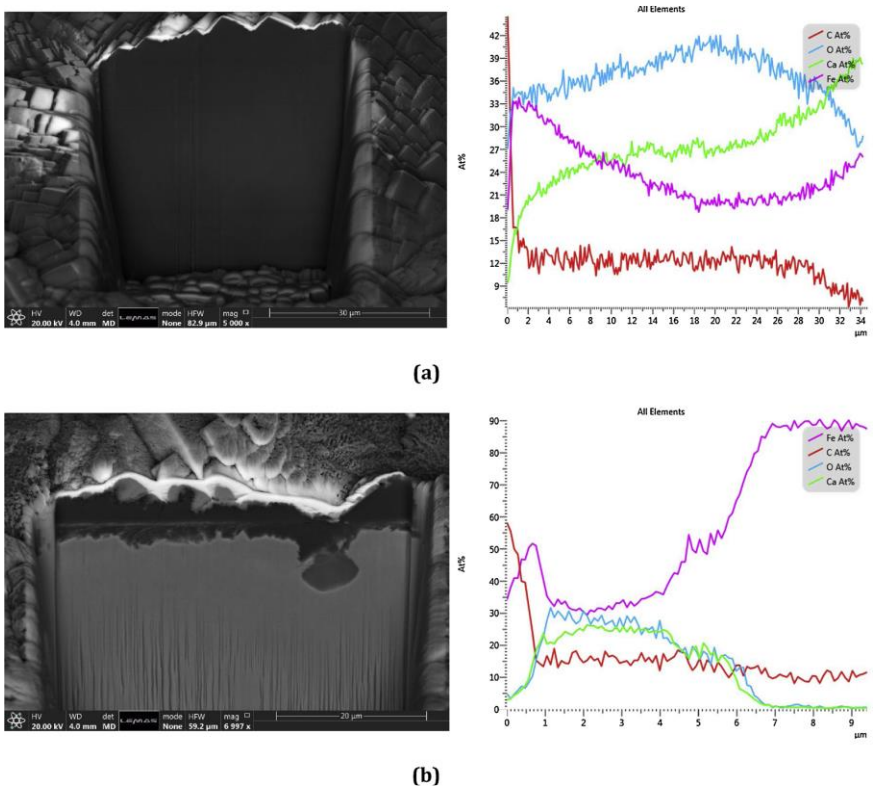

Figure 3.12: FIB section and EDX line scan of X65 steel cross-section after exposure to CO_2 saturated 1.54wt% NaCl 1.83wt% $CaCl_2 \cdot 2H_2O$ after 96 hours at (a) 80 °C (b) 150 °C. Taken from [52]

Conversely, Wang et al. [111] found that increased Ca^{2+} in the solution actually decreased corrosion rates on 3Cr steel and corresponded to a greater uptake of calcium in the corrosion layer, this also led to a less porous layer. They also observed a bilayer formation with higher calcium in the outer layer and $Cr(OH)_3$ in the sub-layer.

Mansoori et al.[112] investigated the effects of Ca^{2+} on CO_2 corrosion of mild steel in a $CaCO_3$ saturated brine solution using a pH and Fe^{2+} ion exchange control system. Solution chemistry was controlled using H-form and Na-form ion-exchange resins to control pH and Fe^{2+} concentration respectively. The hydrodynamics of the test solution were defined using a Rushton type impeller calibrated using ferri-ferrocyanide coupled reactions to obtain a mass transfer coefficient representative of a 0.5m/s pipe flow. Experiments were conducted at pH of 6.2 and ambient pressure over 7 days, with and without calcium. For Ca tests, a reservoir of Ca^{2+} ions was created by adding $CaCO_3$ in to the bulk until 3 times its saturation limit. For the baseline experiment with no calcium, $NaHCO_3$ was added to the solution until the pH matched that of the calcified solution. Corrosion rate was monitored using mass loss and LPR techniques.

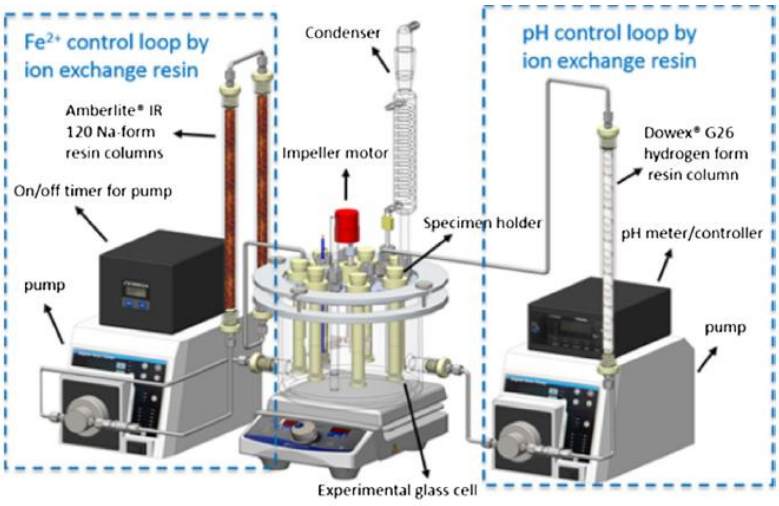

Figure 3.31: Experimental apparatus developed by Mansoori et al. [112] to control system chemistry

LPR tests indicated three distinct phases of the corrosion process. Active dissolution revealing the Fe_3C matrix enhancing cathodic reactions. Nucleation and growth of carbonate crystals within the Fe_3C matrix where the solution was quiescent and therefore pH and Fe^{2+} were able to increase until local supersaturation of $FeCO_3$ occurred. Finally, formation of a densely packed layer of protective iron carbonate crystals which acted as a diffusion barrier to dramatically reduce corrosion rates. In Ca tests, an equally protective layer was observed on the steel surface giving similarly low corrosion rates after 7 days of immersion. XRD data after 2 days of testing revealed almost identical crystal composition with and without Ca and not until days 4 and 7 could $Fe_xCa_yCO_3$ be observed, indicating heterogeneous substitution of Fe by Ca in the crystal lattice.

In a further study using the same experimental setup [113] Mansoori et al. looked at the effect of high concentrations of Ca^{2+} on CO_2 corrosion mechanisms of UNS G10180 steel specifically investigating protectiveness of pure $CaCO_3$ and $Fe_xCa_{1-x}CO_3$ at a lower pH of 5.5. Pure $CaCO_3$ was precipitated without Fe by cathodic polarisation of samples to -200mV_{OCP} for 5 days. Both $CaCO_3$ and $Fe_xCa_{1-x}CO_3$ were found to act as mass transfer barriers for Fe^{2+} creating favourable local conditions for the precipitation of protective $FeCO_3$ within the Fe_3C pores exposed during preferential dissolution of the ferrite phase. $CaCO_3$ was not found to provide protection against corrosion unlike $FeCO_3$ due to the better adhesion of the $FeCO_3$ to the steel substrate.

3.3.6 Effects of Calcium Incorporation on Localised Corrosion

A study in 2001 by Sun et al. investigated the effect of Ca^{2+} on localised corrosion of P110 steel. The results showed that the addition of Ca^{2+} in the brine solution transitioned the pitting morphology from a typical V-shape to V-shape together with semi-spherical and closed spherical pits.

In a study by Jiang et al. in 2006 [114] the susceptibility of N80 steel to pitting corrosion under stagnant and flowing conditions with and without pre-corrosion in the presence and absence of Ca^{2+} ions was investigated. The tests were conducted at 57 °C and ambient pressure. All test solutions contained 3% NaCl, 4.6% NaCl or 3% NaCl + 1.5% $CaCl_2$ (equivalent Cl^- to 4.6% NaCl) and saturated with CO_2 by continuous bubbling during test. A 3 electrode setup was used with a modified rotating disk electrode for flow tests. Exposed sample area was 2.01 cm^2. For pre-corrosion tests, samples were pre-corroded in stagnant conditions for 41 hours before rotation at 5m/s for 12 hours. Corrosion product and pitting were assessed by surface and cross section SEM as well as EIS. For stagnant conditions at a constant Cl^- content, Ca^{2+} decreased corrosion rate and increased initiation period for pits. In flowing conditions, pre-corrosion decreased overall corrosion rates. For the pre-corroded specimens in flowing conditions, addition of Ca^{2+} further decreased overall corrosion rates. Pitting was attributed to local acidification by formation of $Fe(OH)_2$ and subsequent diffusion of Cl^- to the area to balance H^+ and Fe^{2+}.

Lab and field investigations on localised corrosion of well casings by Ren et al. in 2012 [115] suggested that Ca^{2+} promoted localised corrosion. Scales formed in autoclave tests showed good adherence to the steel but many micropores thought to be the cause of pit initiation. Field samples showed that 74% of wells analysed suffered from noticeable pitting of the casing. Well brines were categorised in to three types, sodium sulfate, sodium bicarbonate and calcium chloride based on dominant mole fraction in each. Calcium chloride brines were shown to have the highest average pit depth of 1.74 mm. However, the $CaCl_2$ brines on average contained 10,000 $mg \cdot L^{-1}$ of Cl^- compared with several hundred $mg \cdot L^{-1}$ in other brines. Pits were found to exhibit a 3 layer structure.

Tavares et al. [110] found that polarisation tests after long term autoclave experiments indicated that Ca-containing films were more porous which increased susceptibility of the substrate to Cl^- penetration, and as a result, pitting.

Esmaeely [109] also suggested that high bulk Ca^{2+} concentrations appeared to roughen the substrate surface and enhance pitting. In a later paper [116], the group made an attempt to decouple chloride addition from calcium addition by adjusting NaCl concentrations to maintain a constant Cl^-. Experiments were conducted in a 2 L glass bubble cell with a standard 3 electrode setup. 0 and 10,000 ppm of Ca^{2+} were investigated by addition of 54.7g $CaCl_2$. In baseline test without $CaCl_2$ additional NaCl was added to maintain Cl^- of 17,800 ppm. Flow was simulated using a magnetic stirrer at 0, 300 and 500 rpm. Samples of the solution were analysed by ICP while UV-vis was used for Fe^{2+} concentration. Due to high a/v ratio the solution was periodically doped with HCl to maintain system pH. pH measurements indicated that high Ca^{2+} concentrations were able to stabilise system pH due to the equilibrium with $CaCO_3$. In absence of Ca^{2+} a partial coverage of $FeCO_3$ was present after 6 days while presence of Ca^{2+} gave a non-uniform coverage of a monolayer of $Fe_xCa_{1-x}CO_3$. The flow rates investigated showed little effect on corrosion product formation however high flow did appear to reduce localised corrosion and increase general corrosion. Presence of Ca^{2+} enhanced localised corrosion compared to a solution with an equal concentration of Cl^-.

In the study by Hua et al. [11], despite not having much effect on general corrosion, addition of Ca^{2+} was observed to increase pit growth and overall penetration depth. Shamsa et al. [52] also noted the presence of Ca^{2+} to accelerate pit growth in addition to increased general corrosion due to the less protective nature of the $Fe_xCa_yCO_3$ scale when compared with a pure $FeCO_3$ layer. Jia et al. [108] found the addition of Ca^{2+} impacted localised corrosion with pits becoming smaller and more evenly distributed over the surface.

In the study by Mansoori et al. [113] with high concentrations of Ca^{2+} localised corrosion was not observed.

3.4 Electrochemical Characterisation of Corrosion Product Layers

EIS has been widely adopted in literature to characterise the properties of corrosion layers in terms of general corrosion, porosity, and even localised corrosion.

In the study by Jia et al. [108] a 3 electrode cell with SCE as reference and Pt as counter were used to conduct ambient pressure polarisation and EIS tests in conjunction with mass loss. Tafel plots showed a trans-passive region in the anodic branch when Ca^{2+} was present, indicating the formation and breakdown of a layer, potentially related to precipitation and subsequent dissolution of $CaCO_3$. Electrical Equivalent Circuit (EEC) models for EIS interpretation used a Randle's circuit with the Warburg diffusion element replaced with a standard parallel RC element, however no attempt was made to quantify properties other than total resistance.

Zhao et al. [106] also used potentiodynamic sweeps and EIS which showed a gradually and continuous change in charge transfer resistance throughout the test. The initial EEC circuit was identical to that of [108] featuring a capacitor C_{dl} which represented the film-electrolyte interface and a separate parallel-connected R_c and C_c to describe film-substrate interface as well as an electrical resistance for the ions through film defects. Later in the experiments a separate series combination of diffusion resistance and impedance were added.

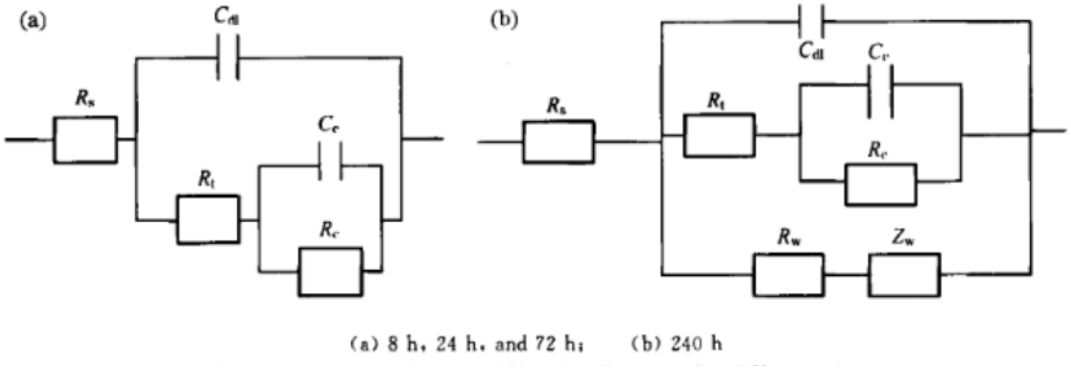

Figure 3.32: EEC Circuits adopted by Zhao et al. [106]

Jiang et al.[114] also used EIS to characterise corrosion products formed with and without calcium. This work opted for a simplified Randle's circuit to characterise just the high frequency range of the data.

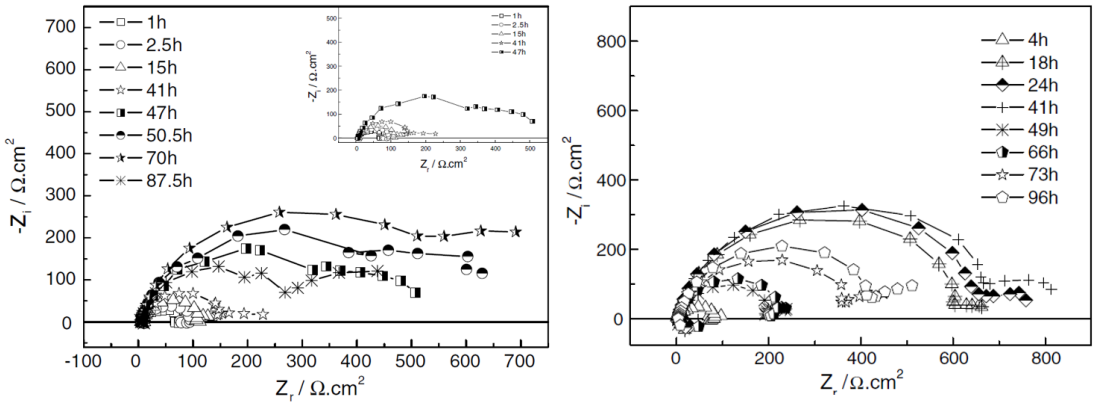

Figure 3.33: EIS Nyquist plots from Jiang et al.[114] with 3% Nacl (left) and 3% NaCl + 1.5% $CaCl_2$ (right)

In 2011, Zhang and Cheng [117] analysed general and localised corrosion behaviour of X65 steel in simulated formation water at atmospheric pressure using various electrochemical techniques including localised EIS (LEIS). Electrodes were made using X65 steel wire surrounded by an X65 cylinder and set in resin. Samples were immersed in simulated formation water pH of ~5.1. Temperature was controlled by water bath at 30, 60 and 90 °C. For the first 10 days of testing only the X65 cylinder was exposed to solution to allow formation of $FeCO_3$. An epoxy coating was then removed from the inner X65 wire to reveal a bare steel surface while still immersed in solution. The bare steel wire and $FeCO_3$ coated cylinder were alternately used as WE.

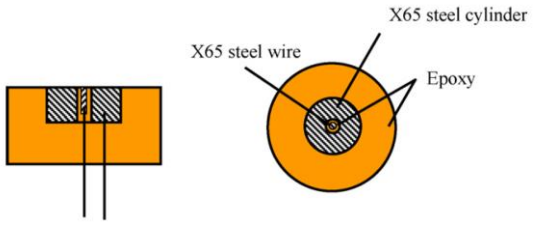

Figure 3.34: Wire electrode for localised corrosion assessment from [117]

LEIS was performed using a scanning electrochemical workstation. Galvanic current and LEIS indicated a galvanic couple with the scale covered cylinder as cathode and bare steel wire as anode which was accentuated as temperature increased. EIS indicated a gradual transition in the nature of the electrode/solution interface with continuously increasing corrosion resistance over time. At 30 °C corrosion scale was extremely limited, at 60 °C the scale was compact and crystalline with approx. 5 µm crystals.

At 90 °C this further reduced to 1 µm with an even more compact layer. EDX analysis showed presence of Fe C and O in corrosion product with Ca and Mg present at 60 °C and above after longer test periods.

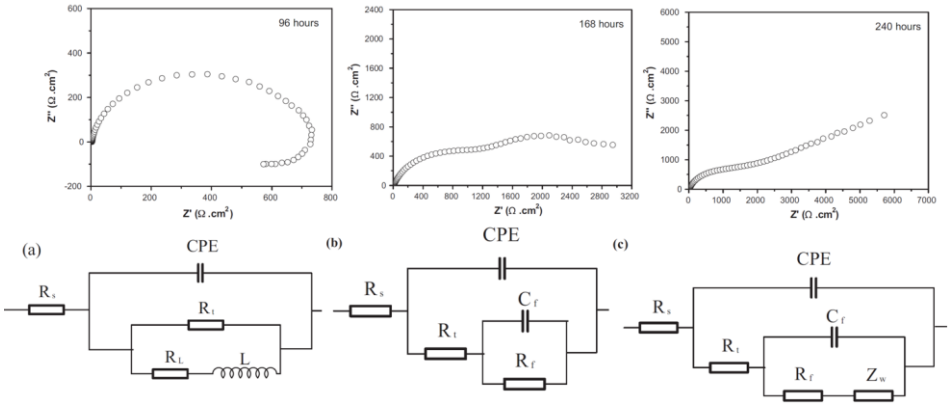

Figure 3.35: Impedance plots at 60 °C and corresponding EEC's from [117]

Wang et al. [111] used EIS to assess the performance of corrosion layers formed on 3 Cr steel as well as cyclic cathodic polarisation. The EEC fitted indicated a higher pore resistance with increased Ca^{2+} concentration. Oddly, electrochemical measurements were performed in a bubble cell at atmospheric pressure whilst mass loss and surface characterisation was performed on samples formed in an autoclave at 8 bar pCO_2.

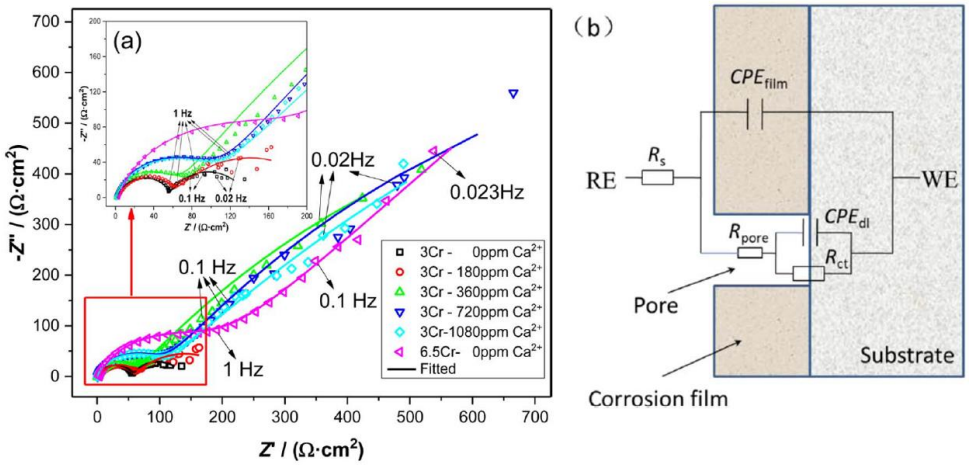

Figure 3.36: Impedance data and EEC from corrosion products formed on 3Cr steel at 80 °C and pH 5.68 - 5.99 after 120 hours [111]

Despite limited EIS analysis performed specifically on $Fe_xCa_yCO_3$ layers a number of papers focused on $FeCO_3$ formation have been produced with more recent papers producing promising methodologies for analysis.

In 2020, De Motte et al. [51] produced a comprehensive impedance based characterisation of corrosion products formed on low alloy steel at pH 6 and 6.6 at 80 °C. Samples of X65 steel were immersed in a 0.2 wt% NaCl solution saturated with CO_2 by continuous bubbling at atmospheric pressure and unstirred. EIS was performed between 15 minute OCP measurements at a perturbation of ±10 mV over the course of 10-12 days. The impedance data revealed a high frequency loop attributed to formation of Fe_3O_4 formed between the substrate steel and top $FeCO_3$ layer. The overall increase in resistance was attributed to the diffusion barrier formed by the thick $FeCO_3$ layer which was modelled using a Finite Length Warburg element represented by the Wd in the EEC in Figure 3.37. Fitted data was used to calculate double layer capacitance and active surface area as well as theoretical pore lengths.

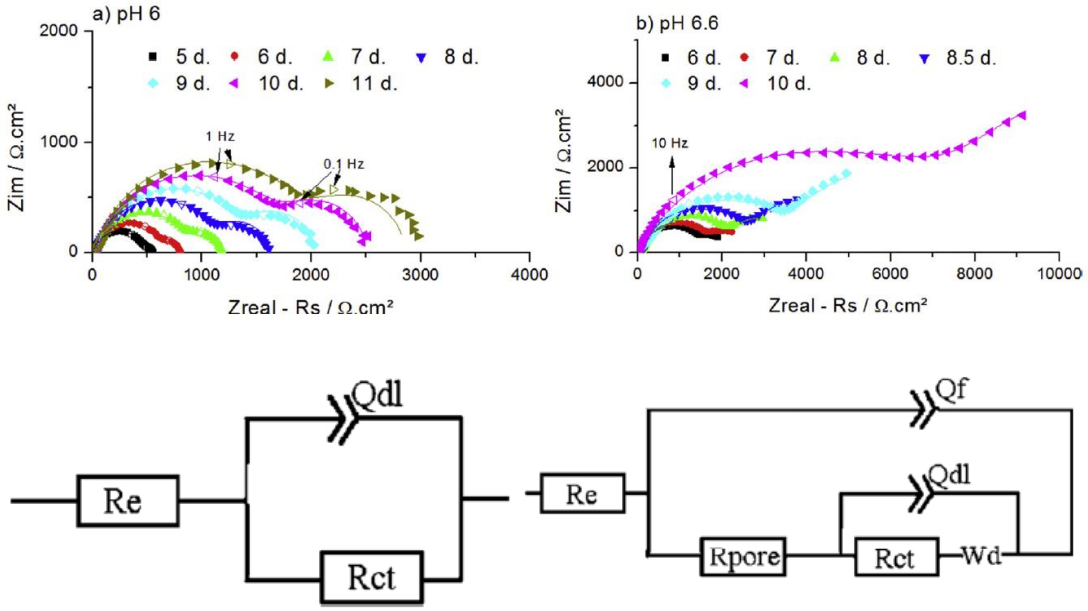

Figure 3.37: Impedance data and corresponding EEC's utilised by De Motte et al. [51]

In 2021, Al Kindi et al. [32] used a similar approach to EIS analysis when they analysed $FecO_3$ formation at pH 6.8 and 80 °C. Experiments were conducted in a specially designed cell for *operando* grazing incidence XRD. Both EIS and LPR measurements were taken multiple times during experiments at perturbation ranges of ± 10 mV vs OCP. The EIS data was fitted to a Randle's circuit with finite length Warburg element and subsequent capacitance values used to predict the effective surface area which was used to correct LPR measurements of corrosion rates.

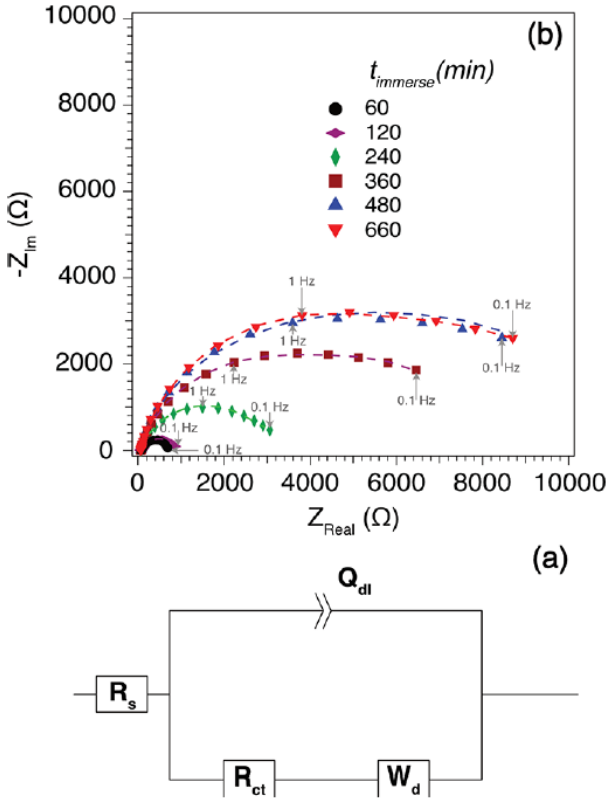

Figure 3.38: Impedance data and corresponding EEC utilised by Al Kindi et al. [32]

3.5 Modelling and Control of System Chemistry

3.5.1 Chemistry Models

A number of geochemical speciation models have been developed over the years to simulate and predict water chemistry in the presence of different dissolved gases and compounds such as PHREEQC [118] and WATERQ [119]. In CO_2 corrosion these have been integrated into full corrosion prediction models [40, 120]. All of these models base the speciation of the system on empirically derived solubility and equilibrium reaction constants. The advantage of chemistry modelling is the ability to predict system speciation without the need for direct measurement, but models are generally limited to the conditions in which the empirical formulas were derived.

3.5.2 Composition Control

One approach to solution composition control is the use of ion exchange resins to entrap or release ions to counteract the corrosion process as attempted by Mansoori et al. [112, 113].

In 2017 Ieamsupapong et al. [75] investigated the effects of pH in CO_2 corrosion of carbon steel using an alternate approach. A stable pH and solution chemistry was maintained over extended test periods by replenishing the test solution continuously to remove excess Fe^{2+}. The test set up included a 20 L and heated 4 L supply tank feeding a 2 L working cell. The pH was controlled by adding 1 M of NaHCO3 to the supply solution. Both pH and Fe^{2+} concentration were maintained by adjusting the flow rate of replenishing fluid into the working cell. This was done periodically when Fe^{2+} was measured using UV/Vis spectrophotometry. Whilst this enhanced the stability of the pH, the methodology was a very reactive rather than proactive means of resolving solution evolution issues.

3.6 Analysis of Literature

3.6.1 General $Fe_xCa_yCO_3$ Studies

Siderite ($FeCO_3$), calcite ($CaCO_3$) and magnesite ($MgCO_3$) all share a hexagonal unit cell which it is believed enables the effective co-precipitation of mixed carbonate solid solutions containing two or more of these elements [25, 87]. The interaction between these cations has been of some interest in geological studies where Fe has been shown to have a significant effect on the precipitation of $CaCO_3$.

Studies by numerous authors [81-85, 87, 121] have all shown how Fe can inhibit the precipitation of calcite, enabling growth of the less stable polymorph, aragonite. In the case of $Fe_xCa_yCO_3$, it is generally agreed that the saturation degree of its pure end members, $FeCO_3$ and $CaCO_3$ are the key parameters governing its composition [87, 91, 112], which in turn are dependent on the chemical activity of reactants, CO_2 fugacity and system temperature [40, 120, 122]. For many mineralogy studies in this area, the focus is on tightly controlled or constant solution chemistry in an attempt to build an exact understanding of its effect on crystal nucleation growth, morphology and composition. These studies are typically conducted at low temperature and atmospheric pressure [87, 94].

3.6.2 $Fe_xCa_yCO_3$ in Corrosion Studies

In the context of a corrosion process, the exact composition of mixed carbonates, herby referred to as a corrosion scale, is incredibly difficult to predict and has been shown to vary over time as system conditions change at the surface [52]. The scenario of an evolving chemistry due to iron flux from the carbon steel, concurrent with ion consumption through carbonate precipitation, is much more difficult to accurately define and control, particularly at elevated pressures. An assessment of the pressure and temperature ranges covered when investigating the effects of calcium in corrosion studies is provided in Figure 3.39. A vast majority of the work is conducted at atmospheric pressure particularly when advanced chemistry control or *in situ* monitoring is utilised [75, 112, 113].

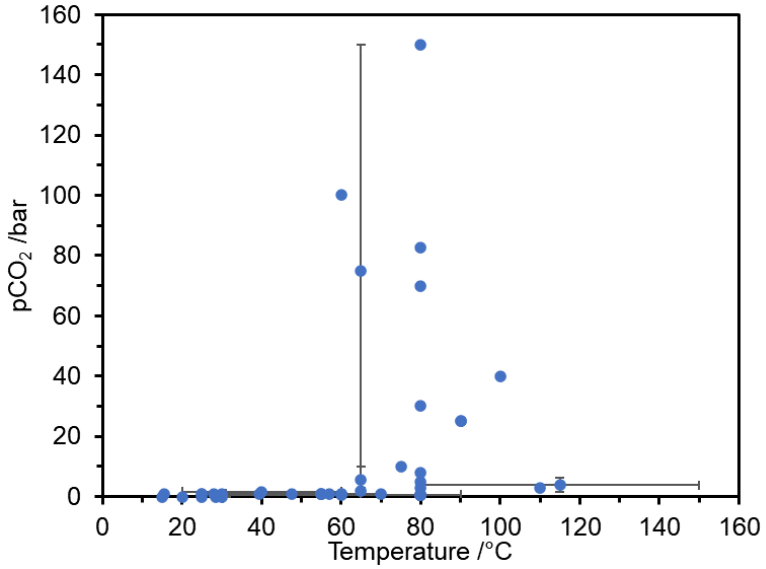

Figure 3.39: Assessment of pressure and temperature ranges covered in literature on $Fe_xCa_yCO_3$ precipitation during CO_2 corrosion. Error bars used to indicate experimental range covered in an individual publication

3.6.3 Influence of Bulk and Surface Conditions

A physical change in environment also plays an important role in carbonate precipitation as carbon steels typically suffer preferential dissolution of their ferrite phase, exposing a porous network of cementite (Fe_3C) [74]. Even when bulk solution chemistry has been closely monitored and controlled, this cementite matrix has been shown to enable onset of mineral precipitation by acting as a diffusion barrier, allowing local supersaturation of $FeCO_3$ and $Fe_xCa_yCO_3$ [113].

Another aspect which is often overlooked in the literature is the relationship between the composition of mixed carbonates and the morphology and coverage particularly at elevated pressures. A limited number of corrosion studies [11, 96, 102, 107, 123] vary the concentration of Ca^{2+} in the solution to achieve different stoichiometries of $Fe_xCa_yCO_3$. These studies often cover a Ca^{2+} concentration range which is either extremely broad or too narrow to capture key transitions in the film properties.

3.7 Research Gaps

3.7.1 Exploring Bulk Chemistry Variation at Elevated Pressures

The CO_2 corrosion process of carbon steel involves the consumption of H^+ ions in the cathodic reaction and a corresponding release of Fe^{2+} ions in the anodic reaction.

Though a CO_2 saturated system has a buffering capacity to replenish H^+, the proliferation of Fe^{2+} in the solution will shift the equilibrium speciation of the system. The magnitude of any transition in solution chemistry is relative to the concentration of metal ions that enter the system as well as the starting conditions such as pH, temperature, and ionic strength.

The complexity is compounded by the fact that these starting conditions also determine the rate at which test specimens will corrode by influencing the kinetics of the corrosion reaction. The corrosion rate is in effect a measure of flux of metal ions into the system.

Rather surprisingly then, one parameter that is often overlooked when conducting corrosion experiments is the size and number of metal specimens that are immersed in a test solution. Increasing the surface area of specimens will increase the amount of iron ions entering the system. If the solution volume is not substantial this flux of iron ions will quickly give rise to high concentrations of bulk Fe^{2+} and higher pH leading to potentially premature precipitation of corrosion and/or scaling products. The relationship between the exposed surface area of the metallic specimen and the volume of solution it is exposed to is referred to as the area/volume (A/V) ratio. ASTM standards G111 [69] and NACE G31 [68] both give arbitrary recommendations for maximum A/V ratio when conducting corrosion experiments but do not offer a systematic approach to establishing sensible values for specific operating conditions. This has also not been systematically addressed in the literature.

3.7.2 Robust Electrochemical Characterisation at Elevated Pressure

EIS has been widely used in $FeCO_3$ and some $Fe_xCa_yCO_3$ studies as a tool for studying the properties of the corrosion layers and to predict onset of localised corrosion. This analysis relies on a strong understanding of the physical system to build representative models. Discrepancy in the literature on EEC selection suggest that in some cases, priority has been given to achieving a good fit of experimental data over realistic modelling. Recent studies [32, 51] have utilised EIS to assess changes in active surface area and have also integrated a Finite Length Warburg impedance to model transmissive diffusion between the substrate and electrolyte, as opposed to using arbitrary CPE components.

An assessment of pressure ranges covered in electrochemical experiments also suggests that data on $Fe_xCa_yCO_3$ formed at elevated pressure is extremely limited due to the complexities associated with autoclave electrochemistry.

3.7.3 Summary of Research Gaps to Address

The following research gaps will be addressed in the present work:

- The effects of bulk CO_2 solution variation over time on corrosion product formation in a restricted volume experiment.
- *In situ* characterisation of $Fe_xCa_yCO_3$ formation at elevated pressures and temperatures.
- Assessment of the protectiveness of $Fe_xCa_yCO_3$ layers formed at elevated pressure and temperature in terms of mechanism for protection and the link between layer properties and localised corrosion.

Chapter 4
Experimental Methodology

4.1 Overview

This chapter details the experimental procedures devised for investigating the effects of solution chemistry on the formation of protective corrosion products at elevated pressures and in the presence and absence of calcium.

The following process was followed in building the research project:

- Development of a refined methodology for conducting autoclave experiments, including electrode fabrication and pressure control for enhanced reproducibility.
- Preliminary mass loss experiments and *ex situ* analysis
- Development of an electrochemistry procedure for *in situ* measurements of the corrosion process
- Further *ex situ* analysis

In parallel with initial autoclave experiments, an equilibrium chemistry model was created for the H_2O-CO_2-NaCl-Fe system to help understand the environmental changes within the autoclave. This work was validated using pH measurements in a bubble cell setup. The experimental procedures have therefore been broken down into the following sections:

- Materials - preparation of the carbon steel under investigation
- Solutions - preparation of the brine solutions
- Apparatus - autoclave used for initial mass loss experiments
- Test conditions – Solution transfer and CO_2 charging procedure for autoclave experiments
- Electrochemistry – apparatus and procedures used for electrochemical experiments in autoclaves and bubble cell
- Analysis - *Ex situ* analysis techniques

4.2 Material Preparation

4.2.1 Raw material

Mass loss specimens and working electrodes were machined from a common pipeline material, American Petroleum Institute (API) 5L X65 carbon steel. The manufacturer’s elemental composition of X65 steel is provided in Table 4.1.

Elemental composition was verified using a Rigaku ZSX Primus II Wavelength Dispersive X-ray Fluorescence (WDXRF) spectrometer. The results are also presented in Table 4.1. For all autoclave experiments mass loss coupons and working electrodes were produced from 25 mm and 12 mm diameter bar respectively. The microstructures of the two bar sizes are compared in the SEM images in Figure 4.1. Specimens were etched in accordance with ASTM E407-99 etchant 74(a). Both sections present a ferritic-pearlitic microstructure however the average grain size is noticeable reduced for the smaller bar size. The grain structure will also differ on the internal wall of pipeline material. To ensure consistency and remove grain structure as a variable, all quantitative and qualitative results presented in this thesis have been made between specimens produced from the same bar of material.

Table 4.1: Elemental composition of API 5L X65 carbon steel
Source: A) Manufacturer datasheet, B) XRF analysis

Source	C	Mn	Ni	Nb	Mo	Si
A	0.12-0.15	1.27-1.42	0.07-0.09	0.05	0.17	0.18-0.22
B	*	1.224	0.08	0.04	0.15	0.34
Source	V	P	S	Cr	Cu	Fe
A	0.06	0.008-0.025	0.002	0.11	0.12	Bal.
B	0.06	0.007	0.012	0.09	0.21	Bal.

*Element detection not compatible with XRF analysis

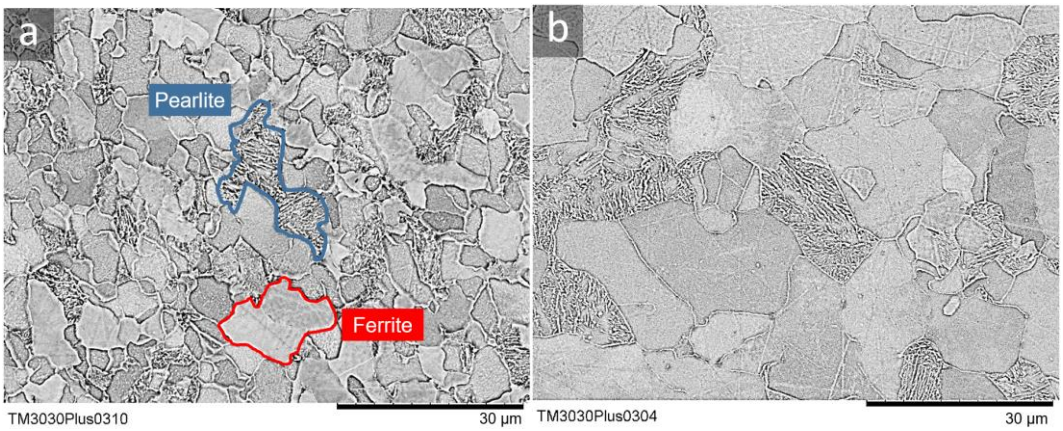

Figure 4.1: SEM images of X65 carbon steel with pearlite-ferrite microstructure produced from different bar sizes (a) 12 mm diameter and (b) 25 mm diameter

4.2.2 Mass loss coupon preparation and A/V Ratio Configuration

The area-to-volume (A/V) ratio was varied using two different mass loss samples listed in Table 4.2 and arranged as shown in Figure 4.2. High A/V experiments contained two cylindrical coupons of 25 mm diameter and 6 mm thickness. For low A/V the coupons were cut into thirds to produce cylindrical-sector specimens of 25 mm diameter, 6 mm thickness and sector angle of 120°. One sector was used per low A/V experiment. Each mass loss coupon had one 3 mm diameter hole drilled through for fixing within the autoclave. A working electrode/surface analysis specimen was also included in each experiment fabricated from the 12 mm diameter bar with a single exposed face.

Table 4.2: Specimen types used in autoclave corrosion experiments

Use	Description	Sample shape	Exposed Area (cm^2)
Mass loss	Ø25 x 6 mm Full cylinder	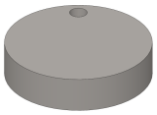	14.95
Mass loss	Ø25 x 6 mm Sector	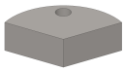	6.77
Working electrode / surface analysis	Ø12 x 8 mm FEP* wrapped	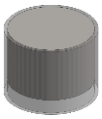	1.13

** Fluorinated Ethylene Propylene*

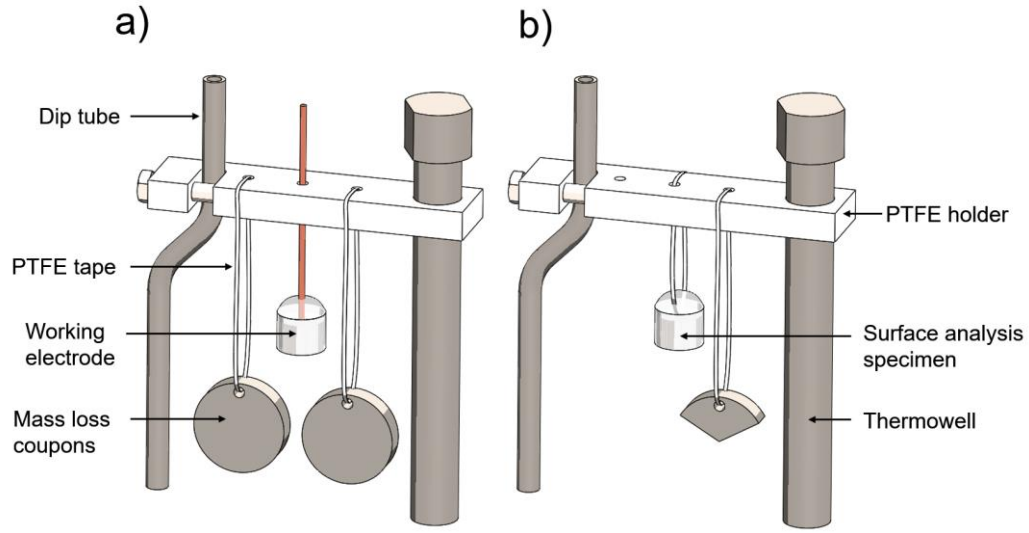

Figure 4.2: Example test specimen arrangements within autoclave experiments (a) High A/V (41.4 $cm^2 \cdot L^{-1}$) Electrochemical experiment (b) Low A/V (10.5 $cm^2 \cdot L^{-1}$) mass loss experiment

Total exposed surface area of carbon steel was 7.9 cm^2 for low A/V and 31 cm^2 for high A/V. All experiments were conducted in 750 mL of brine solution giving A/V ratios of 10.5 and 41.4 cm^2/L. Immediately prior to the experiment, all exposed surfaces of the mass loss coupons were wet ground successively with P120, P240, P400 and P600 silicon carbide (SiC) grit paper. Specimens were rinsed with acetone and distilled water to degrease and remove debris between each stage before drying with compressed air and then a hot air gun.

4.2.3 Autoclave Electrode Fabrication

Figure 4.4 illustrates the stages of electrode fabrication. Working electrodes were fabricated from 8 mm lengths of the 12 mm diameter X65 bar (Figure 4.4(a)). Each sample was first wet ground on all surfaces up to P600 grit and dried (Figure 4.4(b)) before being attached to 20 AWG (American Wire Gauge) Kapton coated copper wire using lead free solder (Loctite 362 99C 5C) (Figure 4.4(c)). To achieve a high-quality solder connection, a vermiculite block was procured for resting the specimens on during heat up (Figure 4.3(b)). The low thermal conductivity of vermiculite helps to retain heat in the specimen allowing the solder to flow more effectively without the need for excessive soldering iron temperatures. Once cooled, the sides of the electrode were coated with high temperature silicone conformal coating (DCA SCC3) using an applicator brush (Figure 4.3(d)) and dried in air for 24 hours before being encapsulated with Fluorinated Ethylene Propylene (FEP) shrink wrap (Adtech FHS10) (Figure 4.4(d)). FEP was selected as it provided a continuous working temperature of up to 200 °C with a low shrink temperature of 110 °C. The back surface of the electrode was then coated with high temperature acetoxy cure silicone sealant (Bostik Bond-flex 100) and left to cure in air for 24 hours (Figure 4.4(e)). Acetoxy cure silicone was selected as a low cost and readily available product during development of the fabrication procedure but does release acetic acid during the curing process unlike a neutral cure silicone. A visual inspection showed no adverse effect on the electrodes prior to or after experiments. For electrochemical tests, the fabrication process was repeated on a 12 mm diameter piece of hastelloy C-276 for use as the counter electrode with the solder replaced with an 80% leaded variety (LOCTITE ALU 45D 4C 1.6).

For mass loss experiments, the soldered Kapton wire of the working electrode was replaced with Polytetrafluoroethylene (PTFE) tape set into the top surface silicone (refer to Figure 4.2(b)). All surface analysis (excluding profilometry) was conducted on FEP encased specimens to make consistent comparisons between electrochemical and standard autoclave experiments. Immediately prior to experiments all FEP encased specimens were carefully re-ground at P600 grit to clean up the working surface. Excess FEP was removed on the exposed side of the specimen using a sharp craft knife prior to grinding.

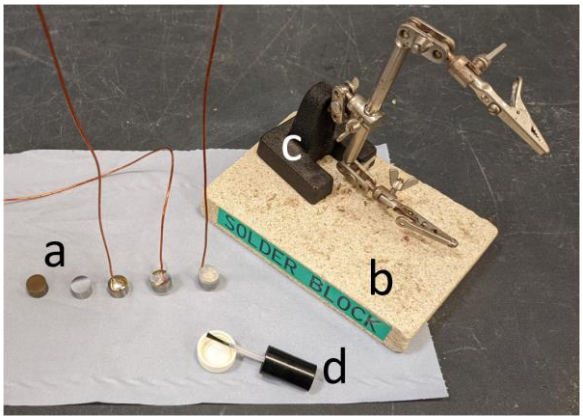

Figure 4.3: Electrode fabrication tools (a) carbon steel electrodes (b) vermiculite refractory brick (c) helping hand tool (d) applicator brush

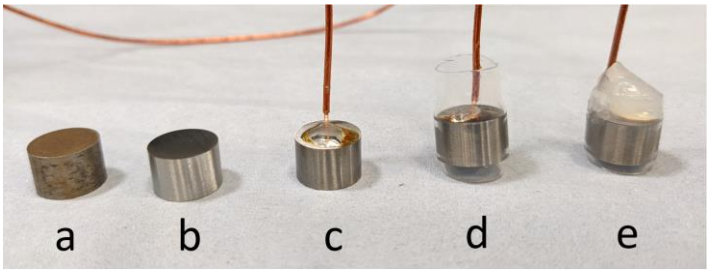

Figure 4.4: Stages of working electrode fabrication (a) raw pre-cut carbon steel (b) initial grinding to remove surface scale (c) soldered and lacquered (d) FEP shrink wrapped (e) top filled with high temperature silicone

4.3 Brine Preparation

Solutions containing 0, 1000 and 5000 $mg \cdot L^{-1}$ of Ca^{2+} were prepared by addition of $CaCl_2 \cdot 2H_2O$ (VWR CAS 10035-04-08 99.5%) and NaCl (Fluka/Honeywell CAS 7647-14-5 ≥ 99 %) to 1 litre of deionized water. The brine compositions selected were comparable with typical field conditions highlighted in Table 1.2. For tests without Ca^{2+}, a baseline 30 $g \cdot L^{-1}$ NaCl solution was prepared.

For subsequent tests NaCl quantities were adjusted to maintain a Cl^- content of 18.2 $g \cdot L^{-1}$ following the previous work of Shamsa et al. [52]. Each solution was prepared in a 1 litre glass beaker and continuously sparged with CO_2 (BOC CAS No. 124-38-9) on a stirred hotplate at ambient pressure and 25 °C for at least 2 hours prior to each test to remove oxygen and saturate the solution with CO_2. Experiments were carried out at both high and low A/V for all brine compositions giving a total of six experimental environments as shown in the test matrix in Table 4.3. The temperature for all experiments was 80 °C, in line with scale forming conditions found in the field [4, 25-27].

Table 4.3: Experimental matrix of brine compositions

Test I.D.	Temperature °C	A/V Ratio $cm^2 \cdot L^{-1}$	Ca^{2+} $mg \cdot L^{-1}$	$CaCl_2.2H_2O$ $g \cdot L^{-1}$	NaCl $g \cdot L^{-1}$	Ionic Strength of Salts $mol \cdot L^{-1}$
0PL	80	10.5	0	0	30	0.513
1PL	80	10.5	1000	3.67	27.08	0.538
5PL	80	10.5	5000	18.34	15.42	0.638
0PH	80	41.4	0	0	30	0.513
1PH	80	41.4	1000	3.67	27.08	0.538
5PH	80	41.4	5000	18.34	15.42	0.638

4.4 Mass Loss Apparatus

Initial mass loss experiments were conducted in a 1 litre 316SS-Ti Parr autoclave as depicted in Figure 4.5.

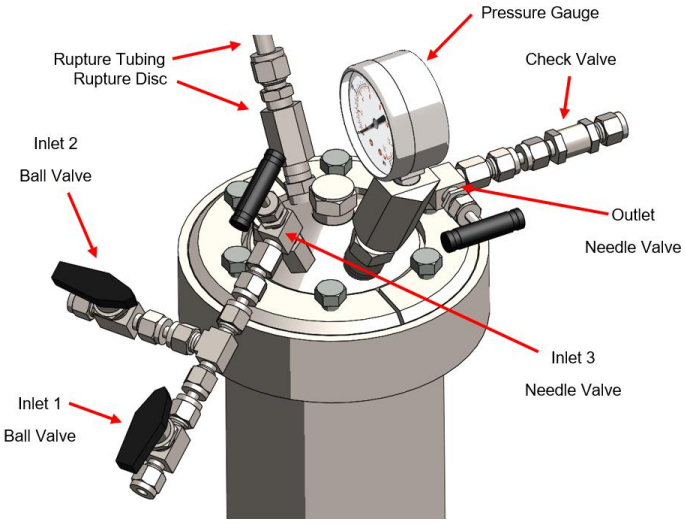

Figure 4.5: Original autoclave head arrangement

Freshly prepared mass loss coupons were suspended inside the vessel by PTFE tape and attached to a specially designed coupon holder also made from PTFE and depicted in Figure 4.2. The holder design allowed for consistent spacing of coupons and mitigated galvanic effects between metallic components. The original autoclave head arrangement is depicted in Figure 4.5.

4.5 Solution Transfer and Autoclave Charging Procedure

The experimental environment for this project was carefully selected to augment corrosion product formation over 3 to 7 day experiments whilst remaining within industrially relevant operating conditions. Selection of these conditions also required a review of current deaeration and CO_2 charging methodologies. This section therefore briefly introduces existing autoclave preparation procedures that were employed before presenting the current revised methodology.

4.5.1 Definition of Charging

CO_2 charging refers to the introduction of high pressure CO_2 within an autoclave to saturate the contained brine solution at an above atmospheric pressure whilst at ambient temperature.

4.5.2 Trial Experiments Using Existing Methods

During initial trials, two existing methodologies were assessed for solution preparation. In both cases, the intention was for system pressure to build naturally from ambient during the heating phase. Results from trial experiments are presented and discussed in detail in Chapter 5.

4.5.2.1 Low Pressure Solution Transfer

Low pressure solution transfer was performed by pre-saturating a brine solution with CO_2 in a bubble cell at 25 °C whilst simultaneously purging the pre-assembled autoclave with CO_2. Solution transfer was performed using a positive displacement gear pump. To purge the pump and transfer lines of oxygen the inlet and outlet tubes of the pump were connected to the bubble cell and solution was circulated around the system. After 30 minutes the pump was stopped, and its outlet was disconnected from the bubble cell and reattached to the inlet of the autoclave.

4.5.2.2 High Pressure Purge

For the high pressure purge technique, a brine solution was again pre-saturated in a bubble cell at 25 °C whilst coupons were assembled within the autoclave head. The solution was then poured in to the vessel and the head immediately fitted before being connected to a high pressure CO_2 line. The pressure was cycled from 0 to 40 barg three times. Each time closing the inlet and venting the vessel back to ambient pressure by slowly opening the outlet.

4.5.3 Revised Methodology

To improve on the previous methods a 'hybrid' approach was taken which featured a closed loop solution transfer followed by charging with the high pressure CO_2 supply. The main advantage of this new technique was that a more precise pressure control system could be used whilst still maintaining an elevated pCO_2 for enhanced corrosion product formation. An overview of the process is shown in Figure 4.6. A number of modifications were also made to the vessel head configuration to further optimise experimental control.

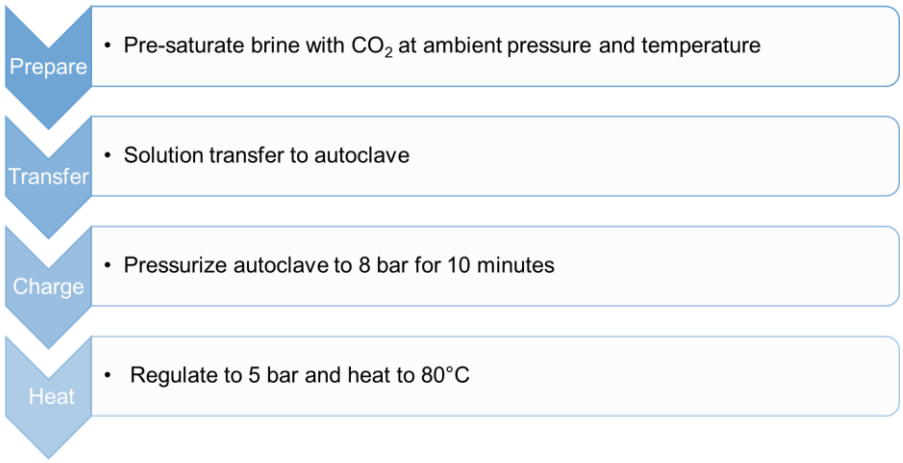

Figure 4.6: Flow diagram of revised autoclave procedure

4.5.3.1 Autoclave Enhancements

To allow for more precise pressure control when initiating a test, the standard 200 bar pressure gauge on the vessel was replaced with a 10 bar gauge. During a standard high pressure purge the slow dissolution and evolution of CO_2 from the brine phase creates a delay in steady state pressure readings which can give a misleading representation of the actual number of moles of CO_2 in the system. To mitigate this a Back Pressure Regulator (BPR) was fitted on the outlet (Swagelok KCB series KCB1H0A2A5P20000).

The BPR maintained the gauge pressure at 5 bar by continuously opening and closing as CO_2 evolved from the solution during heat up. To allow the system to be purged at low pressure and for gas to escape during solution transfer, the outlet was split using a tee joint to create BPR bypass which could be closed off using a ball valve. The modifications are depicted in Figure 4.7.

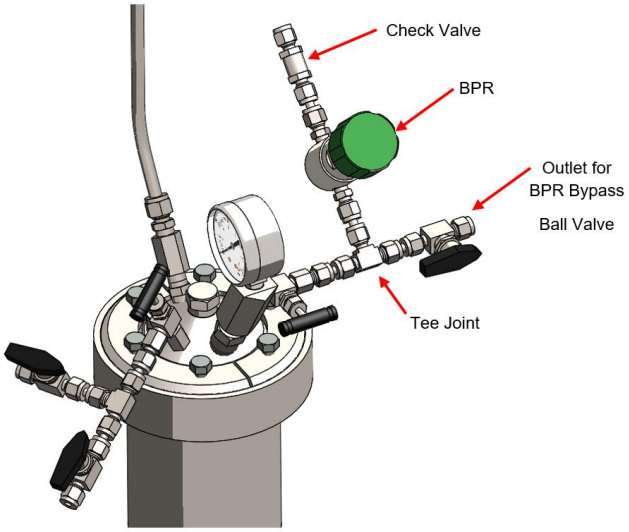

Figure 4.7: Autoclave outlet modifications for enhanced pressure control

4.5.3.2 Deaeration and Solution Transfer

With the corrosion coupons assembled within the autoclave, the vessel was sealed following the appropriate bolt up sequence. A CO_2 supply was then connected to one of two inlet ports as depicted in Figure 4.8. The vessel was flushed with CO_2 at high flow for 30 minutes. Before every experiment, the pump was flushed through with deionised water, followed by compressed air before being connected to a nitrogen line to dry. Once dry the outlet of the pump was connected to the second inlet of the autoclave and CO_2 was diverted through the pump to purge the transfer line, the outlet and inlet needle valve of the autoclave were also closed at this stage. After 5-10 minutes the transfer line was inserted in to the beaker of brine solution and the CO_2 supply through the pump closed off. After re-opening the inlet needle valve the pump was activated, the autoclave outlet was then immediately re-opened to allow 750 mL of solution to be transferred to the vessel at atmospheric pressure. After solution transfer the CO_2 supply to the vessel was reopened, first to flush the transfer line, and then to continue bubbling the transferred solution while the bubble cell and pump were cleaned.

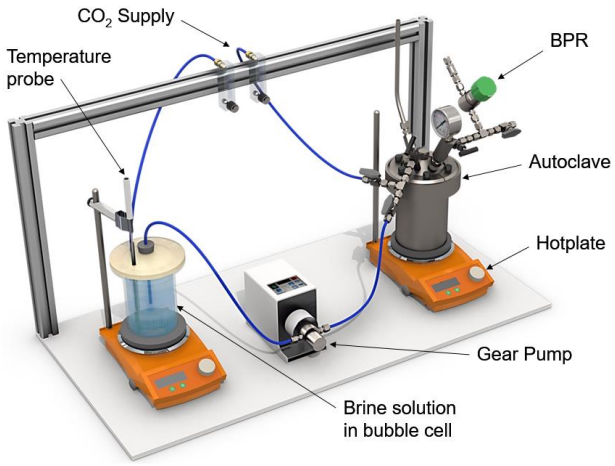

Figure 4.8: Solution transfer apparatus for autoclave experiments

4.5.3.3 CO_2 Charging

To increase dissolved CO_2 in the system, the vessel was connected to a high pressure CO_2 liquid withdrawal cylinder for charging. The high pressure line was first flushed through by opening the spare inlet connection on the autoclave. Once the line was purged the inlet needle valve was carefully opened and pressure allowed to build to 8 barg – 3 bar over the test pressure to expedite the saturation process. The purge pressure was maintained using the BPR and the vessel flushed through for 5 minutes before all inlets and outlets were closed. The sealed vessel was left to saturate for a further 10 minutes with pressure typically dropping down to 7.5 barg in this time as CO_2 slowly dissolved in to the solution from the headspace.

4.5.3.4 Heat Up

Once saturated, the autoclave was placed on a hotplate and heated steadily on precise setting up to the target temperature of 80 °C. During heat up the outlet needle valve to the BPR was opened carefully to allow the pressure to be regulated down to and maintained at 5 barg. Once target temperature had been reached (after ~30 minutes) the outlet needle valve was closed to allow system pressure to evolve naturally. The experiment start time was also recorded at this point.

4.6 Electrochemical Methodology

The autoclave experiments discussed previously were repeated with the addition of electrochemical measurements for *in-situ* data collection.

Electrochemical measurements of open circuit potential, polarisation resistance and impedance allowed for the characterisation of the interface properties as corrosion scales formed on the surface of the carbon steel. Potentiodynamic sweeps were also conducted to isolate cathodic and anodic behaviours. The solution transfer and charging methodology discussed previously was also incorporated into electrochemical experiments with the following additional hardware.

4.6.1 Autoclave Electrochemical Hardware Setup and Preparation

All electrochemical measurements were taken using a 3 electrode configuration. The additional probes were mounted in to an upgraded 1.3 litre 316SS-Ti LBBC Baskerville CTAS1300 autoclave. Working and counter electrodes were inserted through a high-pressure cable gland with PTFE seal (Conax PL-20-A2-T supplied by Thermal Detection). A Corr Instruments refillable type external pressure balanced Silver/Silver Chloride probe was used as the reference electrode. Measurements were performed using an Ivium Compactstat Potentiostat interfaced through IviumSoft software.

4.6.1.1 Grounding

Grounding is a typically encountered problem with electrochemical measurements, particularly with autoclaves. Multiple independently powered components (sensors, controllers etc.) can lead to the presence of ground loops within an electrochemical cell which can cause significant noise and measurement error in sensitive measurements [124]. If the system is not grounded the potential of the system can ‘float’ over time. In a standard glass beaker experiment the only route to ground is through the potentiostat.

For autoclave experiments a ground connection is also made through the connection of the metallic vessel with the hotplate. To prevent a potential ground loop disturbance the Compactstat was operated in floating mode by removal of an external grounding pin on the device. This ensured the only route to ground for the system was through the electrically conductive surface of the hotplate (Asynt Model ADS-HP-NT) as verified by resistivity measurements between the autoclave and ground pin of the hotplate power cable (see Figure 4.9).

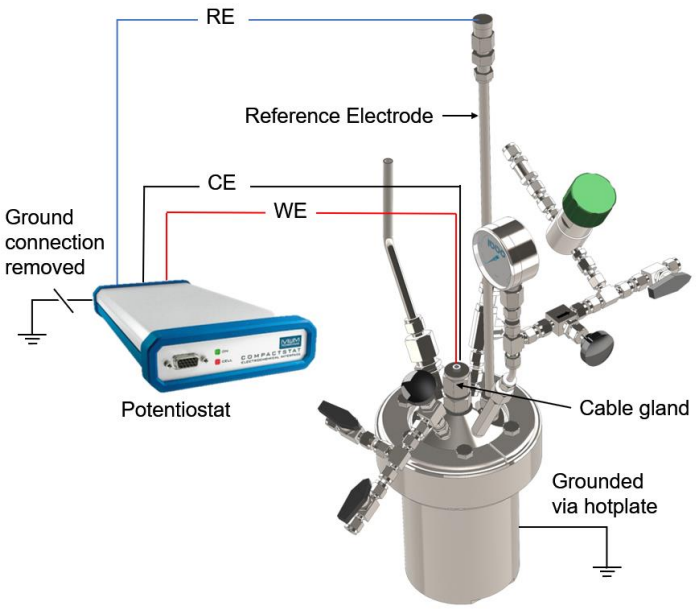

Figure 4.9: Connections and grounding for electrochemical autoclave experiments

4.6.2 Autoclave Electrochemical Measurements and Batch Processing

Open Circuit Potential (OCP) was monitored during heat up and throughout the experiments. LPR measurements were conducted across a potential range of -15 mV to +15 mV vs OCP at a scan rate of 0.25 $mV \cdot s^{-1}$ and step size of 0.25 mV. EIS measurements were acquired every 2 hours at a 15 mV amplitude through a frequency range of 20 kHz to 10 mHz with 10 frequencies per decade (64 measurements per scan). The experiments were concluded when the reciprocal of R_p had notably stabilised below 10^{-4} Ω^{-1}. To acquire LPR and EIS measurements sequentially throughout the test a loop sequence was developed as shown in Figure 4.10 using the batch mode within Iviumsoft.

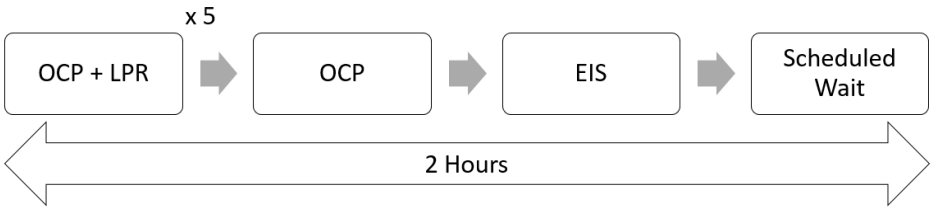

Figure 4.10: Flow diagram of batch loop electrochemical measurements

The sequence included five LPR measurements with a 15 minute interval prior to each measurement. The final LPR sweep was followed by a 5 minute stabilisation period before the EIS measurement was performed. Due to software limitations, the timing of the batch sequence had to be controlled using a scheduled wait function within Iviumsoft.

The wait function ensured that every sequence started exactly two hours after the previous loop making it possible to quickly compile the data in Excel.

4.6.2.1 Current ranging

Within a potentiostat current is forced to flow through a highly accurate resistor. The resulting voltage drop measured across the resistor is used to obtain the current measurement by Ohm's law. If the current is very low a large resistance is required to produce an accurate voltage drop measurement while a lower resistance is required for larger currents to avoid overloading. The potentiostat contains multiple independently selectable resistors to cover a wide range of currents to a good level of accuracy as depicted in Figure 4.11. Due to the large transition in interfacial kinetics from corrosion product precipitation, trial experiments indicated that corrosion currents could vary by three orders of magnitude within each experiment. To account for this, the potentiostat was set to auto current range whereby the device automatically selected the appropriate range based on the measured signal.

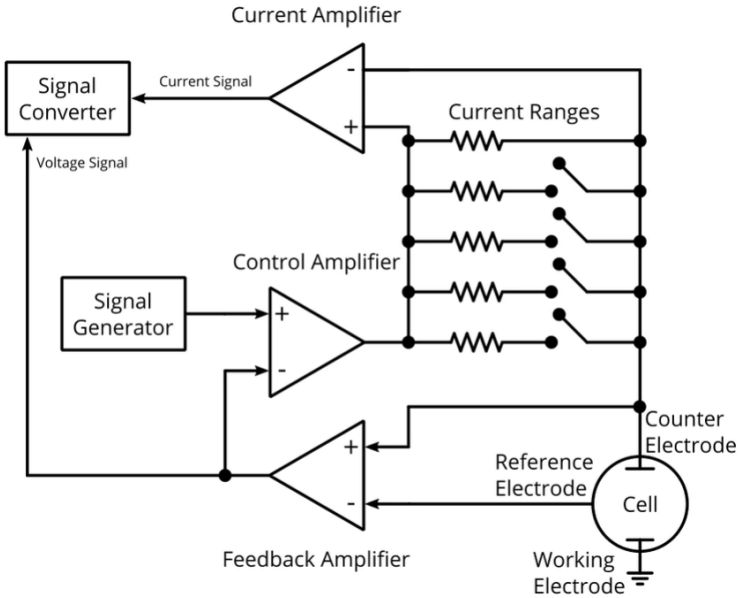

Figure 4.11: Simplified schematic of a potentiostat showing current ranging resistors [125]

4.6.2.2 Potentiodynamic Sweeps

For the first repeat of each experiment a potentiodynamic sweep was performed at the end to evaluate Tafel behaviour. A cathodic sweep of +15 mV to -250 mV vs OCP was performed followed by anodic sweep of -15 mV to +250 mV vs OCP at a sweep rate of 0.5 $mV \cdot s^{-1}$.

Two more experiments were conducted to evaluate Tafel behaviour under initial conditions and to investigate whether the calcium had any affect initially. To cover the full range of conditions one Tafel sweep was conducted at high A/V ratio in the absence of calcium and another at low A/V with the maximum 5000 $mg \cdot L^{-1}$ of Ca^{2+}.

4.6.3 Bubble Cell Experimental Procedure

Ambient pressure experiments for chemistry model validation were conducted in a bubble cell setup as shown in Figure 4.12. In addition, a Mettler Toledo InLab Viscous combination probe was included for *in situ* pH measurements. The solution preparation followed the same procedure as outlined previously using 30 g of NaCl with no additional calcium and bubbled with CO_2 for at least 2 hours prior to the experiment. Two 25 mm diameter samples were soldered and cast in a two part acrylic resin system (Buehler VariDur 10). Immediately prior to experiments the bottom cylindrical faces of the samples were wet ground to P600 grit leaving a single 4.9 cm^2 exposed face on each electrode as shown in Figure 4.13. This resulted in a total A/V ratio of 9.8 cm^2.

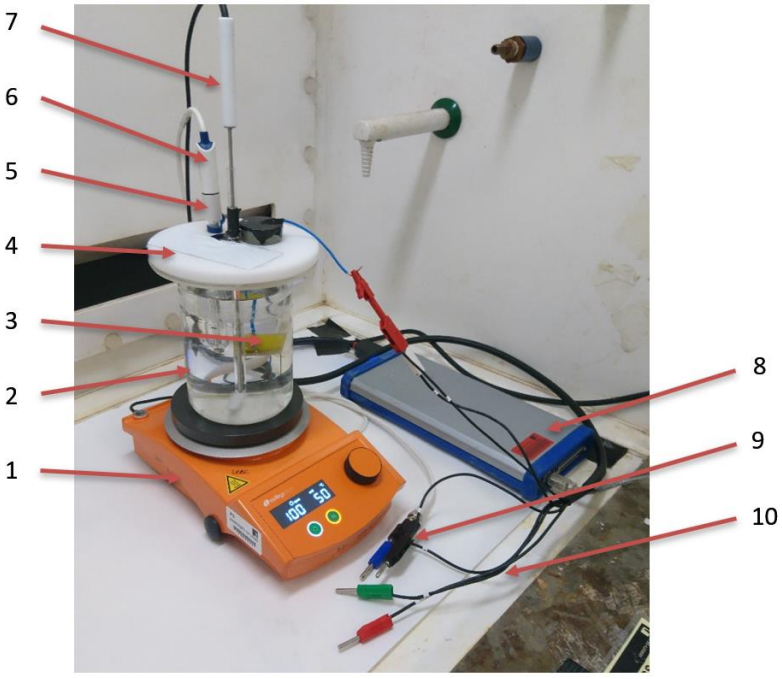

Figure 4.12: Bubble cell apparatus for chemistry model validation: 1) Hotplate with magnetic stirrer; 2) Glass beaker; 3) Two X65 carbon steel working electrodes; 4) Acetal Lid; 5) Ag/AgCl Reference Electrode with integrated platinum Counter Electrode (Mettler Toledo InLab Redox 3M KCl filled); 6) RE/CE coaxial cable (S7 to BNC); 7) Temperature probe; 8) Ivium Potentiostat; 9) BNC Connector; 10) Potentiostat cabling.

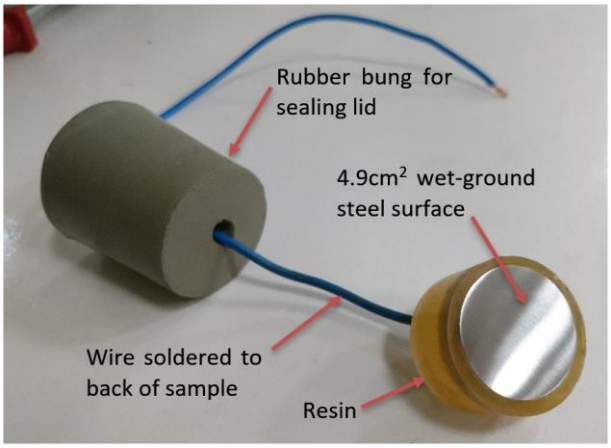

Figure 4.13: Working electrodes used for bubble cell experiments

The brine solution was heated to 80 °C before the two samples were inserted through the acetal lid and sealed using the rubber bung shown in Figure 4.13. The solution was continuously stirred at 100 RPM during experiments to homogenize Fe^{2+} distribution between the specimens and bulk brine. One of the samples was used for the three electrode corrosion cell by connecting the WE/S cables as shown in Figure 4.14. The three electrode corrosion cell and the pH probe were connected through separate potentiostat channels so that pH and corrosion rate could be monitored in parallel. Corrosion rate was monitored using LPR measurements taken every 15 minutes at -15 to +15 mV Vs OCP. Potentiodynamic sweeps at the end of the experiment and at the start with a fresh brine were used to obtain Tafel constants to convert the LPR data to a corrosion rate following equations (2.37) and (2.2).

The combination pH probe featured an internal reference and was connected to the potentiostat as shown in Figure 4.15(a) to continuously monitor pH. Since the electrode was not passing current, only sensing connections (RE and S) were actually required as shown in Figure 4.15(b) and discussed previously in section 2.8.1.2. The pH probe was calibrated prior to the experiments using a 3 point calibration procedure with pH 4, 7 and 10 buffers heated to the experiment temperature of 80 °C. The potential reading for each buffer was recorded to create a linear calibration curve which allowed for conversion of the potential readings when the pH probe was placed in the brine solution. pH measurements were collected continuously for 10 hours using the E_{OC} monitor within Iviumsoft.

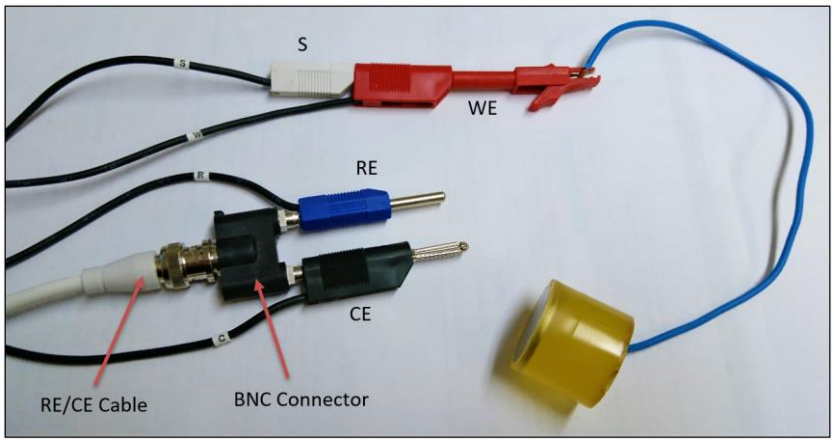

Figure 4.14: Potentiostat connections for three electrode bubble cell experiments

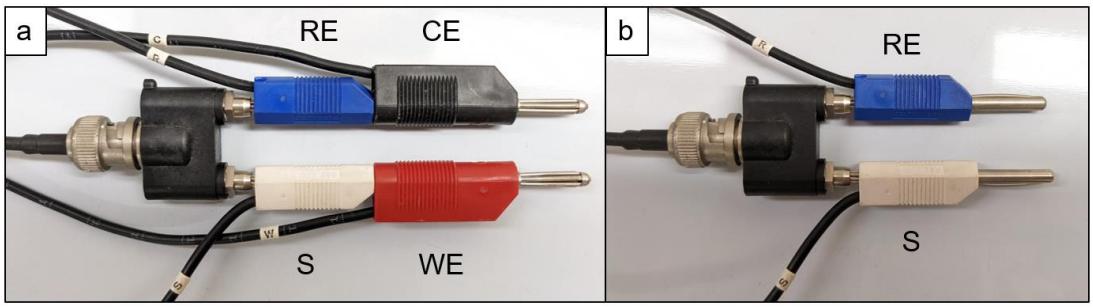

Figure 4.15: Potentiostat connections for pH measurement in bubble cell experiments (a) 4 connection option (b) alternative 2 connection option

To validate the modelled effect of temperature on system pH (in absence of corrosion), two additional experiments were conducted on brine solutions without corrosion coupons. For the first experiment, the stock brine solution described previously was used with the solution dropping to a pH of around 3.7 after CO_2 saturation at 25 °C. For the second experiment the initial pH at 25 °C was raised to approximately 6.2 by addition of 3.8 grams of $NaHCO_3$ (Alfa Aesar 99% CAS 144-55-8). The pH was measured using an Orion Triode 9157BNMD 3-in-1 pH/ATC (automatic temperature correction) probe connected to an Orion Star A111 pH meter. Before starting the test, pH was monitored to ensure it had stabilised after the addition of $NaHCO_3$. pH measurements were taken at 10 °C increments from 25 to 80 °C by ramping the temperature of the hotplate. pH 4 and 7 buffers where heated concurrently on a separate hotplate to calibrate the pH probe accurately for each temperature. The experiments were repeated three times.

4.7 Ex-situ Analysis

Ex-situ analysis was conducted on both mass loss and FEP wrapped samples following the flow process outlined in Figure 4.16. All surface and compositional analysis was performed on FEP wrapped specimens while mass loss coupons were used for quantitative analysis such as gravimetric and profilometry after corrosion products had been removed.

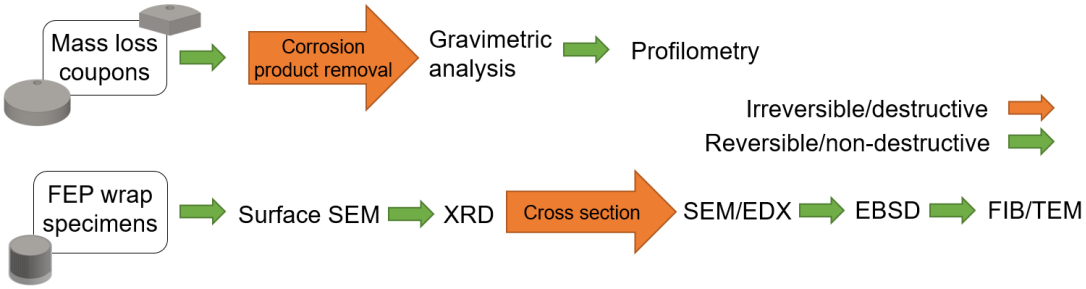

Figure 4.16: Flow diagram for *ex situ* analysis of test specimens

4.7.1 Gravimetric Analysis

Immediately prior to each autoclave experiment, mass loss coupons were weighed to obtain the original coupon mass (m_0) recorded using an electronic mass balance with accuracy of 0.1 mg. At the end of the experiment, the specimens were removed from the autoclave, rinsed with distilled water and dried with a hot air gun. Working electrodes were stored in a desiccator under vacuum for surface characterization. For gravimetric analysis, the mass loss coupons were weighed before and after corrosion product removal to obtain the Corrosion Product Mass (CPM) and total Metal Loss (M_L). Corrosion product was removed using Clarke's solution: 20 g antimony trioxide (Fisher CAS 1309-64-4 ≥ 99%) + 50 g tin (II) chloride (Alfa Aesar CAS 7772-99-8 98%) + 1000 mL concentrated hydrochloric acid (Fisher CAS 7647-01-0 ~37%) in accordance with ASTM Standard G1-03 (2017) Table A1.1 Designation C.3.1 [126]. After application of Clarke's solution samples were immediately rinsed and dried before taking the final mass loss measurement. CPM was taken as the difference between the mass of the coupon with corrosion products (m_{cp}) and the final mass (m_f) after treatment with Clarke's solution. M_L was taken as the original specimen mass (m_0) minus m_f.

$$M_L = m_f - m_0 \quad (4.1)$$

$$CPM = m_{cp} - m_f \quad (4.2)$$

The metal loss was used to obtain the average corrosion rate over the duration of the experiment in units of mm·year^{-1} (based on the original specimen surface area exposed to the test solution).

$$\mathrm{CR}\ (\mathrm{mm}\cdot\mathrm{year}^{-1}) = \frac{\mathrm{M_L}}{\mathrm{t}\times\mathrm{A_0}\times\rho} \tag{4.3}$$

Where t is test duration in years; A_0 is original exposed surface area in cm^2 and ρ is metal density in g·cm^3.

4.7.2 Surface SEM Imaging

Scanning Electron Microscope (SEM) images of surface corrosion product layers were produced using a Hitachi TM3030Plus benchtop SEM. The samples were prepared by first removing the shrink wrap casing before careful removal of solder on the reverse side of the sample by gentle grinding to leave a flat surface. Grinding was followed by a light application of compressed air to remove debris. The samples were placed on SEM stubs using carbon adhesive discs. The SEM has both backscattered and secondary electron detectors. Backscattered electrons (BSE) are primary electrons reflected back after elastic interactions within the sample. Secondary electrons (SE) are produced from inelastic interactions when primary electrons excite an electron within the sample that then loses energy and moves towards and excites the surface. Secondary electrons are generally only detectable when they originated close to the sample surface, this makes them highly effective for examining topography. BSE come from deeper regions of the sample and show high sensitivity to differences in atomic number; the higher the atomic number, the brighter the material appears in the image. For this reason, BSE was selected to provide better contrast between corrosion products and substrate material. For optimal resolution and contrast the maximum accelerating voltage of 15 kV in EDX (large current) mode was selected.

4.7.3 X-ray Powder Diffraction

X-ray Diffraction (XRD) was used for identification of crystalline materials. The basic principle of XRD is to irradiate a crystalline sample with monochromatic X-rays which are diffracted by sets of lattice planes. Lattice planes are crystallographic planes characterised by their *hkl* Miller indices. In an ideal crystalline structure parallel planes have the same indices and are equally spaced, separated by the distance d_{hkl} referred to as the d-spacing.

Since all X-rays are reflected in the same direction, superposition of the scattered X-rays occurs. Figure 4.17 illustrates that constructive interference of the reflected X-rays occurs only if the following equation, known as Bragg's law, is satisfied:

$$n_i\lambda = 2d_{hkl} \cdot \sin\theta_i \quad (4.4)$$

Where n_i is any integer value, λ is the X-ray wavelength and θ_i is the incident angle. High intensity maxima (peaks) emerge from the sample only at angles where Bragg's law is met. The resulting peak profile is unique to each crystalline material providing a 'fingerprint' for identification. The International Centre for Diffraction Data (ICDD) holds a mass database of standard diffraction patterns known as references.

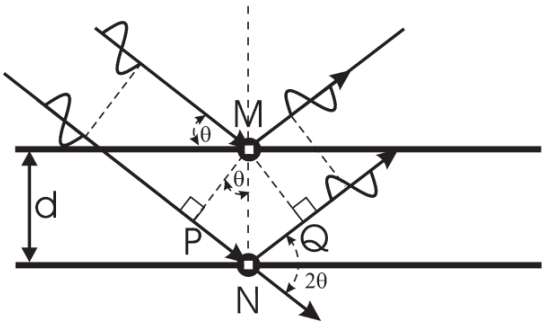

Figure 4.17: Geometry used for the simplified derivation of Bragg's law [127]

In this work a Bruker D8 X-ray diffractometer with Cu Kα source was used for crystalline phase identification. The X65 carbon steel specimens were pressed into plasticine in the centre of a sample holder, ensuring the specimen surface was completely level with top reference face of the holder. The incident rays provided a 10 x 10 mm surface coverage. The scan range selected was 20 to 70° 2θ which covered the most intense Bragg peaks for Calcite and Siderite. A step size of 0.016° and scan rate of 0.02°/s was selected to provide an adequate resolution giving a total scan time of approximately 42 minutes. The resultant diffraction patterns were used to identify the phases present along with the molar fraction of Ca in $Fe_xCa_yCO_3$ for experiments conducted in the presence of Ca^{2+}.

4.7.4 Cross-sectioning

Specimens were cross-sectioned to investigate sub surface features such as pores and substrate adhesion.

The smooth planar surface from cross-sectioning also enabled topographically sensitive analytical tools such as EDX and EBSD to be utilised. The samples were placed sideways in a resin mould and covered with a two part acrylic resin (Kermet Acrylic VLK) as depicted in Figure 4.18(a) and left to cure for 24 hours. The specimens were sectioned by wet grinding with coarse P60 grit paper tangential to their cylindrical surface on two parallel sides (Figure 4.18(b)). One surface was used for analysis while the other provided a conductive path for electrons when placed on sample stubs. The analysis surface was then successively ground with P120, P240, P400, P600, P800 and P1200 grit paper before being transferred to an automatic polisher to be polished with 9, 6 and then 3 µm diamond suspension. Between each step samples were rinsed and dried to prevent damage to the corrosion product layers. For EBSD analysis samples were further polished to 0.25 µm.

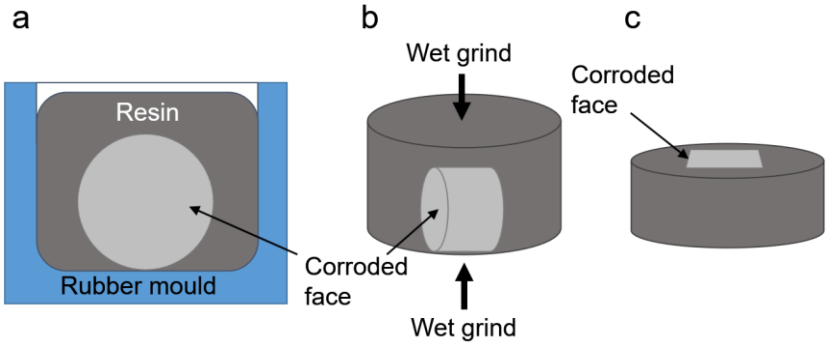

Figure 4.18: Process of cross-section fabrication

4.7.5 Cross-sectional SEM/EDX

Energy Dispersive X-ray Spectroscopy (referred to as EDX, EDS or EDXS) was conducted using a Carl Zeiss EVO MA15 SEM with Oxford Instruments AZtecEnergy EDX system with 80 mm X-Max Silicone Drift Detector (SDD). As previously mentioned, when the SEM's electron beam bombards the sample, some electrons are ejected from their atoms. This ejection creates an electron vacancy which becomes filled by an electron from a higher shell, emitting an X-ray in the process. The EDX system detects the quantity and energy levels of these X-rays which are characteristic of the elements present allowing quantitative and qualitative measurement of the type and relative amount of elements present. The detected X-rays can be affected by surface topography, this was evidenced by a shadowing effecting during early attempts to analyse surface crystal formations.

As a consequence, EDX analysis was only performed on cross-sections. The cross-sections were prepared for analysis by placing on SEM stubs using carbon adhesive discs. The sides and top surface (excluding the exposed steel) were coated using a carbon paint. The contact edge between the resin and stub was also coated and one edge of the exposed steel. This provided a secondary conductive path from the specimen to the stub to reduce charge up. Specimens were then sputter coated with a 10 nm layer of iridium to further reduce surface charging.

4.7.6 EBSD

Electron Back-Scattered Diffraction is another SEM based technique for microstructural analysis. In EBSD, a fixed electron beam interacts with a tilted crystalline sample. As with the X-ray diffraction techniques described previously, the diffracted electrons form a pattern that can be detected with a fluorescent screen. Rapid processing of the resulting patterns allows software to index the diffraction data on a pixel by pixel basis to discriminate between different crystallographic properties such as orientation and phase. The limitation of EBSD is the need for a highly polished and flat surface while the diffraction data needs to be easily indexed. For this reason, only pure $FeCO_3$ samples were analysed with this technique. EBSD was conducted on an FEI Quanta 650: FEGESEM environmental SEM with Oxford Instruments INCA 350 EDX system/80mm X-Max SDD detector, EBSD and KE Centaurus EBSD system. Pixel resolution for mapping was between 0.3 and 0.5 µm.

4.7.7 FIB and TEM/STEM

For high resolution analysis of corrosion layer compositions a Transmission Electron Microscope (TEM) and Scanning Transmission Electron Microscope (STEM) were employed. TEM/STEM offers a highly localised assessment of compositional and crystallographic phase changes within the corrosion product layers. Where SEM detects rebounded or secondary electrons, a TEM transmits electrons through a sample on to various detectors. TEM therefore requires extremely thin samples of below 200 nm to be electron transparent. For this work, sample preparation was performed using a Focused Ion Beam (FIB) system (FEI Helios G4 CX DualBeam) with gallium source. Samples of $FeCO_3$ and $Fe_xCa_yCO_3$ were removed from the carbon steel cross-sections by first depositing a protective layer of platinum onto the surface.

The surface was then milled with the ion beam to produce a 15 µm wide by 10 µm deep section across the steel/corrosion product interface (Figure 4.19(a)). The milled lamella was transferred to a TEM grid using micromanipulators and fixed in place by precise milling of the edges of the sample causing redeposited matter to act as a bonding agent (Figure 4.19(b) and (c)). Once fixed in place the lamella was further thinned using the gallium ion beam to produce two electron transparent windows of approximately 50 to 100 nm thickness for TEM and STEM analysis (Figure 4.19(d)). An FEI Titan3 Themis 300: X-FEG 300 kV S/TEM with S-TWIN objective lens, monochromator and FEI Super-X 4-detector EDX system was used to produce highly localised EDX maps and electron diffraction patterns for local crystallographic phase shifts.

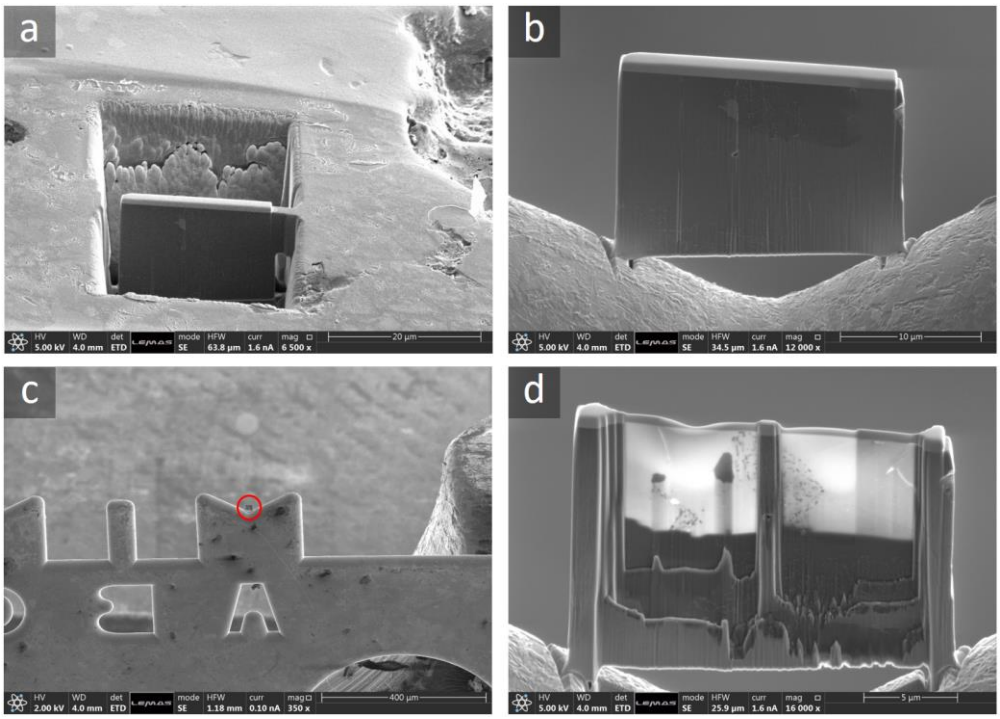

Figure 4.19: Stages of sample preparation for TEM and STEM using FIB (a) milling of carbonate layer cross-section to produce TEM lamella (b) lamella mounted to TEM lift-out grid at 12000x magnification (c) lamella mounted to TEM lift-out grid at 350x magnification (d) electron transparent windows milled in to lamella

4.7.8 Profilometry

To investigate whether localised attack had occurred on the substrate steel beneath corrosion product layers, white light interferometry was performed to build a topographical map of the specimen surface.

White light interferometry works by splitting a collimated light source beam into a reference and measurement beam which recombine after striking their respective targets. The reference beam is reflected from a high precision mirror while the measurement beam strikes the specimen. The recombined beam produces an interference pattern when the two beam lengths are nearly equal.

By moving the measurement beam relative to the reference, a topographical map of the surface can be produced. The surface mapping was performed using a Bruker NPFlex 3D surface profilometer. Before analysis, all corrosion products were removed using Clarke's solution. This ensured any areas of localised attack were not masked by corrosion product. The system was operated using Vision64 software. A 10x objective was used providing an individual scan area of 619.4 x 464.5 µm. A 5x scan speed and 0.1% threshold were also selected for data acquisition. The stitching tool within Vision64 allowed 48 images to be automatically compiled into 3 x 3 mm square maps with a 15% overlap. A total of three maps were created on each specimen to obtain an average of the top 10 pit depths. The high level of surface roughness combined with minor surface slope from initial grinding meant that a large scan length of 120 µm with back scan of 40 µm was required to ensure the entire surface was analysed within the stitching mode. The acquired data was initially processed using Vision64's in built tools to de-trend the surface and to interpolate missing data points. Due to the high level of surface porosity the raw data quality (acquired points) was generally around 70 % which increased to > 95 % after processing. Missing pixels were generally isolated and well dispersed across the surface meaning they had negligible effect on pit depth assessment.

4.7.8.1 Pit-like-Feature (PLF) Measurements

Processed profilometry data was exported first to an ASCII file and then converted to text (.txt) for further analysis within MATLAB. A Pit-like-feature (PLF), i.e. area of highly localised corrosion, was identified systematically using the script written in MATLAB. Due to the severity of underlying corrosion prior to corrosion product formation the general surface was extremely rough on all specimens.

The MATLAB script allowed for a methodical approach to PLF selection using a peak finding function that identified the deepest region within a 50 µm radius. An example output is shown in Figure 4.20. Once located, PLF depth was measured from the mean surface plane.

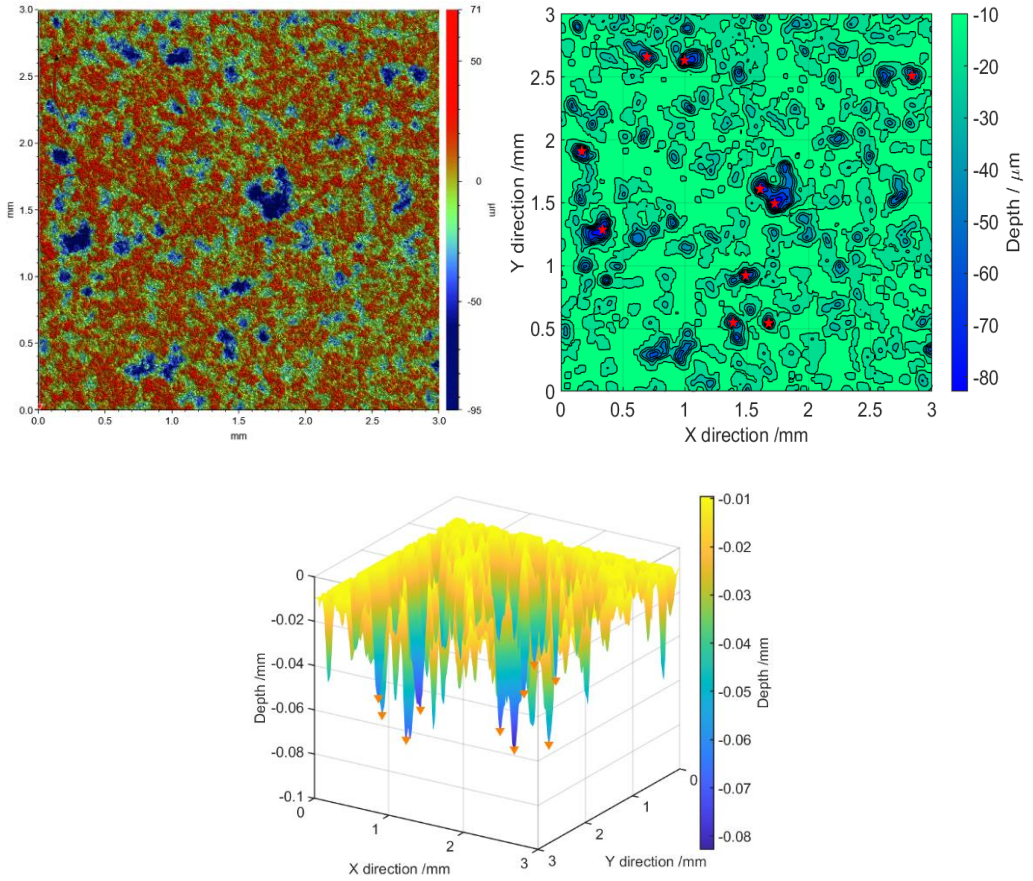

Figure 4.20: Example profilometry data from Vision64 after surface levelling and missing pixel restoration (top left) Contour plot from MATLAB highlighting ten deepest PLFs (top right) 3D surface plot from MATLAB (bottom)

Chapter 5
Preliminary Study on the Effects of Fe^{2+} Flux and Bulk Ca^{2+} Concentration on Formation of $FeCO_3$ and $Fe_xCa_yCO_3$ Corrosion Scales

5.1 Chapter Introduction

A review of literature on the co-precipitation of Fe/Ca carbonates highlighted that solution control was limited at elevated pressure. The aim of this Chapter is therefore to understand the impact of evolving system chemistry by identifying industry relevant operating conditions that are highly sensitive to Fe^{2+} flux. Subsequently, preliminary experiments will establish if A/V ratio has any effect on the observed corrosion product formation and protectiveness when replicating these conditions in the laboratory.

5.1.1 Chapter Outline

The first part of this Chapter will establish the experimental conditions and methodology (i.e. design of experiments) for the project based on the results of theoretical modelling and trial experiments as depicted in Figure 5.1. This is followed by a series of 3-day mass loss experiments to validate the selected conditions and methodology and forms the basis for subsequent investigations in later Chapters.

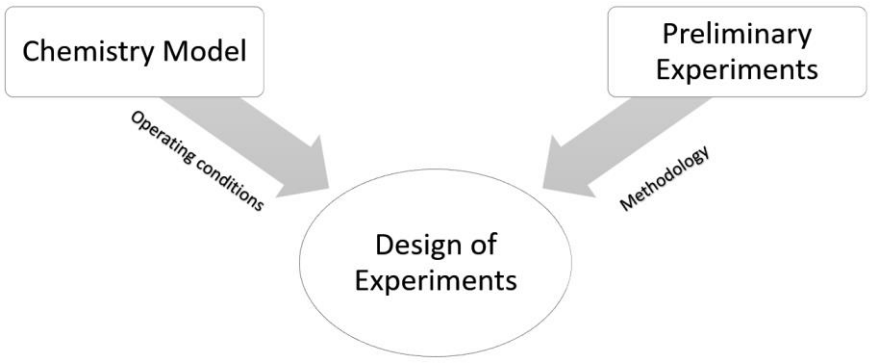

Figure 5.1: Approach to experimental design

To understand the transient behaviour of brine chemistry in an enclosed CO_2 environment, a series of empirical models have been employed to map out the equilibrium speciation of the system at various acidic operating conditions. The effects of additional cations such as Na^+ and Fe^{2+} are ascertained through manipulation of the charge neutrality equation.

The modelling approach is validated at ambient pressure using electrochemical techniques to measure corrosion rate and system pH.The model is used to perform a parametric analysis of CO_2 operating environments to help identify suitable experimental conditions. In conjunction, a series of trial experiments are presented to establish an appropriate methodology for preparation of the CO_2 environment. The information gathered from both chemistry modelling and initial experiments is used to select industry relevant conditions that optimise corrosion product formation and to inform the development of a refined methodology for CO_2 saturation. The experimental conditions and methodology were validated by experiments in a standard autoclave system using two different A/V ratios and 0, 1000 and 5000 $mg \cdot L^{-1}$ of Ca^{2+} to evaluate the effects of A/V ratio on corrosion-scale formation and general corrosion rates. Average corrosion rates and corrosion product mass (CPM) were obtained by mass loss method while corrosion product morphology and composition were examined by SEM and XRD respectively.

5.2 Chemistry Model Development and Validation

In order to understand the effects of the corrosion process on chemical changes in the bulk brine solution of closed vessel experiments, particularly as a function of initial pH, temperature and pCO_2, a solution chemistry model was developed that incorporates the effects of cation addition in to the brine. The model uses established empirical relationships for equilibrium constants coupled with a charge neutrality equation to determine steady state concentrations of species in a H_2O-CO_2-NaCl-$NaHCO_3$-Fe^{2+} system. The model includes two methodologies for solution speciation compiled by Nordsveen et al. [120] and Kahyarian et al. [40].

5.2.1 Nordsveen (2003) Formulation

Table 5.1 lists the relevant chemical reactions and the respective equilibrium constants extracted from the mechanistic model of Nordsveen et al. [120]. The corresponding empirical expression selected for each equilibrium constant are given in Table 5.2. The selected expressions factor in ionic strength, allowing for direct calculation of concentrations as opposed to activities as shown in Table 5.1.

Table 5.1: Chemical reactions and equilibrium constants taken from mechanistic model of Nordsveen et al.[120]

Process	Reaction	Equilibrium Constant	
CO_2 dissolution	$CO_{2(g)} \rightleftharpoons CO_{2(aq)}$	$K_{sol} = \frac{[CO_{2(aq)}]}{pCO_{2(g)}}$	(5.1)
Water dissociation	$H_2O \rightleftharpoons H^+ + OH^-$	$K_{wa} = [H^+][OH^-]$	(5.2)
CO_2 hydration	$CO_{2(aq)} + H_2O \rightleftharpoons H_2CO_3$	$K_{hy} = \frac{[H_2CO_3]}{[CO_{2(aq)}]}$	(5.3)
Carbonic acid dissociation	$H_2CO_3 \rightleftharpoons H^+ + HCO_3^-$	$K_{ca} = \frac{[H^+][HCO_3^-]}{[H_2CO_3]}$	(5.4)
Bicarbonate ion dissociation	$HCO_3^- \rightleftharpoons H^+ + CO_3^{2-}$	$K_{bi} = \frac{[H^+][CO_3^{2-}]}{[HCO_3^-]}$	(5.5)

Table 5.2: Chemical Equilibrium Constants used in Nordsveen model [120]

Equilibrium Constant Formulae	
$K_{sol} = \frac{14.5}{1.00258} \times 10^{-(2.27+5.65\times10^{-3}\cdot T_f - 8.06\times10^{-6}\cdot T_f^2 + 0.075I)}\ \text{molar}\cdot\text{bar}^{-1}$ †	(5.6)
$K_{hy} = 2.58 \times 10^{-3}$ †††	(5.7)
$K_{bi} = 10^{-(10.61-4.97\times10^{-3}\cdot T_f + 1.331\times10^{-5}\cdot T_f^2 - 2.624\times10^{-5}\cdot p - 1.166\cdot I^{0.5} + 0.3466\cdot I)}\text{molar}$ †	(5.8)
$K_{ca} = 387.6 \times 10^{-(6.41-1.594\times10^{-3}\cdot T_f + 8.52\times10^{-6}\cdot T_f^2 - 3.07\times10^{-5}\cdot p - 0.4772\cdot I^{0.5} + 0.1180\cdot I)}\text{molar}$ †	(5.9)
$K_{wa} = 10^{-(29.3868 - 0.0737549\cdot T_k + 7.47881\times10^{-5}\cdot T_k^2)}\ \text{molar}^2$ ††	(5.10)

† Oddo and Tomson [128], †† Kharaka et al. [129], ††† Palmer and van Eldik [130]

Where T_f is temperature in Fahrenheit, T_k is temperature in Kelvin, I is ionic strength and *p* is total absolute pressure.

5.2.2 Kahyarian (2019) Formulation

Kahyarian et al. [40] used the same reactions listed in Table 5.1 with some slight variation to the calculation of dissolved CO_2.

The Henry's constant derived by Li and Duan [131] was used to establish the aqueous dissolved CO_2 concentration, a formula which also accounts for fugacity:

$$\mathrm{H}^{*}_{\mathrm{CO}^{*}_{2}} = \frac{\phi\mathrm{CO}_2 \cdot \mathrm{pCO}_2}{\left[\mathrm{CO}^{*}_{2(\mathrm{aq})}\right]} \tag{5.11}$$

Where ϕCO_2 denotes the fugacity coefficient for CO_2 developed by Duan et al. [132]:

$$\begin{aligned}\phi\mathrm{CO}_2 = \mathrm{c}_1 + \left[\mathrm{c}_2 + \mathrm{c}_3\mathrm{T}_\mathrm{k} + \mathrm{c}_4\mathrm{T}_\mathrm{k}^{-1} + \mathrm{c}_5(\mathrm{T}_\mathrm{k} - 150)^{-1}\right]\mathrm{p} \\ + \left[\mathrm{c}_6 + \mathrm{c}_7\mathrm{T}_\mathrm{k} + \mathrm{c}_8\mathrm{T}_\mathrm{k}^{-1}\right]\mathrm{p}^2\end{aligned} \tag{5.12}$$

For the temperature and pressure range considered in the current work the coefficients are shown in Table 5.3.

Table 5.3: Coefficients for CO_2 fugacity from Duan et al. [132]

c_1	c_2	c_3	c_4	c_5	c_6	c_7	c_8
1	4.76E-3	-3.36×10^{-6}	0	-1.32	-3.84×10^{-6}	0	2.28×10^{-3}

The asterisk * in (5.11) indicates a combination of dissolved CO_2 and H_2CO_3:

$$\left[\mathrm{CO}^{*}_{2(\mathrm{aq})}\right] = \left[\mathrm{CO}_{2(\mathrm{aq})}\right] + \left[\mathrm{H}_2\mathrm{CO}_3\right] \tag{5.13}$$

Kahyarian extracted the individual aqueous CO_2 and carbonic acid concentrations using the hydration reaction equilibrium constant of Wang et al. [133] (denoted K_{hy_w}) to give:

$$\mathrm{H}_{\mathrm{CO}_2} = 1 + (\mathrm{K}_{\mathrm{hy}_\mathrm{w}})\mathrm{H}^{*}_{\mathrm{CO}^{*}_{2}} \tag{5.14}$$

Equilibrium constant expressions K_{bi} and K_{ca} of Oddo and Tomson [128] were also replaced with those of Duan and Li [134] making K_{ca} in particular more sensitive to changes in temperature. The ionization constant for water by Marshall and Franck [135] was preferred to the more conservative formula of Kharaka et al. [129].

5.2.3 Solver Approach

The five equilibrium reactions listed in Table 5.1 contain six individual species to be resolved. In order to solve for the molarity of each species the charge neutrality equation (5.15) is included.

$$\sum_{\mathrm{i}} n_\mathrm{i}\mathrm{c}_\mathrm{i} = 0 \tag{5.15}$$

Where n_i and c_i are the charge and concentration on the i^{th} species.

Applying this to a real laboratory experiment in which the H_2O-CO_2-NaCl brine is pre-buffered with $NaHCO_3$ to raise the initial pH and where Fe^{2+} has also been released from the corrosion process would give:

$$[H^+] + [Na^+] + 2[Fe^{2+}] - [OH^-] - [Cl^-] - [HCO_3^-] - 2[CO_3^{2-}] = 0 \qquad (5.16)$$

Where charge neutral terms have been ignored.

For further simplification $[Cl^-]$ can be removed by removing the concentration of $[Na^+]$ added as NaCl giving:

$$[H^+] + \left[Na^+_{NaHCO_3}\right] + 2[Fe^{2+}] - [OH^-] - [HCO_3^-] - 2[CO_3^{2-}] = 0 \qquad (5.17)$$

Where $[Na^+_{NaHCO3}]$ refers to the concentration of sodium added specifically from $NaHCO_3$. Since $[Na^+_{NaHCO3}]$ is numerically equal to $[NaHCO_3]$ the $NaHCO_3$ concentration is inputted into the charge transfer equation within the model for convenience:

$$[H^+] + [NaHCO_3] + 2[Fe^{2+}] - [OH^-] - [HCO_3^-] - 2[CO_3^{2-}] = 0 \qquad (5.18)$$

By substituting the formulae in Table 5.1 into the charge neutrality equation and re-arranging in terms of $[H^+]$, the following cubic equation is derived:

$$\mathbb{C}_1[H^+]^3 + \mathbb{C}_2[H^+]^2 - \mathbb{C}_3[H^+] - \mathbb{C}_4 = 0 \qquad (5.19)$$

Where:

$$\mathbb{C}_1 = 1; \qquad \mathbb{C}_2 = [NaHCO_3] + 2[Fe^{2+}]; \qquad \mathbb{C}_3 = K_{wa} + K_{ca} \cdot [CO_2]_{aq} \cdot K_{hy}$$

$$\mathbb{C}_4 = 2 \cdot K_{bi} \cdot (\mathbb{C}_3 - K_{wa})$$

It is noted here that $\mathbb{C}_2$ simply represents the sum of base cations multiplied by their respective charge that have been added to the solution and can represent the addition of other compounds such as under-saturated $CaCO_3$ and NaOH. This can also include anions from strong acids such as HCl.

5.2.3.1 Solver

For comparison, two approaches have been built into the model for solving equation (5.19). The primary approach is with iterative solution refinement using the Newton Raphson formula:

$$x_{n+1} = x_n - \frac{f(x_n)}{f'(x_n)} \qquad (5.20)$$

Where x represents $[H^+]$ at the n^{th} iteration and $f(x_n)$ is equation (5.19).

To avoid building iteration loops into the code an alternative approach was adopted using the polynomial roots function to solve the cubic equation (5.19).

Both methods provided adequate solving speed with a negligible performance difference. Overall, the Newton Raphson approach was preferred as the roots function provides multiple solutions which need to be assessed.

5.2.3.2 Note on Ionic Strength

To solve the set of equations described above the ionic strength of the system is required, however in some instances the speciation of the system has a considerable contribution to ionic strength, such as in low or no salt solutions. In these instances, the model is iterated with a first initial guess of ionic strength to determine an approximate speciation. The calculated speciation is then fed back into the model to calculate a refined ionic strength value and the model re-iterated until both speciation and ionic strength values reach convergence. It should also be noted that many of the solubility and equilibria constants used in these models are only validated at lower ionic strengths (typically up to 0.5 molar).

5.2.3.3 Carbonate Saturation

In order to predict the saturation of both $FeCO_3$ and $CaCO_3$ during autoclave experiments, solubility constants (K_{sp}) are also included within the model. $CaCO_3$ saturation is calculated based on inputted quantities of calcium added as either calcium chloride dihydrate ($CaCl_2 \cdot 2H_2O$) or hexahydrate ($CaCl_2 \cdot 6H_2O$). For $FeCO_3$, K_{sp} was determined using equation (3.1) derived by Sun and Nešić [64]. For $CaCO_3$ the widely used K_{sp} of Plummer et al. [122] for calcite was selected.

$$\log\left(K_{sp_{CaCO_3}}\right) = -171.9065 - 0.077993T_k + \frac{2839.319}{T_k} + 71.595 \cdot log(T_k) \qquad (5.21)$$

From review of literature, it was evidenced that Calcite is the primary polymorph to consider because it is the most stable polymorph of $CaCO_3$ and is isostructural with $FeCO_3$ enabling its co-precipitation.

5.2.4 Model Validation Experiments

5.2.4.1 pH versus Temperature (Non-Corroding System)

Validation experiments were conducted following the solution preparation procedures outlined in section 4.6.3. The results of brine pH experiments at discrete increments of temperature and two different start $NaHCO_3$ are presented in Figure 5.2 alongside the modelled pH using both the Nordsveen [120] and Kahyarian [40] methods.

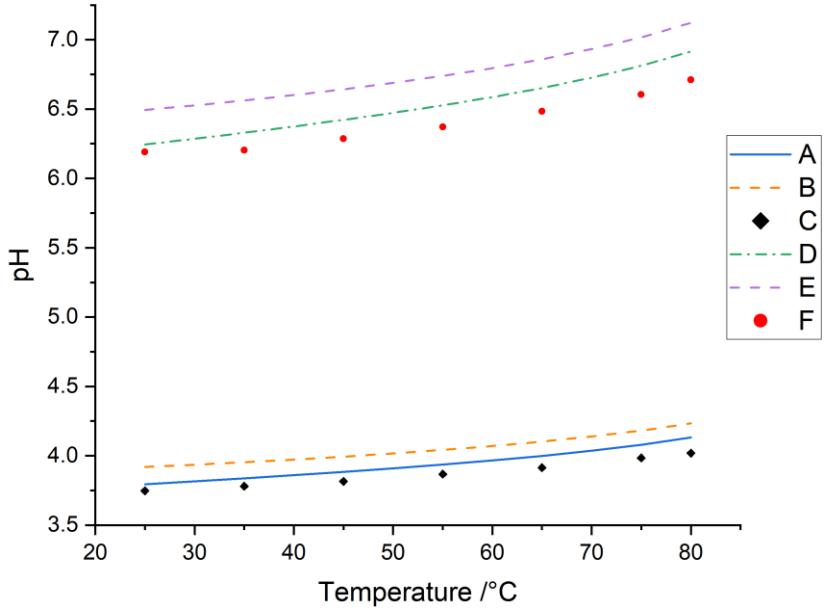

Figure 5.2: Validation test results for solution pH prediction models. A) Nordsveen 0 $NaHCO_3$. B) Kahyarian 0 $NaHCO_3$. C) Experimental 0 $NaHCO_3$. D) Nordsveen 3.8g $NaHCO_3$. E) Kahyarian 3.8g $NaHCO_3$. F) Experimental 3.8g $NaHCO_3$.

5.2.4.2 pH versus Fe^{2+} (Corroding System)

The results of a second experiment conducted in a corroding environment with continuous pH measurement are presented in Figure 5.3. For this experiment only the more well established method of Nordsveen was compared.

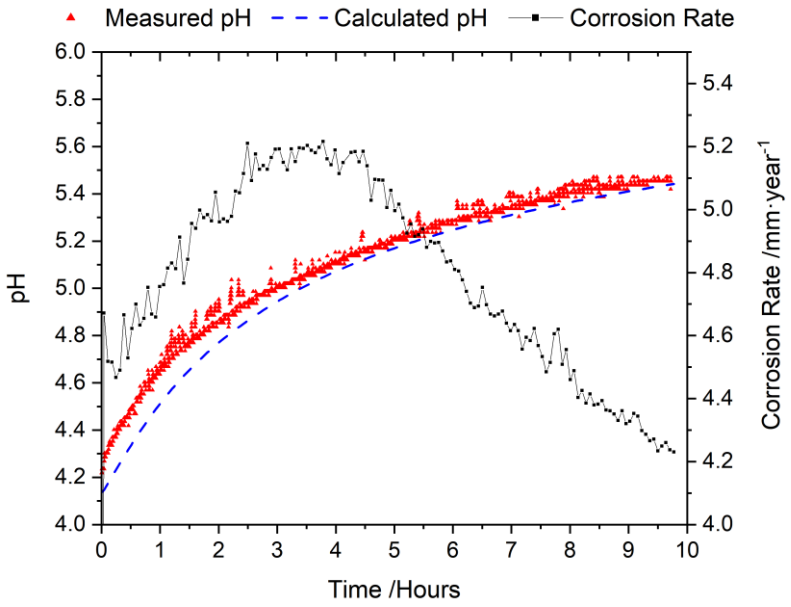

Figure 5.3: Results of validation experiment for modelled bulk pH increase due to Fe^{2+} from X65 carbon steel corroding in a 30 $g \cdot L^{-1}$ NaCl CO_2 saturated brine solution at 80 °C

The corrosion rate in Figure 5.3 was obtained from the corrosion current density i_{corr} by conversion of equation (2.2) to produce (5.22):

$$\mathrm{CR}\ (\mathrm{mm}\cdot\mathrm{year}^{-1}) = \frac{\mathrm{K_u}\cdot\ i_{\mathrm{corr}}\cdot\mathrm{Mr}_{Fe}}{\mathrm{n}\cdot\mathrm{F}\cdot\rho} \qquad (5.22)$$

Where K_u is a unit conversion factor equal to 315.36 x 10^3 when i_{corr} is in units of mA·cm^{-2}, molar mass of Fe (M_{rFe}) is in units of g·mol^{-1} and density of Fe is in g·cm^{-3}. I_{corr} was also used to directly calculate iron flux in moles per second:

$$\mathrm{Fe}^{2+}\mathrm{Flux}\ (\mathrm{mol}\cdot\mathrm{s}^{-1}) = \frac{i_{\mathrm{corr}}}{\mathrm{n}\cdot\mathrm{F}} \qquad (5.23)$$

i_{corr} was obtained using equation (2.37) and Tafel constants of 65.6 mV·dec^{-1} and 233.8 mV·dec^{-1} for β_a and β_c respectively, obtained from the potentiodynamic sweep plotted in Figure 5.4(a).

(a)

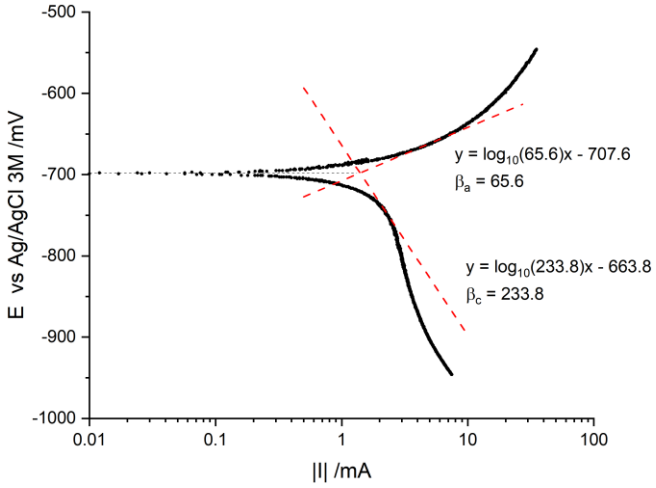

(b)

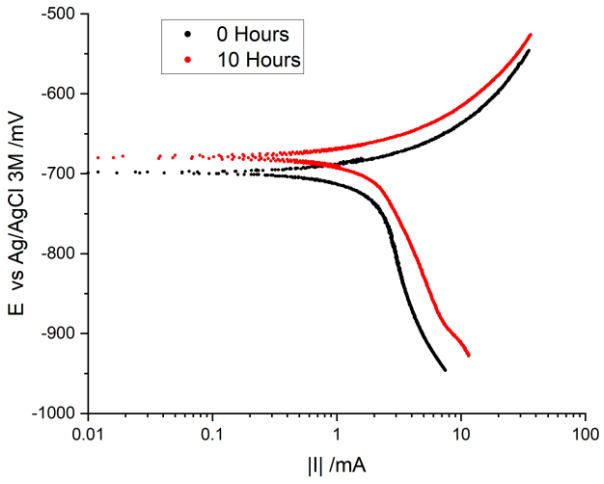

Figure 5.4: Tafel plots from X65 carbon steel corroding in a 30 g·L^{-1} NaCl CO_2 saturated brine solution at 80 °C (a) Tafel extrapolation under initial conditions to obtain β_a and β_c values (b) Tafel behaviour at initial conditions and after 10 hours of corrosion

5.2.4.3 Elevated Pressure pH Measurements versus Fe^{2+}

An attempt was made to repeat the test in Figure 5.3 at elevated pressure of 5 barg (5.5 bar pCO_2) and 80 °C. For this method a high pressure high temperature ZrO_2 pH probe (Corr Instruments) was used alongside the electrochemical setup described in Section 4.6.1. Calibration was performed using a 3 point calibration as described in Section 4.6.3 using pH buffers of 1.77 (Orion 910168), 4.16 (Orion 910104) and 7.03 (Orion 910107) at 80 °C. According to the manufacturer recommendation, the pH probe reading is not affected by pressure until in excess of 100 bar [136]. This allowed for calibration to be performed at room pressure in glass beakers heated to 80 °C before the pH probe was assembled into an autoclave. Unfortunately the sensitivity of the measurements coupled with periodic interference from an unconfirmed external source meant that the pH measurements were not sufficiently stable to provide reliable information. The data in Figure 5.5 does however provide a reasonable trend in agreement with the model prediction. The results in Figure 5.3 and Figure 5.5 provide sufficient evidence that the model can be reliably used to qualitatively assess the effects of corrosion on system chemistry.

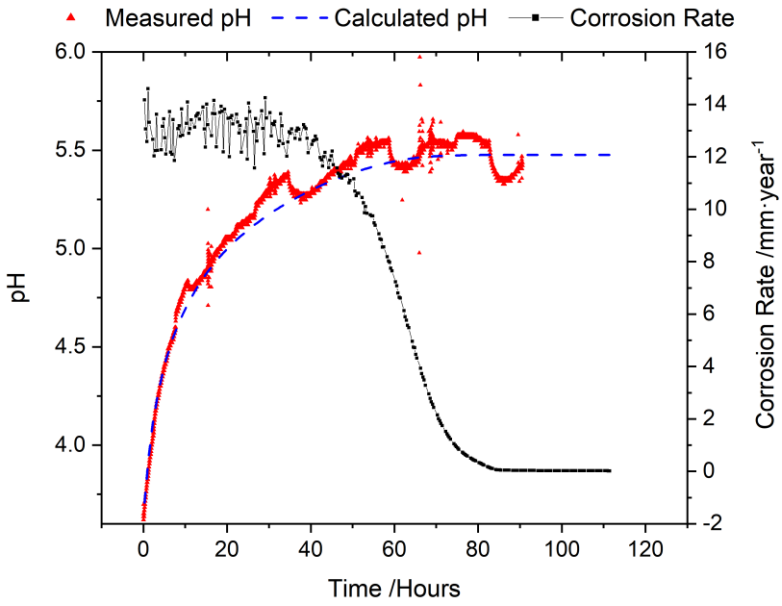

Figure 5.5: Results of validation experiment at elevated pressure for modelled bulk pH increase due to Fe^{2+} from X65 carbon steel corroding in a 30 $g \cdot L^{-1}$ NaCl CO_2 saturated brine solution at 80 °C and 5.5 bar pCO_2

5.2.5 Interpretation of Validation Results

The validation test results at different temperatures presented in Figure 5.2 show reasonable agreement between both models and experimental measurements. The methodology of Nordsveen [120] provides the most accurate prediction, particularly at low temperature where average errors at 25 °C were 1.25% and 0.87% at low and high pH respectively. This was closer to 5% for the Kahyarian model. At 80 °C and high pH the discrepancies were approximately 3% for the Nordsveen model and 6.1% for Kahyarian. Both models slightly overestimate the value of pH, this is likely due to experimental accuracy and modelling assumptions such as chemical purity. The equilibrium constants in the model are also empirically derived and are therefore subject to experimental error that could have occurred when they were formulated.

5.3 Parametric Analysis of CO_2 Environments

5.3.1 Effects of Experimental Conditions on CO_2 Chemistry

Figure 5.6 illustrates how the relative concentration of species changes as a function of pH. In an unbuffered system with no additional alkalinity the charge balance is dominated by H^+ and HCO_3^- which as a consequence are almost identical. As pH increases the contribution of OH^- and CO_3^{2-} becomes significant and H^+ and HCO_3^- concentrations diverge. At low pH the total moles of CO_2 in the system is dominated by the aqueous CO_2, however as pH increases, HCO_3^- concentrations start to become significant. At around pH 6 HCO_3^- concentrations exceed those of aqueous CO_2.

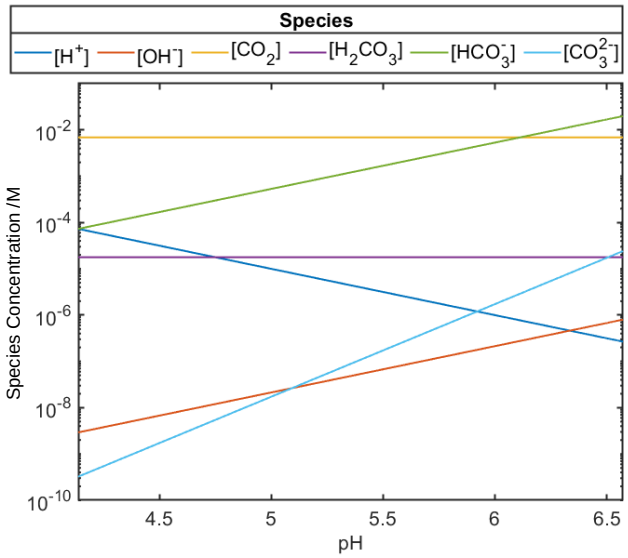

Figure 5.6: Equilibrium species concentrations as a function of pH in 30 $g \cdot L^{-1}$ NaCl CO_2 saturated solution at 80 °C and 0.54 bar pCO_2

Figure 5.7 shows how temperature affects speciation in a low pH system. The inverse solubility of CO_2 means that aqueous CO_2 reduces with temperature. The consequence is that carbonic acid concentrations decrease, resulting in an increase in pH and increase in CO_3^{2-}. This effect is largely down to the reduction in pCO_2 with increasing temperature.

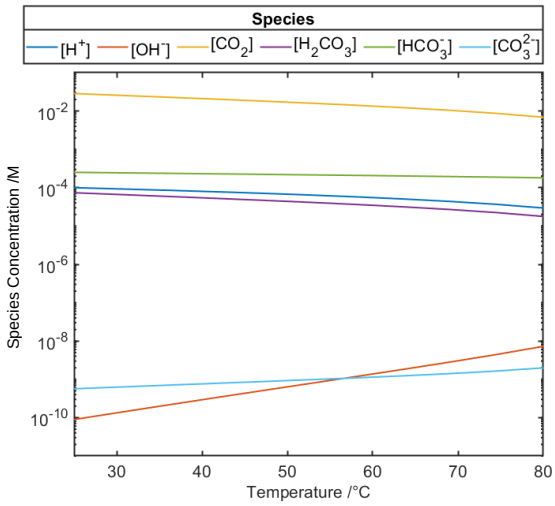

Figure 5.7: Equilibrium species concentrations as a function of temperature in 30 g·L^{-1} NaCl CO_2 saturated solution at initial pH of 4 at 25 °C and 0.54 bar pCO_2

The effect of pCO_2 is highlighted in Figure 5.8 which shows how the system is affected at different initial pH levels.

(a) (b)

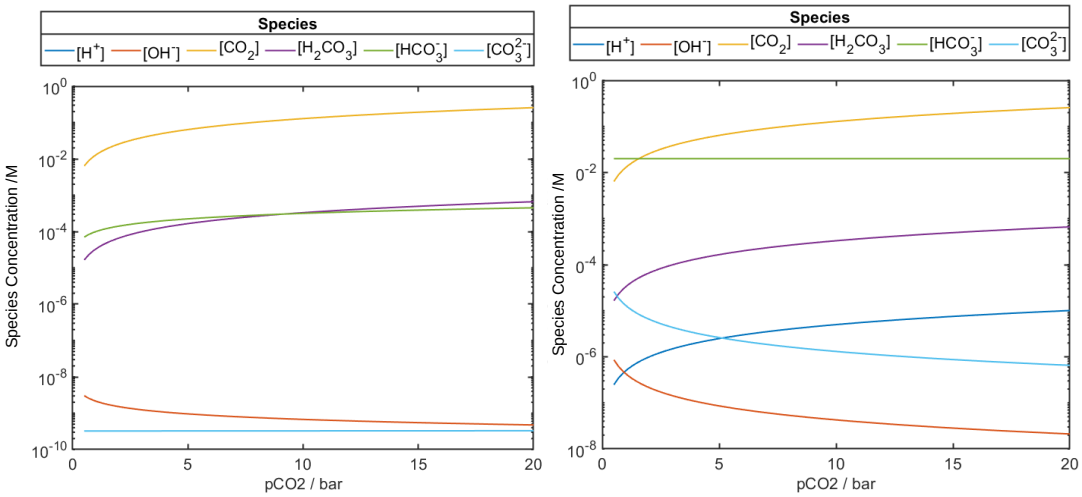

Figure 5.8: Equilibrium species concentrations as a function of pCO_2 in 30 g·L^{-1} NaCl CO_2 saturated solution at 80 °C (a) initial pH of 4 at 0.5 bar pCO_2 (b) initial pH of 6.6 at 0.5 bar pCO_2

If the solution pH is low (~4) as shown in Figure 5.8(a), pCO_2 will slightly increase both H^+ and HCO_3^- concentrations concurrently making them indistinguishable on the plot. This also means that CO_3^- remains almost constant. If the solution pH is higher (~6.6) as shown in Figure 5.8(b), the initial concentrations of HCO_3^- will be much higher than H^+ and CO_3^{2-}. This means that H^+ will increase more dramatically with increasing pCO_2 and CO_3^{2-} will decrease significantly while HCO_3^- remains relatively stable.

5.3.2 Effects of Fe^{2+} from Anodic Dissolution on CO_2 Chemistry

The sensitivity of the brine chemistry to Fe^{2+} at different pressure and temperature conditions is illustrated in Figure 5.9 and Figure 5.10. For practical purposes, the pressure is presented as the total absolute pressure of the system meaning that the actual pCO_2 will be higher at low temperature. Figure 5.9 demonstrates how the system is more sensitive to Fe^{2+} as pCO_2 is decreased and temperature increases.

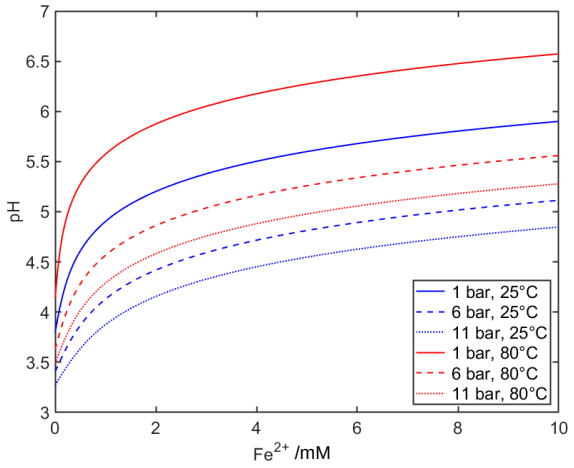

Figure 5.9: Effects of Fe^{2+} concentration on bulk pH in a 30 $g \cdot L^{-1}$ NaCl CO_2 saturated solution at various temperatures and absolute total pressures

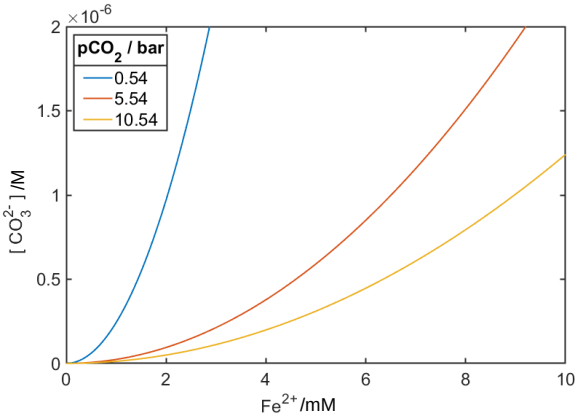

Figure 5.10: Effects of Fe^{2+} concentration on CO_3^{2-} concentration in a 30 $g \cdot L^{-1}$ NaCl CO_2 saturated solution at 80 °C and various pCO_2

Figure 5.10 further elaborates on this point by illustrating how CO_3^{2-} will increase more rapidly with Fe^{2+} at lower pCO_2, this increase in CO_3^{2-} will lead to saturation of both $FeCO_3$ and $CaCO_3$ if calcium is present in the brine.

5.3.2.1 $FeCO_3$ Saturation

Figure 5.11 indicates an inverse solubility of $FeCO_3$ as the amount of Fe^{2+} required to reach saturation decreases with temperature. This can be attributed to a number of factors. Firstly, the solubility product K_{sp} of $FeCO_3$ falls with temperature. In addition, an increase in temperature also means a decrease in pCO_2 which increases CO_3^{2-} concentrations. Further, the bicarbonate dissociation constant also increases with temperature, further increasing CO_3^{2-} concentrations. This effect is accentuated at higher pH where CO_3^{2-} concentrations are already high. The net effect is that the supersaturation of $FeCO_3$ increases with both temperature and pH.

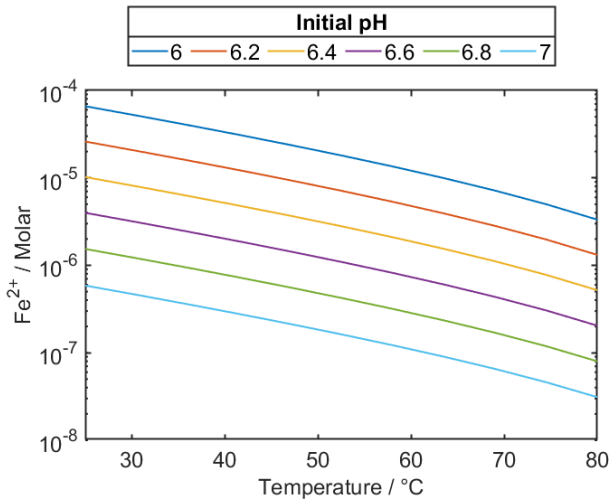

Figure 5.11: Amount of Fe^{2+} required to reach $FeCO_3$ saturation at various temperatures and initial pH values in a 30 $g \cdot L^{-1}$ NaCl CO_2 saturated solution

As further verification, results were generated for Fe^{2+} required for $FeCO_3$ saturation as a function of initial solution pH in a corroding system where Fe^{2+} is produced from anodic dissolution. The results were compared to published data by Dugstad [26] in Figure 5.12. Figure 5.12(a) shows good agreement with the previous work of Dugstad [26] shown in Figure 5.12(b). The plots exhibit a complex relationship between Fe^{2+} required to reach $FeCO_3$ saturation and pH.This is in part due to the relative concentrations of species, which has already been shown to change considerably between low and high pH.

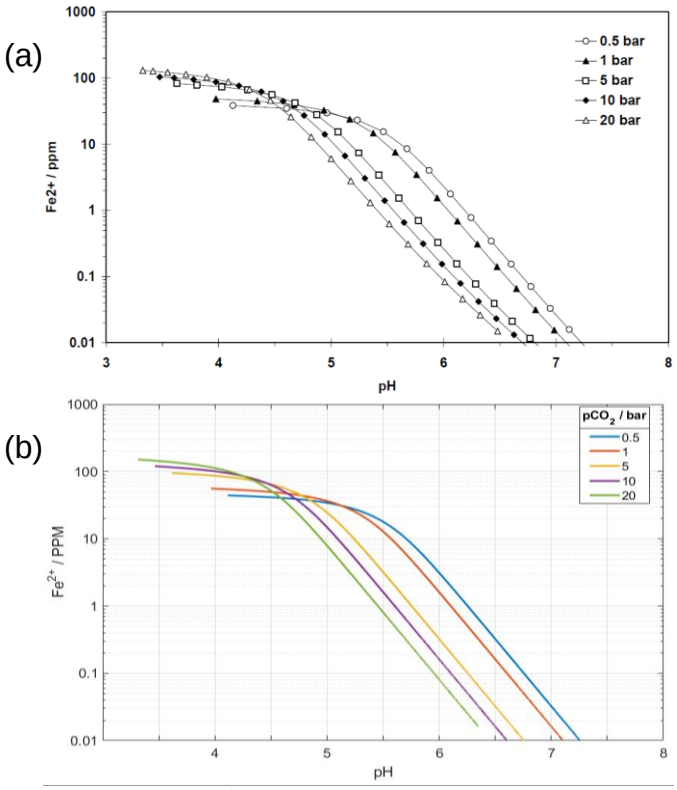

Figure 5.12: Amount of Fe^{2+} required to reach $FeCO_3$ saturation as a function of initial pH in a 1 wt% NaCl CO_2 saturated brine (a) taken from Dugstad [26] (b) calculated by current chemistry model

At higher pH, increasing pCO_2 decreases the concentration of CO_3^{2-} as demonstrated in Figure 5.8(b). The observation in Figure 5.12 seems to suggest the contrary as at high pH the Fe^{2+} required for saturation reduces dramatically with increasing pCO_2. This implies an increase in CO_3^{2-} due to increasing pCO_2. In reality, increasing pCO_2 increases H^+ concentration so for a given value of initial pH on the plot, the initial alkalinity (additional cations) will be greater for greater pCO_2. This in turn dramatically increases the initial CO_3^{2-}. Increasing cation concentration drastically increases CO_3^{2-} concentrations even at high pCO_2 and therefore disguises any drop in CO_3^{2-} due to pCO_2 increase. At low pH, CO_3^{2-} is present in very low concentrations and does not change much with increasing pCO_2 as highlighted in Figure 5.8(b). Meanwhile H^+ and HCO^- concentrations are almost identical. Further, increasing pCO_2 at low pH requires much lower concentrations of buffer cations to be added to maintain pH. This means that the dominant effect becomes the response of the system to production of Fe^{2+}.To reach $FeCO_3$ saturation at low pH (i.e. low CO_3^{2-}) Fe^{2+} is required in concentrations that are orders of magnitude above that required at high pH.

Moreover, a system with lower pCO_2 responds much faster to increasing Fe^{2+} both in terms of pH increase and especially CO_3^{2-} increase. The result is that saturation can happen faster at low pH when pCO_2 is low. In essence, the system changes from a CO_3^{2-} controlled regime at high pH, to an anodically produced, Fe^{2+} controlled regime at low pH.

5.3.3 Rationale for Selection of Initial Experimental Conditions

The results of system chemistry modelling in Section 5.3 were used in conjunction with the analysis of literature in Section 3.6 and industry conditions reviewed in 1.2, to identify field conditions that appear particularly sensitive to Fe^{2+} from the corrosion process when simulated in a closed autoclave environment. This led to the following decisions on brine conditions:

- pCO_2 was minimised by saturation at ambient pressure to maximise sensitivity of system pH to Fe^{2+} concentration.
- The brine was unbuffered (no additional alkalinity) to keep the initial pH low at around 3.7.

The above conditions aligned with the previous experimental conditions of Shamsa [52] which were selected as a bench mark for initial experiments. The temperature was set to 80 °C which has been shown to provide favourable conditions for $FeCO_3$ formation [4, 25-27]. The initial brine chemistry was unbuffered (no additional alkalinity) and the system pressure was allowed to evolve naturally from ambient during autoclave heat up.

5.4 Evaluation of Existing CO_2 Charging Methods

An assessment of the existing CO_2 charging methods outlined in Section 4.5.2 was performed to develop the experimental methodology. Experiments were conducted over 4 days using two 25 mm diameter mass loss coupons and 5000 $mg \cdot L^{-1}$ of Ca^{2+} with the brine prepared as described in Section 4.3. The first experiment was conducted using low pressure solution transfer with a gear pump outlined in Section 4.5.2.1 while subsequent experiments involved a high pressure purge described in Section 4.5.2.2. Variations in start pressure were observed once the autoclave had reached target temperature when using the high pressure purge technique so to investigate the impact this had on corrosion rates and corrosion product formation, tests were conducted at gauge pressures of 4, 6 and 8 bar.

The results of gravimetric analysis are presented in Figure 5.13. An additional test was also conducted using the solution transfer approach with a total absolute pressure calculated to be ~ 2.3 bara. As this was an initial trial, repeat experiments were not conducted. The data plotted represents the average of two mass loss coupons from the same experiment while error bars represent the minimum and maximum measurements. SEM images of the corrosion product formation are presented in Figure 5.14.

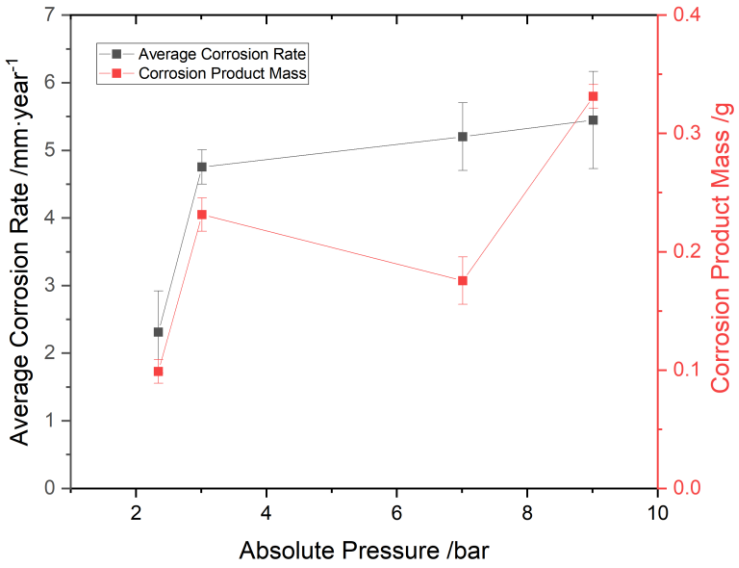

Figure 5.13: Average corrosion rates of X65 carbon steel and corrosion product mass measurements from 4 day experiments under various system pressures and at 80 °C with 5000mg·L^{-1} Ca^{2+}

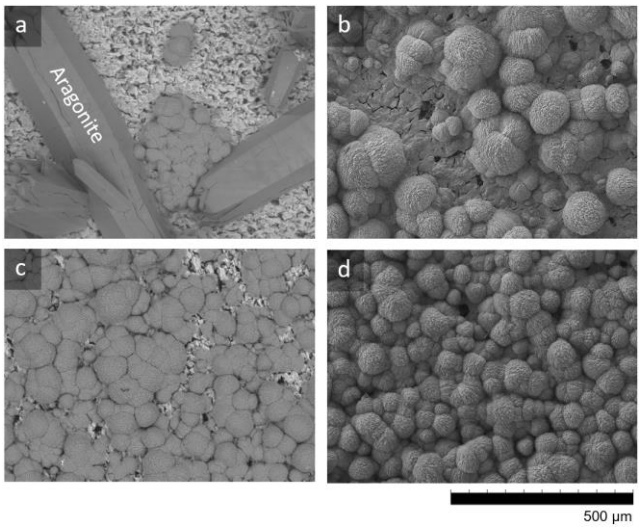

Figure 5.14: SEM images of corrosion products formed on X65 carbon steel after 4 day experiments at 80 °C with 5 g·L^{-1} Ca^{2+} under different system pressures (a) 2.3 bar using low pressure solution transfer (b),(c),(d) using high pressure purge and 3, 7 and 9 bar respectively

The corrosion products that formed were typical mixed iron calcium carbonate as previously observed under the same conditions by Shamsa [52]. The aragonite crystals that Shamsa also observed were only present at lower pressure using the solution transfer approach.

5.4.1 Assessment of Existing CO_2 Charging Methods

5.4.1.1 Estimating Autoclave Pressure Increase from Heating

In Figure 5.13, the total pressure of the system is based on the pressure gauge reading. As the original pressure gauge was rated up to 200 bar the resolution of the gauge made accurate reading difficult. For the low pressure solution transfer approach, system pressure could be calculated with greater accuracy. Such calculation also provides insight into the mechanism of CO_2 saturation and pressure evolution.

In a closed vessel with CO_2 saturated water, pressure will build during heat up due to the increase in water vapour pressure and the inverse solubility of CO_2. To calculate the pressure build the initial conditions need to first be established, namely the total number of moles of CO_2 in the system as this will remain constant (ignoring effects of corrosion). Assuming that the conditions of CO_2 equilibrium established in the bubble cell are constant when the solution is transferred to the autoclave, the total number of moles of CO_2 prior to heat up will be:

$$n_t = n_v + n_{aq} \tag{5.24}$$

Where n_t is the total number of moles of CO_2, n_v and n_{aq} are the moles in the vapour and aqueous phases respectively.

The initial number of moles in the vapour phase is calculated using the ideal gas law:

$$n_v = \frac{V_v \cdot pCO_{2_i}}{R \cdot T_{k_i}} \tag{5.25}$$

Where V_v is the volume of the vapour phase or autoclave headspace, R is the universal gas constant, pCO_{2i} and T_{ki} are the initial values of CO_2 partial pressure and absolute temperature.

An empty 1 litre autoclave has a total void space of approximately 1000 mL, adding 750 mL of brine solution saturated at 25 °C would give an n_v of 0.01 mol. To calculate the initial number of moles of dissolved CO_2 in the aqueous phase the fugacity equations described in 5.2.2 were used.

For an unbuffered low pH system the contribution to the total number of CO_2 moles in the aqueous phase is dominated by the aqueous CO_2 as shown in Figure 5.6 and so CO_2 stored as HCO_3^- and CO_3^{2-} can be ignored. For further simplification, the change in total pressure of the system has negligible impact on the fugacity coefficient described in equation (5.11) and so the value of pressure, *p* in (5.12) can remain constant. Using these simplifications and by combining equations (5.11), (5.24) and (5.25) the following expression can be written for final partial pressure of CO_2 (pCO_{2f}) at target temperature:

$$pCO_{2_f} = \left(\frac{V_v}{R \cdot T_{k_f}} + \frac{\Phi_{CO_{2f}} \cdot V_{aq}}{H^*_{CO^*_{2f}}} \right) \cdot n_t{}^{-1} \qquad (5.26)$$

Where V_{aq} is the volume of liquid or aqueous phase. Adding the vapour pressure of water at target temperature gives the final absolute pressure. The total absolute pressure after heating up to 80 °C is plotted as a function of fill volume in Figure 5.15 at various initial CO_2 saturation temperatures. Figure 5.15 illustrates the importance of having well controlled pre-saturation temperatures when performing ambient pressure solution transfer to an autoclave as this dictates the total amount of CO_2 carried in to the system.

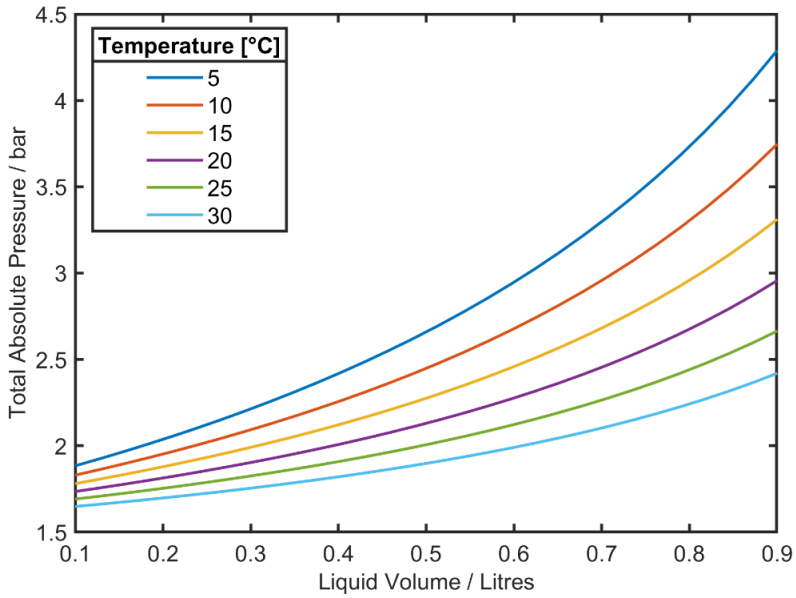

Figure 5.15: Effect of liquid volume in a 1 litre autoclave on the final vessel pressure after heating to 80 °C at various initial saturation temperatures

5.4.1.2 Poor CO_2 Saturation Control using High Pressure Purge Method

Using the high pressure purge method outlined in section 4.5.2.2 the final gas pressure appeared to vary considerably depending on the rate and pressure at which CO_2 was introduced into the vessel.

It is well noted within the literature [27, 40, 120] that the slow hydration reaction is a rate determining step for equilibration of a CO_2 system. Further to this are the physical parameters that effect rates of gas dissolution such as the interface area and residence time of the gas in contact with the liquid. An example of this is a gas sparger that creates micro bubbles to enhance dissolution rates by increasing the total surface area of the gas/liquid interface for a given volume of gas. Conversely, evolution of CO_2 gas is dependent on physical factors such as surface roughness which creates nucleation sites for bubbles to form. Some classic examples include champagne flutes which have a low surface area to volume, minimising the loss of CO_2 through bubble nucleation on the glass surface. Conversely mints added to carbonated drinks will rapidly evolve CO_2 due to the porous surface of the mint providing the perfect environment for bubble nucleation. In terms of dissolution, applying a large over pressure of CO_2 to the system will expedite the dissolution process but also lead to excess dissolved CO_2 due to Henry's law, which in turn will be slow to evolve after release of the headspace pressure.

After releasing headspace pressure that has built up from an over-saturated brine the system will then re-equilibrate redistributing the remaining moles of CO_2 in the system. This releases more CO_2 to the headspace and again increasing pressure at the gauge as depicted in Figure 5.16. This lag in CO_2 release can induce variability in the final test pressure depending on how long the vessel is left to settle.

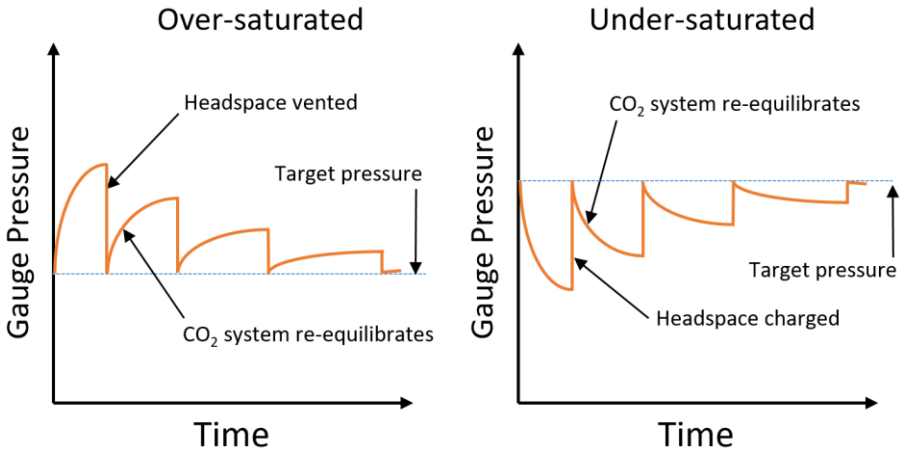

Figure 5.16: Effects of slow equilibration between brine and head space in a CO_2 autoclave experiment due to over-saturation (left) and under-saturation (right)

5.4.1.3 Effects of Pressure on Corrosion Product Formation

The mass loss data in Figure 5.13 shows that average corrosion rates increase with increasing pressure. This was expected as increasing pCO_2 decreases pH making the environment more acidic. Increased corrosion rates are commonly attributed to greater acidity but some also claim the dissolved CO_2 enhances reactions at the steel surface [43]. The increase in corrosion rate is most noticeable between 2 bar and 3 bar absolute pressure. Figure 5.13 also shows that CPM generally increased with pressure despite a slight drop in the measured mass at 7 bar. Increasing pressure will result in a lower initial concentration of CO_3^{2-} however this is likely offset by the greater quantities of Fe^{2+} from increased corrosion kinetics which leads to increased CO_3^{2-}. The drop in CPM at 7 bar could be anomalous or as a consequence of lower corrosion rates than at 9 bar but also lower initial CO_3^{2-} than 2.3 bar and 3 bar. The SEM images in Figure 5.14 corroborate the findings of gravimetric analysis showing greater corrosion product coverage with increasing pressure. At the low pressure of 2.3 bar a mixed iron calcium carbonate is accompanied by large crystals of the $CaCO_3$ polymorph, aragonite.

Aragonite was also observed by Shamsa [52] under similar conditions and has been reported to form in iron rich brines which suppress the transformation of aragonite to more stable calcite [82-84, 86, 87, 90]. In this case the presence of aragonite suggests the saturation of $CaCO_3$ was much higher than $FeCO_3$ which would be due to the higher concentrations of CO_3^{2-} at low pCO_2 and lower Fe^{2+} from the reduced corrosion rates.

5.4.2 Chemistry Modelling and Experimental Methodology Evaluation

Based on the information gathered from initial experiments the following experimental improvements were identified due to the sensitivity of the system to pressure variation:

- The pressure gauge or pressure transducer should be sized to allow precise measurements within the experimental range selected.
- System pressure should be regulated in a consistent and repeatable way to ensure the initial conditions of each experiment are identical.

The above conclusions led to the methodological improvements outlined in Section 4.5.3 which include a smaller more precise 10 bar pressure gauge and a back pressure regulator (BPR).

In addition, an elevated system pressure of 6 bar (5.5 bar pCO_2) was selected to accelerate corrosion product formation based on the data in Figure 5.13 and Figure 5.14 whilst remaining within industrially relevant operating conditions. Figure 5.17 highlights the benefits of using a BPR in elevated pressure conditions especially during heat up to avoid dramatic fluctuations in system pressure and potential overshoots on pressure release that could lead to under-saturation.

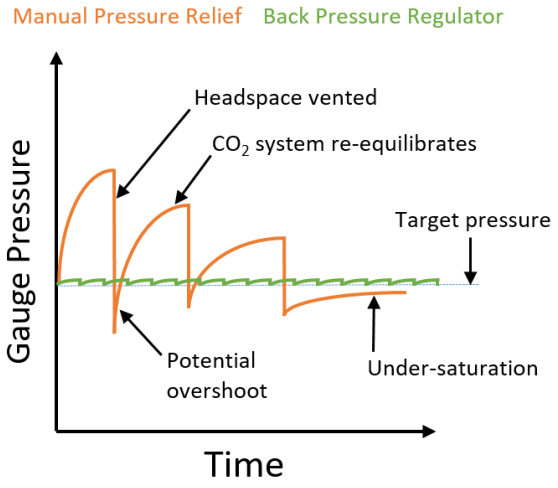

Figure 5.17: Comparison of pressure control using back pressure regulator versus manual regulation

5.5 Autoclave Mass Loss Experiments

Having refined the methodology, mass loss experiments were performed using the conditions and area to volume ratios outlined in Table 4.3. Further information on the total ionic strength and pH calculated using the chemistry model are provided in Table 5.4 (Total ionic strength includes the contribution of all ionic species). Experiments were conducted over 3 days at a gauge pressure of 5 barg (absolute pressure 6 bara) giving a pCO_2 of 5.54 bar. *Ex situ* analysis was performed in accordance with Section 4.7 which included gravimetric analysis, surface SEM imaging, X-ray powder diffraction and cross-sectional SEM and EDX.

Table 5.4: Conditions for autoclave experiments at low and high A/V and predicted initial pH

Parameter	Units	Value		
Test Duration	days		3	
Total Pressure	bar		6	
pCO_2	bar		5.5	
Temperature	°C		80	
Ca^{2+}	$mg \cdot L^{-1}$	0	1000	5000
$CaCl_2.2H_2O$	$g \cdot L^{-1}$	0	3.67	18.34
NaCl	$g \cdot L^{-1}$	30	27.08	15.42
Cl^-	$g \cdot L^{-1}$	18.2	18.2	18.2
Ionic Strength of Salts	$mol \cdot L^{-1}$	0.5133	0.5383	0.6381
Total Ionic Strength	$mol \cdot L^{-1}$	0.5136	0.5385	0.6383
Calculated pH		3.63	3.63	3.62

5.5.1 Gravimetric Analysis

Average corrosion rates and corrosion product mass (CPM) are provided in Figure 5.18 and Figure 5.19 respectively. Data are plotted as the average of two repeats with error plotted as the minimum and maximum values. Due to a limited number of data points some error bars have been increased to provide a more realistic representation of experimental repeatability based on experiments conducted throughout this project and in similar work [52]. From Figure 5.18, at low A/V corrosion rates were higher in the absence of calcium, in contrast at high A/V the corrosion rate increased almost linearly with calcium concentration. The observed corrosion rates were significantly higher at low A/V. Similarly contrasting trends were also observed for CPM in Figure 5.19. At low A/V CPM was much higher in the absence of calcium and almost identical to the CPM at high A/V. Increasing calcium decreased the CPM at low A/V while increasing CPM at high A/V. The reason for these contrasting trends becomes more transparent when reviewing the images of surface coverage.

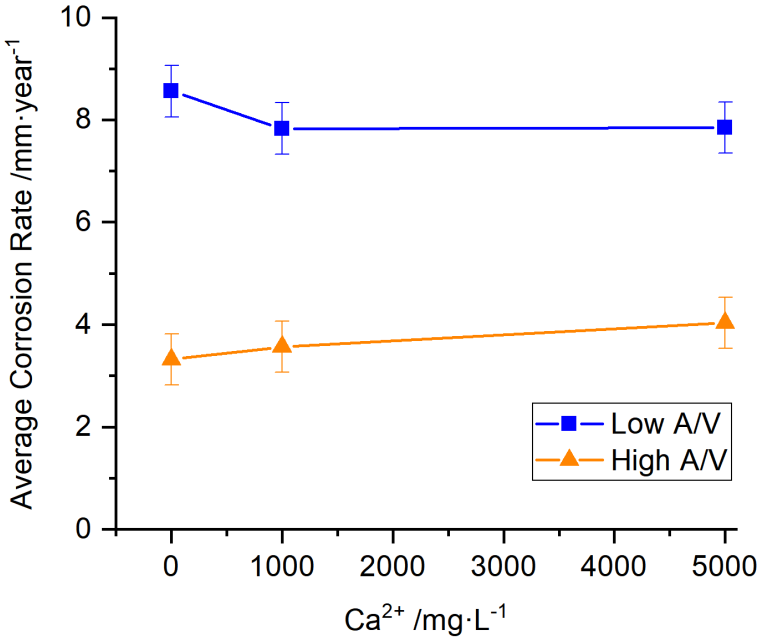

Figure 5.18: Average corrosion rates from mass loss of X65 carbon steel after 3 days at 80 °C and 5.5 bar pCO_2 with 0, 1000 and 5000 mg·L^{-1} of initial bulk Ca^{2+} using high and low (41.4 and 10.5 cm^2·L^{-1}) A/V ratios

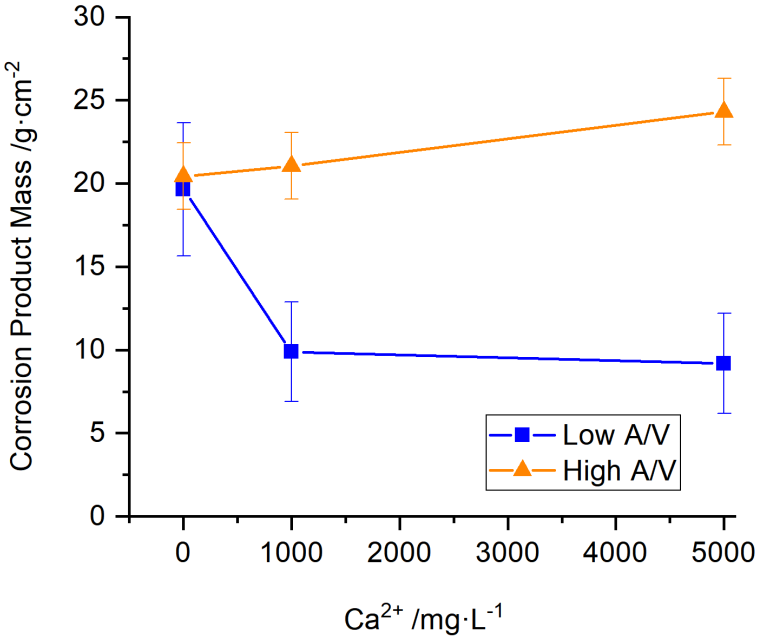

Figure 5.19: Average corrosion product mass per cm^2 on X65 carbon steel after 3 days at 80 °C and 5.5 bar pCO_2 with 0, 1000 and 5000 mg·L^{-1} of initial bulk Ca^{2+} using high and low (41.4 and 10.5 cm^2·L^{-1}) A/V ratios

5.5.2 Surface Coverage

The SEM images in Figure 5.20 show the effects of calcium addition in the bulk brine solution as well as the A/V ratio on the surface coverage of corrosion products.

Images have been selected that give the most representative picture of the overall surface. Grey areas are typically corrosion products while lighter areas are the substrate steel.

Low A/V High A/V

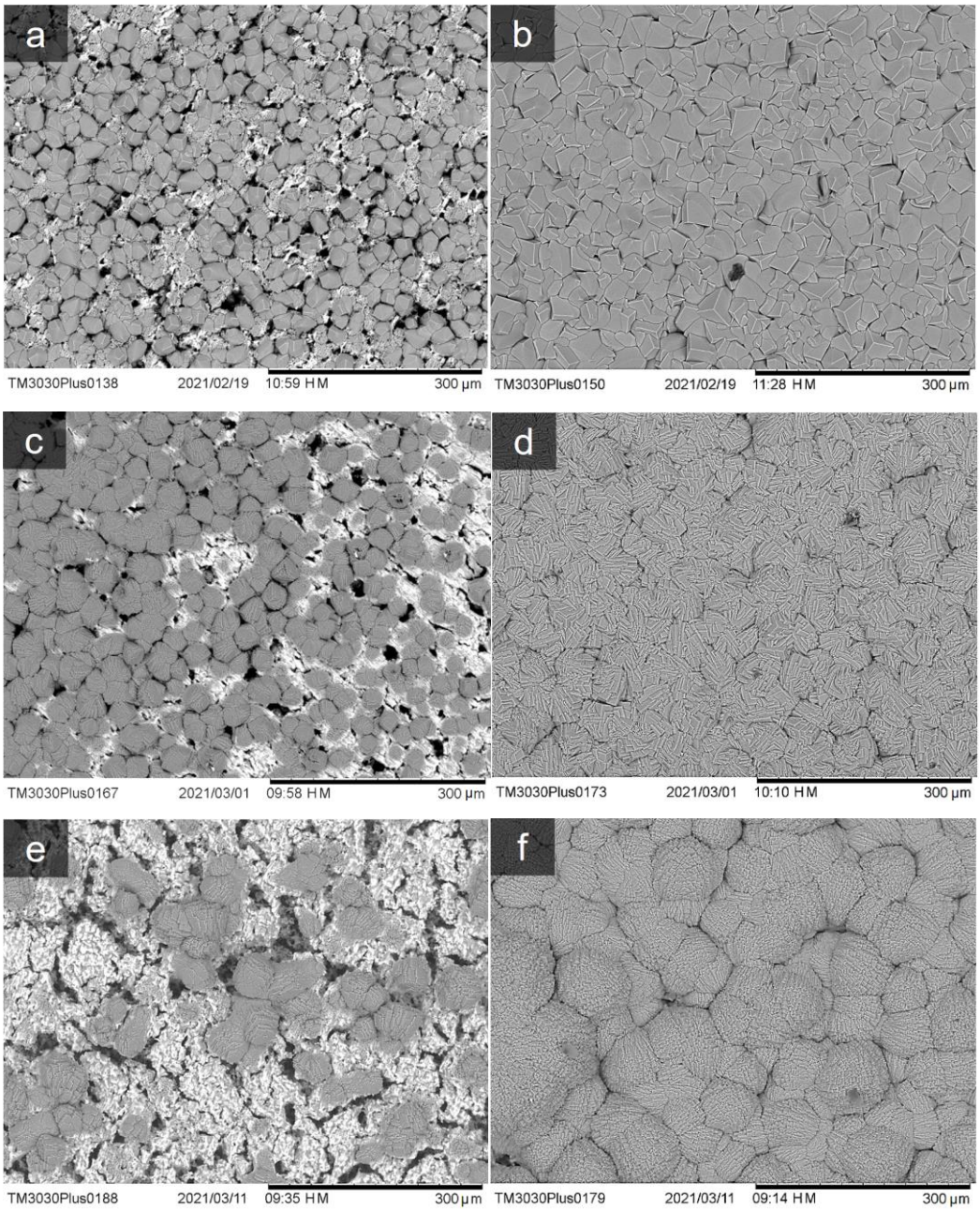

Figure 5.20: 250x Magnification top surface SEM images of corrosion product coverage on X65 carbon steel after 3 days at 80 °C and 5.5 bar pCO_2 using high (41.4 $cm^2 \cdot L^{-1}$) and low (10.5 $cm^2 \cdot L^{-1}$) A/V ratios (a) No Ca^{2+} low A/V (b) No Ca^{2+} high A/V (c) 1000 $mg \cdot L^{-1}$ Ca^{2+} low A/V (d) 1000 $mg \cdot L^{-1}$ Ca^{2+} high A/V (e) 5000 $mg \cdot L^{-1}$ Ca^{2+} low A/V (f) 5000 $mg \cdot L^{-1}$ Ca^{2+} high A/V

SEM images of surface corrosion scale in Figure 5.20 show that at low A/V the inclusion of calcium decreased coverage. Despite similar CPM at 1000 and 5000 $mg \cdot L^{-1}$ Ca^{2+} and low A/V, surface coverage is significantly decreased with increase in calcium due to a clustering effect producing larger crystal formations locally. In the absence of calcium at low A/V, crystal growth was more uniform providing enhanced surface coverage with the surface almost entirely covered with typical rhombohedral $FeCO_3$. At high A/V the surface is entirely covered with corrosion scale across all calcium concentrations. These results suggest that corrosion rates may initially be higher in the absence of calcium but as corrosion products begin to form the average corrosion rate over the course of the test drops more quickly in the absence of calcium. This effect can either be attributed the induction time for precipitation of corrosion products or to the rate at which corrosion rate drops once crystal nucleation has occurred, i.e the actual protectiveness offered by the type of corrosion product. To evaluate this, *in situ* corrosion rate measurements are required.

5.5.3 Crystal Morphology

Higher magnification images of the corrosion products are provided in Figure 5.21 to highlight the changes in morphology as a result of both calcium incorporation and A/V ratio. Notable crystal morphology changes occur with increasing calcium content at both high and low A/V. Figure 5.21 shows how calcium incorporation reduces the crystallite size and favours the formation of large polycrystalline clusters.

Low A/V High A/V

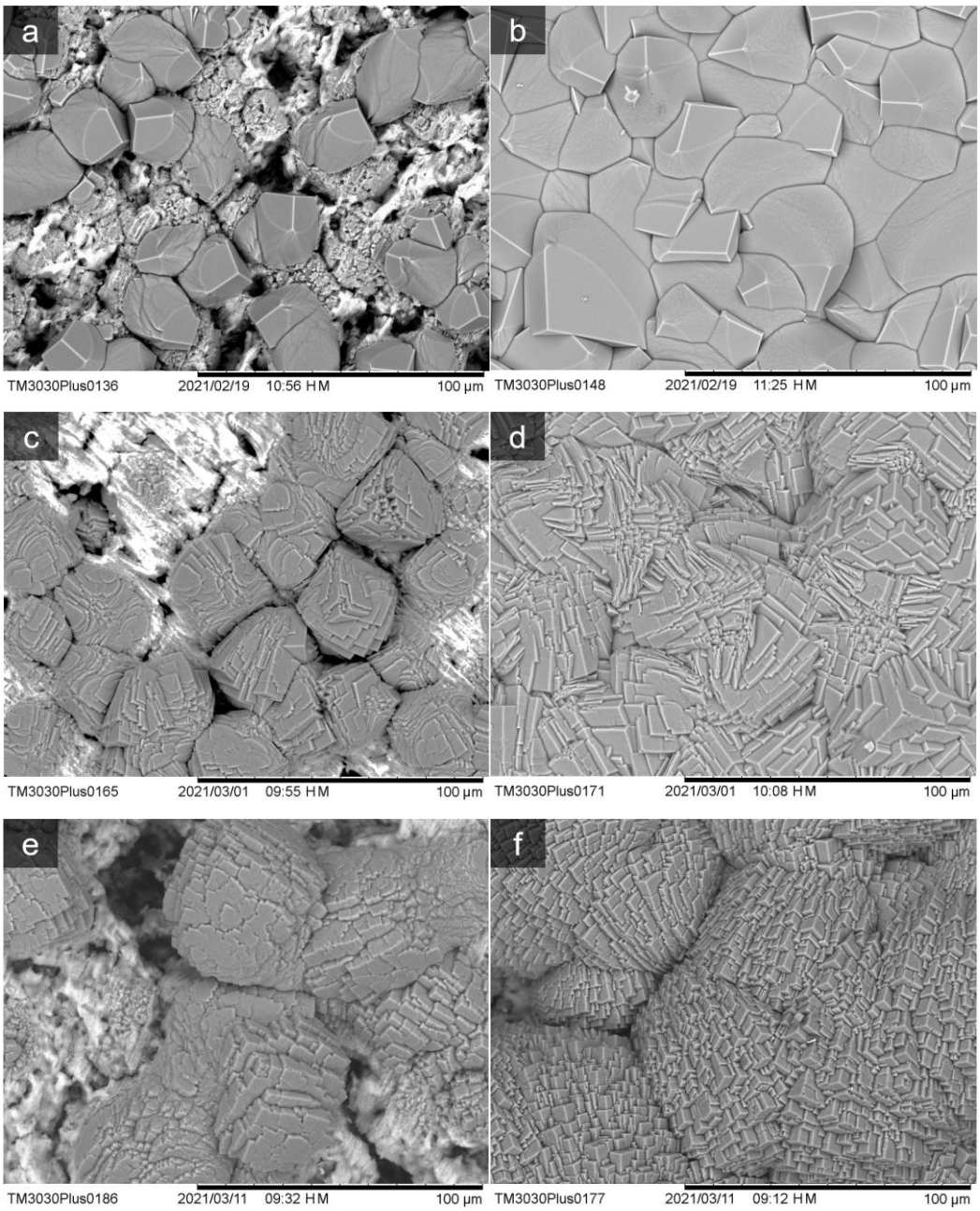

Figure 5.21: 1000x Magnification SEM images of corrosion product morphology on X65 carbon steel after 3 days at 80 °C and 5.5 bar pCO_2 using high (41.4 $cm^2 \cdot L^{-1}$) and low (10.5 $cm^2 \cdot L^{-1}$) A/V ratios (a) No Ca^{2+} low A/V (b) No Ca^{2+} high A/V (c) 1000 $mg \cdot L^{-1}$ Ca^{2+} low A/V (d) 1000 $mg \cdot L^{-1}$ Ca^{2+} high A/V (e) 5000 $mg \cdot L^{-1}$ Ca^{2+} low A/V (f) 5000 $mg \cdot L^{-1}$ Ca^{2+} high A/V

5.5.4 XRD Analysis

The results of X-ray diffraction are presented in Figure 5.22. ICDD Reference data for pure Siderite (00-008-0133) and pure Calcite (00-005-0586) were used to compare peak shifts.

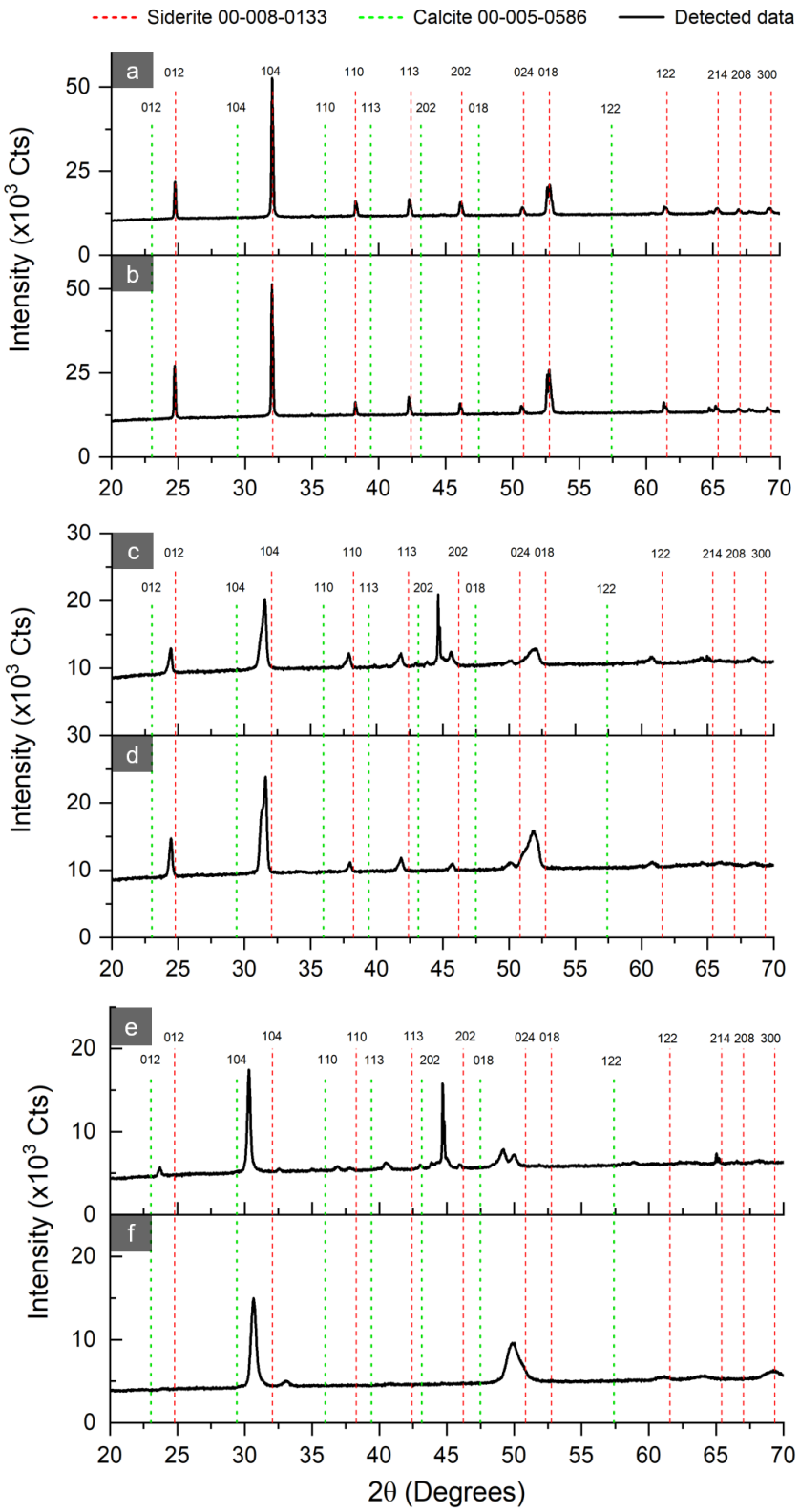

Figure 5.22: Powder diffraction patterns of corrosion scales grown over 3 days at 80 °C and 5.5 bar pCO_2 using high (41.4 $cm^2 \cdot L^{-1}$) and low (10.5 $cm^2 \cdot L^{-1}$) A/V ratios (a) No Ca^{2+} low A/V (b) No Ca^{2+} high A/V (c) 1000 $mg \cdot L^{-1}$ Ca^{2+} low A/V (d) 1000 $mg \cdot L^{-1}$ Ca^{2+} high A/V (e) 5000 $mg \cdot L^{-1}$ Ca^{2+} low A/V (f) 5000 $mg \cdot L^{-1}$ Ca^{2+} high A/V

An equation derived previously by Shamsa et al. [52] was used to determine the average molar fraction of calcium in the corrosion product based on peak shifts in the powder diffraction data. This equation is based on the inter-planar d-spacing and unit cell volume formulae for hexagonal Bravais lattices which $Fe_xCa_yCO_3$ end members, siderite ($FeCO_3$) and calcite ($CaCO_3$) both share. The equations are combined with correlations devised by Davidson et al. [79], which relate unit cell parameters and volume to the mole fraction of Ca (y) in $Fe_xCa_yCO_3$. In this instance, the value of d in equation (5.27) corresponds to the inter-planar spacing of the most intense Bragg peak for $Fe_xCa_yCO_3$ located at the (104) inter-planar d-spacing.

$$\frac{1}{d^2} = \frac{4}{3}\left(\frac{2.924y + 26.626}{148.214y + 582.680}\right) + \frac{16}{(1.688y + 15.373)^2} \tag{5.27}$$

In the original derivation Shamsa observed that the equation behaved almost linearly within the bounds of $0 \leq y \leq 1$. By taking a Taylor series expansion of equation (5.27) about y = 0.5 and up to the first degree polynomial the following simplified linear equation can be obtained:

$$d = 0.242y + 2.79 \tag{5.28}$$

Or in a more general form:

$$d_{Fe_xCa_yCO_3} = \Delta d \cdot y + d_{FeCO_3} \tag{5.29}$$

$$\therefore y = \frac{d_{Fe_xCa_yCO_3} - d_{FeCO_3}}{\Delta d} \tag{5.30}$$

Where Δd is the difference in 104 d spacing between end members Siderite and Calcite. Figure 5.23 shows the peak shift and broadening caused by the incorporation of calcium into the corrosion products.

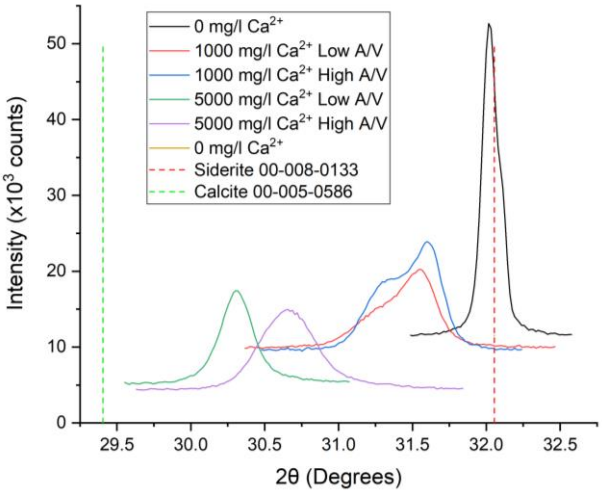

Figure 5.23: Powder diffraction 104 peak shift and broadening caused by incorporation of calcium in to the $FeCO_3$ lattice

Figure 5.23 shows the 104 peak shifts away from pure siderite to calcite as brine calcium is increased indicating greater incorporation of calcium into the corrosion scale. At 1000 mg·L^{-1} Ca^{2+} and high A/V the 104 peak appears to separate suggesting that two distinct phases of mixed carbonate could be present, this effect is less pronounced at low A/V. Overall, the top of 104 peaks at 1000 mg·L^{-1} Ca^{2+} are well aligned at both high and low A/V suggesting A/V ratio has not affected the average composition of the corrosion scale that formed. This is not the case at the higher concentration of 5000 mg·L^{-1} Ca^{2+} where there is a clear separation between the high and low A/V peaks suggesting a greater concentration of calcium in the corrosion scale that formed at low A/V. Excluding the effects of peak separation at 1000 mg·L^{-1} Ca^{2+} the peaks appear to broaden with calcium incorporation as peak shift approaches 50% of the total distance between siderite and calcite. At 5000 mg·L^{-1} Ca^{2+} and low A/V the peak shift has gone beyond 50% and the peak appears to narrow compared to 5000 mg·L^{-1} Ca^{2+} high A/V which is at around the 50% mark. When analysing powder diffraction patterns some level of peak broadening occurs due to non-idealities of the instrumental setup such as the finite breadth of the X-ray beams which are also not perfectly collimated [137]. This instrumental broadening is evident in the 104 peak profile for 0 mg·L^{-1} Ca^{2+} in Figure 5.23 which was effectively pure siderite. Though instrumental broadening should be considered, a more significant cause of broadening is associated with crystallite size, perfection and lattice strain [137].

5.5.5 Cross-section EDX Analysis

Elemental maps of cross-sections of the corrosion products are provided in Figure 5.24. For each specimen, three point scans were also conducted at different regions of the film to get an average % composition of Fe and Ca. The cross-sections in Figure 5.24 clearly show that a much thicker corrosion scale forms in the presence of calcium. At 5000 mg·L^{-1} Ca^{2+} and high A/V a duplex corrosion scale layer can be observed with a more iron rich sub surface layer as shown in the EDX line scan in Figure 5.25. The line scan also indicates that the top surface layer is more iron rich at its outer surface.

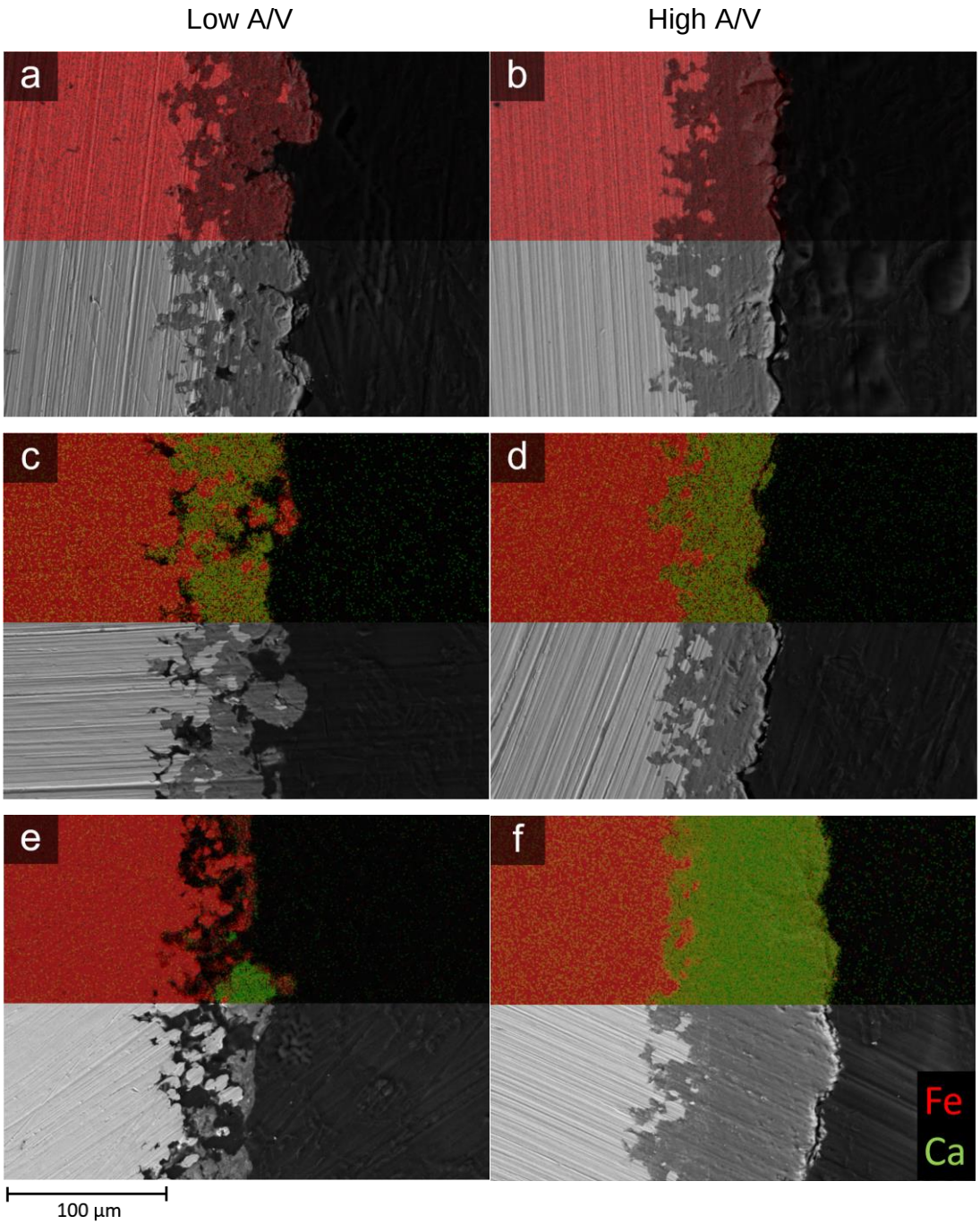

Figure 5.24: Cross-sectional SEM and EDX maps of Fe (red) and Ca (green) illustrating composition of corrosion scales grown over 3 days at 80 °C and 5.5 bar pCO_2 using high (41.4 $cm^2 \cdot L^{-1}$) and low (10.5 $cm^2 \cdot L^{-1}$) A/V ratios (a) No Ca^{2+} low A/V (b) No Ca^{2+} high A/V (c) 1000 $mg \cdot L^{-1}$ Ca^{2+} low A/V (d) 1000 $mg \cdot L^{-1}$ Ca^{2+} high A/V (e) 5000 $mg \cdot L^{-1}$ Ca^{2+} low A/V (f) 5000 $mg \cdot L^{-1}$ Ca^{2+} high A/V

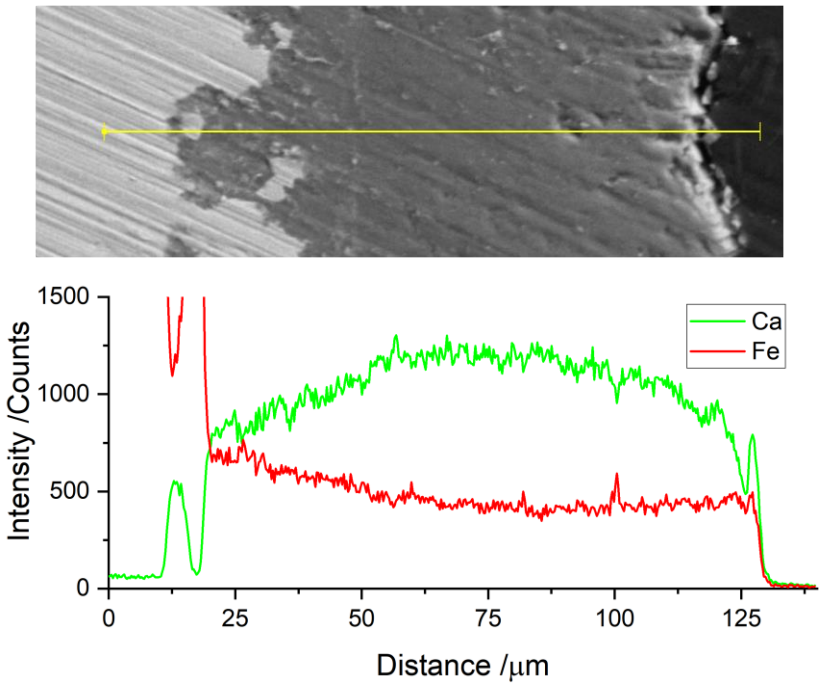

Figure 5.25: EDX line scan through $Fe_xCa_yCO_3$ layer formed in 5000 mg·L^{-1} Ca^{2+} high A/V conditions

The powder diffraction data and through layer EDX point scans are compared in Table 5.5 to evaluate the average compositions of corrosion scales grown at high and low A/V ratios. Comparing the peak broadening in Figure 5.23 to the SEM images of Figure 5.21 and compositional data in Table 5.5 suggests that peak broadening is at a maximum when the average molar concentrations of Fe and Ca in the film are approximately equal and that crystallite size is also at a minimum.

Table 5.5: Comparison of y values for $Fe_xCa_yCO_3$

A/V Ratio (cm^2·L^{-1})	**Bulk Ca^{2+} (mg·L^{-1})**					
	0		**1000**		**5000**	
	XRD	EDX	XRD	EDX	XRD	EDX
10.5	0	0	0.18	0.16	0.64	0.62
41.4	0	0	0.16	0.18	0.50	0.55

5.6 Chapter 5 Summary

5.6.1 Influence of Corrosion on Bulk Chemistry

Brine evolution due to the corrosion process has been modelled using chemical equilibria expressions from literature, in particular those collated by Nordsveen et al. [120] which showed good agreement with validation experiments. The model indicates that low pCO_2 and pH systems have higher sensitivity to the corrosion process which increases pH due to the reduction of H^+ to H_2 and concurrently releases Fe^{2+} in the anodic reaction shifting the speciation to maintain charge. As a result, this increases CO_3^{2-} concentrations, rapidly increasing saturation for $FeCO_3$ and to a lesser extent $CaCO_3$.

5.6.2 Influence of A/V Ratio

Mass loss experiments showed how increasing A/V ratio expedited the precipitation of corrosion products leading to higher corrosion product mass and lower average corrosion rates after 3 day experiments as shown in Figure 5.18 and Figure 5.19. In the presence of Ca^{2+}, increased A/V ratio led to greater mole fractions of Fe in the mixed $Fe_xCa_yCO_3$ corrosion products that formed. The result was likely due to increased concentrations of Fe in the bulk solution early in the nucleation and growth stages of corrosion product formation.

5.6.3 Influence of Calcium

Addition of Ca^{2+} ions in the bulk solution changed the morphology of the corrosion products, creating clusters of crystallites as opposed to evenly dispersed crystals in the absence of calcium. The clustering effect reduced overall surface coverage while increasing corrosion product mass. XRD indicated that increasing bulk Ca^{2+} and lowering A/V ratio increased the mole fraction of calcium in the corrosion product. Crystallite size also appeared to decrease as the mole fraction of calcium approached that of iron in $Fe_xCa_yCO_3$.

Chapter 6
Development of Impedance Models to Characterise the Evolution of $FeCO_3$ Layers

6.1 Chapter Introduction

The results of Chapter 5 suggest that surface coverage is slowed by the clustering effect from reduced crystallite size, but it is not clear if the instantaneous corrosion rates at the end of the experiments at high A/V are equal for the different types of corrosion products. To address this question, *in situ* measurements of instantaneous corrosion rates are required. It is also evident from the data that a full corrosion scale layer did not form after 3 days at low A/V, this raises the question of would the corrosion rates and corrosion product compositions eventually converge at high and low A/V over longer durations.

Further experiments were therefore conducted using *in situ* electrochemical techniques to elucidate the development process of corrosion layers on the steel surface. LPR and OCP measurements provided an indication of key characteristic changes in the development process. However, these techniques are limited when it comes to evaluating non-faradaic behaviour once corrosion products start to form. EIS was therefore employed to obtain information about the interface between the steel/corrosion product and solution. EIS is often utilised for the sole purpose of fitting equivalent circuits in order to assign quantitative values to what are often arbitrary circuit elements. This chapter, which focuses on the $FeCO_3$ layer formation at low A/V, proposes a more methodical and substantive approach to extracting information about the characteristics of the corrosion product layers by prioritising physical system characterisation and graphical interpretation over simple circuit fitting. As a result, a more robust set of parameters can be obtained, allowing straightforward comparisons to be made in later Chapters between different types of corrosion product layers.

6.1.1 Chapter Outline

The chapter focuses on data obtained in the absence of calcium and at low A/V (10.5 $cm^2 \cdot L^{-1}$) following the methodology outlined in Sections 4.6.1 and 4.6.2.

LPR (presented as reciprocal of polarisation resistance R_p^{-1} analogous to corrosion rate) and OCP data are first presented before the data are categorised into distinct stages. The EIS response at each stage is presented alongside data from separate shorter experiments that were terminated during each stage to image cross-sections of the corrosion layer. Finally, characteristic parameters are extracted by a combination of graphical and regression analysis and plotted over time to compare against the LPR and OCP response as well as SEM cross-sections.

6.2 Linear Polarisation Resistance and Open Circuit Potential

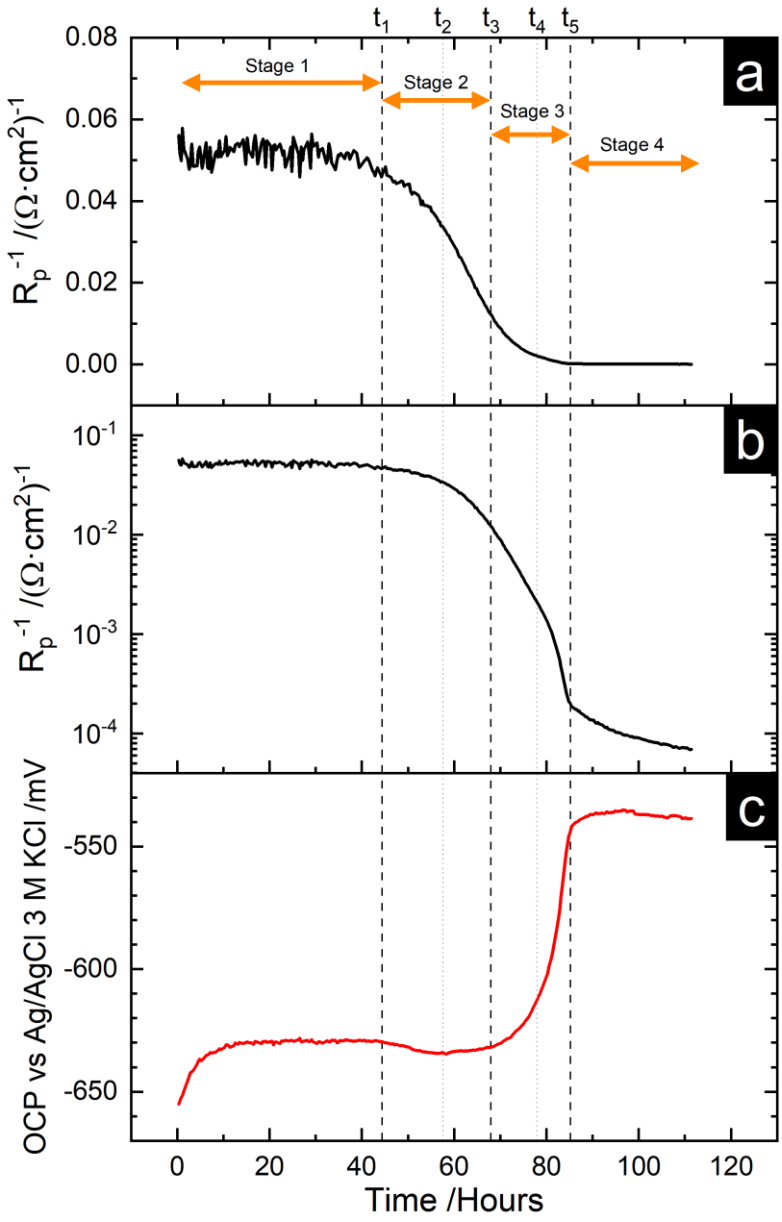

Figure 6.1: Electrochemical measurements over time from X65 carbon steel in 30 g·L^{-1} NaCl CO_2 saturated brine at 80 °C, 5.5 bar pCO_2 and 10.5 cm^2·L^{-1} A/V ratios (a) R_p^{-1} on linear scale (b) R_p^{-1} on $\log_{10}$ scale (c) OCP

6.3 Analysis of Stages of $FeCO_3$ Formation

Analysis of the LPR and OCP data reveals up to 5 key transitions in the electrochemical response of the system, these transitions are categorised in to 4 significantly unique stages as follows.

6.3.1 Stage 1 – OCP Increase (0 to 44 h)

During the first 10 hours of the experiment OCP increases before reaching a steady state until between 44 and 48 hours (t_1 in Figure 6.1). During this time the R_p^{-1} is high and relatively noisy, the magnitude of R_p^{-1} and associated noise begin to reduce around 40 hours. Nyquist plots in Figure 6.2 during the first stage show a depressed semi-circle often associated with Constant Phase Element (CPE) behaviour (non-perfect capacitance).

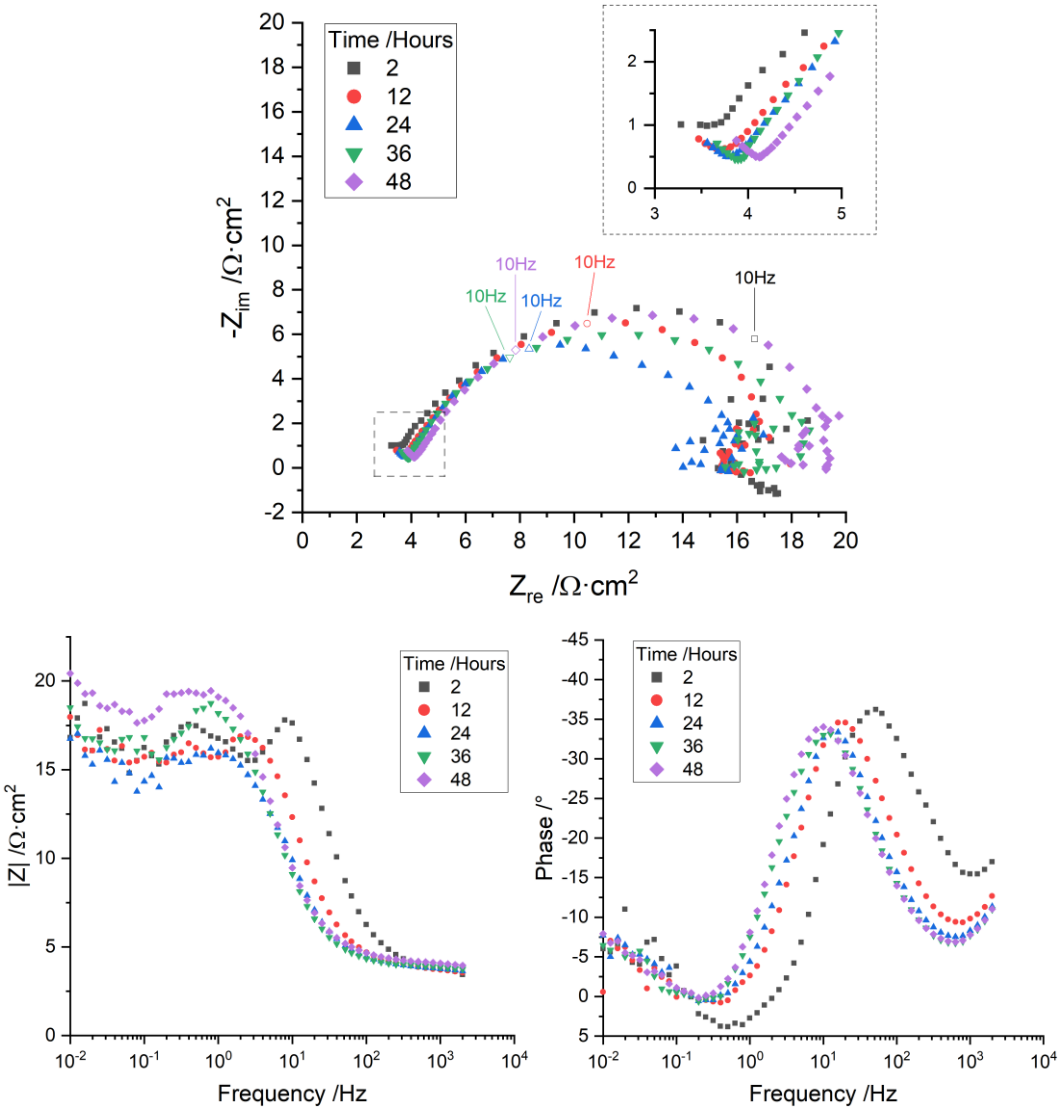

Figure 6.2: Nyquist and Bode plots of impedance response from X65 carbon steel in 30 g·L^{-1} NaCl CO_2 solution at 80 °C, 5.5 bar pCO_2 and 10.5 cm^2·L^{-1} A/V ratio over first 48 hours

The shift of the semi-circle along the real impedance axis indicates the ohmic potential drop associated with solution resistance. As highlighted in the Nyquist plot inset of Figure 6.2 this shift increases with time. In the low frequency range it appears an inductive loop is present, suggestive of an adsorption process, associated with the anodic dissolution of iron, as reported previously under acidic conditions [66, 138-150]. Raw impedance modulus and phase shift (inclusive of electrolyte resistance) over the first 48 hours indicate the characteristic frequency shifts to a lower value over time.

6.3.1.1 *Ex situ* Analysis of Stage 1

A separate experiment that was terminated during Stage 1 after approximately 38 hours is presented in Figure 6.3 to assess how the interface was evolving. The Nyquist plots from this experiment are presented in Figure 6.3(a) and show good agreement with the data from the initial experiment at this stage with less than 1 $\Omega \cdot cm^2$ (5%) difference in maximum real and imaginary impedance values. An SEM image of the interface after the 38 hour experiment is shown in Figure 6.3(b) and reveals that $FeCO_3$ has just started to precipitate (darker grey areas on the BSE image). Approximate steel penetration at the end of the stage 1 experiment was 50 µm from cross-section analysis. For all cross-sectional images the steel penetration is measured as the perpendicular distance from the highest point where Fe_3C is visible (thin grey lamellae structures) to the deepest point where ferrite (light grey/white area) has been visibly removed. The measurements are taken from images at multiple different magnifications to ensure consistency over the full surface and that the measurement is correctly aligned with the original surface plane. The corresponding penetration based on mass loss measurement for the same experiment was 47.29 µm.

(a)

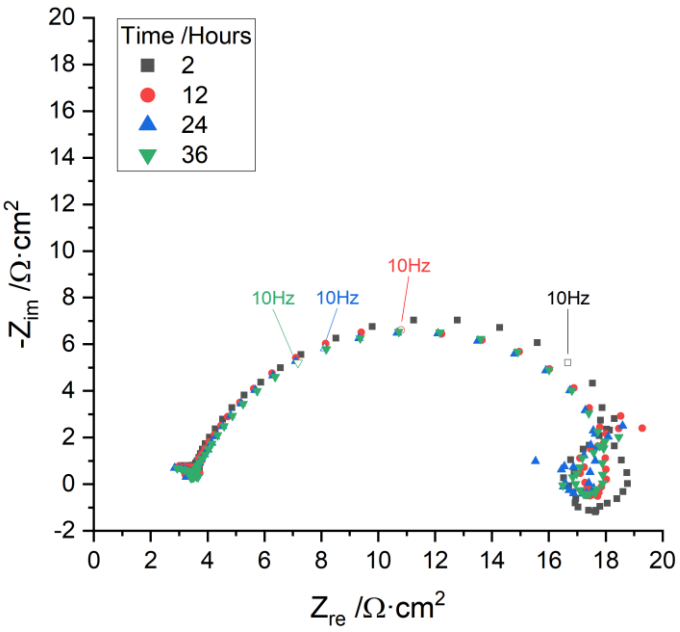

(b)

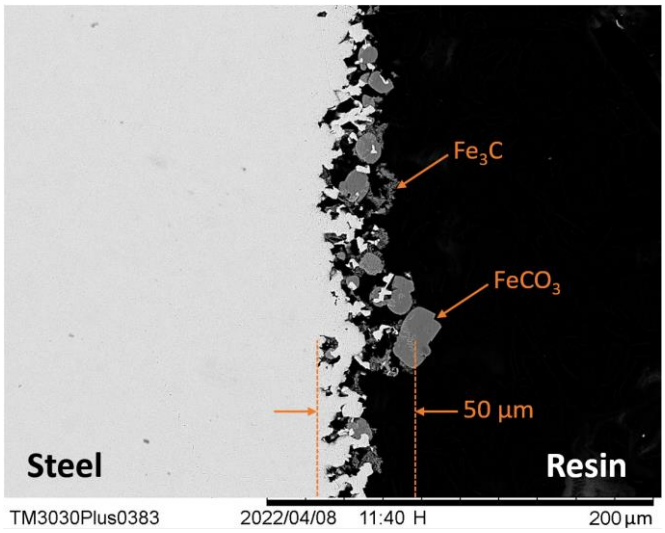

Figure 6.3: Stage 1 of corrosion product development on X65 steel in 30 g·L^{-1} NaCl CO_2 solution at 80 °C, 5.5 bar pCO_2 and 10.5 cm^2·L^{-1} A/V (a) Nyquist plot of impedance response (b) 500x magnification SEM image of the X65 steel interface after 38 hours of exposure

6.3.2 Stage 2 – Linear Decrease in R_p^{-1} (44 h to 68 h)

After around 44 hours of the experiment (t_1 shown in Figure 6.1) R_p^{-1} drops noticeably, observing a linear decrease between 58 and 68 hours (t_2 and t_3 in Figure 6.1). Concurrently, OCP starts to dip at t_1 reaching a minimum at 58 hours (t_2). Nyquist plots of the second stage show the development of a second characteristic loop with the inductive behaviour still noticeable. During this period the magnitude of the impedance grows substantially. Bode plots of stage 2 show that the characteristic frequency of the high frequency loop begins to increase having initially fallen during the first stage.

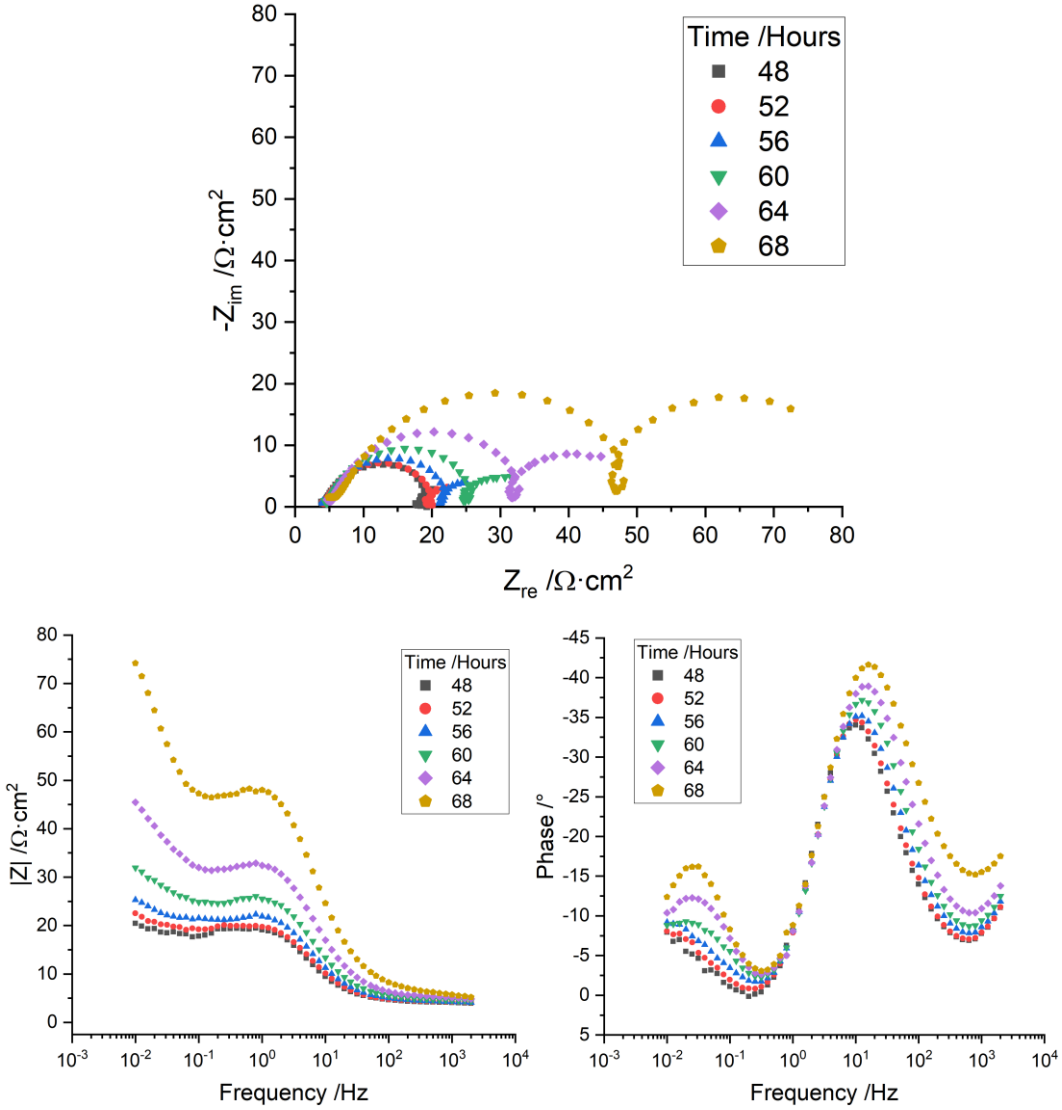

Figure 6.4: Nyquist and bode plots of impedance response from X65 carbon steel in 30 g·L^{-1} NaCl CO_2 solution at 80 °C, 5.5 bar pCO_2 and 10.5 cm^2·L^{-1} A/V ratio between 48 and 68 hours

6.3.2.1 *Ex situ* Analysis of Stage 2

A separate experiment that was terminated during Stage 2 after approximately 60 hours is presented in Figure 6.5 to assess how the interface was evolving. The Nyquist plots from this experiment again show excellent agreement with the data from the initial experiment at this stage. An SEM image of the interface after the 60 hour experiment is shown in Figure 6.5(b). At this stage total penetration of the steel has increased to around 76 µm and significant $FeCO_3$ has precipitated within the Fe_3C structure. Noticeably however, there are large gaps between the $FeCO_3$ layer and the steel substrate.

(a)

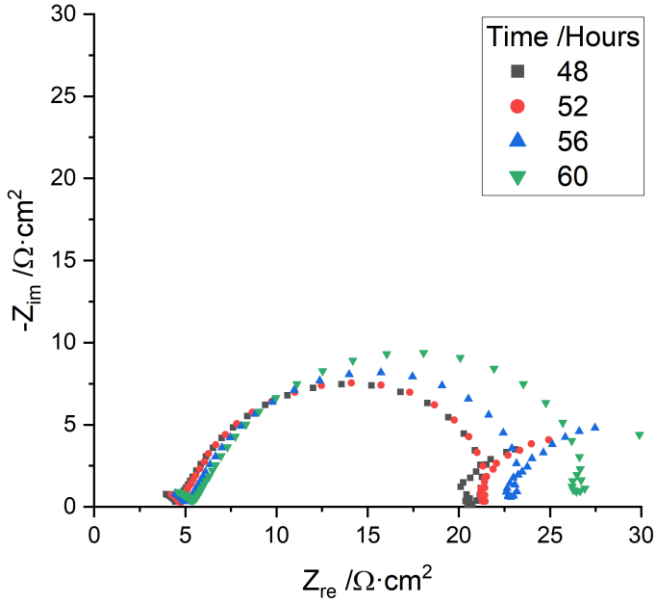

(b)

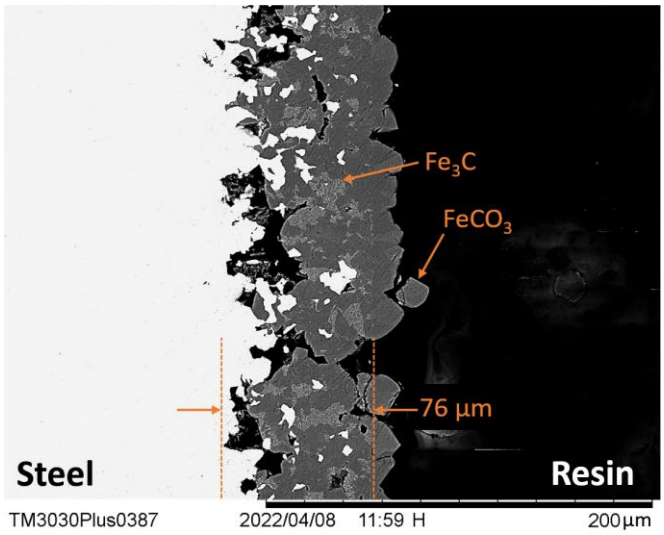

Figure 6.5: Stage 2 of corrosion product development on X65 steel in 30 g·L^{-1} NaCl CO_2 solution at 80 °C, 5.5 bar pCO_2 and 10.5 cm^2·L^{-1} A/V (a) Nyquist plot of impedance response (b) 500x magnification SEM image of the X65 steel interface after 60 hours of exposure

6.3.3 Stage 3 – Logarithmic Decrease in R_p^{-1} (68 h to 85 h)

After around 68 hours of the experiment (t_3 shown in Figure 6.1) the decrease in R_p^{-1} transitions from a linear trend to logarithmic whilst OCP rapidly increases from -632 mV to -540 mV vs Ag/AgCl. At around 78 hours (t_4 in Figure 6.1) there is a secondary transition in the trend of decreasing R_p^{-1}. OCP rises dramatically throughout this time period until both OCP and R_p^{-1} appear to stabilise around 85 hours. The Nyquist plot in Figure 6.6 shows how the impedance response changes in conjunction with the observations of the LPR and OCP data.

The inset plot focuses on the impedance response between 68 and 78 hours (t_3 to t_4) due to the large change in impedance. At 78 hours the transition in R_p^{-1} coincides with the disappearance of the inductive loop followed by a dramatic increase in the magnitude of the impedance.

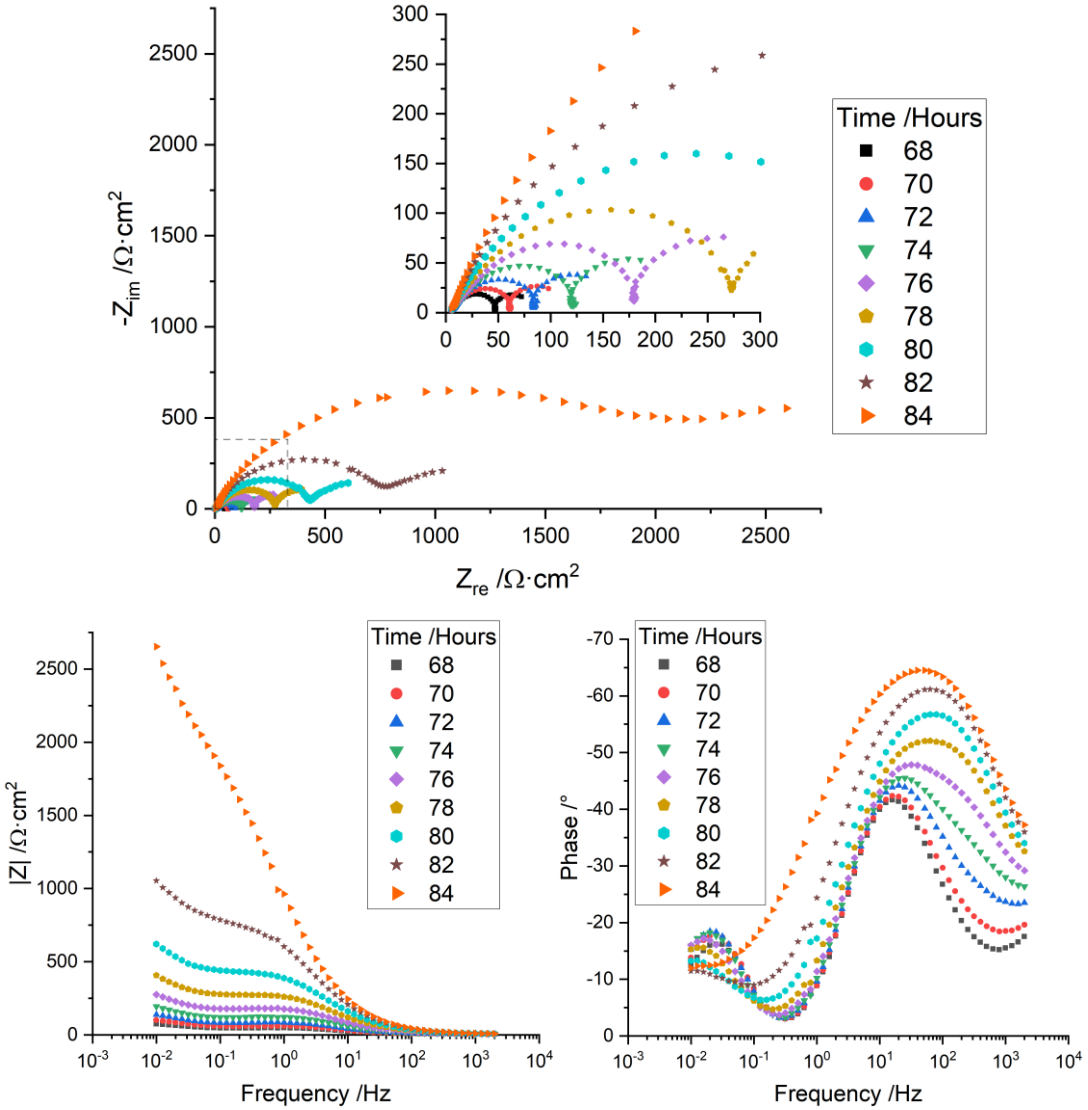

Figure 6.6: Nyquist and Bode plots of impedance response from X65 carbon steel in 30 g·L^{-1} NaCl CO_2 solution at 80 °C, 5.5 bar pCO_2 and 10.5 cm^2·L^{-1} A/V ratio between 68 and 84 hours

6.3.3.1 *Ex situ* Analysis of Stage 3

A separate experiment that was terminated during Stage 3 after approximately 74 hours is presented in Figure 6.7 to assess how the interface was evolving. The Nyquist plots in this instance show the film development was marginally more advanced when compared to the original experiment and more comparable to the 78 hour data.

An SEM image of the interface after the 74 hour experiment is shown in Figure 6.7(b). At this stage total penetration of the steel has increased to around 92 µm and the $FeCO_3$ layer has grown further down in to the Fe_3C matrix leaving smaller but still visible voids at the interface to the steel. Other larger voids exist throughout the layer indicating significant porosity may still exist.

(a)

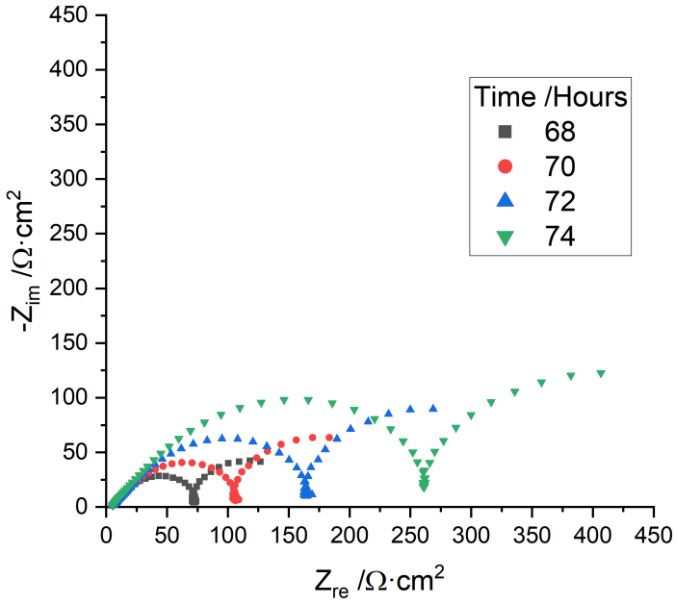

(b)

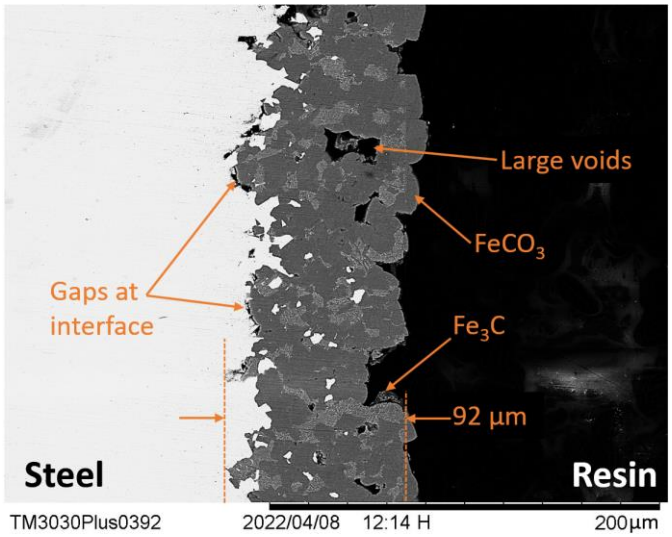

Figure 6.7: Stage 3 of corrosion product development on X65 steel in 30 $g \cdot L^{-1}$ NaCl CO_2 solution at 80 °C, 5.5 bar pCO_2 and 10.5 $cm^2 \cdot L^{-1}$ A/V (a) Nyquist plot of impedance response (b) 500x magnification SEM image of the X65 steel interface after 74 hours of exposure

6.3.4 Stage 4 – OCP and R_p^{-1} Stabilisation (85 h to 112 h)

At 85 hours (t_5 in Figure 6.1) the OCP and R_p^{-1} plateau simultaneously suggesting the system has reached a steady state. The Nyquist plot in Figure 6.8 shows how the first and second time constants become indistinguishable.

A Bode plot of the imaginary component of impedance during the final stage of the corrosion layer evolution is provided in Figure 6.9 to clarify the position of the peak frequency.

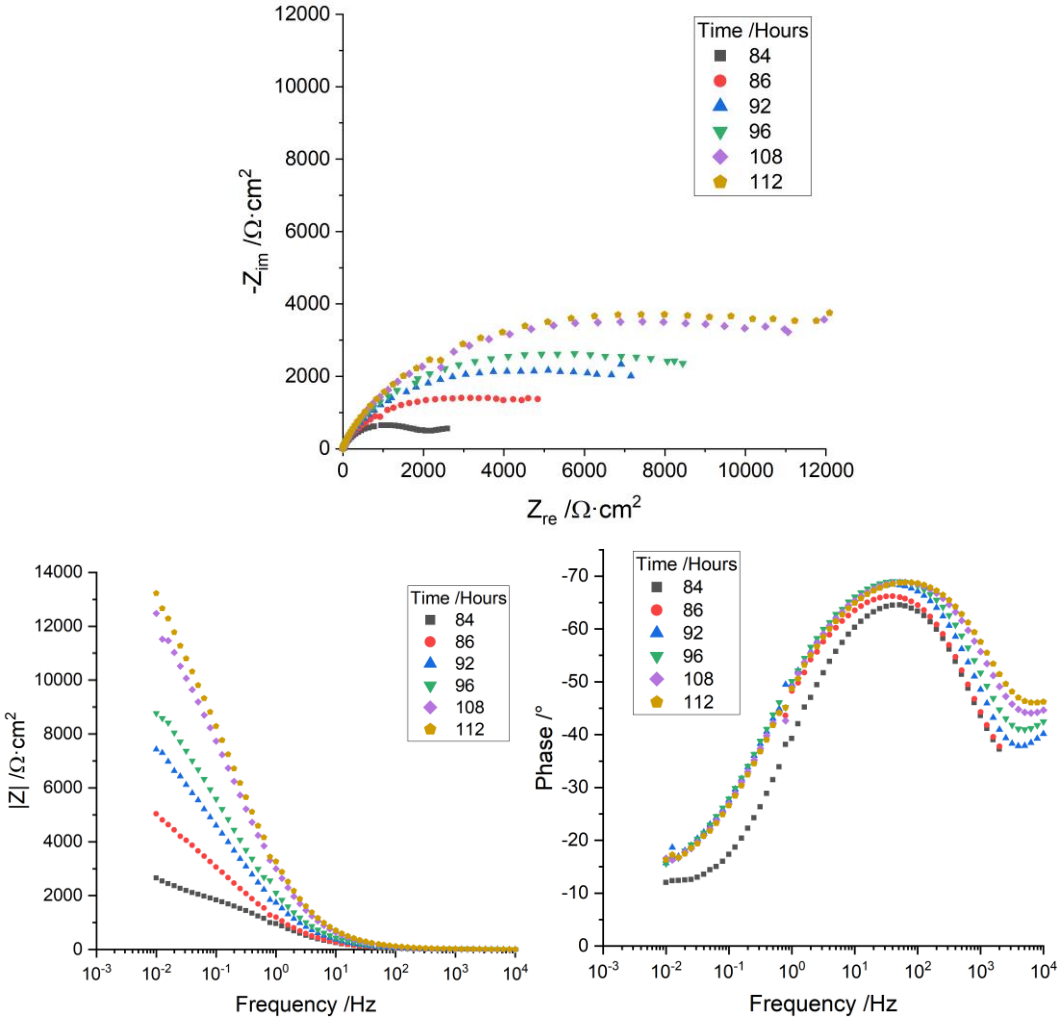

Figure 6.8: Nyquist and Bode plots of impedance response from X65 carbon steel in 30 g·L^{-1} NaCl CO_2 solution at 80 °C, 5.5 bar pCO_2 and 10.5 cm^2·L^{-1} A/V ratio between 84 and 112 hours

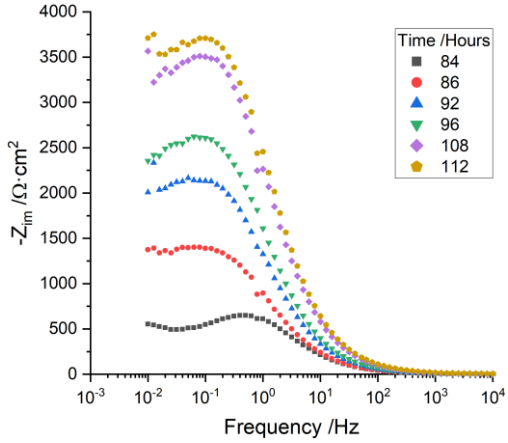

Figure 6.9: Bode plot of -Z_{im} for X65 steel in 30 g·L^{-1} NaCl CO_2 solution at 80 °C, 5.5 bar pCO_2 and 10.5 cm^2·L^{-1} A/V ratio between 84 and 112 hours

6.3.4.1 *Ex situ* Analysis of Stage 4

A cross-section through the film that had formed after 112 hours of exposure is shown in Figure 6.10. At this stage the maximum penetration of the steel is between 100 and 105 µm. Gaps between the substrate and the $FeCO_3$ have largely been filled but significant porosity still exists in the layer which has grown almost entirely within the Fe_3C matrix.

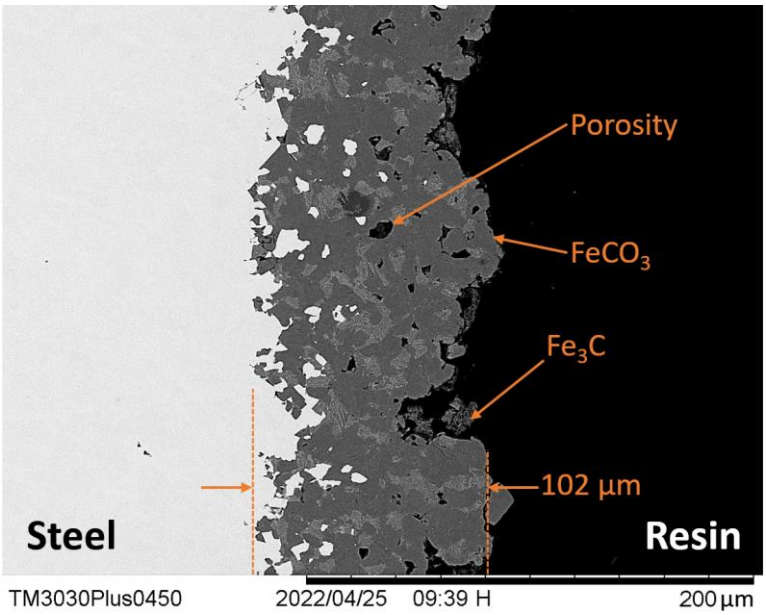

Figure 6.10: Stage 4 of corrosion product development on X65 steel in 30 g·L^{-1} NaCl CO_2 solution at 80 °C, 5.5 bar pCO_2 and 10.5 cm^2·L^{-1} A/V: 500x magnification SEM image of the X65 steel interface after 112 hours of exposure

6.4 Error Analysis on Raw Impedance Data

As part of the EIS data fitting approach described earlier Section 2.8.5.4 and Figure 2.16, the raw impedance data was first assessed for compliance with the rules of Kramer-Kronig (KK) to identify potentially erroneous measurements. A sample of data was analysed using a KK analysis built into a commercial EIS software (EChem Analyst) which implements the methodology outlined by Boukamp [151]. The results of KK analysis are provided in Figure 6.11(a) which highlights some distinctly erroneous data points in the high frequency region leading to a goodness of fit χ^2 of 0.04 for the KK model. After removal of high frequency noise χ^2 decreased to 1.95x10^{-5} with the resulting residual plot provided in Figure 6.11(b). High frequency noise was evident across a majority of the data sets and was subsequently removed.

In the mid and lower frequency regions some data points were retained despite falling slightly outside of the usually acceptable limits of KK analysis (>5% error). Data at these frequencies was only removed if significantly out of trend with surrounding measurements due to the limited number of data points in these regions for fitting.

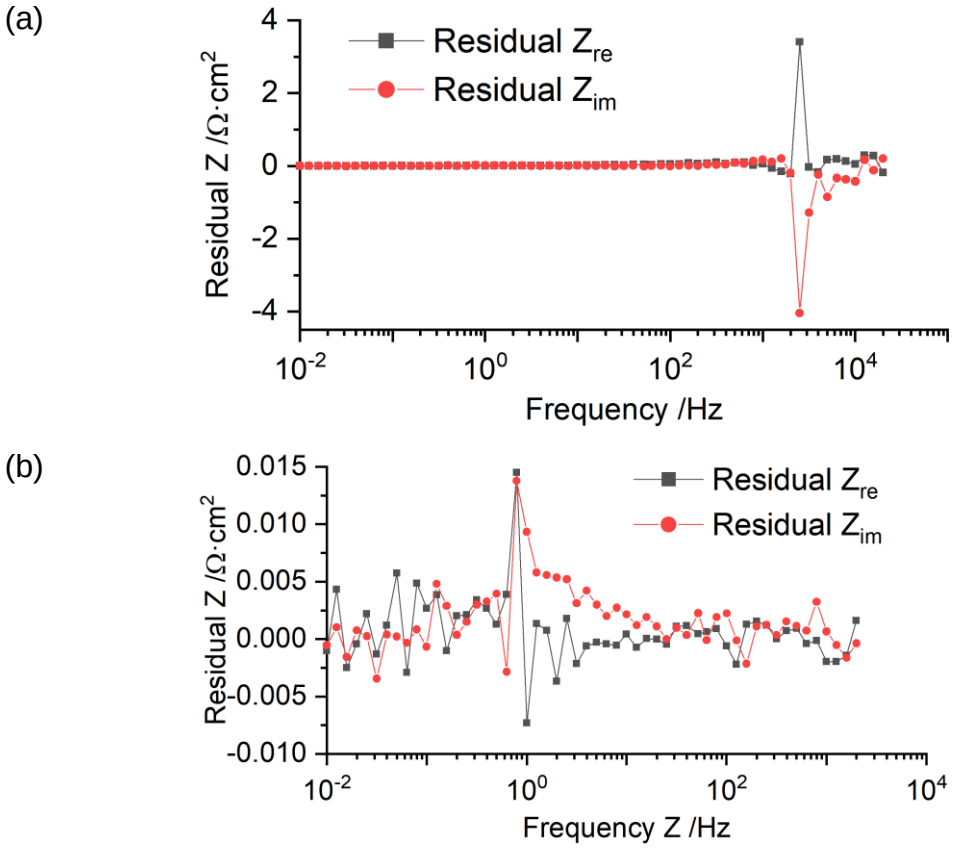

Figure 6.11: Example KK residual analysis of 74 hour data (a) analysis of raw data (b) analysis after high frequency noise removal

6.5 Extraction of Impedance Properties - Kinetics

Having broken down the impedance data into key stages, a number of properties can be estimated directly from Nyquist and Bode plots at each stage depending on the type of response observed. The parameters obtained are subsequently used as initialisation values for regression analysis to selected equivalent circuit models. This first section looks at the impedance response associated with charge-transfer kinetics.

6.5.1 Characteristic Frequency

In the high frequency region of the Nyquist plots is a depressed capacitive loop associated with the electrical double layer capacitance (C_{dl}) and charge transfer resistance (R_{ct}).

An important parameter in estimating the value of double layer capacitance is the characteristic frequency. The characteristic frequency (ω_c) is located at the minima of Z_{im} (maxima of $-Z_{im}$) for the high frequency loop. ω_c is most readily extracted from a Bode plot of frequency against $-Z_{im}$ as highlighted in Figure 6.12.

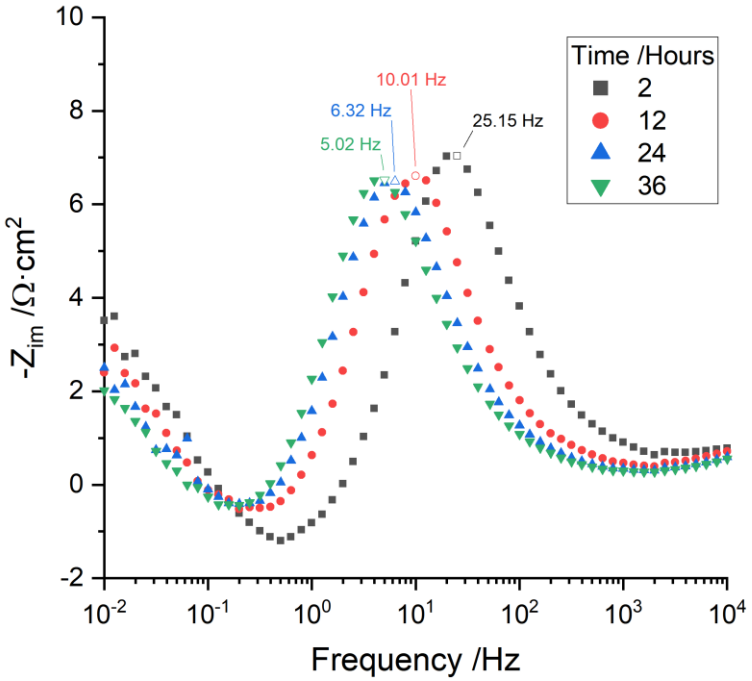

Figure 6.12: Characteristic 'peak' frequency at different time intervals from Stage 1 of corrosion product development on X65 steel in 30 g·L^{-1} NaCl CO_2 solution at 80 °C, 5.5 bar pCO_2 and 10.5 cm^2·L^{-1} A/V ratio

6.5.2 CPE Verification

A depressed semi-circle on a Nyquist plot (as shown in Figure 6.2 and Figure 6.3) is often immediately attributed to constant phase element (CPE) behaviour, but this can be a misnomer. To satisfy the definition of a true CPE, the ohmic-resistance corrected Bode plot of phase angle should be constant in the high frequency region and tend towards a phase angle of <90°, while the change in impedance modulus should be linear in the same frequency range. These attributes distinguish the shape of the impedance response from other effects such as diffusion or multiple relaxation process with similar time constants [58]. Due to significant noise in the high frequency region only the final two measurements from the Stage 1 experiment could be reliably analysed but both provided excellent agreement with the constraints of CPE behaviour.

The ohmic-resistance corrected Bode plot of phase angle for the measurements is shown in Figure 6.13. The correction was performed by subtracting the value of R_e (measured from the Nyquist plot) from the value of Z_{re} used in the calculation of phase angle.

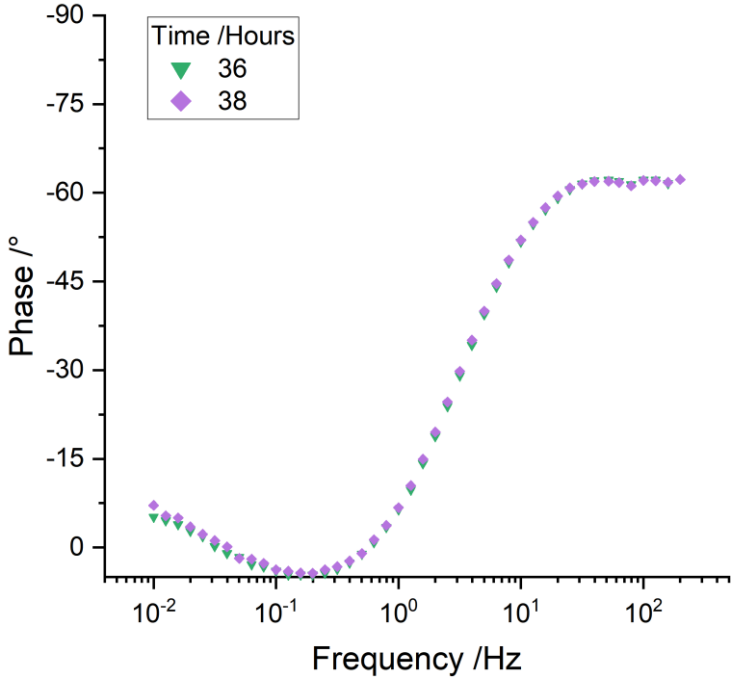

Figure 6.13: Ohmic-resistance corrected Bode plot of impedance phase angle from stage 1 experiment of corrosion product development on X65 carbon steel in 30 g·L^{-1} NaCl CO_2 solution at 80 °C, 5.5 bar pCO_2 and 10.5 cm^2·L^{-1} A/V ratio

Having established the use of a CPE to model the charge-transfer response, an initial estimate of the model parameters can be obtained using the 3 points on a circle approach. In a simplified Randle's circuit analogy, the electrolyte resistance (R_e) is measured where the semi-circle meets the real axis in the high frequency range (effectively infinite frequency resistance R_∞). The charge transfer resistance (R_{ct}) is measured as the distance between the high and low frequency (ω_∞ and ω_0) real axis intercepts as illustrated in Figure 6.14. The effect of time constant dispersion due to surface heterogeneity depresses the semicircle so that its centroid is shifted below the x axis whilst the arc of the circle still intersects the x axis when $Z_{re} = R_e$ and $Z_{re} = R_e+R_{ct}$ as depicted in Figure 6.14. A simple way to obtain a 'first guess' of R_{ct} is to take the imaginary impedance at the characteristic frequency and double it, giving a reasonable value of resistance when α is close to 1.

When the loop is considerably depressed a more robust method for extracting the resistance is to pick 3 points along the arc of the Nyquist data as described by Basoukov and Macdonald [152] which defines the properties of a circle as shown in Figure 6.15.

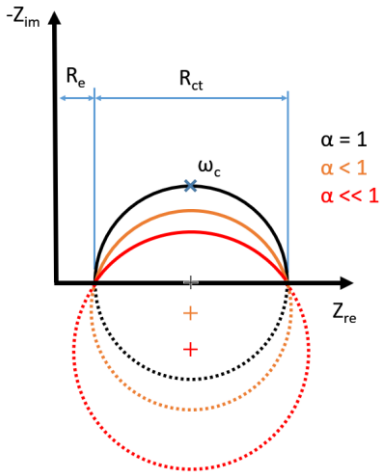

Figure 6.14: Effect of time constant dispersion on apparent semi-circle depression in a Nyquist plot for a simplified Randle's circuit

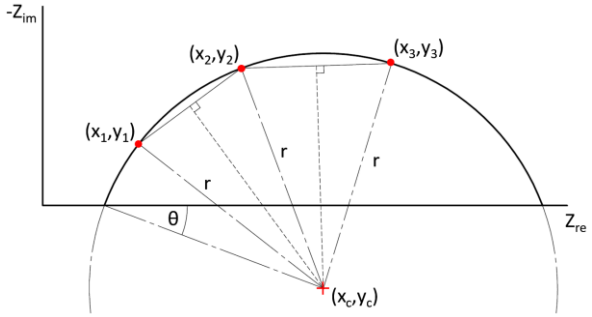

Figure 6.15: Circumscribed circle from 3 points as a method to obtain impedance parameters

An example method for computing the centroid coordinates and radius of a circle through 3 points is provided:

$$x_c = \frac{d \cdot e - b \cdot f}{g} \tag{6.1}$$

$$y_c = \frac{a \cdot f - c \cdot e}{g} \tag{6.2}$$

$$r = \sqrt{(x_1 - x_c)^2 + (y_1 - y_c)^2} \tag{6.3}$$

Where:

$$a = x_2 - x_1; b = y_2 - y_1; c = x_3 - x_1; d = y_3 - y_1$$

$$e = a(x_1 + x_2) + b(y_1 + y_2); \quad f = c(x_1 + x_3) + d(y_1 + y_3)$$

$$g = 2\big(a(y_3 - y_2) - b(x_3 - x_2)\big)$$

With centroid coordinates and radius calculated the depression angle θ (in radians) shown in Figure 6.15 can also be obtained:

$$\theta = \sin^{-1}\left(\frac{y_c}{r}\right) /\text{rads} \tag{6.4}$$

Using this angle the resistances can be approximated as follows:

$$R_e = x_c - r\cos\theta \tag{6.5}$$

$$R_{ct} = 2r\cos\theta \tag{6.6}$$

The fractional exponent (α) can also be estimated using the depression angle using the following relationship [152]:

$$\alpha = 1 - \frac{2\theta}{\pi} \tag{6.7}$$

With α and R_{ct} estimated the values can be entered into the equation for Q_{dl} knowing that at the characteristic frequency (ω_c):

$$Q_{dl} = \frac{1}{\omega_c{}^{\alpha} R_{ct}} \tag{6.8}$$

An example fit using only the initial guess parameters described above and no additional regression is shown in Figure 6.16. It is important to note here that a visually good fit can be obtained on a Nyquist plot without a good estimate of Q_{dl} as the capacitance in this case does not change the shape of the Nyquist plot. Q_{dl} is also highly sensitive to the estimated value of the characteristic frequency. Low resolution of data points around the characteristic frequency will therefore affect the initial estimate of Q_{dl} but still provide an excellent initial guess for regression.

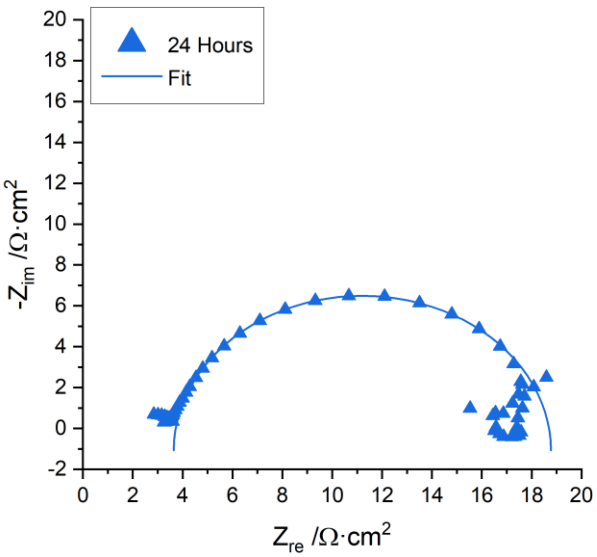

Figure 6.16: Use of 3 points on a circle approach to fit impedance data

6.5.3 Effective Capacitance

In order to relate CPE parameters α and Q to actual physical properties such as active surface area, an effective capacitance needs to be established. The approach to obtaining an effective capacitance depends on the type of time constant dispersion observed. The formula of Brug et al. [153] has largely been applied to systems with apparent surface distributed properties to establish double layer capacitance and factors in the contribution of ohmic resistance to the observed behaviour [58]:

$$C_{dl,surf} = {Q_{dl}}^{1/\alpha} \left(\frac{R_e R_{ct}}{R_e + R_{ct}} \right)^{(1-\alpha)/\alpha} \quad (6.9)$$

Where $C_{dl,surf}$ distinguishes that the effective double layer capacitance is valid when the time constant is surface distributed.

6.5.4 Active Surface Area and Faradaic Time Constant

As the corrosion process proceeds the physical surface area available for the anodic reaction changes. The active surface area can be estimated from the ratio of the effective double layer capacitance at the beginning of the experiment to that determined at time t:

$$\%S_a(t) = \frac{C_{dl}(t)}{C_{dl}(0)} \times 100 \quad (6.10)$$

This relationship assumes that any change in C_{dl} is caused directly by changes in effective area and not due to other factors such as local chemistry. It has been shown previously that decreasing active surface area decreases double layer capacitance (C_{dl}) and proportionally increases charge transfer resistance R_{ct} [51, 154]. The time constant associated with faradaic process $\tau_f = R_{ct} \cdot C_{dl}$ should therefore remain constant while the impedance is controlled by active surface area. When τ_f starts to change it could be an indication that the mechanism controlling the system is also changing.

6.5.5 Adsorption

Up to 78 hours into the experiment an ‘inductive’ loop is evident in the lower frequency region between 0.1 and 1 Hz. Previous work in similar fields [66, 138-150] has attributed this phenomenon to the adsorption of intermediary Iron(II) Hydroxide ($FeOH_{ads}$) at the electrode surface as originally described by Bockris et al. [42] in their mechanism for anodic dissolution of iron in strong acids.

Within the field of steel corrosion in CO_2 environments this feature of the impedance response has only been evidenced at elevated pCO_2 and/or lower pH [147-150], coinciding with the observations of Nešić et al. [43] that the Bockris mechanism may not apply to CO_2 systems at pH > 5. Due to the controversial nature of the 'inductive' property a quantitative evaluation is not attempted in this work other than for the purpose of equivalent circuit fitting. Initialisation values for the inductor (L_{ads}) use the characteristic frequency (ω_L) taken at the peak value of the loop and resistance (R_{ads}) based on the height of the loop as depicted in Figure 6.17.The estimated value of R_{ads} is then used to obtain an initial estimate of L_{ads} using the following expression:

$$L_{ads.estimate} = \frac{R_{ads.estimate}}{\omega_L} \tag{6.11}$$

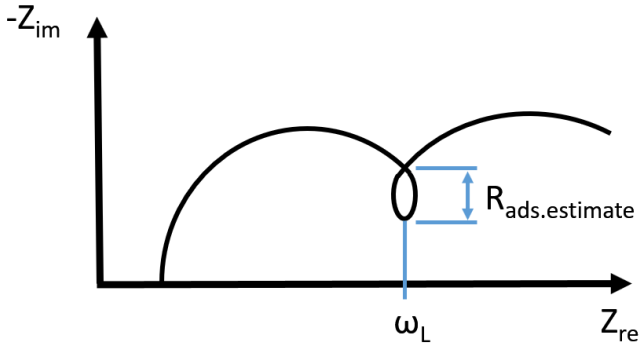

Figure 6.17: Method of extracting initial estimates for adsorption loop

6.5.6 Film Capacitance

The capacitance of a solid film can be calculated based on the relative permittivity, surface area and film thickness.

$$C_{film} = \frac{\varepsilon_0 \varepsilon \cdot A}{\delta_f} \tag{6.12}$$

Where ε_0 is the relative permittivity of a vacuum (8.85×10^{-12} F·m^{-1}), ε is the permittivity of the film material (i.e. 9.3 for Siderite) A is electrode area and δ_f is film thickness. This is typically relevant for thin highly stable films such as oxide layers on passive materials or for coatings. In this work the corrosion layer that eventually forms is evidently highly porous with the impedance response controlled by slow diffusion (mass transport) of reactants through the thick layer that forms. De Motte et al. [51] showed previously that the capacitance associated with permittivity of $FeCO_3$ for a similar corrosion product layer (20 μm thick) is 0.4 nF·cm^{-2}, orders of magnitude smaller than the characteristic response of the double layer and mass transport processes.

6.6 Extraction of Impedance Properties - Diffusion

6.6.1 Impedance Due to Diffusive Mass Transport

The transport of species between an electrode and electrolyte occurs in response to a potential gradient (migration), concentration gradient (diffusion) or a pressure gradient (convection) [155]. Convection in the current case is negligible as the system is hydrodynamically stagnant. When a layer forms on the surface of the electrode it acts as a diffusion barrier which behaves according to one of the following properties:

- Electroactive species exchange occurs with bulk electrolyte (transmissive boundary)
- Electroactive species exchange does not occur with bulk electrolyte (reflective boundary)

In the first case diffusion models are developed by neglecting convection and migration terms. The diffusion process in the bulk is also assumed to be negligible [58] which leads to Fick's second law:

$$\frac{\partial c_i}{\partial t} - D_i \frac{\partial^2 c_i}{\partial y^2} = 0 \tag{6.13}$$

Where c_i is the concentration of the i^{th} species and D_i the corresponding diffusion coefficient, t is time and y is an axial position variable.

Under steady-state conditions and at bounds of:

$$\bar{c}_i = \bar{c}_i(0) \text{ at } y = 0 \tag{6.14}$$

$$\bar{c}_i = \bar{c}_i(\infty) \text{ at } y = \delta_f \tag{6.15}$$

The concentration gradient becomes:

$$\frac{\partial \bar{c}_i}{\partial y} = \frac{\bar{c}_i(\infty) - \bar{c}_i(0)}{\delta_f} \tag{6.16}$$

Where δ_f is the diffusion layer thickness.

Under the assumption that the diffusion coefficients for oxidants (D_O) and reductants (D_R) are equal, the following equation for diffusion impedance in a finite domain has been derived [59]:

$$Z_O = \frac{\sqrt{2}\sigma}{\sqrt{j\omega}} \tanh\left(\sqrt{\frac{j\omega}{D}} \cdot \delta_f\right) \tag{6.17}$$

This is referred to as Finite Length or transmissive boundary diffusion.

σ is the mass transfer coefficient also known as the Warburg coefficient and is defined as Equation (6.18).

$$\sigma = \frac{RT}{n^2F^2\sqrt{2}}\left(\frac{1}{\sqrt{D_O C_O(0)}} + \frac{1}{\sqrt{D_R C_R(0)}}\right) \tag{6.18}$$

Where $C_O(0)$ and $C_R(0)$ are bulk concentrations of oxidants and reactants. Similarly, when electroactive species are not exchanged with the bulk solution the finite space (reflective boundary) formula is derived:

$$Z_S = \frac{\sqrt{2}\sigma}{\sqrt{j\omega}}\coth\left(\sqrt{\frac{j\omega}{D}}\cdot\delta_f\right) \tag{6.19}$$

A special case referred to as semi-infinite or simply as a Warburg impedance occurs when layer thickness approaches an infinite domain:

$$Z_W = \frac{\sigma}{\sqrt{\omega}}(1-j) \tag{6.20}$$

The Nyquist plot in Figure 6.18 illustrates the typical responses for the three types of Warburg boundary condition when integrated in to a standard Randle's circuit.

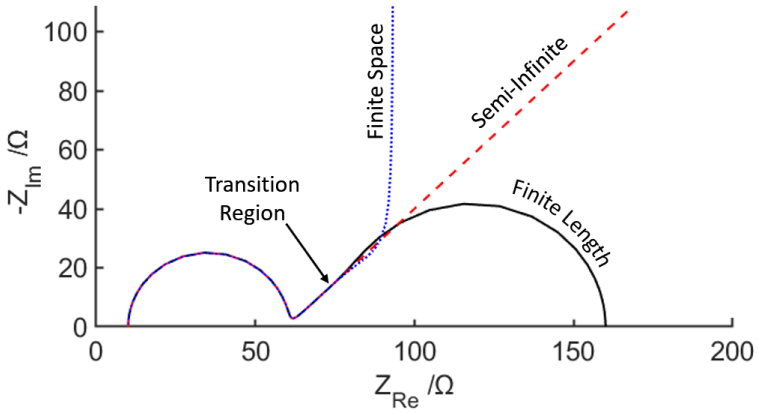

Figure 6.18: Types of Warburg impedance and transition region on a Nyquist plot adapted from [156]

6.6.1.1 Generalised (Fractal) Warburg Element

In practice the above equations may not accurately represent the physical system due to non-uniform diffusion and the existence of multiple transport pathways [59, 152, 157]. The generalised (fractal) Warburg model was devised applying distributive effects of a Constant Phase Element (CPE) to that of diffusion. For a transmissive boundary with dispersion:

$$Z_{O_G} = \frac{\sqrt{2}\sigma\delta_f}{\sqrt{D}\left(\sqrt{\frac{j\omega}{D}}\cdot\delta_f\right)^{\phi_W}}\tanh\left(\sqrt{\frac{j\omega}{D}}\cdot\delta_f\right)^{\phi_W} \tag{6.21}$$

Where ϕ_W is the exponent ≤ 1 comparable to α in a CPE.

Based on impedance response and SEM images of the current system, the low frequency relaxation process that materialises clearly after the first 48 hours is attributed to transmissive diffusion effects. A rearranged version of the finite length model has been presented by Nguyen and Breitkopf [156] as:

$$Z_O = \frac{R_W}{\sqrt{j\omega\tau_D}} \tanh\left(\sqrt{j\omega\tau_D}\right) \tag{6.22}$$

Where R_W is the limiting diffusion resistance as a function of the concentration of mobility and τ_D is the diffusion time constant:

$$\tau_D = \frac{{\delta_f}^2}{D} \tag{6.23}$$

By combining equation (6.21) and (6.23) the following expression is derived for transmissive diffusion with dispersion as a function of time constant [157]:

$$Z_{O_G} = \frac{R_W}{\left(\sqrt{j\omega\tau_D}\right)^{\phi_W}} \tanh\left(\sqrt{j\omega\tau_D}\right)^{\phi_W} \tag{6.24}$$

The value of τ_D can be estimated from the local minima of the imaginary impedance against frequency (f_{min}) according to the following expression derived by Cruz-Manzo and Greenwood [158]:

$$f_{min} = \frac{2.54}{2 \cdot \pi \cdot \tau_D} \tag{6.25}$$

Where f_{min} is in units of Hz. The finite length Warburg resistance (R_w) can be estimated following the three points on a circle procedure outlined previously to provide an initial estimate for regression.

6.7 Impedance Models and Equivalent Circuits

For the first 78 hours of the experiment there is evidence of three distinct time constants. The first is the high frequency capacitive loop associated with faradaic charge transfer. The second is the inductive behaviour that has previously been attributed to an adsorption process. The third relaxation process, most clearly evident after the first 48 hours is attributed to transmissive mass transport diffusion. The system is modelled using a Randle's circuit with a generalised finite length Warburg diffusion element and a parallel combination of an inductor and resistor to model the adsorption profile. The resulting impedance formula is given in Equation (6.26) with the equivalent circuit provided in Figure 6.19(a).

$$Z = R_e + \frac{1}{\left(R_{ct} + \left(R_{ads}{}^{-1} + L_{ads}{}^{-1}\right)^{-1} + Z_{O_G}\right)^{-1} + (j\omega)^{\alpha} Q_{dl}} \quad (6.26)$$

After 78 hours the inductive loop is no longer evident and is therefore removed from the model giving Equation (6.27) and circuit model Figure 6.19(b).

$$Z = R_e + \frac{1}{\left(R_{ct} + Z_{O_G}\right)^{-1} + (j\omega)^{\alpha} Q_{dl}} \quad (6.27)$$

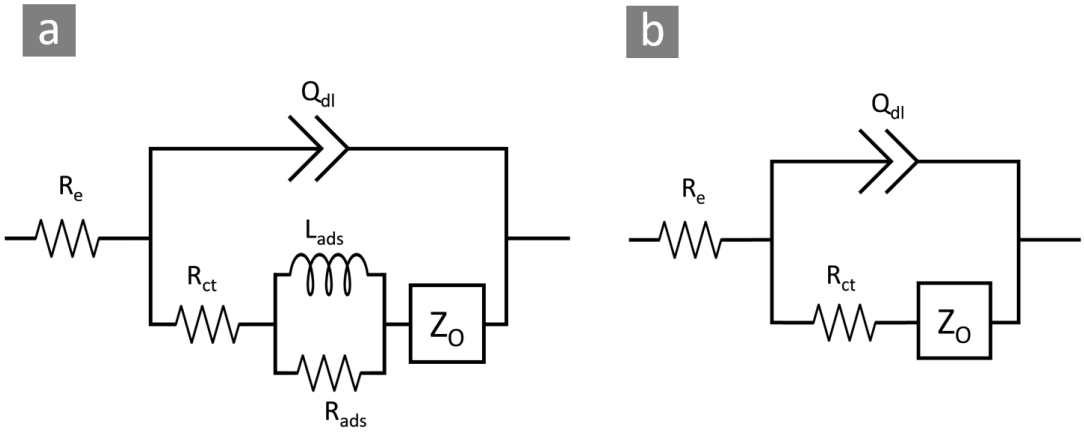

Figure 6.19: Equivalent circuit models used to fit impedance data from X65 carbon steel in 30 g·L^{-1} NaCl CO_2 solution at 80 °C, 5.5 bar pCO_2 and 10.5 cm^2·L^{-1} A/V ratio (a) First 78 hours while inductive behaviour is present (b) At late stages when system is dominated by mass transport diffusion

6.8 Non-linear Regression Fitting

Regression analysis was performed using MATLAB with impedance expressions coded using the symbolic math toolbox. Initial parameter estimates were obtained using graphical selection as described in the previous section and compiled in to an initialisation vector. The circuit model expression was converted to a MATLAB function and fitted to the real and imaginary impedance data using a non-linear least squares curve fitting routine (Lsqcurvefit) within the optimization toolbox. Lsqcurvefit is a numerical minimisation routine with two in-built solver algorithms, Trust-Region-Reflective (TRR) and Levenberg-Marquardt (LM). Both algorithms provided comparable fits however TRR was preferred due to the ability to apply boundary conditions on model parameters such as dispersion exponents. The fitting routine is highly sensitive to the initial value of each parameter meaning it is imperative to have a reasonable first guess for each component.

Where data was too noisy or difficult to interpret using the methods outlined in Sections 6.4 and 6.6, the initial guess was based on the previous fit.

6.8.1 Example Fits

Example impedance fits from the different stages of corrosion product development are shown in Figure 6.20 and Figure 6.21 using the expression given in Equation (6.26) corresponding to the equivalent circuit model in Figure 6.19(a). The Nyquist plot in Figure 6.22 shows impedance fits from the final stage of layer development using the expression in Equation (6.27) and circuit model Figure 6.19(b).

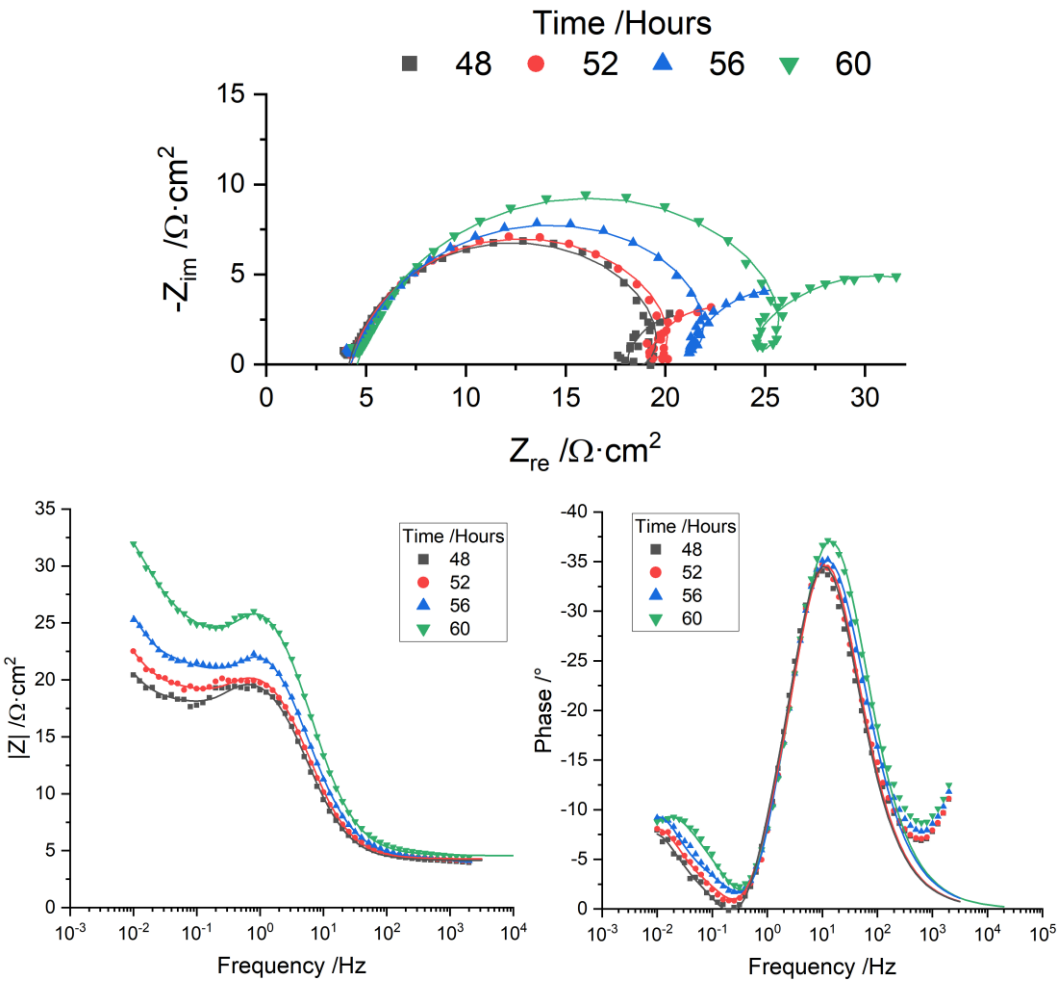

Figure 6.20: Nyquist and Bode plots of impedance fits (shown with solid lines) from Stage 2 of corrosion product development on X65 carbon steel in 30 g·L^{-1} NaCl CO_2 solution at 80 °C, 5.5 bar pCO_2 and 10.5 cm^2·L^{-1} A/V ratio

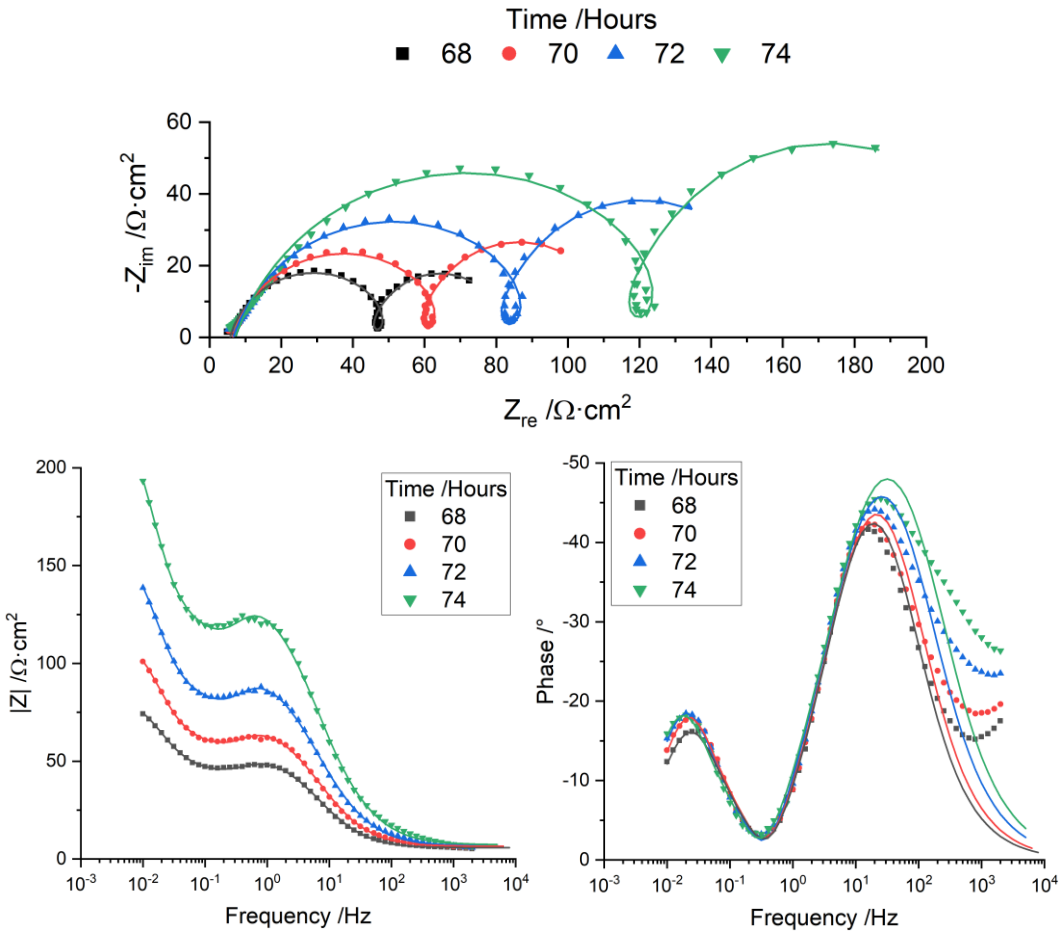

Figure 6.21: Nyquist and Bode plots of impedance fits (shown with solid lines) from Stage 3 of corrosion product development on X65 carbon steel in 30 g·L^{-1} NaCl CO_2 solution at 80 °C, 5.5 bar pCO_2 and 10.5 cm^2·L^{-1} A/V ratio

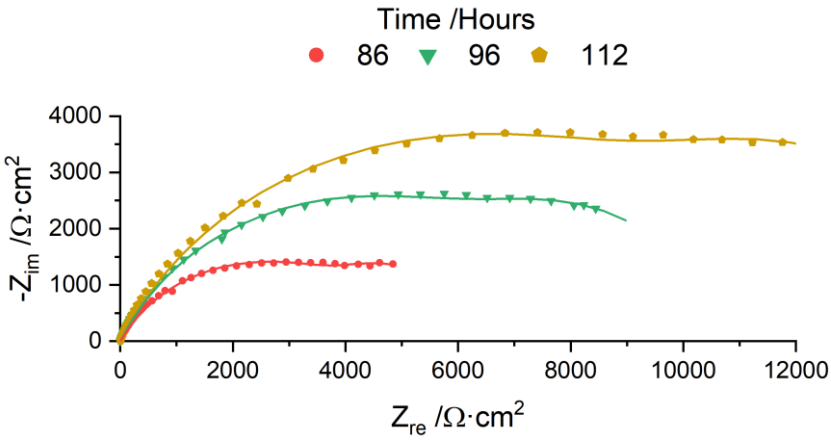

Figure 6.22: Nyquist plot of impedance fits (shown with solid lines) from Stage 4 of corrosion product development on X65 carbon steel in 30 g·L^{-1} NaCl CO_2 solution at 80 °C, 5.5 bar pCO_2 and 10.5 cm^2·L^{-1} A/V ratio

Variations on the selected impedance model have been used extensively for analysing $FeCO_3$ formation with more recent work including the finite length diffusion model [32, 51]. The inclusion of the modified generalised Warburg finite length diffusion element in this work proved insightful as the dispersion exponent ϕ_W generally regressed to a value of 1 when the low frequency loop was fully evident (between 68 and 78 hours). This suggests that the standard finite length model (Equation (6.22)) is a reasonable approximation in this type of system and diffusion is relatively homogeneous at the length scale measured. At the later stages of the experiment data fitting could become highly subjective and a reasonable first guess of the impedance parameters was essential. Plotting of impedance parameters every two hours allows identification of clear outlier fits and a refined first guess of parameters could be employed by extrapolation from a previous fit, this was particularly useful for the low frequency data at the early and late stages of the experiment. Even with refined first guess approximations some fitting parameters are extremely sensitive to the raw data, particularly the diffusion time constant when a dispersion coefficient ϕ_W is employed. In the stage 4 data for example, a reasonable fit could be achieved with a very low value of ϕ_W (~0.25) and subsequently extremely high value of τ_D. For this reason ϕ_W was constrained to a value of 1, effectively reverting to a standard Finite Length Warburg impedance as per Equation (6.22) and in line with the observations at the earlier stages in the experiment. Extending the measurement range to a lower frequency could have improved fitting, however the acquisition time for such low frequency perturbations could introduce inaccuracies due to the transient nature of the system, contravening the KK relations in Section 2.8.5.4.

6.9 Plots of Characteristic Impedance Properties with Time

Plots of regressed impedance parameters as a function of time are presented in this section to illustrate how the system changes as the interface evolves.

6.9.1 Polarisation Resistance

The estimated values of R_{ct} and R_W over time on a linear scale are shown in Figure 6.23. The results suggest that both resistance values start to increase significantly around 68 hours (also t_3 in Figure 6.1). R_{ct} increases at a greater rate than R_W. At around 84 hours (also t_5 in Figure 6.1) the rate of increase in both R_{ct} and R_W changes from an exponential increase to a linear increase.

This suggests a step change in the system or some critical condition has been reached.

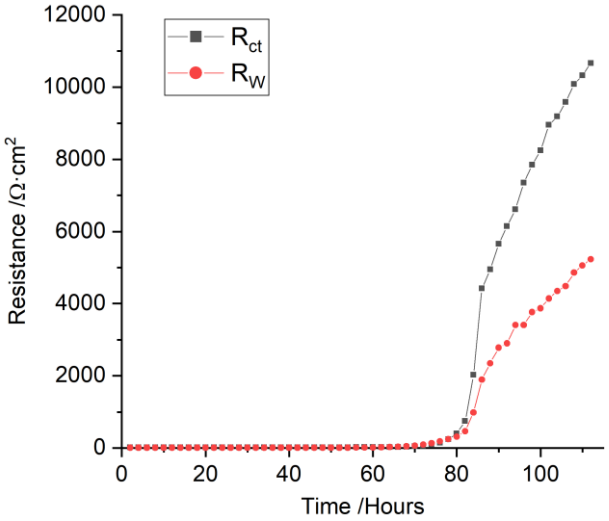

Figure 6.23: Charge-transfer (R_{ct}) and diffusion resistance (R_W) over time obtained from fitted impedance data for X65 steel in 30 g·L^{-1} NaCl CO_2 solution at 80 °C, 5.5 bar pCO_2 and 10.5 cm^2·L^{-1} A/V ratio

To compare the trend with that observed from LPR measurements the reciprocal of the sum of resistances R_e, R_{ct} and R_w was plotted against the reciprocal R_p data from Figure 6.1 and plotted in Figure 6.24. The data shows excellent agreement between the two sources of polarisation resistance particularly in the middle stages of the experiments, this was also the time period with the highest quality of fitting data and well defined time constants.

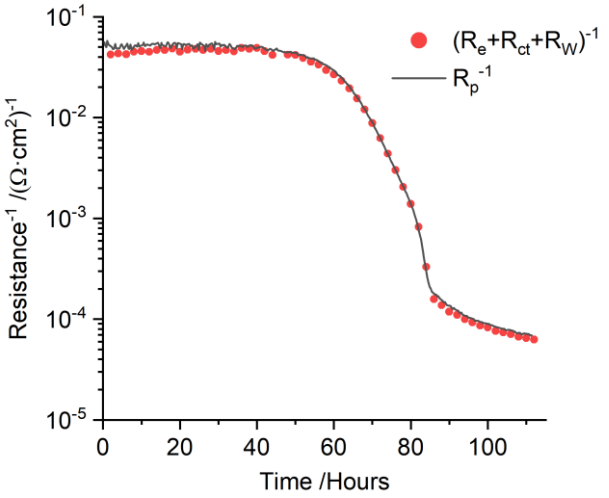

Figure 6.24: Comparison of reciprocal of total polarisation resistance over time based on fitted EIS data (red dots) and LPR measurement (black line) for X65 carbon steel in 30 g·L^{-1} NaCl CO_2 solution at 80 °C, 5.5 bar pCO_2 and 10.5 cm^2·L^{-1} A/V ratio

6.9.2 Double Layer Capacitance and Active Surface Area

The data plotted in Figure 6.25 shows distinct transitions in the estimated double layer capacitance which again correlates with the trends shown in the OCP and LPR response in Figure 6.1. To illustrate this, the time markers from Figure 6.1 (t_1, t_3 and t_5) have been added to Figure 6.25. Up to the first 44-48 hours (t_1) the value of C_{dl} is increasing which can be attributed to changes in active surface area and/or local chemistry [32, 51]. Beyond 48 hours C_{dl} decreases linearly until 68 hours where the trend becomes logarithmic again following the same pattern observed in LPR data. The conversion of C_{dl} to a relative active surface area requires the assumption that C_{dl} is changing due to changes in active area only and not local chemistry or other factors. As previously covered, R_{ct} has been shown to be inversely proportional to active surface area [51, 154] and the time constant $R_{ct}{\cdot}C_{dl}$ should remain stable in an active area controlled regime. In this experiment R_{ct} is shown to be relatively low and stable over the first 48 hours compared with C_{dl} which increases significantly. The result is that $R_{ct}{\cdot}C_{dl}$ changes, this could suggest that the system is not entirely controlled by active surface area. The comparison is shown in the normalised plot in Figure 6.26.

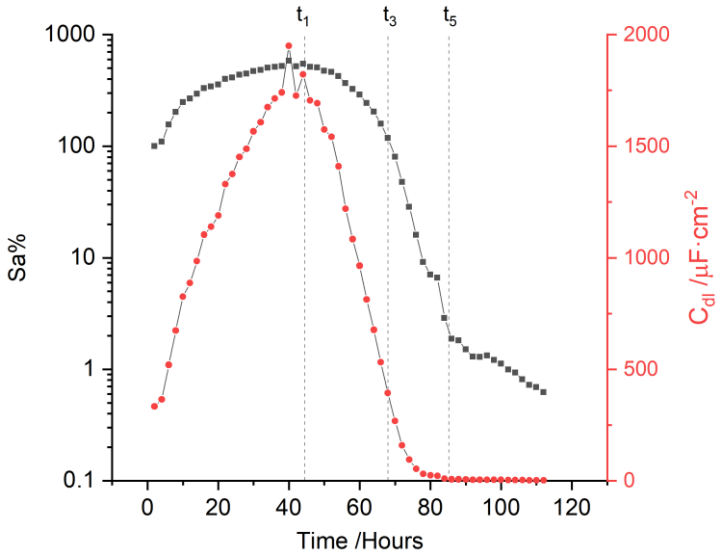

Figure 6.25: Active surface area (black) and double layer capacitance (red) over time obtained from fitted impedance data for X65 carbon steel in 30 $g{\cdot}L^{-1}$ NaCl CO_2 solution at 80 °C, 5.5 bar pCO_2 and 10.5 $cm^2{\cdot}L^{-1}$ A/V ratio

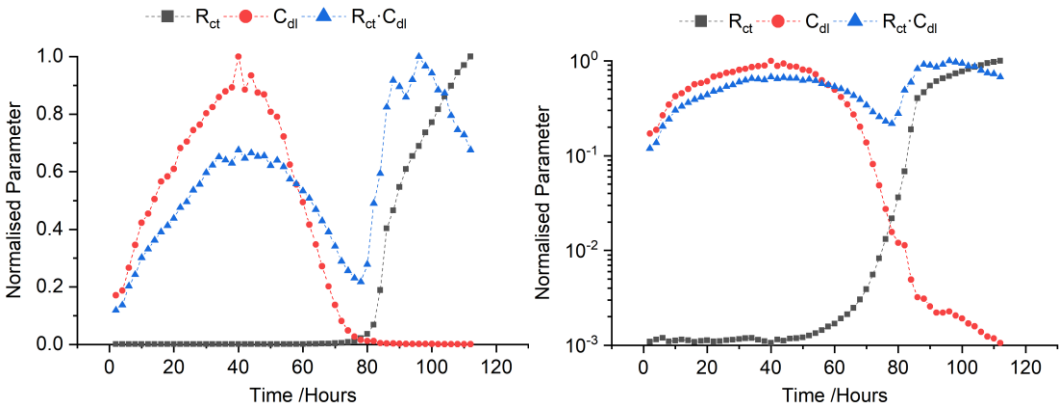

Figure 6.26: Normalised plot of charge transfer parameters over time based on fitted impedance data for X65 carbon steel in 30 g·L^{-1} NaCl CO_2 solution at 80 °C, 5.5 bar pCO_2 and 10.5 cm^2·L^{-1} A/V ratio. Linear scale (left) and $\log_{10}$ scale (right)

6.9.3 Goodness of Fit

The full list of fitted parameters for the first repeat experiment is provided in Table 6.1 at the end of this chapter. The quality of each fit is reported as a sum of weighted residuals using the following equation [159]:

$$\chi^2 = \sum_{i=1}^{N} {w_i}^2 \left(Z_{re_{meas}} - Z_{re_{fit}}\right)^2 + \left(Z_{im_{meas}} - Z_{im_{fit}}\right)^2 \tag{6.28}$$

$$w_i = \left({Z_{re_{meas,i}}}^2 + {Z_{im_{meas,i}}}^2\right)^{-\frac{1}{2}} \tag{6.29}$$

Quantification of error in circuit element values requires a reasonable approximation of stochastic error (as a function of frequency) in the raw measurements. This can be estimated based on the fitted data but the approach has been criticised more recently [58]. Goodness of fit has therefore only been provided to make comparisons between fits at each time interval.

6.10 Chapter 6 Summary

In this chapter a methodology has been devised that implements EIS to extract the fundamental interfacial parameters associated with the faradaic and non-faradaic relaxation processes occurring on carbon steel during the formation of carbonate-based corrosion products at elevated pressure and temperature. This methodology has also elucidated critical stages in the evolution of the metallic interface as the local environment changes due to anodic dissolution followed by precipitation of corrosion products. The next stage is to apply this methodology to the investigation of A/V ratio.

Table 6.1: Fitted impedance parameter values for X65 steel in 30 $g \cdot L^{-1}$ NaCl CO_2 solution at 80 °C, 5.5 bar pCO_2 and 10.5 $cm^2 \cdot L^{-1}$ A/V ratio

Time Hours	R_e $\Omega \cdot cm^2$	R_{ct} $\Omega \cdot cm^2$	Q_{dl} $(\mu F \cdot cm^{-2})^{\alpha}$	α	R_W $\Omega \cdot cm^2$	τ_D s	ϕ_W	R_{ads} $\Omega \cdot cm^2$	L_{ads} $H \cdot cm^2$	χ^2
2	3.5	12	602	0.92	8	39.2	1.0	3.8	0.88	0.178
4	3.5	13	1009	0.85	7	35.2	1.0	3.7	0.97	0.145
6	3.6	13	1019	0.90	7	45.2	1.0	4.1	0.74	0.103
8	3.6	12	1106	0.92	7	33.2	1.0*	4.2	1.51	0.187
10	3.6	12	1226	0.93	6	36.2	1.0	2.6	0.84	0.150
12	3.5	13	1572	0.90	6	47.8	1.0	2.8	0.98	0.117
14	3.5	12	1902	0.89	5	42.1	1.0	3.4	1.14	0.100
16	3.7	12	1801	0.92	6	42.1	1.0	3.3	1.68	0.102
18	3.5	12	2239	0.88	5	39.3	1.0	4.1	1.56	0.103
20	3.4	12	2371	0.88	7	53.6	1.0	3.4	1.64	0.072
22	3.5	12	2465	0.89	6	45.9	1.0	3.3	1.22	0.075
24	3.4	12	2584	0.89	5	43.2	1.0	3.3	1.40	0.083
26	3.5	12	2766	0.88	5	51.4	1.0	3.6	1.43	0.054
28	3.5	13	3378	0.85	5	49.8	1.0	4.5	1.00	0.054
30	3.5	13	3010	0.88	6	65.3	1.0	3.6	1.45	0.047
32	3.5	13	3230	0.87	5	54.2	1.0	3.6	1.34	0.042
34	3.5	13	3216	0.88	6	70.1	1.0	3.4	1.55	0.049
36	3.5	13	3306	0.88	4	45.9	1.0	3.3	1.46	0.057
38	3.6	12	3359	0.88	5	47.5	1.0	3.6	1.49	0.055
40	3.8	12	2942	0.92	5	41.5	1.0	2.3	1.22	0.168
42	4.1	13	3740	0.86	5	50.0	1.0*	4.3	1.58	0.127
44	3.9	12	3178	0.89	7	53.0	1.0	3.3	2.31	0.162
46	3.9	13	3893	0.85	7	55.1	1.0	4.4	1.41	0.124
48	4.1	13	3439	0.87	7	50.0	1.0	3.6	1.62	0.128
50	4.0	13	3678	0.84	7	36.8	1.0*	4.7	1.70	0.116
52	4.3	14	3109	0.87	8	44.1	1.0	3.1	1.19	0.121
54	4.3	15	3081	0.86	9	44.7	1.0*	3.8	1.15	0.116
56	4.2	16	3129	0.83	10	44.6	1.0	4.4	1.04	0.110
58	4.3	17	2896	0.83	11	40.0	1.0*	5.0	1.04	0.114
60	4.5	19	2433	0.84	12	24.9	1.0*	5.1	1.24	0.126
62	4.7	21	2121	0.84	15	23.0	1.0*	5.8	1.37	0.139
64	5.0	23	1812	0.84	21	21.6	1.0*	7.3	1.91	0.157
66	5.1*	27	1488	0.84	29	21.2	1.0*	9.5	2.80	0.224
68	5.1*	33	1176	0.84	43	22.2	1.0*	12.4	4.23	0.338
70	5.1*	43	915	0.83	64	24.1	1.0	17.4	6.52	0.495
72	5.1*	61	725	0.80	92	27.0	1.0	26.0	9.97	0.664
74	5.1*	91	516	0.79	130	30.2	1.0	34.9	15.03	0.789
76	5.1*	144	378	0.77	180	34.0	1.0	47.2	20.36	0.638
78	5.1*	238	286	0.76	244	36.6	1.0	58.4	23.49	0.404
80	5.1*	397	215	0.77	310	33.5	1.0	55.7	28.14	0.119
82	5.1*	746	163	0.79	438	33.2	1.0*			0.382
84	5.1*	2070	204	0.70	909	28.4	1.0*			1.649
86	5.1*	4424	210	0.67	1895	34.8	1.0			4.801
88	5.1*	5108	181	0.68	2132	27.3	1.0*			4.580
90	5.1*	5996	161	0.68	2604	33.0	1.0*			3.586
92	5.1*	6678	143	0.68	2747	35.1	1.0*			4.401
94	5.1*	7177	127	0.69	3081	30.9	1.0*			3.805
96	5.1*	7560	114	0.71	3087	21.4	1.0*			4.405
98	5.1*	8072	105	0.71	3418	22.6	1.0*			4.313
100	5.1*	8467	98	0.71	3515	22.4	1.0*			3.556
102	5.1*	8957	92	0.71	3710	22.5	1.0*			3.058
104	5.1*	9448	87	0.71	3943	22.0	1.0*			3.967
106	5.1*	9854	83	0.70	4069	22.7	1.0*			4.498
108	5.1*	10363	79	0.70	4427	24.3	1.0*			4.613
110	5.1*	10638	75	0.70	4587	22.5	1.0*			4.508
112	5.1*	10968	72	0.70	4755	23.5	1.0*			4.750

*Bound applied

Chapter 7
The Effects of System Chemistry Evolution Rates on $FeCO_3$ Formation Explored by A/V Ratio Variation

7.1 Chapter Introduction

The initial study on the effects of A/V ratio presented in Chapter 5 - Section 5.5 raises a number of questions on the properties of the corrosion layers that develop over time under different rates of bulk solution change. The experimental methodology and EIS analysis techniques developed in Chapter 6 for evaluating the evolution of interfacial properties can be extended to the $FeCO_3$ corrosion layers that form at a higher A/V ratio. In doing so the nature and protectiveness of the layer over time can be evaluated as well as the mechanism for protection. Further, the impact of varying A/V ratio on the perceived protectiveness of the layer can be expounded. The aim of this chapter is therefore to investigate the effect that A/V ratio has on the development stages of $FeCO_3$ corrosion products and the long term impact this may have on properties of the layer.

7.1.1 Chapter Outline

The chapter is broken down in to *in situ* and *ex situ* analysis of $FeCO_3$ layers formed on carbon steel at both high and low A/V ratios (41.4 and 10.5 $cm^2 \cdot L^{-1}$ respectively). *In situ* data is extracted from electrochemical measurements in an autoclave using LPR, OCP, EIS and potentiodynamic sweeps as described in Section 4.6.1 and 4.6.2. E*x situ* surface analysis is conducted using Scanning Electron Microscopy (Section 4.7.2) while Electron Back-Scattered Diffraction of the cross-section is used to evaluate crystallographic properties of the corrosion layers following the methodology in Sections 4.7.4 and 4.7.6.

7.2 Comparison of Electrochemistry Results

7.2.1 Linear Polarisation Resistance

Figure 7.1 charts the transition in R_p^{-1} over time at both low and high A/V (10.5 and 41.4 $cm^2 \cdot L^{-1}$ respectively) across two repeats. To clearly show the change in trends, R_p^{-1} has been plotted on both a linear and $\log_{10}$ scale.

The data shows four distinct development stages as shown in Chapter 6 for low A/V are clearly present at high A/V with different transition rates between stages. R_p^{-1} drops immediately at high A/V while at low A/V it tends to increase over the first 30 hours before dropping. Both A/V ratios have distinct regions of linear decrease in R_p^{-1} followed by logarithmic decrease of comparable gradients. A significant decrease in R_p^{-1} happens after approximately 30 hours at high A/V while at low A/V this takes around 48 hours with the decay taking slightly longer in the second repeat. On a $\log_{10}$ scale the drop in R_p^{-1} plateaus suddenly at around 60 hours at high A/V while the process is much slower at low A/V. On the second repeat at low A/V the test was allowed to run longer and showed an eventual stabilisation after 110 hours.

(a)

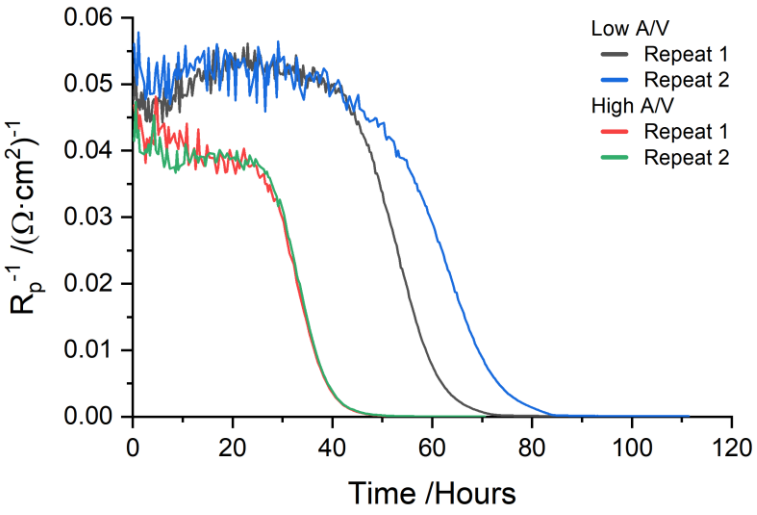

(b)

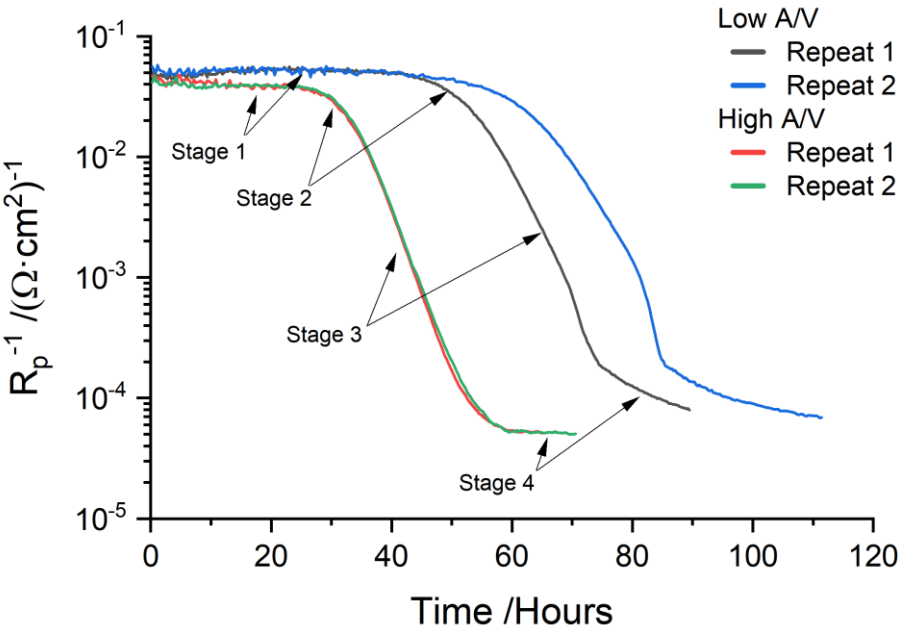

Figure 7.1: Comparison of R_p^{-1} over time for low and high (10.5 and 41.4 $cm^2 \cdot L^{-1}$) A/V ratio experiments on X65 steel in 30 $g \cdot L^{-1}$ NaCl CO_2 solution at 80 °C, 5.5 bar pCO_2 (a) on linear scale (b) on $\log_{10}$ scale

7.2.2 Open Circuit Potential

A comparison of OCP measurements is presented in Figure 7.2. A newer reference probe was used for the second repeat of each experiment with a variation of 25 mV on the initial OCP value at high A/V. Despite the variation the trends agree well between the experiments showing a much greater transition in OCP at low A/V. At high A/V the OCP initially increases by 30 mV in both repeats before dipping between 20 and 50 hours. After around 50 hours the OCP increases by 30 mV in the first repeat and 45 mV in the second. At low A/V the initial increase in OCP is also approximately 30 mV with OCP starting to drop after 40 hour in both repeats. After 52 hours in the first repeat the OCP increases by approximately 100 mV. In the second repeat OCP increases after 58 hours, again increase by around 100 mV.

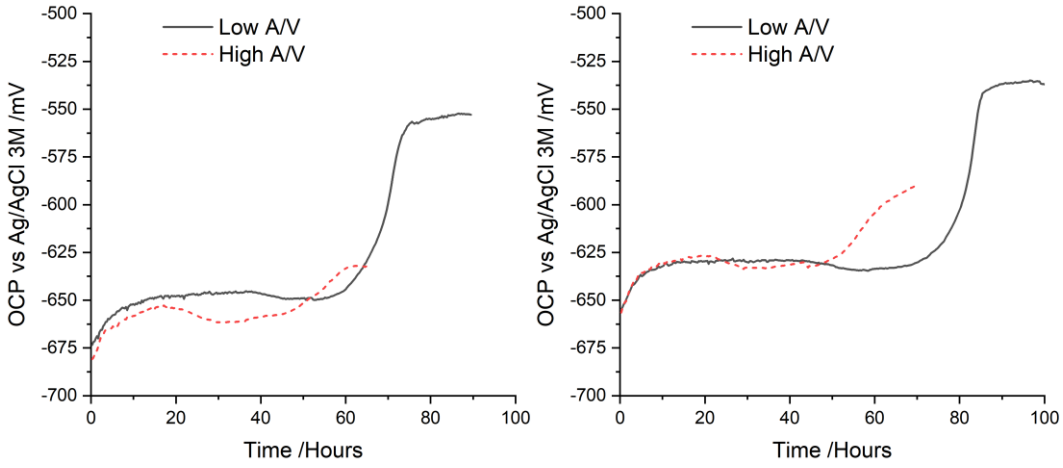

Figure 7.2: Comparison of OCP over time for low and high (10.5 and 41.4 $cm^2 \cdot L^{-1}$) A/V ratio experiments on X65 steel in 30 $g \cdot L^{-1}$ NaCl CO_2 solution at 80 °C, 5.5 bar pCO_2. Repeat 1 (left) and Repeat 2 with a new RE (right)

7.2.3 Potentiodynamic Sweeps

Potentiodynamic sweeps were conducted at the end of the first repeat of each experiment and are presented in Figure 7.3. Despite a more positive OCP at low A/V corrosion current density (i_{corr}) is clearly lower at high A/V. This effect is predominately attributed to the suppression of the cathodic branch of the potential curve at high A/V.

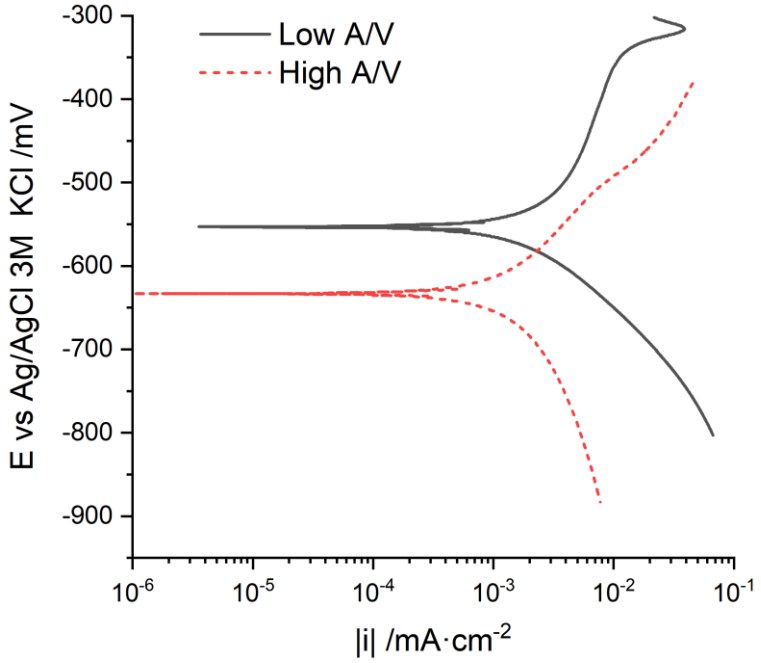

Figure 7.3: Comparison of Tafel behaviour for low and high (10.5 and 41.4 $cm^2 \cdot L^{-1}$) A/V ratio experiments on X65 steel in 30 $g \cdot L^{-1}$ NaCl CO_2 solution at 80 °C, 5.5 bar pCO_2.

7.2.4 Electrochemical Impedance Spectroscopy

The detailed EIS analysis performed in Chapter 6 correlated the transition stages in LPR measurements and OCP with changes in impedance response at low A/V. Nyquist plots of impedance response at the corresponding stages at high and low A/V are presented in Figure 7.4 and Figure 7.5. The data illustrates how quickly the impedance response changes under the conditions of high A/V with a noticeable increase in R_{ct} from around 25 to 30 $\Omega \cdot cm^2$ over the first 6 hours. During Stage 2, at both A/V conditions the LF loop becomes more pronounced and both HF and LF loops start to increase in magnitude. In Stage 3 a dramatic increase in impedance of over two orders of magnitude occurs in the high A/V case (~75 at 36 hours to 10000 $\Omega \cdot cm^2$ at 54 hours). This is much greater than the increase at low A/V (~75 at 68 hours to 2750 $\Omega \cdot cm^2$ at 84 hours). During Stage 3, despite the difference in magnitude the loop form is still comparable and also features the disappearance of the adsorption loop in both cases.

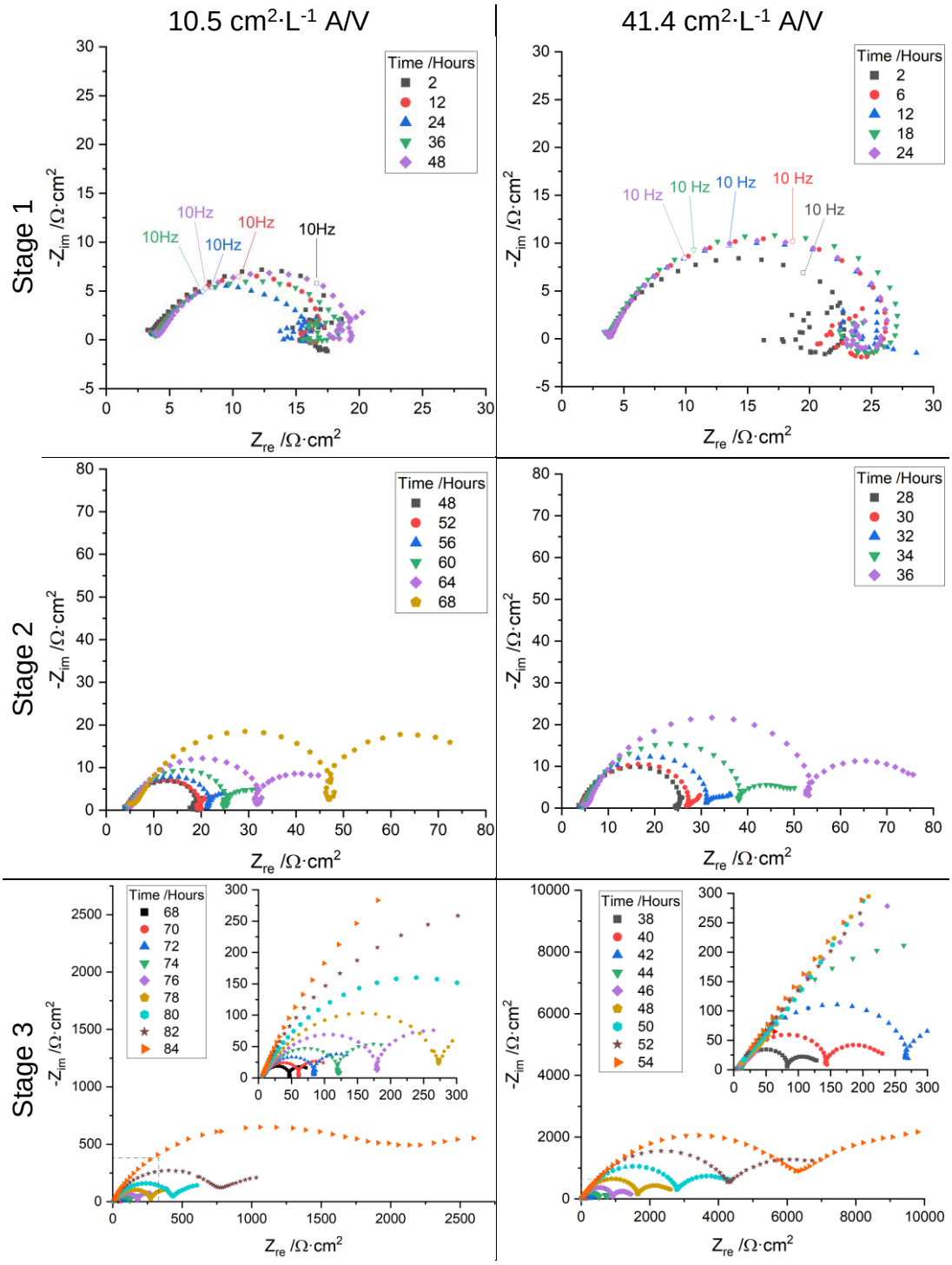

Figure 7.4: Nyquist plots to compare impedance response during corrosion product formation on X65 steel at low and high (10.5 and 41.4 $cm^2 \cdot L^{-1}$) A/V ratios in 30 $g \cdot L^{-1}$ NaCl CO_2 solution at 80 °C, 5.5 bar pCO_2

Stage 4 of the corrosion product layer formation shown in the Nyquist plot Figure 7.5, shows a clear divergence in the properties of the high and low A/V layers. At low A/V the HF charge-transfer loop appears to dominate the frequency response with the LF diffusion loop having a similar time constant but lower resistivity as shown in Chapter 6. At high A/V this trend appears to have been reversed with the LF diffusion loop dominating the response with an almost semi-infinite Warburg appearance comparable to that of De Motte et al. [51]. The HF loop is also highly depressed signifying considerable time constant dispersion. A Bode phase plot in Figure 7.6 shows how the characteristic frequency of the HF loop is also continuing to shift throughout the final stage of the experiment at high A/V.

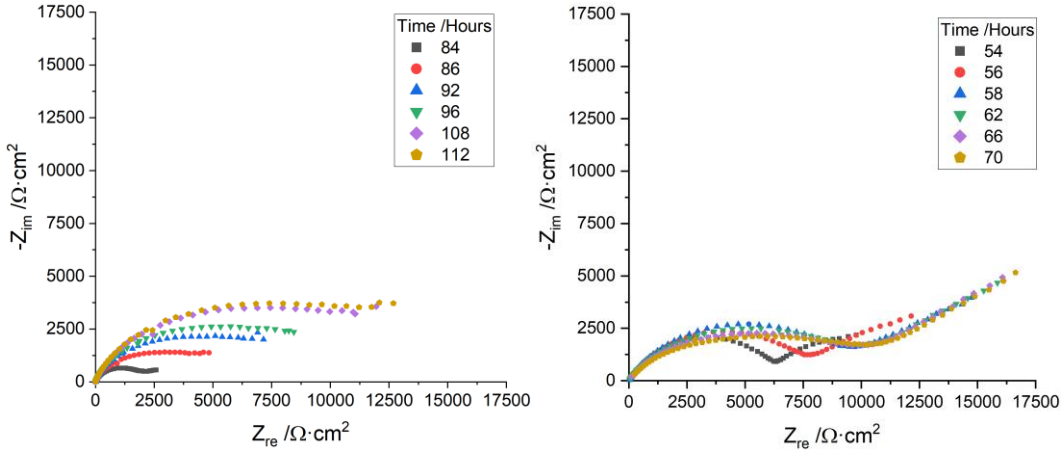

Figure 7.5: Nyquist plots to compare impedance response after corrosion product formation on X65 steel at low and high (10.5 and 41.4 $cm^2 \cdot L^{-1}$) A/V ratios in 30 $g \cdot L^{-1}$ NaCl CO_2 solution at 80 °C, 5.5 bar pCO_2

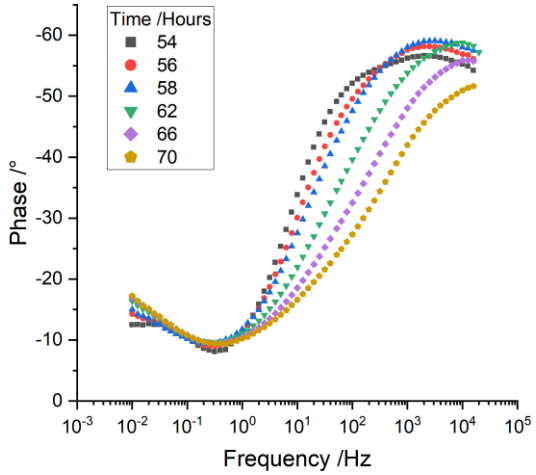

Figure 7.6: Bode phase plot of Stage 4 of corrosion product formation on X65 steel at high A/V (41.4 $cm^2 \cdot L^{-1}$) in 30 $g \cdot L^{-1}$ NaCl CO_2 solution at 80 °C, 5.5 bar pCO_2

7.3 Temporal Evolution of Impedance Properties

The reciprocal of total polarisation resistance from LPR measurements and EIS analysis at high A/V is compared in Figure 7.7. The data from EIS fitting shows good agreement with the LPR data until the later stages of the experiment around 54 hours. This potentially indicates the limitation of the LPR scan rate and resolution due to extremely low current and high impedance and re-enforces the value of a combined LPR-EIS approach.

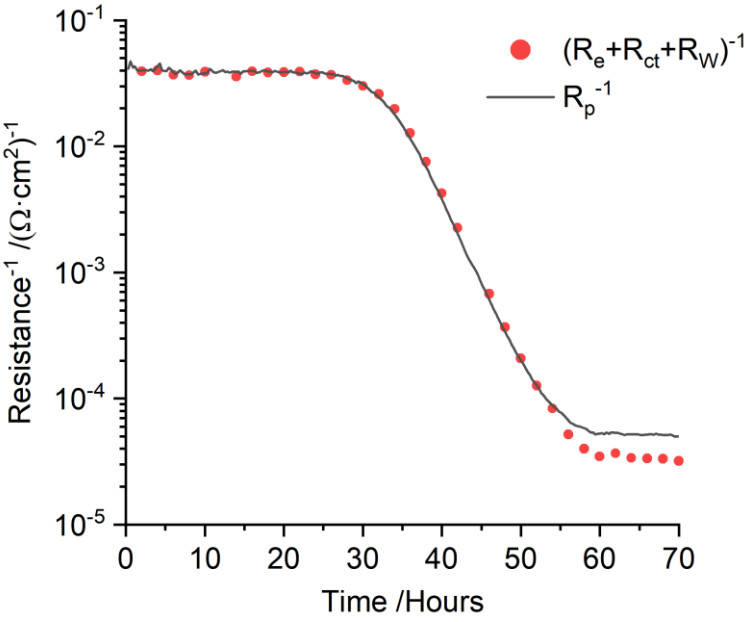

Figure 7.7: Comparison of reciprocal of total polarisation resistance over time based on fitted EIS data (red dots) and LPR measurement (black line) for X65 carbon steel in 30 g·L^{-1} NaCl CO_2 solution at 80 °C, 5.5 bar pCO_2 and 41.4 cm^2·L^{-1} A/V ratio

Characteristic properties of $FeCO_3$ corrosion product formation over time are compared at both high and low A/V. Figure 7.8 shows how both the faradaic charge-transfer resistance R_{ct} and diffusion resistance R_w vary for the two sets of conditions. In the final stage of the experiment at low A/V the resistance is dominated by R_{ct} with a resistance of around 11000 Ω·cm^2 for R_{ct} compared to 4750 Ω·cm^2 for R_W. At high A/V the opposite is true with a much larger value for R_W of 21600 Ω·cm^2 and 9400 Ω·cm^2 for R_{ct} by the end of the experiment. There is also a significant difference in the double layer capacitance as illustrated in Figure 7.9 which indicates that C_{dl} continues to fall logarithmically in the final stage of $FeCO_3$ formation at high A/V reaching an extremely low value of 0.55 nF·cm^{-2}.

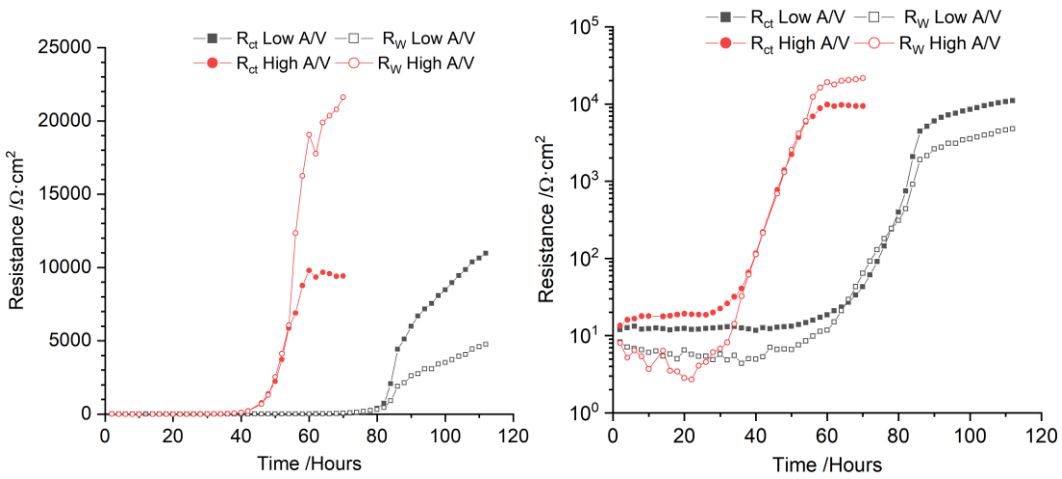

Figure 7.8: Comparison of R_{ct} and R_W obtained from fitted impedance data for X65 steel at low and high (10.5 and 41.4 $cm^2 \cdot L^{-1}$) A/V ratios in 30 $g \cdot L^{-1}$ NaCl CO_2 solution at 80 °C, 5.5 bar pCO_2. Plotted on linear scale (left) and log_{10} scale (right)

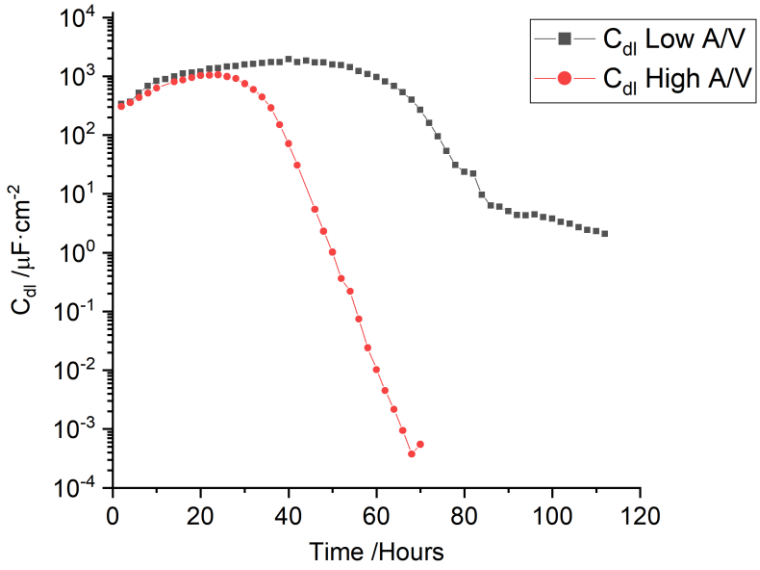

Figure 7.9: Comparison of C_{dl} obtained from fitted impedance data for X65 steel at low and high (10.5 and 41.4 $cm^2 \cdot L^{-1}$) A/V ratios in 30 $g \cdot L^{-1}$ NaCl CO_2 solution at 80 °C, 5.5 bar pCO_2

To elaborate on the observations on C_{dl}, the value of Q_{dl} is plotted in Figure 7.10 which does suggest a plateau in the capacitance at around 54 hours. The reason that C_{dl} continues to fall at high A/V after 54 hours is therefore predominantly attributed to the decrease in the CPE coefficient α which falls sharply in the final stage of the high A/V experiment. This is also evident in Nyquist plot in Figure 7.5 which shows continued depression of the charge transfer loop at the end of the experiment.

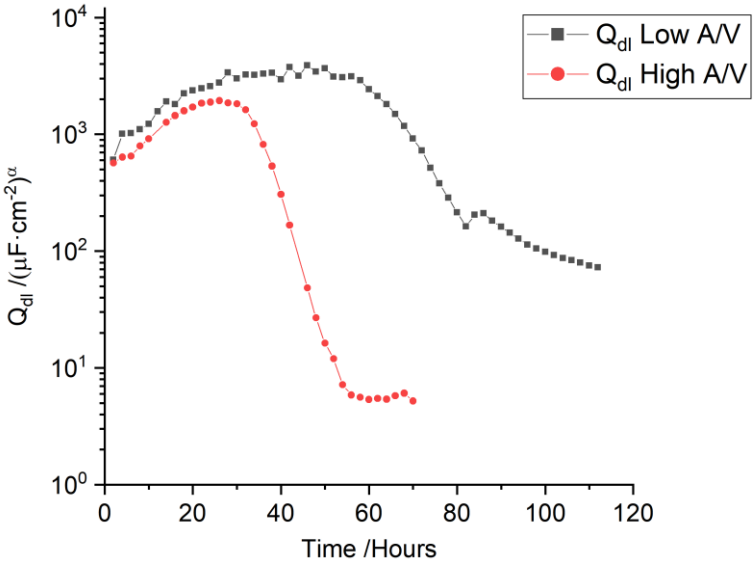

Figure 7.10: Comparison of Q_{dl} obtained from fitted impedance data for X65 steel at low and high (10.5 and 41.4 cm^2·L^{-1}) A/V ratios in 30 g·L^{-1} NaCl CO_2 solution at 80 °C, 5.5 bar pCO_2

To investigate the effects of dispersion further, a plot of α at low and high A/V is provided in Figure 7.11. At high A/V ϕ_W could also be reliably fitted without bounds due to the clear linearity of the start of the diffusion loop and has also been included in Figure 7.11. The results show that α is relatively stable at low A/V prior to $FeCO_3$ development, gradually reducing from a value of 0.9 to 0.7 by the end of the experiment and stabilising during the final stage of the experiment (85 to 112 hours).

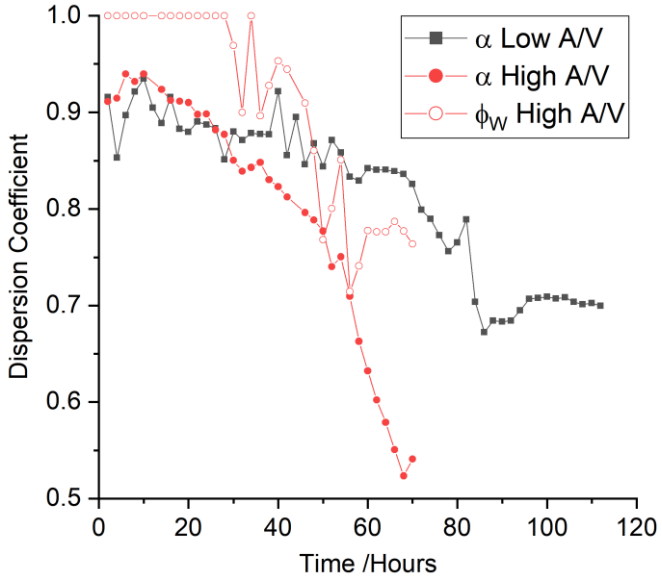

Figure 7.11: Comparison of dispersion coefficients obtained from fitted impedance data for X65 steel at low and high (10.5 and 41.4 cm^2·L^{-1}) A/V ratios in 30 g·L^{-1} NaCl CO_2 solution at 80 °C, 5.5 bar pCO_2

At high A/V α starts decreasing linearly between 24 and 50 hours then starts to drop more sharply between 50 and 70 hours reaching a value of almost 0.54. Diffusion dispersion at high A/V also appears to increase in the later stages of the experiment as the characteristic 45° line of the Warburg element is clearly depressed to a lower angle in this system. The result is a decay in ϕ_W to a value of approximately 0.78.

7.4 Comparison of Surface Morphology

Top surface SEM at the end of high and low A/V experiments show a stark contrast in the way in which the corrosion product has formed. Figure 7.12(a) and (c) show a compact and uniform layer of $FeCO_3$ covering the entire surface at high A/V. At low A/V significant Fe_3C (white areas) is still visible at the surface.

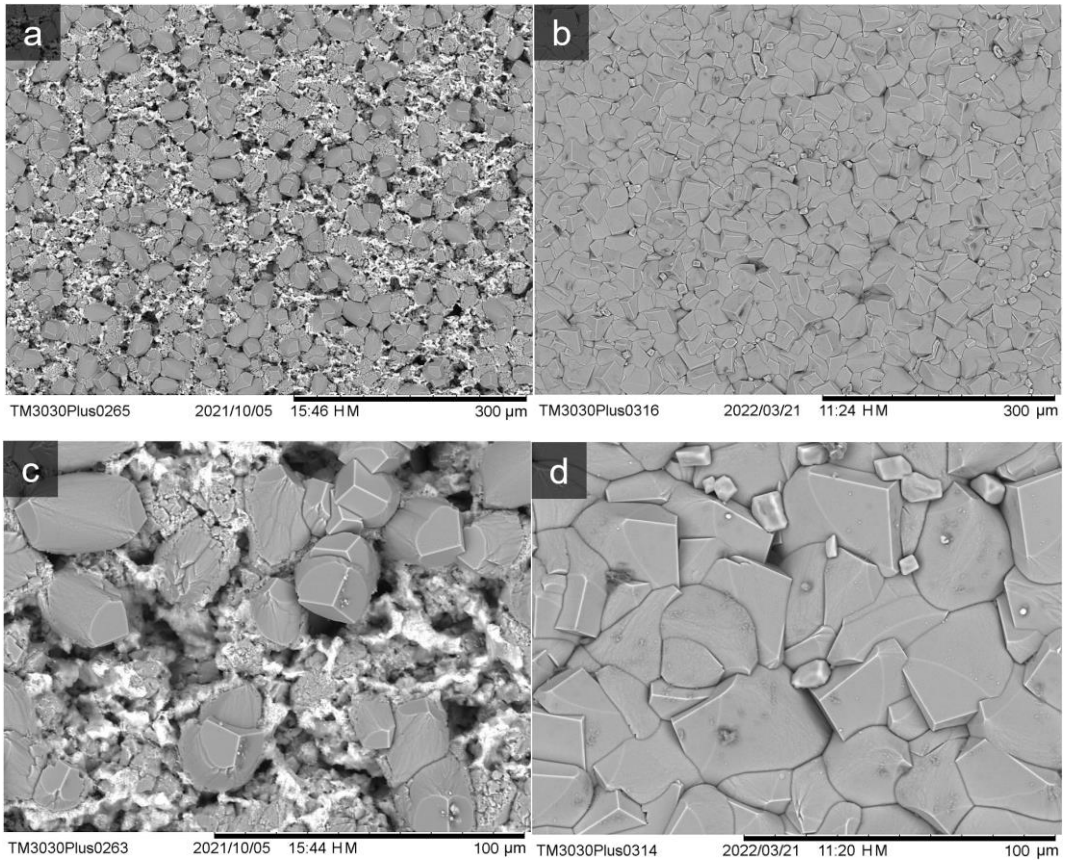

Figure 7.12: BSE SEM images of top surface of X65 steel after corrosion product formation in 30 $g \cdot L^{-1}$ NaCl CO_2 solution at 80 °C, 5.5 bar pCO_2. (a) Low A/V 10.5 $cm^2 \cdot L^{-1}$ at 250x magnification (b) High A/V 41.4 $cm^2 \cdot L^{-1}$ at 250x magnification (c) Low A/V 10.5 $cm^2 \cdot L^{-1}$ at 1000x magnification (d) High A/V 41.4 $cm^2 \cdot L^{-1}$ at 1000x magnification

7.5 Comparison of Corrosion Layer Cross-section

Cross sectional SEM images through the corrosion layers in Figure 7.13 reveal more detail on the differences in how the layer forms at different A/V ratios.

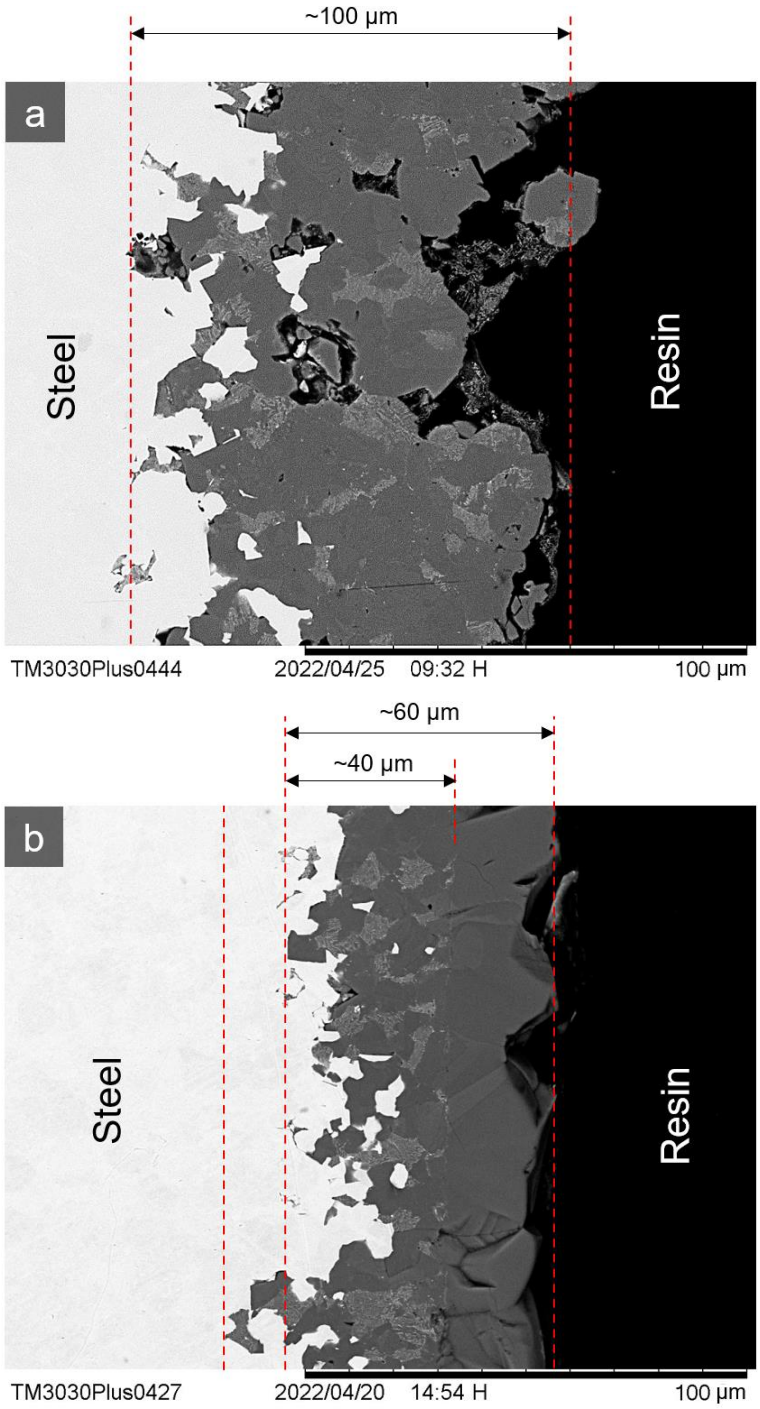

Figure 7.13: Back Scattered SEM images of cross section through corrosion product layer on X65 steel after immersion in 30 g·L^{-1} NaCl CO_2 solution at 80 °C, 5.5 bar pCO_2. (a) Low A/V 10.5 cm^2·L^{-1} (b) High A/V 41.4 cm^2·L^{-1}

At low A/V the layer thickness is approximately 100 µm and has formed almost entirely with the exposed Fe_3C matrix with only isolated crystals that have grown out and above the original surface. At high A/V the formation is significantly different, comprising an apparent duplex layer of ~40 µm sub-surface $FeCO_3$ embedded into the Fe_3C and a ~20 µm top $FeCO_3$ layer. The apparent duplex layer has been reported previously in literature by Gao *et al.* [160] but it has not been elucidated whether the crystal formation is entirely separate above and below the original surface. To investigate this, the cross sections were subsequently analysed using EBSD.

7.6 Comparison of Crystal Growth Using EBSD

Figure 7.14 shows electron images of $FeCO_3$ corrosion products formed at low A/V.

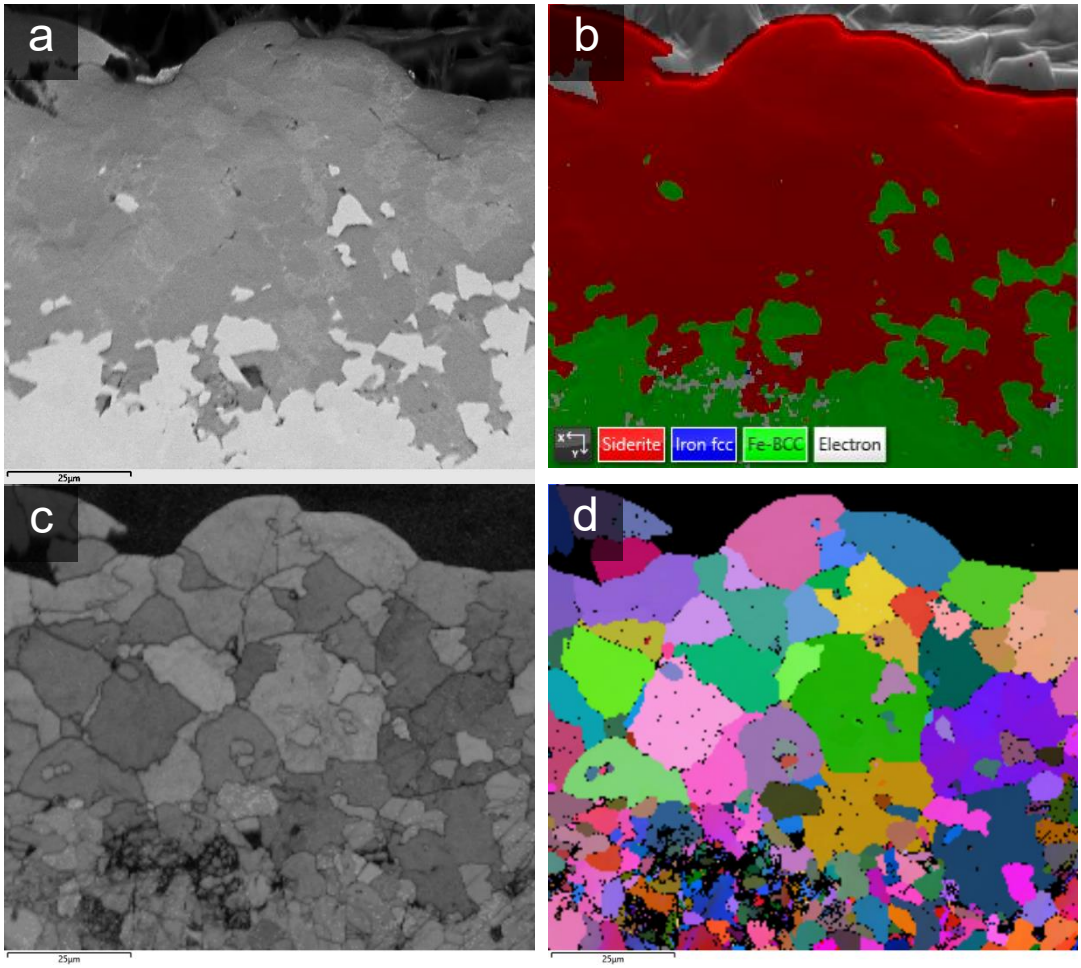

Figure 7.14: EBSD images of crystallographic properties of $FeCO_3$ corrosion products formed at low A/V ratio (10.5 $cm^2 \cdot L^{-1}$) on X65 steel in 30 $g \cdot L^{-1}$ NaCl CO_2 solution at 80 °C, 5.5 bar pCO_2 (a) forward scatter image (b) phase colour image (c) band contrast image (d) Euler colour image

Figure 7.14(a) is the image from a forward scatter detector (FSD) which shows contrast between $FeCO_3$ (dark grey) and the ferrite phase from the substrate (light grey/white). Also visible in this image is the Fe_3C within which the $FeCO_3$ is embedded as shown in the SEM images in Figure 7.13. Figure 7.14(b) is a phase colour image which clearly identifies the $FeCO_3$ (Siderite) and body-centre-cubic (BCC) α-ferrite of the substrate but is unable to detect the thin lamella Fe_3C. Figure 7.14(c) is a band contrast image which identifies grain boundaries and crystallographic orientation in different shades of grey. Figure 7.14(d) is the same image on a colour scale to enhance visualisation of individual crystals. Figure 7.15 is the corresponding EBSD images for $FeCO_3$ formed at high A/V ratio at a higher magnification due to the size of the layer.

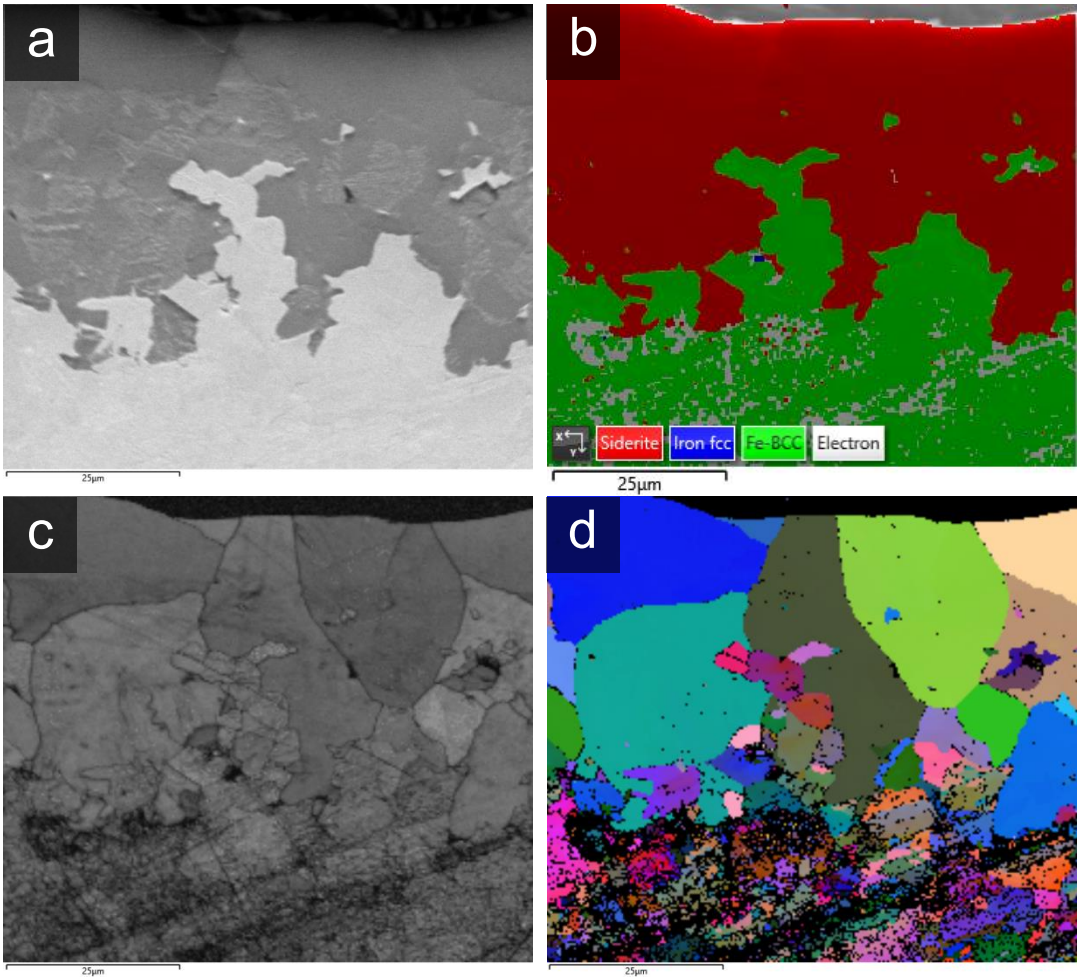

Figure 7.15: EBSD images of crystallographic properties of $FeCO_3$ corrosion products formed at high A/V ratio (41.4 $cm^2 \cdot L^{-1}$) on X65 steel in 30 g·L-1 NaCl CO_2 solution at 80 °C, 5.5 bar pCO_2 (a) forward scatter image (b) phase colour image (c) band contrast image (d) Euler colour image

Figure 7.16 is a comparison of the colour plots at high and low A/V set on the same scale to compare crystal sizes. All α-Ferrite in these images has been recoloured to white to isolate $FeCO_3$ crystals.

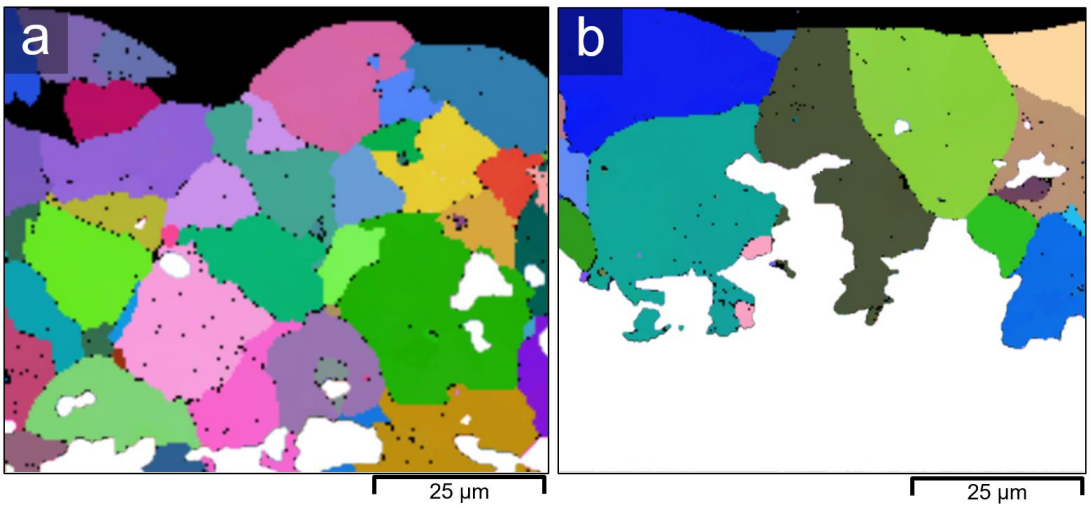

Figure 7.16: Comparison of crystal grain structure of $FeCO_3$ products formed at high and low A/V ratio on X65 steel in 30 g·L-1 NaCl CO_2 solution at 80 °C, 5.5 bar pCO_2. White and black areas indicate substrate Fe and resin respectively. (a) Low A/V ratio (10.5 $cm^2 \cdot L^{-1}$) (b) High A/V ratio (41.4 $cm^2 \cdot L^{-1}$)

EBSD analysis reveals that at high A/V the crystal size is generally larger than at low A/V. The EBSD data also shows that there is no obvious separation of crystals at the interface of the original steel surface. At high A/V multiple large crystals have formed through the entire depth of the corrosion product from the substrate all the way through to the surface. This also highlights that crystal growth does not appear to be bounded by the Fe_3C with crystals growing over the thin Fe_3C lamella. The findings suggest that high A/V $FeCO_3$ formation and subsequent protectiveness could be controlled by growth of a few large crystals while at low A/V crystal nucleation is the controlling mechanism.

7.7 Summary

This chapter has demonstrated that area-to-volume (A/V) ratio has a significant effect on the formation of $FeCO_3$ corrosion products both in terms of the rate of formation and also the subsequent morphology and performance of the layer. *In situ* electrochemical measurements indicate that the mechanism for protection of the substrate changes due to the morphology of the layer.

At high A/V the increased rate of corrosion product formation results in a dense top surface layer of $FeCO_3$ which provides a higher level of diffusion resistance compared to the thicker more porous layer that grows almost entirely within the exposed Fe_3C from the substrate at low A/V. The results have also shown that the two systems do not converge over time due to significant differences in evolution of the layers during the early stages of the experiment when dissolution rates and Fe^{2+} flux is high. The layer thickness at high A/V will likely never reach the same thickness as at low A/V while at low A/V it is unlikely that a thick outer layer will form due to the lack of Fe^{2+} reaching the outer surface. While LPR and EIS measurements have indicated the corrosion product formed at high A/V appears to be more protective, it is not clear what effect the difference in morphology has on localised corrosion. A further question that this analysis raises is the effect that A/V ratio has longer term in the more complex brine compositions discussed in Chapter 5.

Chapter 8

Relating $FeCO_3$ and $Fe_xCa_yCO_3$ Corrosion Scale Nucleation and Growth Behaviour to Substrate Protection

8.1 Chapter Introduction

In Chapter 5, the effects of an evolving brine chemistry were linked to the evolution of mixed Ca/Fe carbonate corrosion product layers through chemistry modelling and a parametric study of A/V ratio and bulk Ca^{2+} concentration. The results suggested that increasing bulk calcium concentrations lead to increased uptake of calcium in the layer and higher average corrosion rates. The latter observation was largely attributed to slower surface coverage and needed longer term experiments to compare the layers once fully formed under all conditions. In Chapter 6, an electrochemical analysis method was developed to characterise the development of these layers with time and their associated properties, focusing on a single test condition of $FeCO_3$ formation at low A/V. The study identified four key stages of $FeCO_3$ corrosion layer development. In Chapter 7 this method was extended to $FeCO_3$ formed at higher A/V to establish what difference if any, a higher rate of bulk Fe concentration change had on the $FeCO_3$ corrosion layer that formed. This analysis was again performed in the absence of calcium to isolate the type of corrosion product as $FeCO_3$, in order to identify how initial corrosion layer build-up could affect long term corrosion product performance for a specific corrosion product composition. The results of this work confirmed that increased rates of bulk Fe concentration change, due to higher A/V ratio, does alter the way in which the corrosion layer forms and protects the substrate. To conclude the investigation, this chapter combines the parametric study of Chapter 5 with the *in situ* electrochemical analysis of Chapters 6 and 7. The result is a comprehensive electrochemical analysis of typical corrosion scales that form in demanding CO_2 environments, coupled with detailed *ex situ* analysis of the composition and morphology of the resulting corrosion/scale layers. Detailed characterisation is then coupled with an assessment of corrosion layer performance against general and localised attack. In short, the aim of this chapter is to relate the mechanisms of corrosion product formation in rapidly evolving calcified brines with the protectiveness of the resulting corrosion/scale layers.

8.1.1 Chapter Outline

In the first section, the general corrosion performance of corrosion products formed on X65 carbon steel exposed to brine compositions listed in Table 5.4 is assessed though the application of *in situ* electrochemical techniques and gravimetric analysis following the methodology described in Sections 4.6.1, 4.6.2 and 4.7.1. The resulting properties from impedance data fitting are also compared. In the next section, surface coverage and corrosion product morphology are compared using SEM imaging described in Section 4.7.2. Average corrosion product compositions are quantified using powder diffraction detailed in Section 4.7.3. Through layer composition is analysed by EDX following the approach in Sections 4.7.4 and 4.7.5. The next section focuses on highly localised analysis of through layer composition and nanoscale defects using TEM and STEM outlined in Section 4.7.7. Finally, profilometry is used to assess the extent of localised corrosion and to relate this to the composition and morphology of the corrosion layers and ultimately the bulk service conditions.

8.2 General Corrosion Performance

General corrosion performance was assessed by LPR experiments followed by potentiodynamic sweeps on the first repeat of each experimental condition once corrosion products had formed and the trends in R_p^{-1} appeared to have stabilised. In the second repeat, LPR data was collected alongside EIS spectra before surface analysis was performed on the carbon steel electrode.

8.2.1 Experiment One - LPR Measurements

Figure 8.1(a) shows the results of LPR measurements for the first repeat of each experiment. In Figure 8.1(b), R_p^{-1} is plotted on a $\log_{10}$ scale which elucidates the trends more clearly. The data suggest that corrosion rates were still decaying on a logarithmic scale for all conditions excluding no Ca^{2+} high A/V. Nevertheless R_p^{-1} was extremely low under all conditions at this stage and was deemed stabilised having fallen below 10^{-3} $\Omega^{-1}\cdot cm^{-2}$.

(a)

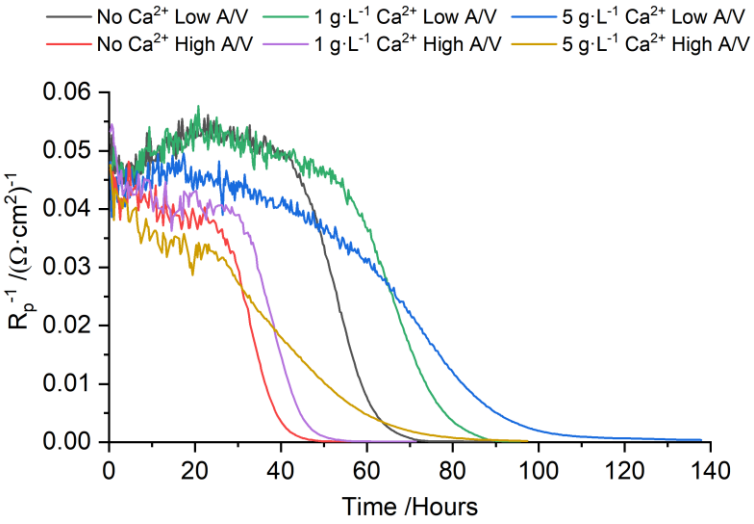

(b)

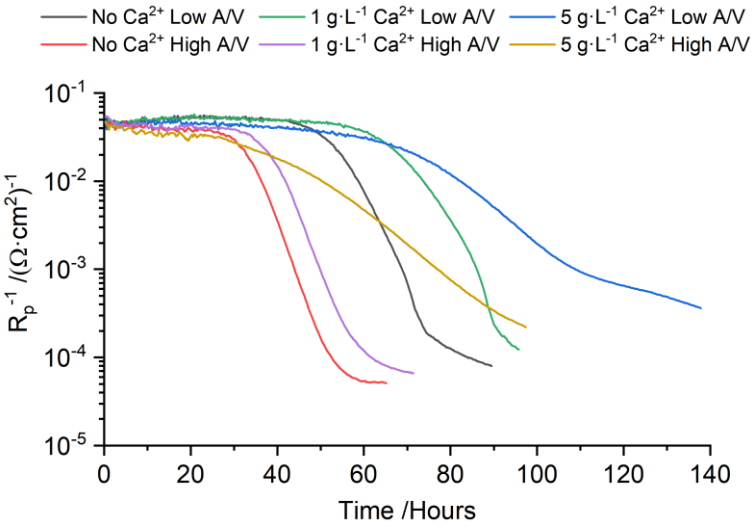

Figure 8.1: First repeat of LPR measurements showing R_p^{-1} on (a) linear and (b) $\log_{10}$ scales over time for X65 steel at various bulk calcium concentrations and low and high (10.5 and 41.4 $cm^2 \cdot L^{-1}$) A/V ratios in CO_2 solution at 80 °C, 5.5 bar pCO_2

8.2.2 Experiment One - OCP Measurements

The corresponding OCP values as a function of time are plotted in Figure 8.2 and show significant differences in the response as a consequence of both A/V ratio and calcium concentration. Both low A/V with no calcium and 1 $g \cdot L^{-1}$ calcium show dramatic increases in OCP of around 100 mV towards the end of the experiment, corresponding with the logarithmic decrease in R_p^{-1}. As discussed in Chapter 7, high A/V no Ca^{2+} also exhibits a notable but much lower increase in OCP of around 50 mV which proceeds a significant dip in OCP during initial corrosion product precipitation.

All other experimental conditions exhibit much more gradual increases in OCP over the course of the experiment. Initially within the first 5-10 hours, under all conditions the OCP increases by approximately 20 mV, this could be related to stabilisation or due to changes in conditions at the steel surface. Slow diffusion of reactants and products to and from the surface and/or surface changes as active area changes and Fe_3C is revealed would all affect OCP.

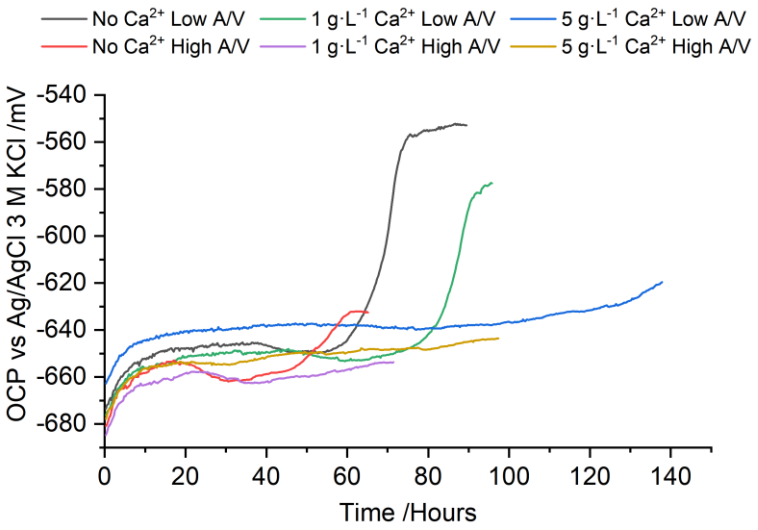

Figure 8.2: Comparison of OCP over time from first repeat of experiments on X65 steel at various bulk calcium concentrations and low and high (10.5 and 41.4 $cm^2 \cdot L^{-1}$) A/V ratios in CO_2 solution at 80 °C, 5.5 bar pCO_2

8.2.3 Potentiodynamic Sweeps

Figure 8.3(a) shows the results of potentiodynamic sweeps collected in accordance with Section 4.6.2.2. The data includes potentiodynamic sweeps conducted at the end of each experiment as well as two additional tests which were conducted under initial conditions. No Ca^{2+} high A/V and 5 $g \cdot L^{-1}$ low A/V were chosen as two extreme cases for initial bulk conditions to assess whether there were any significant differences in surface reactions. The results show good agreement between the two initial cases and therefore removed the need to conduct further potentiodynamic sweeps for the remaining conditions. Figure 8.3(b) shows the same sweeps aligned in terms of starting OCP value for additional comparison of cathodic and anodic branches. This also negates the effects of potential drift from the reference probe. The data shows how the cathodic reaction is supressed at high A/V while the absence of calcium greatly supresses the anodic reaction.

(a)

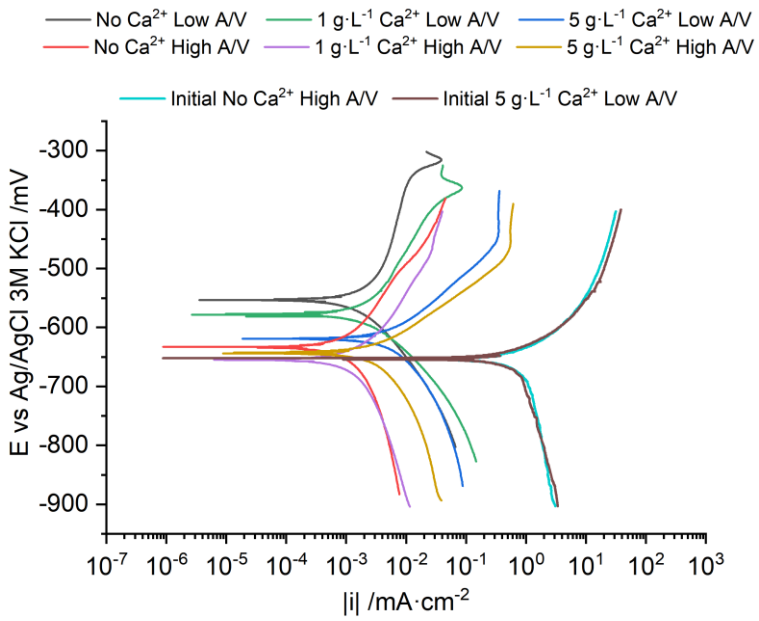

(b)

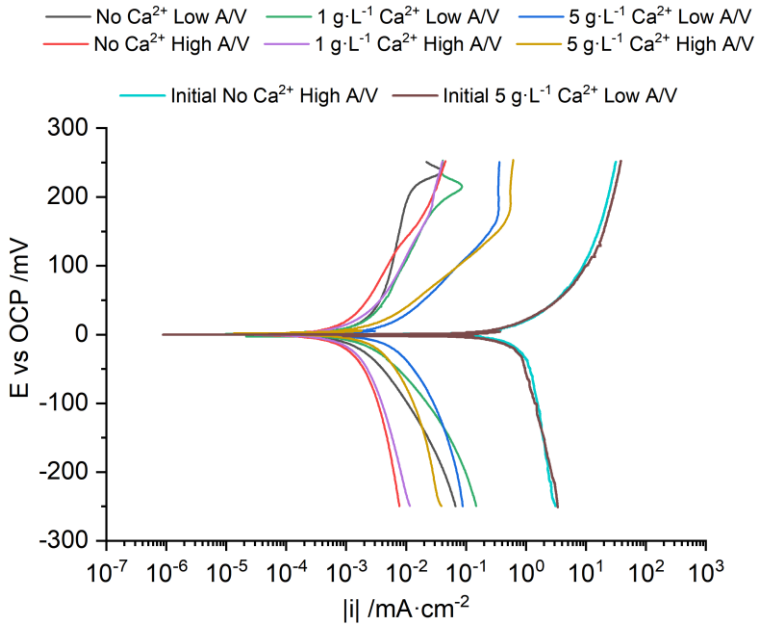

Figure 8.3: Potentiodynamic sweeps of X65 steel under initial conditions and after corrosion product formation at various bulk calcium concentrations and low and high (10.5 and 41.4 $cm^2 \cdot L^{-1}$) A/V ratios in CO_2 solution at 80 °C, 5.5 bar pCO_2 (a) E vs Ag/AgCl (b) E vs OCP

8.2.4 Experiment Two – LPR Measurements

For the second repeat of each experiment the test duration was increased to a maximum of 7 days to evaluate whether the corrosion rates would stabilise further. EIS measurements which had previously only been taken at high A/V were also taken across all conditions in accordance with Section 4.6.2.

(a)

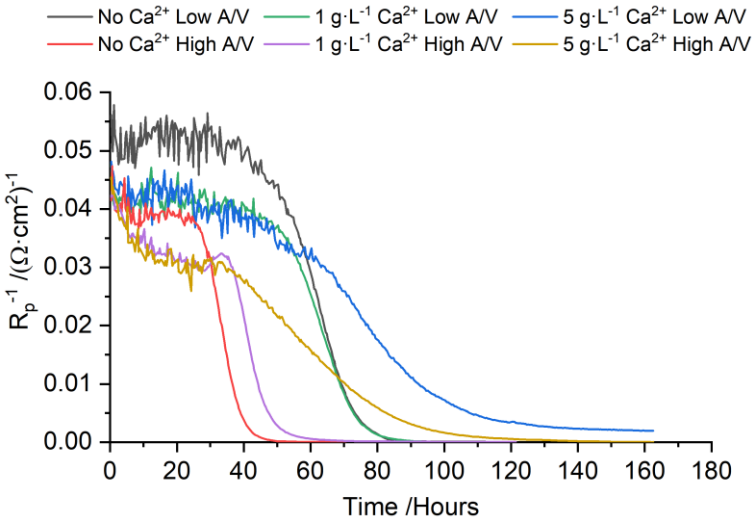

(b)

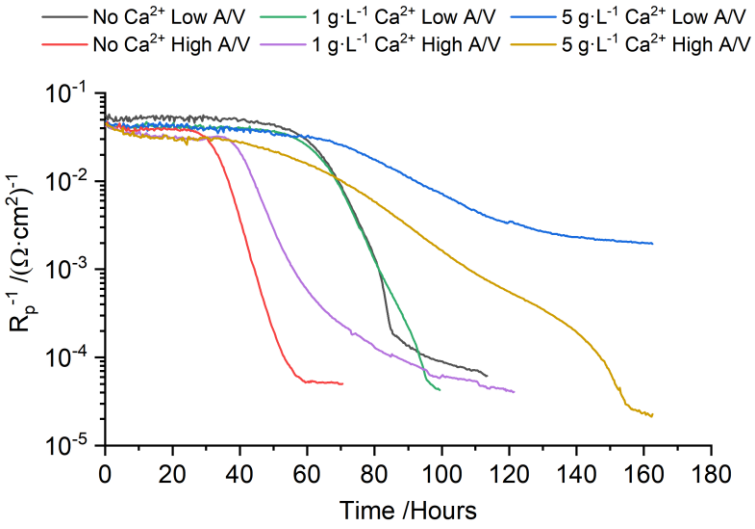

Figure 8.4: Second repeat of LPR measurements showing R_p^{-1} on (a) linear and (b) $\log_{10}$ scales over time for X65 steel at various bulk calcium concentrations and low and high (10.5 and 41.4 $cm^2 \cdot L^{-1}$) A/V ratios in CO_2 solution at 80 °C, 5.5 bar pCO_2

The second repeats show similar general trends to the initial experiments with increasing A/V ratio considerably decreasing the induction time for corrosion product formation and subsequent corrosion rate reduction. The presence of calcium also slowed down the rate of decrease in R_p^{-1}. While no Ca^{2+} and 5 $g \cdot L^{-1}$ Ca^{2+} experiments showed good agreement with the first repeat experiments, there were noticeable changes in the LPR curves at both high and low A/V for 1 $g \cdot L^{-1}$ Ca^{2+} experiments. At 1 $g \cdot L^{-1}$ Ca^{2+} high A/V the second experiment had a much slower decay in R_p^{-1} which coincided with a much lower average corrosion rate from the mass loss samples (See Section 8.2.6).

At 1 g·L^{-1} Ca^{2+} low A/V R_p^{-1} continued to decay to a very low value of less than 10^{-4} Ω^{-1}·cm^{-2} before the typical 'kink' associated with the start of stage 4 of corrosion product formation identified in Chapter 6. The initiation of stage 4 happened at a much lower value of R_p^{-1} when compared to no Ca^{2+} low A/V which initiated at around $3x10^{-4}$ Ω^{-1}·cm^{-2}. At 5 g·L^{-1} Ca^{2+} high A/V, running the test for longer showed that the value of R_p^{-1} did eventually drop substantially below 10^{-4} Ω^{-1}·cm^{-2} and also presented the kink referred to earlier as the initiation of stage 4 of corrosion product growth.

8.2.5 Experiment Two – OCP Measurements

The corresponding OCP measurements from the second round of experiments are provided in Figure 8.5. The trends follow a similar pattern to the first round of experiments with OCP increasing significantly at low A/V no Ca^{2+} and 1 g·L^{-1} Ca^{2+}. Noticeably having left the test to run longer, the OCP at 5 g·L^{-1} Ca^{2+} high A/V also increased by around 100 mV by the end of the test showing a similar but delayed trend to that of low A/V experiments with no Ca^{2+} or 1 g·L^{-1} Ca^{2+}.

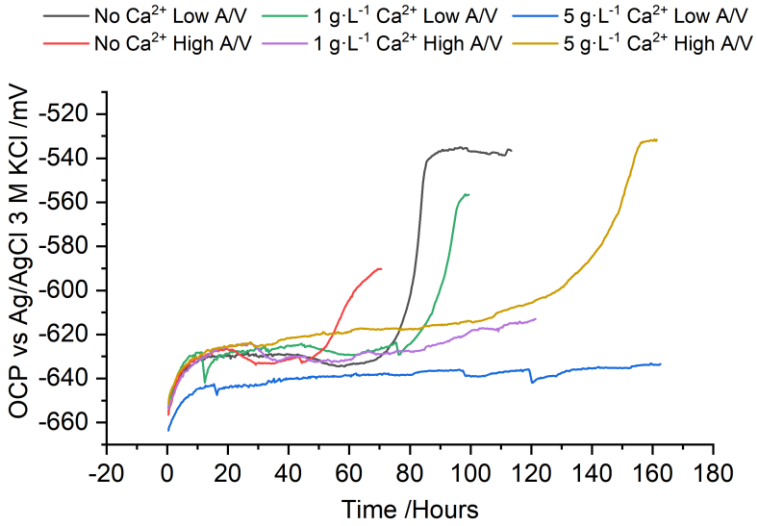

Figure 8.5: Comparison of OCP over time from second repeat of experiments on X65 steel at various bulk calcium concentrations and low and high (10.5 and 41.4 cm^2·L^{-1}) A/V ratios in CO_2 solution at 80 °C, 5.5 bar pCO_2

8.2.6 Gravimetric Analysis

To quantitively compare the general corrosion required before a protective layer is formed, the total metal loss per unit area of mass loss coupons is compared in Figure 8.6(a). The data corroborates the findings from LPR measurements, showing that greater metal loss across all calcium concentrations occurs with lower A/V when compared to high A/V. The data also shows that at low A/V there is a steady increase in metal loss as bulk calcium increases. At high A/V there is a less noticeable difference in metal loss at 0 and 1 g·L^{-1} Ca^{2+} but this increases at 5 g·L^{-1} Ca^{2+}.Very similar trends are also observed in corrosion product mass shown in Figure 8.6(b).

(a)

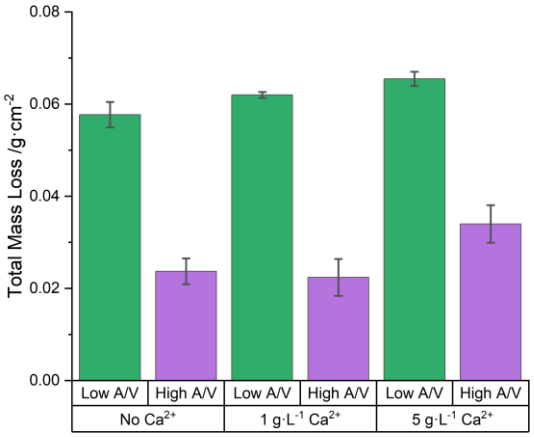

(b)

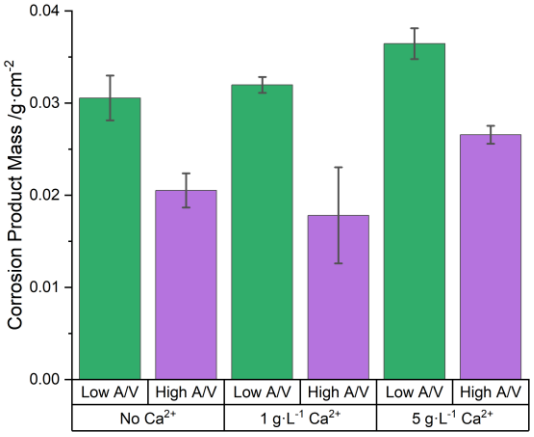

Figure 8.6: Gravimetric Analysis of X65 steel at various bulk calcium concentrations and low and high (10.5 and 41.4 cm^2·L^{-1}) A/V ratios in CO_2 solution at 80 °C, 5.5 bar pCO_2 (a) Total metal loss (b) Total corrosion product mass

8.3 Electrochemical Impedance Spectroscopy

To make comparisons between the different EIS spectra, the Nyquist response for each condition has been plotted in Figure 8.7 at comparable values of polarisation resistance based on the data in Figure 8.4.

(a)

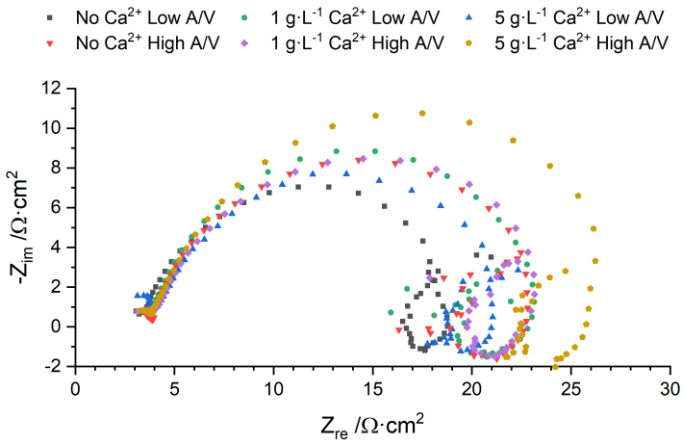

(b)

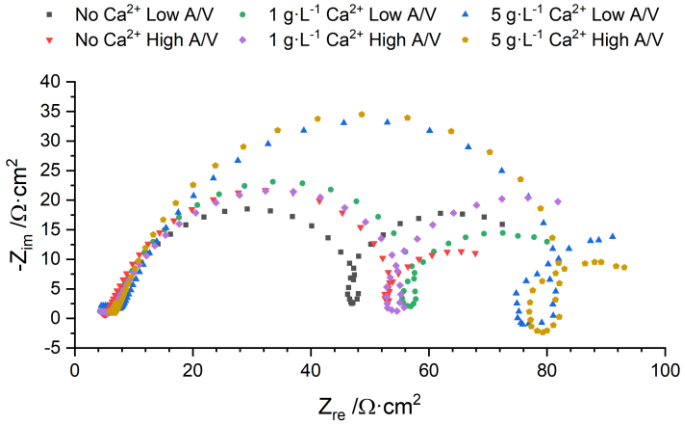

(c)

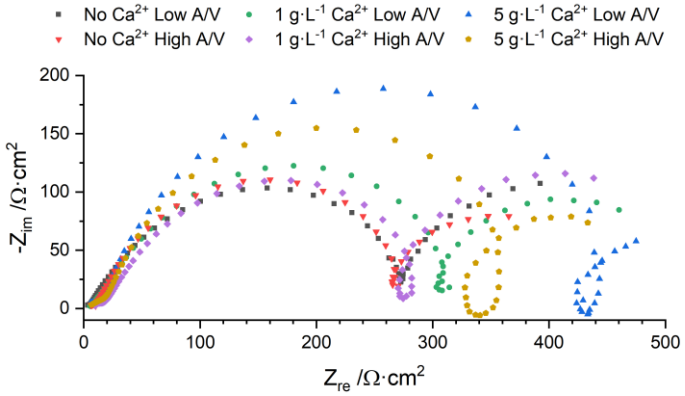

(d)

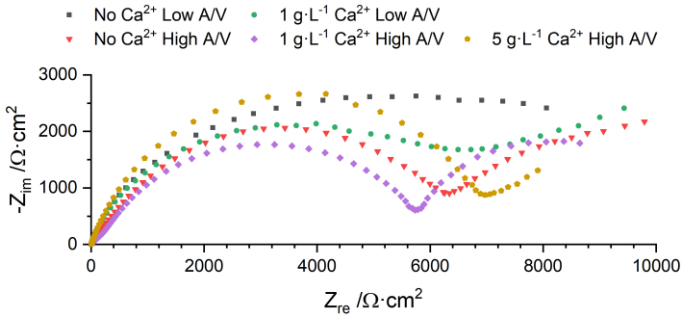

Figure 8.7: EIS Nyquist plots from experiments on X65 steel at various bulk calcium concentrations and low and high (10.5 and 41.4 $cm^2 \cdot L^{-1}$) A/V ratios in CO_2 solution at 80 °C, 5.5 bar pCO_2 (a) at the start of experiments (b) when R_p^{-1} reached ≈0.01 $\Omega^{-1} \cdot cm^{-2}$ (c) R_p^{-1} ≈ 0.002 $\Omega^{-1} \cdot cm^{-2}$ (d) R_p^{-1} ≈0.0001 $\Omega^{-1} \cdot cm^{-2}$

Figure 8.7(a) shows a very similar response profile across all conditions at the start of experiments with some differences in the magnitude of the response curve. Most notable is the reduced size of the high frequency loop at low A/V in the absence of calcium. This corroborates previous findings from polarisation data which shows this condition having a higher R_p^{-1} during the initial active corrosion stage. In contrast high A/V and 5 $g \cdot L^{-1}$ Ca^{2+} had the highest starting impedance and a notably larger adsorption loop. In Figure 8.7(b) the closest available Nyquist spectra that corresponds to a measured R_p^{-1} value of 0.01 $\Omega^{-1} \cdot cm^{-2}$ is plotted. In this data, the profile of the response is again very similar with the diffusion loop starting to become more distinguished at this stage for all conditions. The most significant comparison is again the conditions at high Ca^{2+} concentration which show a much larger adsorption loop and charge transfer loop relative to the low frequency diffusion loop when compared to lower Ca^{2+} concentration conditions.

Figure 8.7(c) provides Nyquist spectra that correspond to a measured R_p^{-1} value of 0.002 as this was the lowest value measured for 5 $g \cdot L^{-1}$ Ca^{2+} low A/V. At this stage the magnitude of low and high frequency loops is relatively similar at all conditions apart from 5 $g \cdot L^{-1}$ Ca^{2+} which is still dominated by the charge transfer loop with a significant adsorption loop.

Nyquist spectra that correspond to a measured R_p^{-1} value of 10^{-4} is plotted in Figure 8.7(d). At this stage the impedance response is starting to diverge at different conditions. Low A/V and no Ca^{2+} analysed in Chapter 6 shows a merged loop due to the close proximity of the time constants of the low and high frequency loops. In contrast, the low frequency loop at low A/V 1 $g \cdot L^{-1}$ Ca^{2+} is starting to straighten out suggesting a much larger diffusion impedance with much greater time constant. At all conditions at this stage, the adsorption loop is no longer visible.

Although not strictly comparable in terms of magnitude, for completeness the impedance response at the end of the experiments is included in Figure 8.8 to show how the profile of the response differs between the different test conditions. The most prominent difference being the response at high A/V with 5 $g \cdot L^{-1}$ Ca^{2+} which appears to show a single high impedance loop and no obvious indication of a second low frequency Warburg diffusion element.

The response curve at 5 g·L^{-1} Ca^{2+} high A/V is also noticeably less depressed when compared to other conditions particularly high A/V no Ca^{2+} and 1 g·L^{-1} Ca^{2+} which have a highly depressed charge transfer loop and straight low frequency portion.

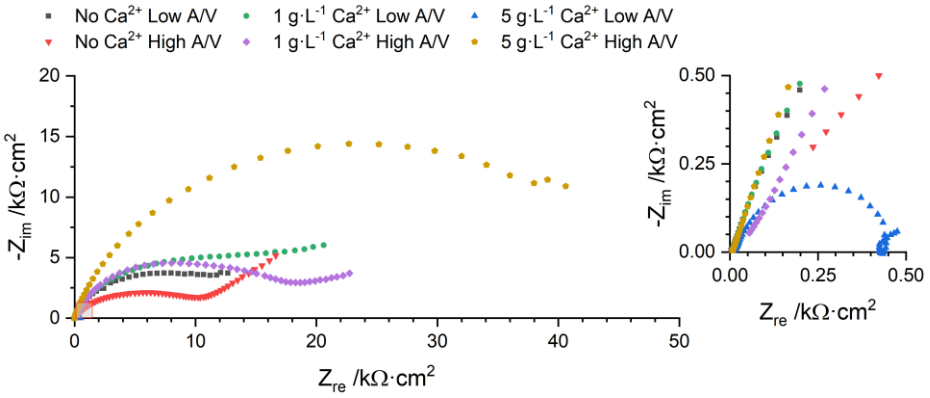

Figure 8.8: EIS Nyquist plots from the end of experiments on X65 steel at various bulk calcium concentrations and low and high (10.5 and 41.4 cm^2·L^{-1}) A/V ratios in CO_2 solution at 80 °C, 5.5 bar pCO_2

8.3.1 Analysis of Impedance Properties

Figure 8.9 to Figure 8.11 and Table 8.1 provide the fitted parameters following the methodology and EEC's developed in Chapter 6. As seen previously, both R_{ct} and R_W in Figure 8.9 increase with similar trends to each other and closely follow the trends observed in LPR data.

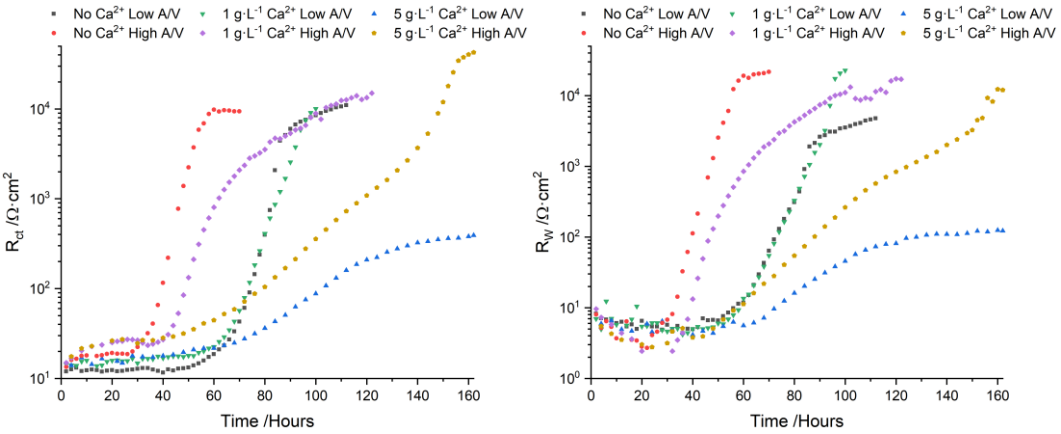

Figure 8.9: R_{ct} (left) and R_W (right) obtained by EIS fitting of impedance data from X65 steel at various bulk calcium concentrations and low and high (10.5 and 41.4 cm^2·L^{-1}) A/V ratios in CO_2 solution at 80 °C, 5.5 bar pCO_2

Figure 8.10 provides the fitted values of Q_{dl} and the conversion to C_{dl} assuming surface distributed capacitance.

The data suggest that the capacitance reduces to a much lower value at high A/V and low calcium concentrations. The data in Figure 8.11 gives the corresponding equivalent time constant $R_{ct}{\cdot}C_{dl}$ and active surface area. Across all conditions the trends are similar with an initial increase in capacitance while R_{ct} is low and relatively stable, this results in an increase in $R_{ct}{\cdot}C_{dl}$ and an increase in active surface area. At the onset of corrosion product nucleation and growth, R_{ct} begins to increase while C_{dl} also decreases. The trend in C_{dl} decrease is highly comparable to R_p^{-1} resulting in some small change in $R_{ct}{\cdot}C_{dl}$. The most notable change in $R_{ct}{\cdot}C_{dl}$ is the experiment at high A/V and 5 $g{\cdot}L^{-1}$ Ca^{2+} where R_{ct} is the dominate contributor to the resistance as opposed to R_W.

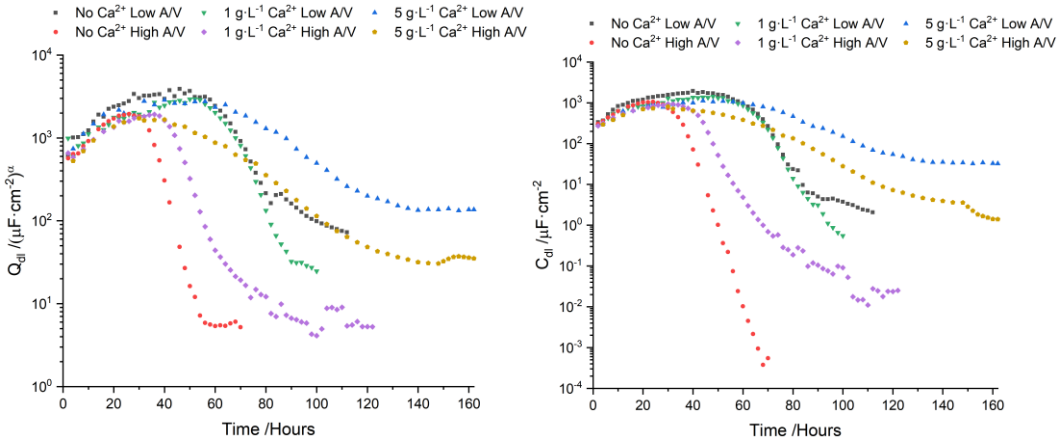

Figure 8.10: Q_{dl} (left) and C_{dl} (right) obtained by EIS fitting of impedance data from X65 steel at various bulk calcium concentrations and low and high (10.5 and 41.4 $cm^2{\cdot}L^{-1}$) A/V ratios in CO_2 solution at 80 °C, 5.5 bar pCO_2

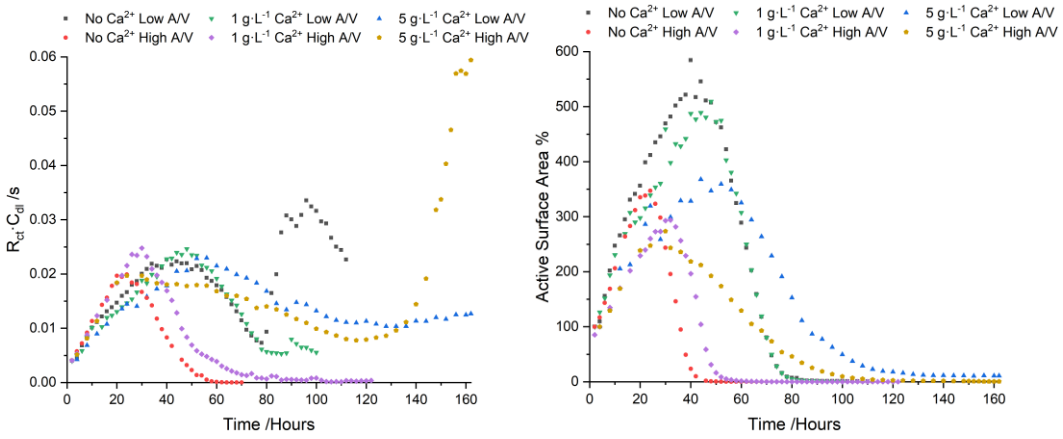

Figure 8.11: $R_{ct}{\cdot}C_{dl}$ (left) and Active Surface Area (right) obtained by EIS fitting of impedance data from X65 steel at various bulk calcium concentrations and low and high (10.5 and 41.4 $cm^2{\cdot}L^{-1}$) A/V ratios in CO_2 solution at 80 °C, 5.5 bar pCO_2

Table 8.1: Fitted Impedance Parameters

Condition	R_e $\Omega \cdot cm^2$	R_{ct} $\Omega \cdot cm^2$	Q_{dl} $(\mu F \cdot cm^{-2})^{\alpha}$	α	R_W $\Omega \cdot cm^2$	τ_D s	ϕ_W	R_{ads} $\Omega \cdot cm^2$	L_{ads} $H \cdot cm^2$	χ^2
4 Hours										
No Ca^{2+} Low A/V	3.5	13	1009	0.85	7	35.2	1.0	3.7	0.97	0.145
No Ca^{2+} High A/V	3.8	16	637	0.91	5	46.6	1.0	5.1	0.84	0.088
1 $g \cdot L^{-1}$ Ca^{2+} Low A/V	3.8	14	598	0.92	5	26.7	1.0	5.8	1.58	0.214
1 $g \cdot L^{-1}$ Ca^{2+} High A/V	3.7	17	584	0.91	7	53.7	1.0	5.4	1.06	0.119
5 $g \cdot L^{-1}$ Ca^{2+} Low A/V	3.9	14	739	0.87	6	35.5	1.0	4.7	0.69	0.200
5 $g \cdot L^{-1}$ Ca^{2+} High A/V	3.9	18	526	0.91	5	50.3	1.0	6.3	1.09	0.154
24 Hours										
No Ca^{2+} Low A/V	3.4	12	2584	0.89	5	43.2	1.0	3.3	1.40	0.083
No Ca^{2+} High A/V	3.9	19	1885	0.90	4	73.0	1.0	5.2	2.40	0.047
1 $g \cdot L^{-1}$ Ca^{2+} Low A/V	4.2	16	1714	0.90	6	53.2	1.0	5.1	2.62	0.062
1 $g \cdot L^{-1}$ Ca^{2+} High A/V	3.6	26	1549	0.89	2	75.0	1.0	7.9	3.88	0.085
5 $g \cdot L^{-1}$ Ca^{2+} Low A/V	4.2	15	1971	0.87	5	35.9	1.0	3.7	1.56	0.267
5 $g \cdot L^{-1}$ Ca^{2+} High A/V	4.11	27	1538	0.87	3	45.4	1.0	7.4	3.14	0.110
48 Hours										
No Ca^{2+} Low A/V	4.1	13	3439	0.87	7	50.0	1.0	3.6	1.62	0.128
No Ca^{2+} High A/V	5.1	1385	27	0.79	1304	11.5	0.9	351.1	67.53	5.184
1 $g \cdot L^{-1}$ Ca^{2+} Low A/V	4.3	17	2637	0.89	5	47.3	1.0	3.9	1.59	0.046
1 $g \cdot L^{-1}$ Ca^{2+} High A/V	9.9	85	505	0.80	130	30.0	1.0	38.2	14.23	0.276
5 $g \cdot L^{-1}$ Ca^{2+} Low A/V	4.5	19	2593	0.84	4	41.7	1.0	5.8	2.38	0.160
5 $g \cdot L^{-1}$ Ca^{2+} High A/V	4.67	32	1359	0.86	5	19.4	1.0	9.3	2.48	0.132
96 Hours										
No Ca^{2+} Low A/V	5.1	7560	114	0.71	3087	21.4	1.0			4.405
No Ca^{2+} High A/V	5.0	9417	5	0.54	21605	174.1	0.8			1.2
1 $g \cdot L^{-1}$ Ca^{2+} Low A/V	5.0	7479	29	0.72	17353	100.0	0.6			16.2
1 $g \cdot L^{-1}$ Ca^{2+} High A/V	5.0	6569	6	0.70	10028	49.7	0.7	1057.7	627.07	0.752
5 $g \cdot L^{-1}$ Ca^{2+} Low A/V	7.61	75	584	0.85	38	29.7	1.0	24.2	8.38	0.568
5 $g \cdot L^{-1}$ Ca^{2+} High A/V	14.71	277	140	0.86	189	25.9	1.0	103.5	37.68	1.630

8.4 Surface Analysis

The SEM images Figure 8.12 reveal that even after long exposure times there is still substantial exposed Fe_3C at the surface at all calcium concentrations when the A/V ratio is lowered. The morphology at the end of electrochemical tests is comparable to that observed in Chapter 5 mass loss experiments and does not appear to have changed as the test duration has increased.

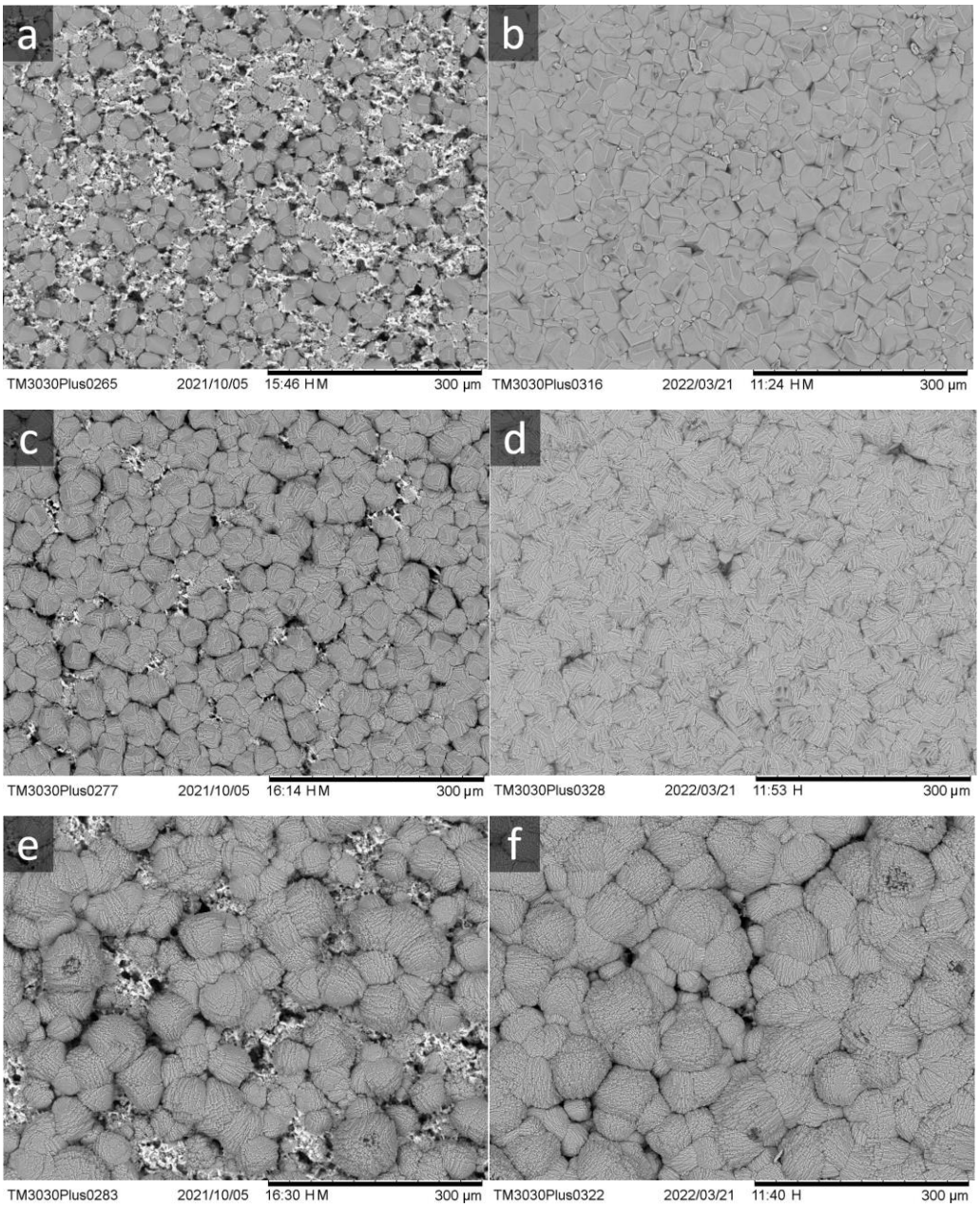

Figure 8.12: 250x Magnification top surface SEM images of corrosion product coverage on X65 steel after immersion at 80 °C and 5.5 bar pCO_2 using high (41.4 $cm^2 \cdot L^{-1}$) and low (10.5 $cm^2 \cdot L^{-1}$) A/V ratios (a) No Ca^{2+} low A/V (b) No Ca^{2+} high A/V (c) 1 $g \cdot L^{-1}$ Ca^{2+} low A/V (d) 1 $g \cdot L^{-1}$ Ca^{2+} high A/V (e) 5 $g \cdot L^{-1}$ Ca^{2+} low A/V (f) 5 $g \cdot L^{-1}$ Ca^{2+} high A/V

8.4.1 XRD Analysis

The results of X-ray diffraction are presented in Figure 5.22. ICDD Reference data for pure siderite (00-008-0133) and pure calcite (00-005-0586) were used to compare peak shifts.

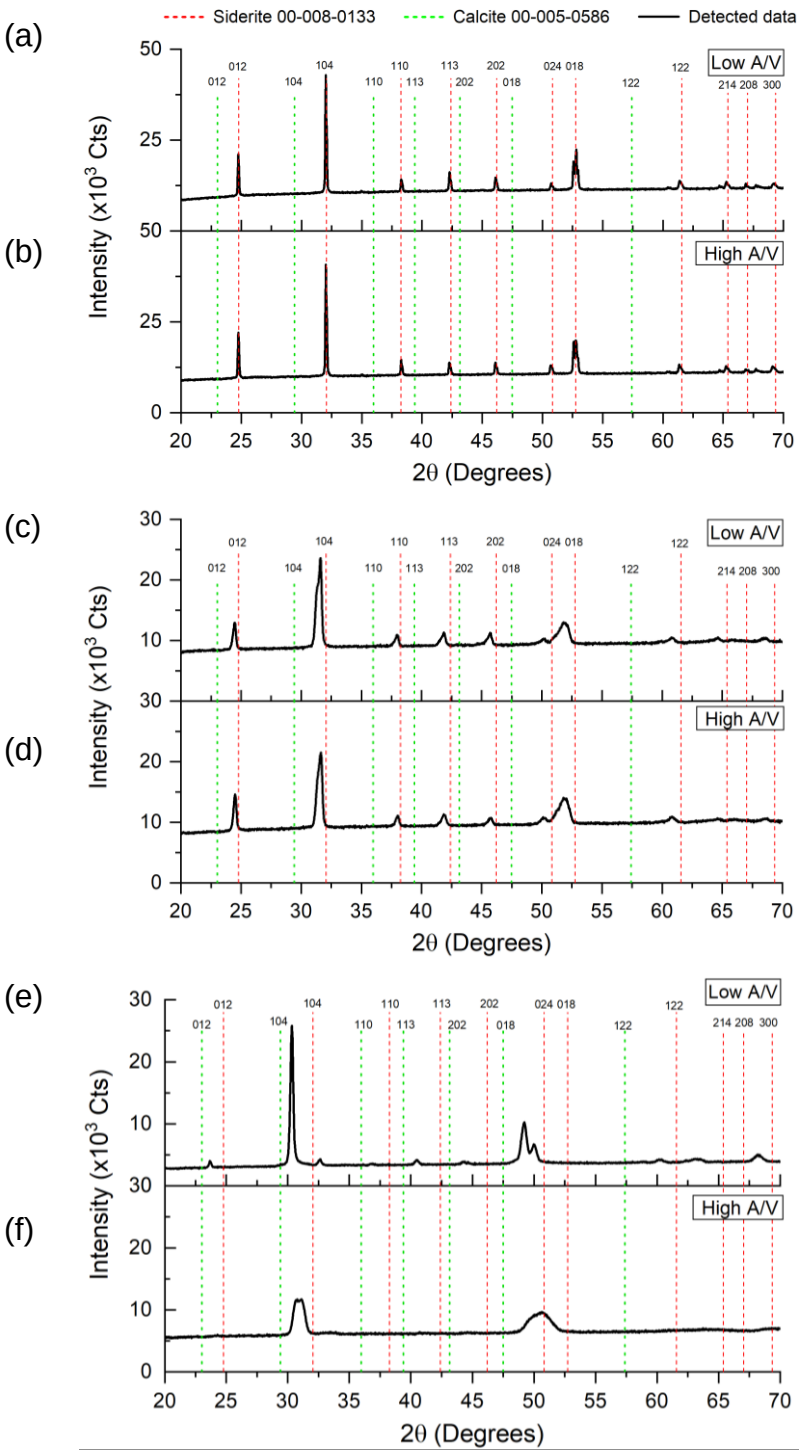

Figure 8.13: Powder diffraction patterns of corrosion scales grown at 80 °C and 5.5 bar pCO_2 using high (41.4 $cm^2 \cdot L^{-1}$) and low (10.5 $cm^2 \cdot L^{-1}$) A/V ratios (a) No Ca^{2+} low A/V (b) No Ca^{2+} high A/V (c) 1 $g \cdot L^{-1}$ Ca^{2+} low A/V (d) 1 $g \cdot L^{-1}$ Ca^{2+} high A/V (e) 5 $g \cdot L^{-1}$ Ca^{2+} low A/V (f) 5 $g \cdot L^{-1}$ Ca^{2+} high A/V

The trends observed in XRD analysis are again comparable to the 3 day study conducted in Chapter 5 as compared in Table 8.2. The data shows a marginal decrease in calcium for the longer electrochemical tests with the only significant change happening at high A/V and 5 $g \cdot L^{-1}$ bulk Ca^{2+} which drops from an average of 50% calcium to 42% in the $Fe_xCa_yCO_3$. It was also shown in Chapter 5 that the calcium concentration can vary through the film with iron enrichment occurring at the outer surface which may influence the powder diffraction analysis. Cross-sections were therefore performed to analyse the through layer properties.

Table 8.2: y values for $Fe_xCa_yCO_3$ using XRD peak shifts – a comparison between (a) 3 day mass loss tests and (b) electrochemical tests

A/V Ratio ($cm^2 \cdot L^{-1}$)	**Bulk Ca^{2+} ($g \cdot L^{-1}$)**					
	0		**1**		**5**	
	(a)	(b)	(a)	(b)	(a)	(b)
10.5	0	0	0.18	0.16	0.64	0.63
41.4	0	0	0.16	0.15	0.50	0.42

8.5 Cross-sectional Analysis

8.5.1 EDX Analysis

The EDX maps in Figure 8.14 reveal how the corrosion scale layers have formed after longer term electrochemical tests. At low A/V and 0 and 1 $g \cdot L^{-1}$ Ca^{2+} the layer has formed almost entirely within the exposed Fe_3C matrix. The deepest layer of Fe_3C occurs at low A/V no Ca^{2+} which suggest the highest level of corrosion occurring before corrosion product formation. This observation agrees with earlier observations from mass loss testing, LPR and EIS measurement though it is not yet clear why the free corrosion rate is lower when calcium is present.

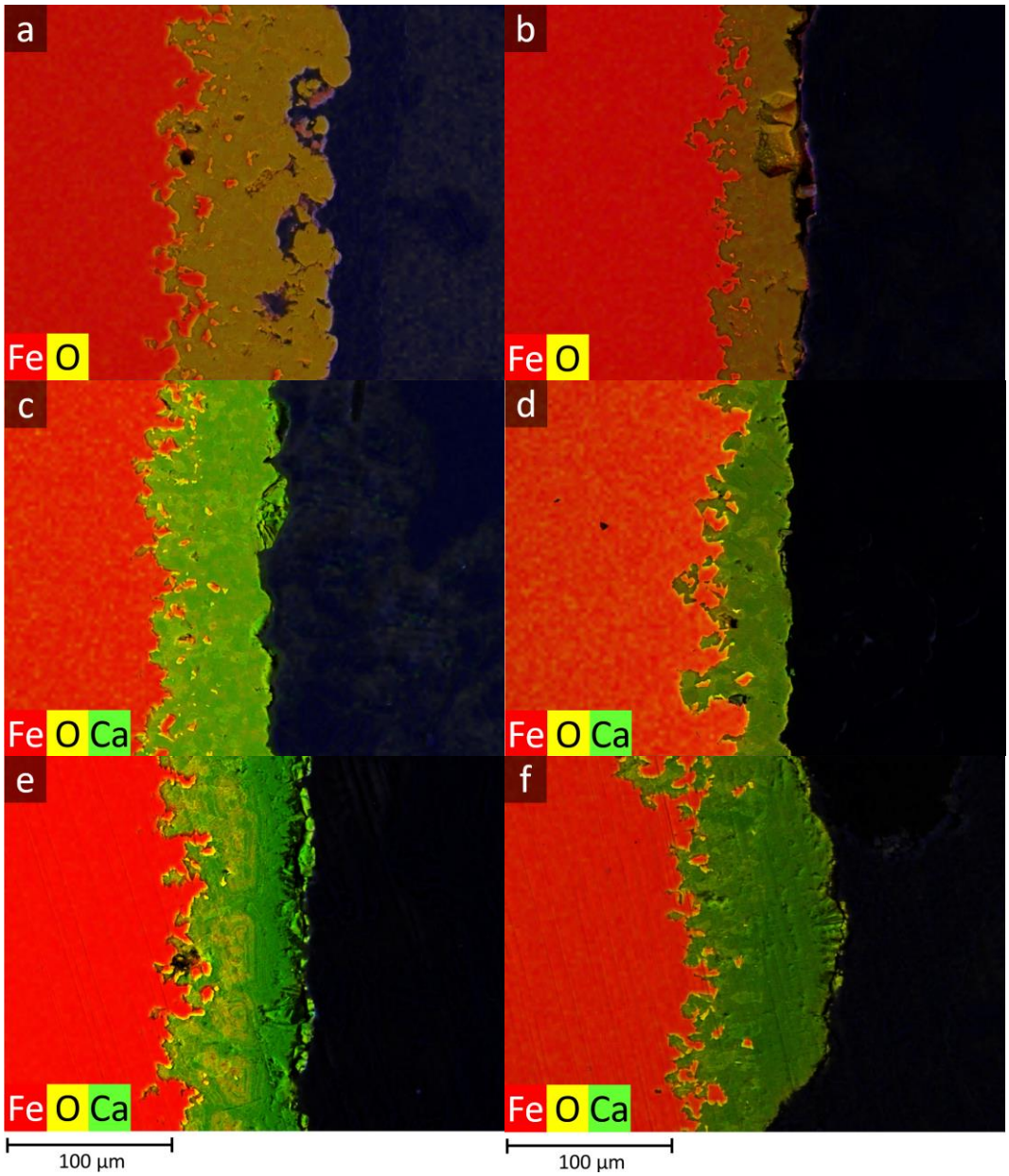

Figure 8.14: Cross-sectional EDX maps of illustrating composition of corrosion scales grown over 3 days at 80 °C and 5.5 bar pCO_2 using high (41.4 $cm^2 \cdot L^{-1}$) and low (10.5 $cm^2 \cdot L^{-1}$) A/V ratios
(a) 0 Ca^{2+} low A/V (b) 0 Ca^{2+} high A/V (c) 1 $g \cdot L^{-1}$ Ca^{2+} low A/V
(d) 1 $g \cdot L^{-1}$ Ca^{2+} high A/V (e) 5 $g \cdot L^{-1}$ Ca^{2+} low A/V (f) 5 $g \cdot L^{-1}$ Ca^{2+} high A/V

In terms of layer composition the corrosion scales appear relatively uniform with the exception of 5 $g \cdot L^{-1}$ Ca^{2+} low A/V which exhibits a complex layered growth pattern as highlighted in Figure 8.15. To investigate this further STEM/TEM analysis was performed.

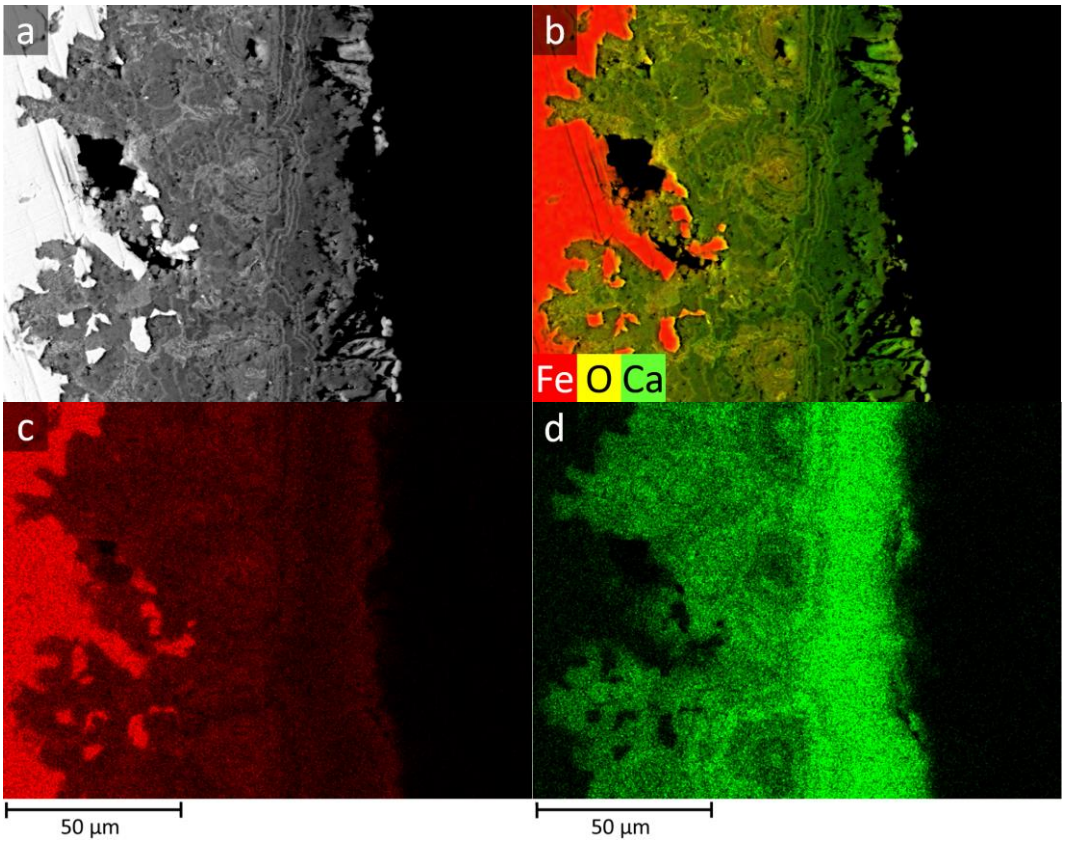

Figure 8.15: Enhanced SEM/EDX maps of corrosion scale formation at 5 g·L^{-1} Ca^{2+} low A/V (a) SEM BSE image (b) layered EDX map (c) Fe map (d) Ca map

8.6 $Fe_xCa_yCO_3$ Growth and Fe_3C Analysis

Selected Area Electron Diffraction (SAED) and STEM EDX were performed in accordance with Section 4.7.7 to evaluate the complex layer that formed at 5 g·L^{-1} Ca^{2+} low A/V. A layer of pure $FeCO_3$ was also analysed for comparison. The electron diffraction was also used as a means to verify the Fe_3C that was observed in all previous cross sectional images. Figure 8.16 provides cross section SEM images which clearly shows the original surface level and the crystal 'bands' that have occurred which appear to emanate from sites around Fe_3C. Figure 8.17 provides images of the TEM lamella milled over the region of interest using a FIB. A defect at a step boundary in the left hand window and Fe_3C lamella in the right hand window were used as reference features to help locate the electron beam when changing between TEM and STEM.

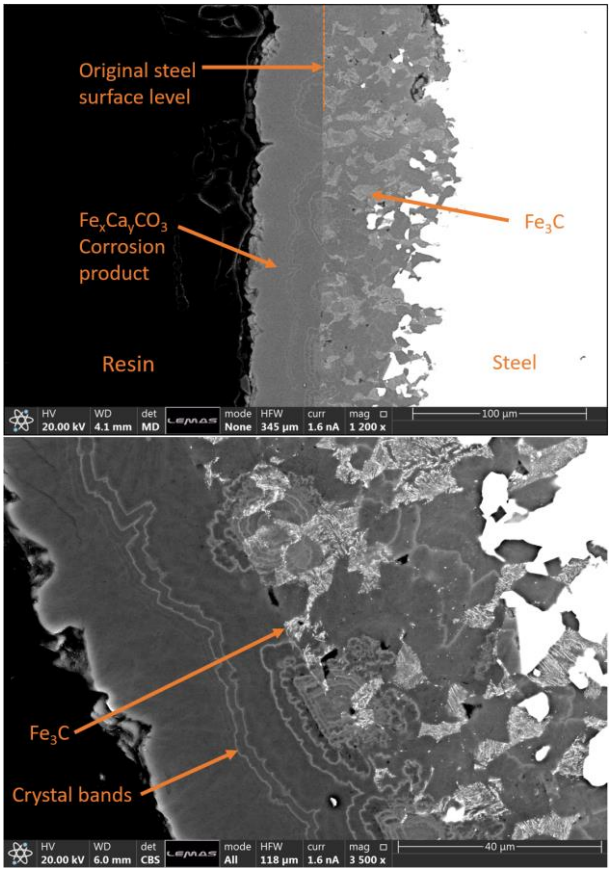

Figure 8.16: SEM images of cross section through corrosion scale formed at 5 g·L^{-1} Ca^{2+} low A/V prior to TEM sample extraction

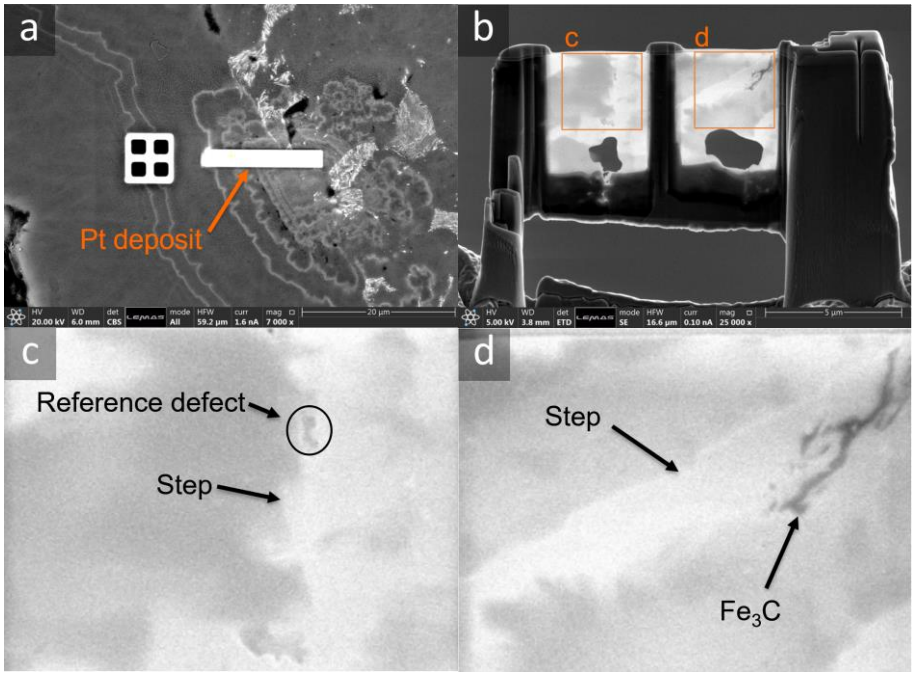

Figure 8.17: SEM images of TEM sample preparation for corrosion product formed at 5 g·L^{-1} Ca^{2+} low A/V (a) Platinum deposition over region of interest (b) Thinned 'windows' for TEM analysis highlighting apparent crystal steps and Fe_3C (c) close up of left-hand window (d) close up of right-hand window

8.6.1 STEM Analysis of Crystal Boundary Compositions and Porosity

STEM EDX analysis around the reference defect highlighted in Figure 8.17(c) is provided in Figure 8.18.

(a)

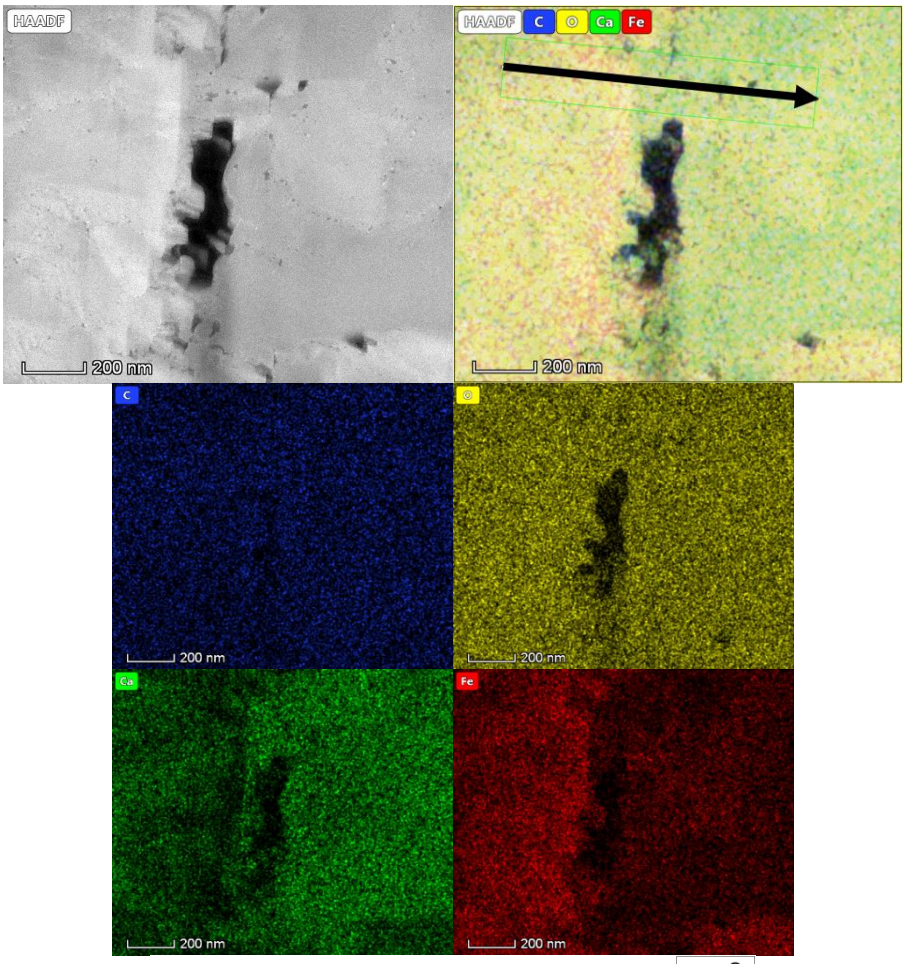

(b)

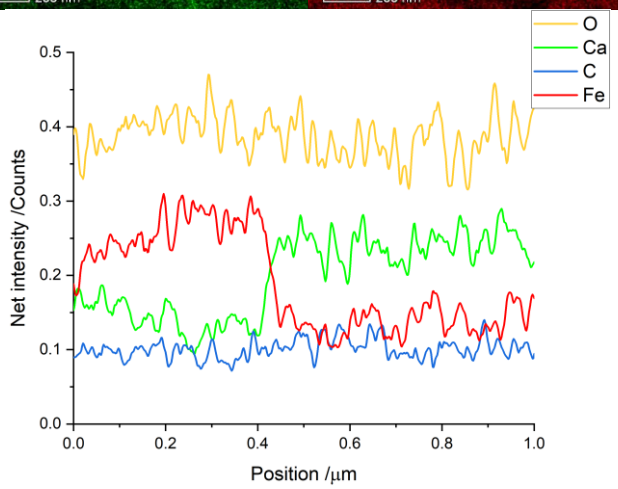

Figure 8.18: STEM EDX analysis of region ‘c’ in Figure 8.17 showing crystal steps in $Fe_xCa_yCO_3$ formed in 5 g·L^{-1} Ca^{2+} low A/V conditions (a) EDX colour maps with top right image indicating length and direction of line scan (b) corresponding intensity data from EDX line scan

STEM EDX analysis around the Fe_3C highlighted in Figure 8.17(d) is provided in Figure 8.19.

(a)

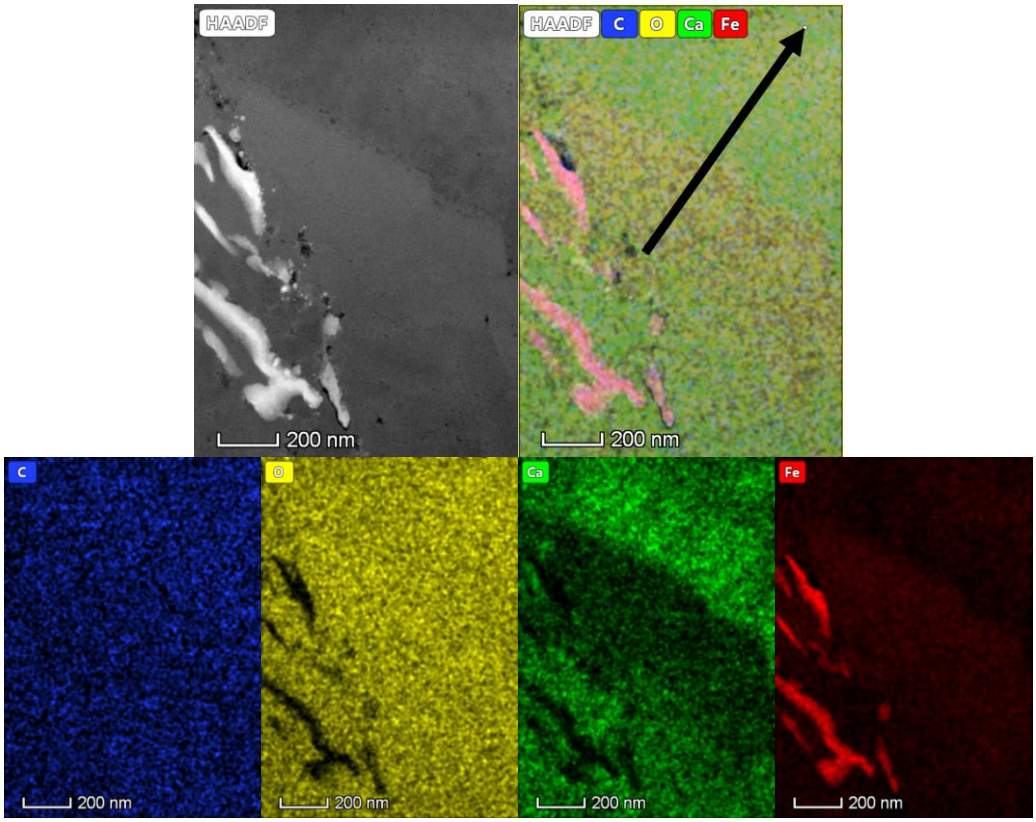

(b)

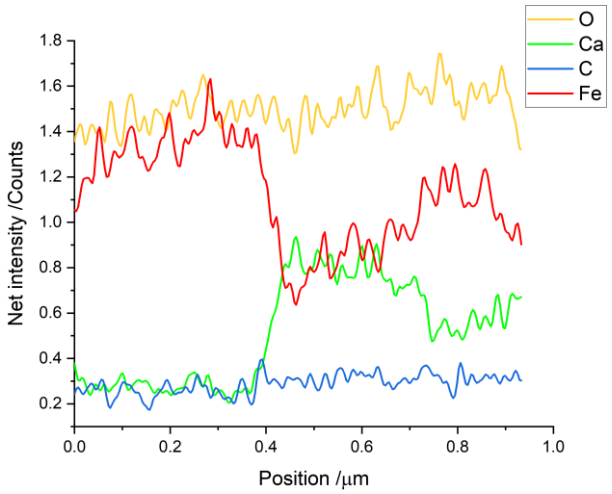

Figure 8.19: STEM EDX analysis of region 'd' in Figure 8.17 showing crystal steps in $Fe_xCa_yCO_3$ formed in 5 $g \cdot L^{-1}$ Ca^{2+} low A/V conditions (a) EDX colour maps with top right image indicating length and direction of line scan (b) corresponding intensity data from EDX line scan

The data from both regions reveals a clear transition in calcium and iron concentrations around the crystal steps that were visible in SEM images. Carbon and Oxygen levels remain stable across the step.

The lighter areas closer to the edge of the step are more iron rich and are immediately followed by a more calcium rich area. The data suggests that the $Fe_xCa_yCO_3$ composition is changing as the crystal grows. The EDX mapping of the Fe_3C is also as expected showing a consistent level of Carbon, high levels of Fe and the absence of Oxygen when compared to the $Fe_xCa_yCO_3$ surrounding it. Another observation from the high resolution images is the level of nano-scale porosity in the layer which is particularly evident at the edges of each crystal step and near to the Fe_3C as highlighted in Figure 8.20. The same porosity was not present in the pure $FeCO_3$ layers analysed.

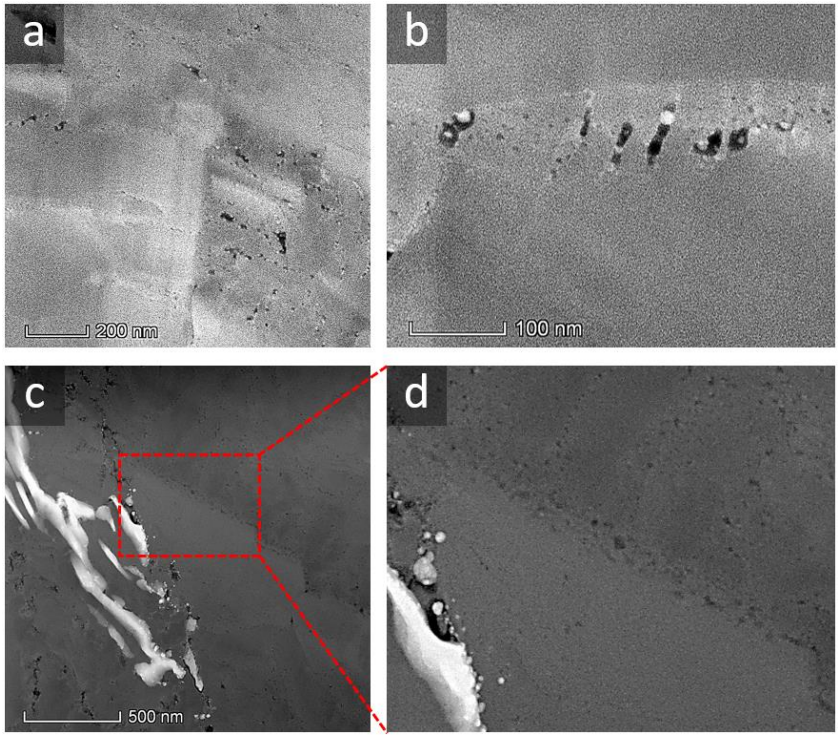

Figure 8.20: Highlighing areas of porosity within $Fe_xCa_yCO_3$ structure (a) general porosity within layer (b) general porosity enlarged (c) porosity near Fe_3C (d) porosity at crystal step/grain boundary

8.6.2 Electron Diffraction

To support the findings from STEM EDX analysis and to verify the presence of crystalline $Fe_xCa_yCO_3$, electron diffraction was performed on the region highlighted in Figure 8.17(c) / Figure 8.18. An area either side of the reference defect was selected as illustrated in Figure 8.21 with region A being more iron rich than region B according to EDX data. The resulting diffraction patterns are presented in Figure 8.22. The pattern in Figure 8.22(a) clearly shows some level of node splitting when compared to the Figure 8.22(b) which will be discussed later.

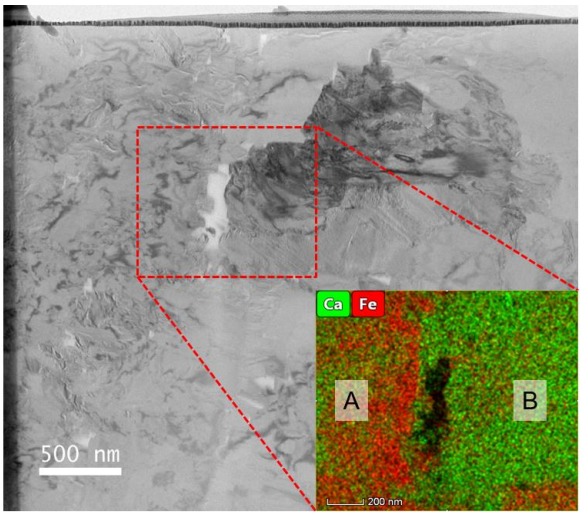

Figure 8.21: TEM image of $Fe_xCa_yCO_3$ region from Figure 8.17(c) showing areas A and B where electron diffraction was performed

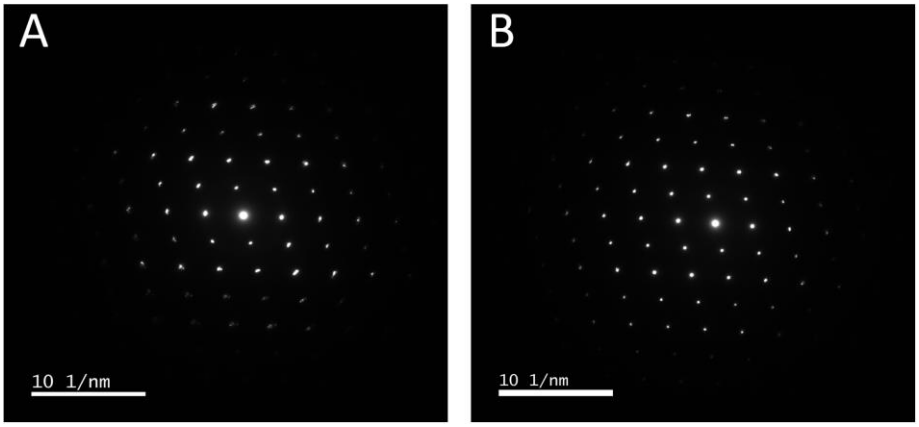

Figure 8.22: Electron diffraction patterns on [010] zone axis from $Fe_xCa_yCO_3$ corresponding to regions A and B in Figure 8.21

8.6.3 Electron Diffraction Pattern Indexing

In order to correctly index the diffraction patterns and to account for shifts due to beam alignment, the analysis was repeated on a second sample from the experiments in the absence of calcium which produced pure $FeCO_3$ as shown in earlier XRD data in Figure 8.13(a). The settings from the TEM were replicated in SingleCrystal® 4.1 to simulate the reciprocal lattice pattern in order to orient and index the observed electron diffraction patterns.

The zone axis for diffraction patterns was identified based on the average distance between at least 5 nodes along each plane of the reciprocal lattice. The measurements were cross-referenced with d-spacing data from the ICDD database to identify each plane. This confirmed that the patterns were oriented on the [010] zone axis.

The simulated lattices for pure Siderite and Calcite on their respective [010] zone axes are overlayed in Figure 8.23 to show the shift in lattice spacing.

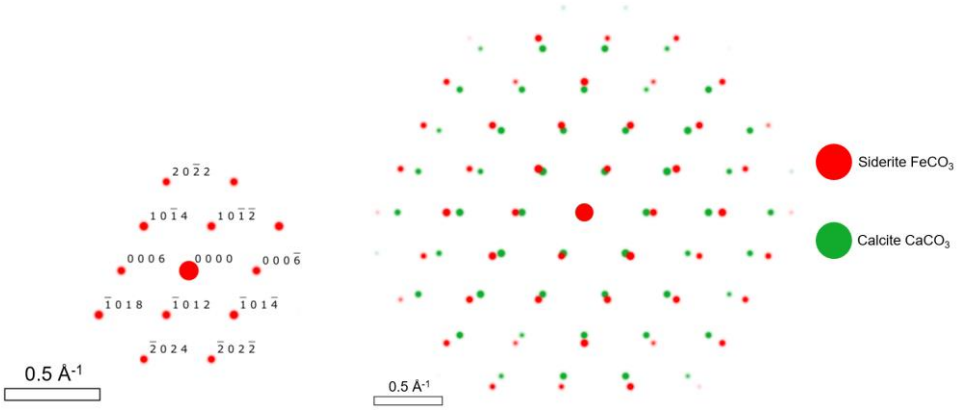

Figure 8.23: Simulated electron diffraction pattern for Siderite on [010] zone axis with plane indexing (left) and overlayed simulation of Calcite and Siderite on [010] zone axis (right) using SingleCrystal® 4.1.

When analysing the diffraction pattern for the $FeCO_3$ layer, the measured values of d-spacing for each crystal plane were between 3.0 and 3.3% greater than the values in the ICDD database for Siderite 00-08-0133 (3.0% for the 104 spacing). To estimate the mole fraction of Ca in the crystal, Equation (5.30) was used assuming the 3% shift in measurements due to beam alignment was consistent between the two specimens analysed giving:

$$\mathrm{y} = \frac{\mathrm{d}_{\mathrm{Fe_xCa_yCO_3}.measured} - \mathrm{d}_{\mathrm{FeCO_3}.measured}}{\Delta \mathrm{d}} \tag{8.1}$$

Where $\Delta \mathrm{d}$ was defined in Equation (5.30) as the difference between ICDD values for 104 d-spacing for Calcite and Siderite.

The estimated compositions for sites A and B in Figure 8.21 are subsequently $Fe_{0.55}Ca_{0.45}CO_3$ and $Fe_{0.26}Ca_{0.74}CO_3$ respectively. This indicates that the composition changes substantially as was suggested in the EDX line scans, switching from Fe rich to Ca rich across the bands. The shift in spacing is visualised in Figure 8.24 which also includes a diffraction pattern for the $FeCO_3$ layer.

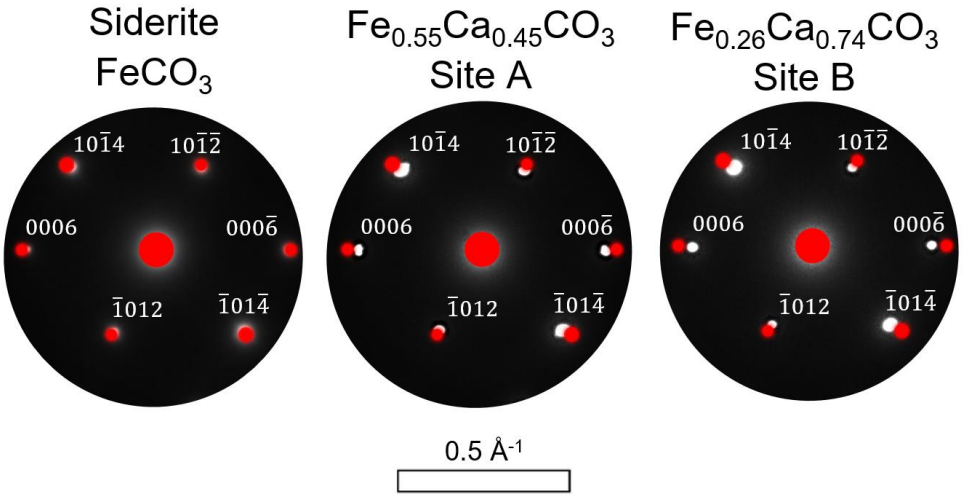

Figure 8.24: Comparison of reciprocal lattice patterns from electron diffraction for $FeCO_3$ and $Fe_xCa_yCO_3$ at two sites. Diffraction images shown with white dots overlayed with simulated [010] pattern for pure Siderite ($FeCO_3$) shown with red dots.

8.6.4 Electron Diffraction Node Splitting

As mentioned, a range of diffraction images taken of the $Fe_xCa_yCO_3$ layer showed some level of distortion or splitting of the observed diffraction nodes. This was only observed in in the $Fe_xCa_yCO_3$ and was more notable when the calculated mole fraction of calcium was close to 0.5. The node splitting could be attributed to lattice misalignment due to discontinuities caused by the incorporation of calcium in to the $FeCO_3$ lattice or conversely Fe in to the $CaCO_3$ lattice. A comparison between the $FeCO_3$ layer diffraction pattern and an area of mixed carbonate showing an almost 50/50 mix of iron and calcium is shown in Figure 8.25.

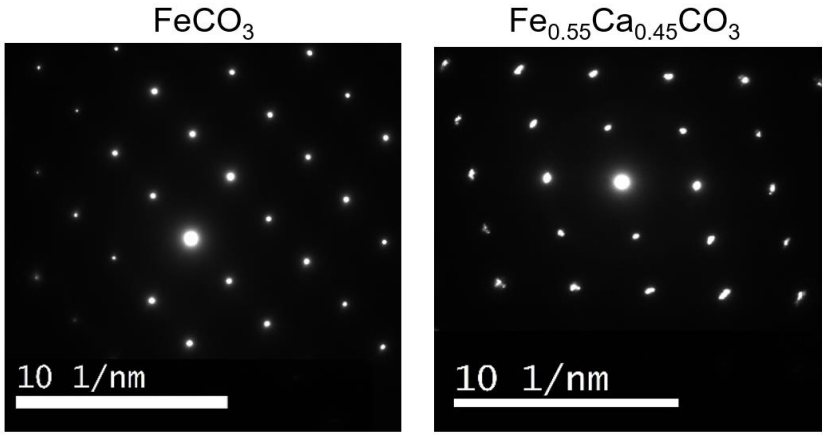

Figure 8.25: Comparison of pure single crystal diffraction of $FeCO_3$ (left) compared with mixed $Fe_{0.55}Ca_{0.45}CO_3$ (right) showing evidence of node divergence

8.6.5 Electron Diffraction of Fe_3C

The Fe_3C lamella identified throughout this work was verified whilst performing electron diffraction. Figure 8.26 shows the TEM image and corresponding diffraction pattern for the Fe_3C highlighted in Figure 8.17 and Figure 8.19. The nano-crystallinity of the material created a complex radial diffraction pattern which was interpreted using ImageJ to obtain the spacing of the most intense rings. The spacing was matched to ICDD reference 00-003-0400 as shown in Table 8.3.

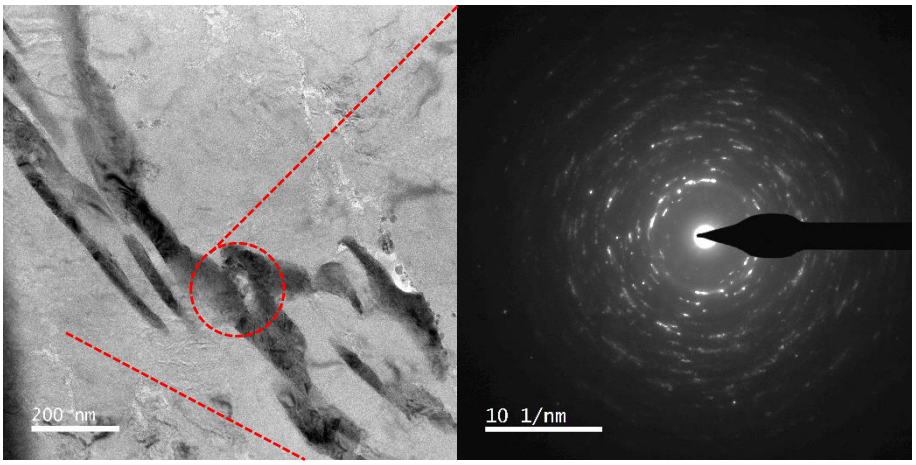

Figure 8.26: TEM image of suspected Fe_3C and corresponding electron diffraction image

Table 8.3: Comparison of ICDD reference data for Fe_3C d-spacings with measured from SAED

Ring ID.	d /Å		% diff.
	00-003-0400	Measured	
1	3.4	3.52	3.5
4	2.5	2.46	-1.4
6	2.06	2.07	0.4
8	1.82	1.82	0
9	1.7	1.75	2.7
16	1.24	1.23	-0.7
17	1.2	1.19	-0.7
18	1.16	1.17	0.8
19	1.12	1.15	2.5
21	1.04	1.04	-0.3

8.7 Localised Corrosion

Having completed an in depth analysis of corrosion layer development under different A/V ratios and bulk Ca^{2+} concentrations, the final stage of research was to assess what affect this would have on localised corrosion behaviour. Mass loss coupons from each experimental condition were analysed with white light interferometry after corrosion product removal following the procedures outlined in Sections 4.7.1 and 4.7.8. Topographic plots from three sites on each specimen are provided in Figure 8.27 and Figure 8.28. The mean of the top ten deepest pit-like-features (PLF's) from each site was taken and averaged for each experimental condition and plotted in Figure 8.29. Surface roughness parameters are also included in Figure 8.30.

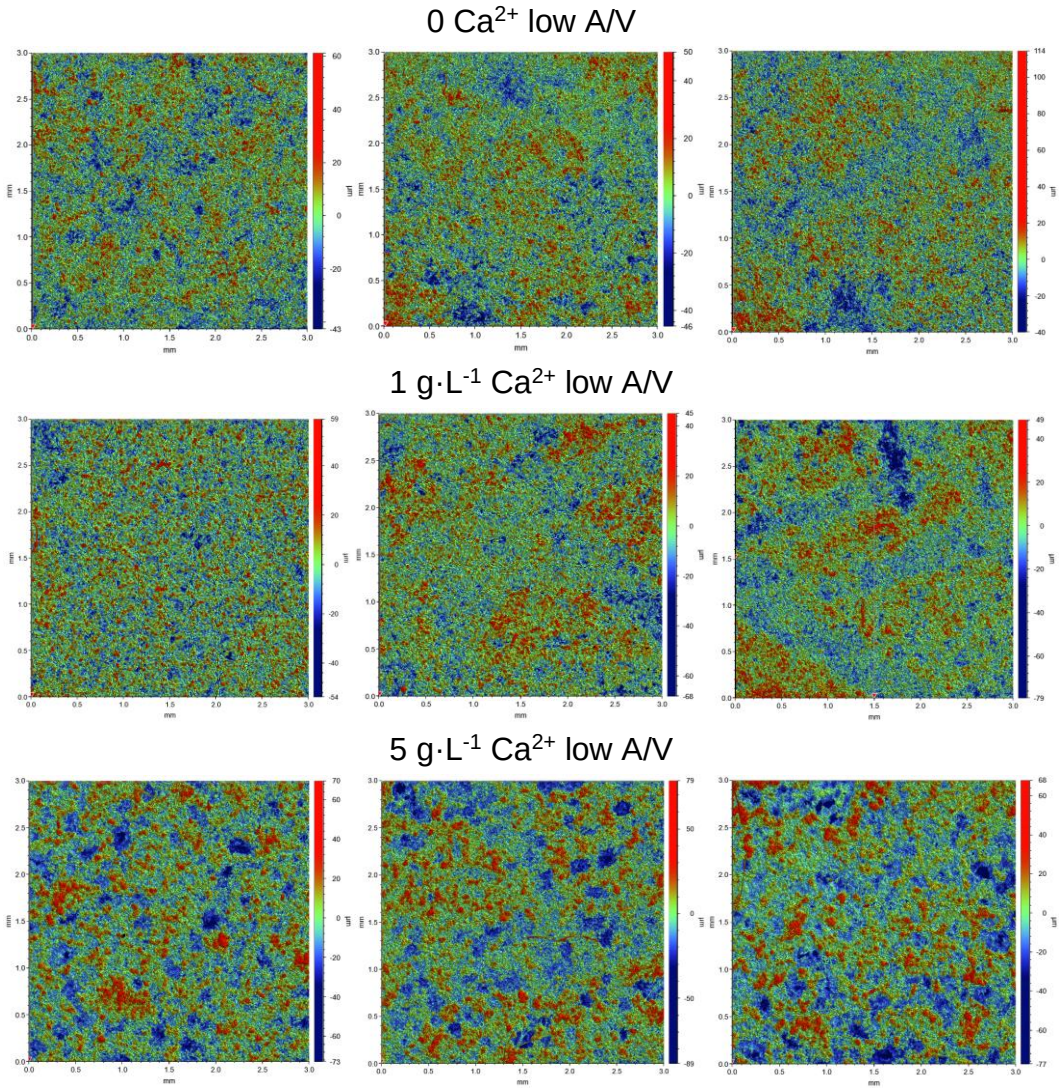

Figure 8.27: Colour maps produced from white light interferometry on surface of X65 carbon steel after corrosion product removal and post exposure to 80 °C and 5.5 bar pCO_2 using low (10.5 $cm^2 \cdot L^{-1}$) A/V ratio and initial bulk Ca^{2+} concentration as stated

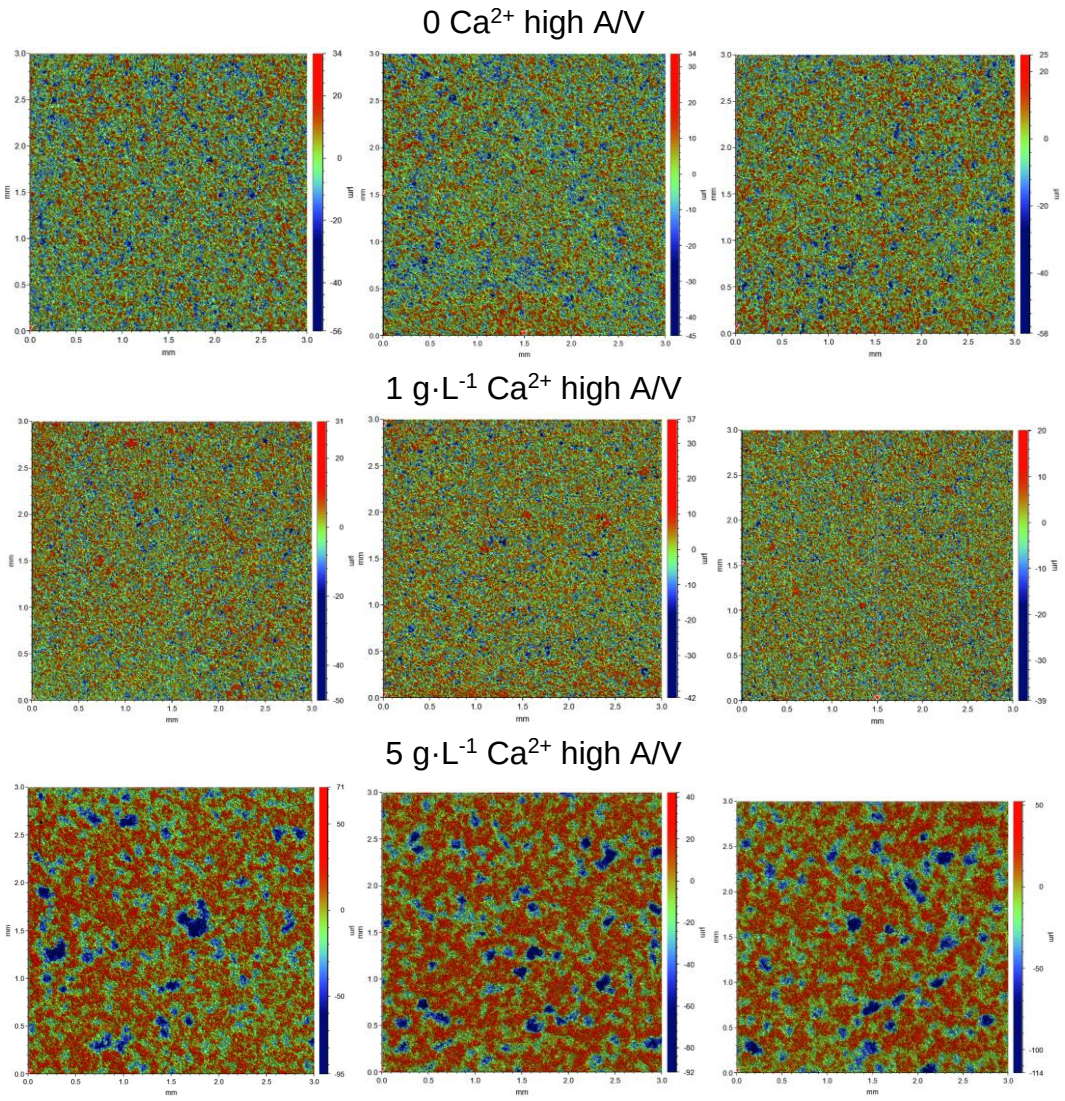

Figure 8.28: Colour maps produced from white light interferometry on surface of X65 carbon steel after corrosion product removal and post exposure to 80 °C and 5.5 bar pCO_2 using high (41.4 $cm^2 \cdot L^{-1}$) A/V ratio and initial bulk Ca^{2+} concentration as stated

The images in Figure 8.27 and Figure 8.28 show that 0 and 1 $g \cdot L^{-1}$ Ca^{2+} are generally comparable to each other with greater heterogeneity of the surface at lower A/V. In contrast the 5 $g \cdot L^{-1}$ Ca^{2+} conditions produce much more notable localised corrosion at both A/V ratios and particularly at the higher A/V. This is evidenced in Figure 8.29 which shows that the average PLF depth is more than doubled when going from 0 Ca^{2+} to 5 $g \cdot L^{-1}$ Ca^{2+} and a high A/V.

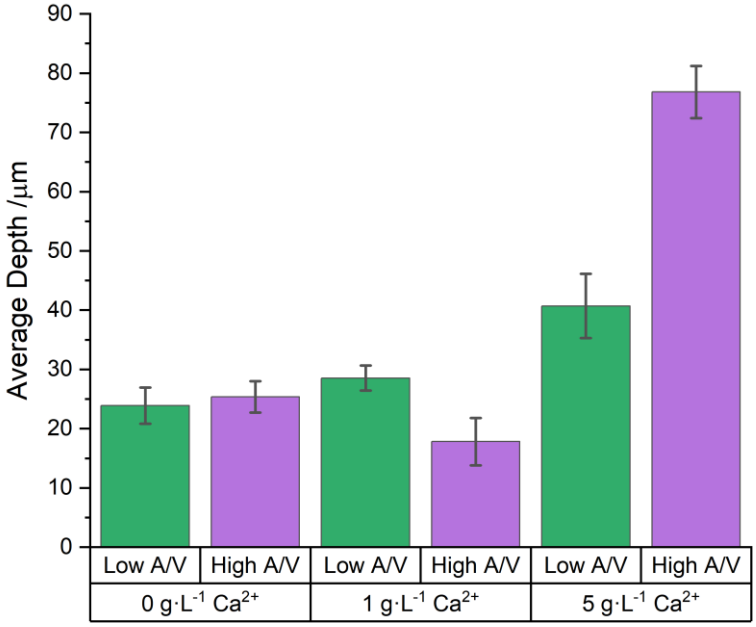

Figure 8.29: Average of ten deepest localised corrosion sites on X65 steel after corrosion product removal and post exposure to various bulk calcium concentrations and low and high (10.5 and 41.4 $cm^2 \cdot L^{-1}$) A/V ratios in CO_2 solution at 80 °C, 5.5 bar pCO_2

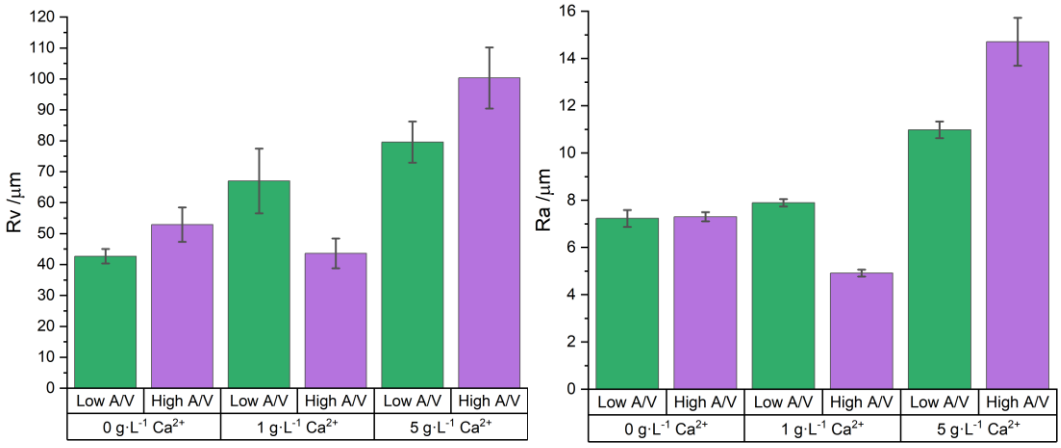

Figure 8.30: Surface roughness properties for X65 steel after corrosion product removal and post exposure to various bulk calcium concentrations and low and high (10.5 and 41.4 $cm^2 \cdot L^{-1}$) A/V ratios in CO_2 solution at 80 °C, 5.5 bar pCO_2

8.7.1 Localised Corrosion and Average Composition of $Fe_xCa_yCO_3$

Based on the results of localised corrosion analysis a potential correlation between average composition of the corrosion product and extent of localised attack was investigated. Figure 8.31 takes the average composition of the layers from 3 day mass loss tests and longer electrochemical tests and plots against average PLF depth.

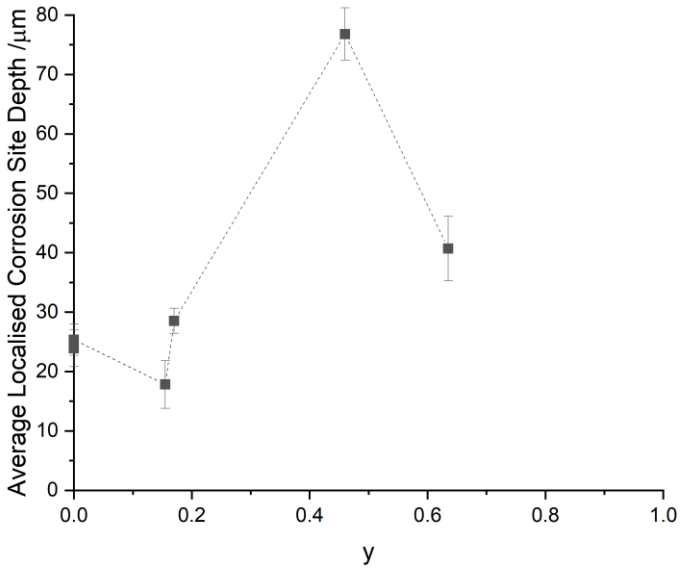

Figure 8.31: Average localised corrosion site depth as a function of the average calcium fraction y in $Fe_xCa_yCO_3$ corrosion products formed under various bulk calcium concentrations and low and high (10.5 and 41.4 $cm^2 \cdot L^{-1}$) A/V ratios in CO_2 solution at 80 °C, 5.5 bar pCO_2

The data suggests a peak in the severity of localised corrosion when y is close to 0.5, i.e. a 50:50 mix of Fe and Ca in the corrosion product. The final Figure 8.32 illustrates this by plotting the average PLF depth as a function of the absolute difference between x and y values in $Fe_xCa_yCO_3$.

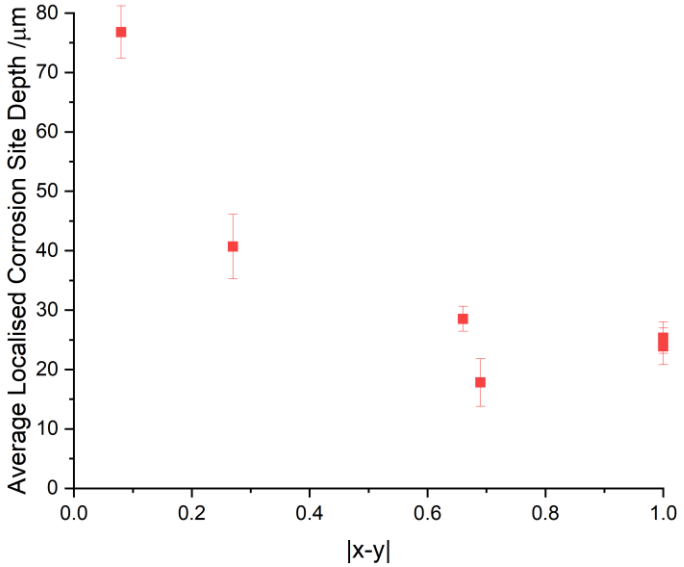

Figure 8.32: Average localised corrosion site depth as a function of the absolute difference in Fe to Ca in $Fe_xCa_yCO_3$ corrosion products formed under various bulk calcium concentrations and low and high (10.5 and 41.4 $cm^2 \cdot L^{-1}$) A/V ratios in CO_2 solution at 80 °C, 5.5 bar pCO_2

Chapter 9
Discussion

9.1 Introduction

The discussion section breaks down the observations from the thesis results into the following sub-sections:

- System chemistry – Based on the results of Chapter 5, the modelled effects of alkalinity addition into the bulk solution and the effect this has on the system chemistry, pressure, and saturation of both $FeCO_3$ and $CaCO_3$ is predicted. How these bulk conditions translate to surface conditions in a stagnant solution is also considered.
- $FeCO_3$ precipitation – A closer look at the *ex-situ* results of Chapter 6 and 7 to assess nucleation and growth characteristics of $FeCO_3$ under different bulk chemistry conditions and the role of Fe_3C.
- Evolution of Interfacial Properties – What can be inferred from the impedance data from Chapter 6 to 8 in terms of the performance and nature of the various corrosion product layers and how they are forming.
- Ca/Fe ion interactions during crystal growth – what effect the dynamic saturations of $FeCO_3$ and $CaCO_3$ have on crystal growth and morphology.
- Relating crystal growth behaviour to substrate protection – the ultimate objective of the project, linking the morphology and heterogeneity of crystal structures to the protection offered as a barrier to both general and localised corrosion.
- Experimental considerations – a final, constructive look at how experimental constraints such as A/V ratio can influence the surface to bulk chemistry and the resulting observations on corrosion product layer performance.

9.2 Evolution of System Chemistry

System chemistry was evaluated in Chapter 5 using a model to predict the naturally evolved pH and speciation. In a simple CO_2 system Figure 5.6 illustrates the logarithmic relationship between pH and speciation of ionic components in the pH range 4 to 6.6 which is of interest in this study.

The importance of this graph is that it demonstrates how the relative concentration of each species changes dramatically over the pH range considered. The change in relative concentrations changes how the system responds to further addition of alkalinity for example, or to changes in pCO_2. Figure 5.6 also shows how CO_3^{2-} is the most sensitive cation to changes in pH, increasing by over two orders of magnitude in concentration per unit increase in pH. This means that $FeCO_3$ and $CaCO_3$ are much more likely to form at near neutral pH than at low pH.

9.2.1 Effects of Corrosion Reactions on Bulk Chemistry and Pressure

In a real system such as the autoclave experiments in the current study with a finite number of moles of CO_2, the reduction of H^+ to H_2 in the cathodic reaction and proliferation of Fe^{2+} from the anodic reaction has a significant impact on both aqueous and vapour phases of the system. Figure 9.1 uses the chemistry model developed in Chapter 5 to illustrate the effects of Fe^{2+} on the equilibrium speciation of the system at the experimental conditions in the current work. Fe^{2+} has been included on the y axis to better visualize its relationship to other species.

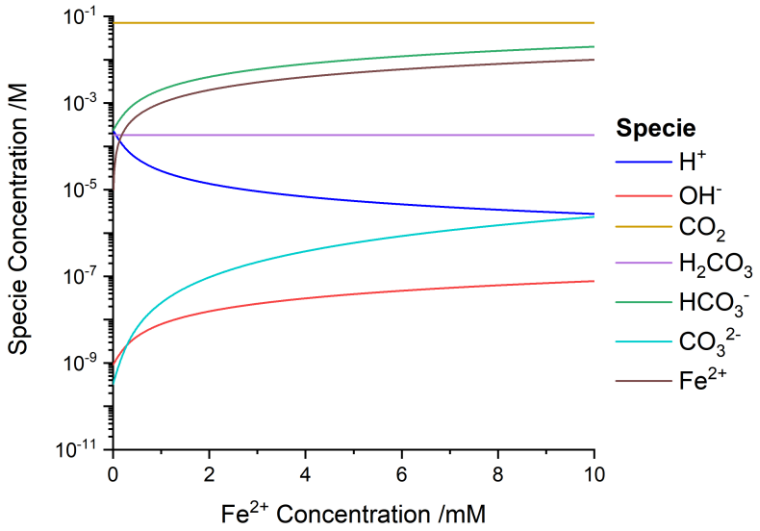

Figure 9.1: Equilibrium species concentrations as a function of bulk Fe^{2+} concentration in a 30 $g \cdot L^{-1}$ NaCl CO_2 saturated solution at 80 °C, 5.5 bar pCO_2. pH and SR_{FeCO3} range from of 3.6 to 5.6 and 0 to 183 respectively

The data shows that negatively charged species concentrations (OH^-, HCO_3^-, CO_3^{2-}) quickly increase while H^+ decreases at low concentrations of Fe^{2+}, the rate of change of species concentrations then decays as Fe^{2+} increases.

From a charge neutrality perspective, as Fe^{2+} is added to the system, negatively charged species must increase or positively charged species must decrease (i.e. H^+ which is removed during the cathodic reaction). The model shows that it is actually a combination of both negatively and positively charged species changing. This is because the species concentrations (OH^-, HCO_3^-, CO_3^{2-}) are all a function of H^+ concentration. This also results in an increase in total dissolved carbonate species. From the chemistry model and based on a continuously sparged experiment with no calcium, 30 $g \cdot L^{-1}$ NaCl, 80 °C and 5.5 bar pCO_2 the system would reach saturation of $FeCO_3$ according to Equation (3.1) at an Fe^{2+} concentration of 1.76 mM. At this point the total moles of dissolved CO_2 species would have increased by 4.6% from 71.3 to 74.6 mM. At a saturation ratio of 100 this would increase to 87.4 mM of CO_2 (22.6% increase).

The consequence of this process on a finite volume system is that more of the available moles of CO_2 in the headspace of the vessel are sequestered into the aqueous phase. This would result in a reduction of the headspace pressure and lower pCO_2. As a result, a further rebalancing of the system speciation will occur due to a reduction in H_2CO_3. To quantify this effect on pCO_2 the calculations of autoclave pressure in Section 5.4.1.1 have been used which show that a majority of the 0.16 moles of CO_2 in the system are initially stored as head space $CO_{2(g)}$ (66%) and dissolved $CO_{2(aq)}$ (34%) with only trace amounts stored as carbonic species as shown in Figure 9.2. This means CO_2 sequestration due to charge rebalancing should have negligible effect on system pressure.

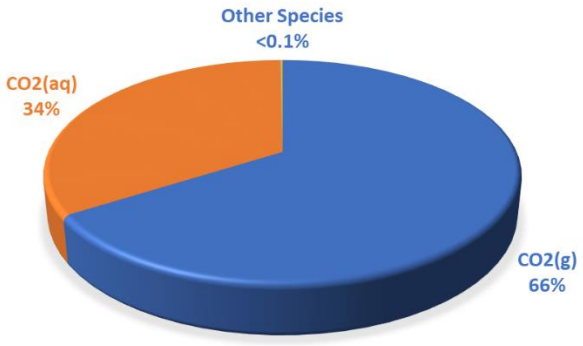

Figure 9.2: Distribution of CO_2 moles in 1.3 L autoclave experiments with 750 mL solution and 5.5 pCO_2 at 80 °C

A further consideration in consumption of CO_2 is the precipitation of corrosion products which lead to depletion of CO_3^{2-}. From a charge neutrality perspective this would also mean a decrease in bulk Fe^{2+} with the system eventually reaching a steady state as observed by Hua et al. [11]. Assuming that the bulk solution settles at an $FeCO_3$ saturation of 1, the system parameters are as shown in Table 9.1.

Table 9.1: Solution chemistry at initial conditions and at $FeCO_3$ saturation

Initial			At $FeCO_3$ saturation		
$[Fe^{2+}]$ / mM	$[CO_3^{2-}]$ / mM	pH	$[Fe^{2+}]$ / mM	$[CO_3^{2-}]$ / mM	pH
0	0.33×10^{-6}	3.6	1.76	73.1×10^{-6}	4.8

Based on corrosion product mass measurements from experiments conducted in the absence of calcium, the total moles of CO_3^{2-} stored as $FeCO_3$ ranged from 1.79 mmol at low A/V to 5.3 mmol at high A/V, (1.1% to 3.4% of total CO_2). Again this is a relatively small quantity of the total CO_2 and would not have a significant effect on overall system chemistry.

Practical verification of the true pCO_2 of the system is difficult as the measurement is obscured by the pressure increase due to the evolution of H_2 during the cathodic reaction. An overall pressure increase of approximately 0.5 bar was observed across all experiments, this typically occurred within the first few hours and demonstrates that the amount of CO_2 consumed from the headspace was more than offset by the quantity of H_2 produced. This was verified by a blank experiment that was conducted with no corrosion specimens that showed a perfectly stable system pressure of 5 barg for 24 hours immediately after the heat up phase. The experiment was evidence that the increase in system pressure in the presence of carbon steel specimens was likely due to the corrosion reaction and not slow evolution of CO_2 due to heat up. This pressure increase can also be predicted based on corrosion rate measurements. The coupled half-cell reactions in Equations (2.12) and (2.16) state that 1 mol of H_2 is produced in the cathodic reaction for every 1 mol of Fe^{2+} released in the anodic reaction.

As ferrite makes up around 98% of total specimen mass (based on elemental analysis in Table 4.1) mass loss measurements indicate a total of approximately 7 and 13 mmol of ferrite were released at low and high A/V respectively. As H_2 is poorly soluble it can be assumed that all moles of H_2 are stored in the vessel headspace. Applying the ideal gas law equation (5.25) to H_2 (Equation (9.1)) gives H_2 partial pressures (pH_2) of 0.37 bar and 0.68 bar respectively which is in line with that observed in experiments.

$$pH_2 = \frac{n \cdot R \cdot T_k}{V_v} \tag{9.1}$$

The alternative to sealing the autoclave at the start of experiments would be to maintain system pressure at 5 barg using the BPR, however this would result in potential loss of CO_2 and water vapour in addition to H_2 as system pressure increased. This would further obscure the understanding of vapour phase chemistry and consequently the bulk solution speciation. Ideally, vapour phase chemistry would be maintained by continuous bubbling of the solution with CO_2 to ensure the headspace pCO_2 is maintained and H_2 is removed. This is a much less economical method and would have to be done through a condenser configuration to avoid water loss.

9.2.2 Effects of Corrosion Reactions on $FeCO_3$ and $CaCO_3$ Saturation

As already highlighted, the flux of Fe^{2+} into the solution causes an increase in CO_3^{2-} which enhances the saturation of $CaCO_3$ and particularly $FeCO_3$ where both ionic components are increasing simultaneously. Using electrochemical data corrected by mass loss measurement to obtain instantaneous corrosion rate, the relative saturation of both $FeCO_3$ and $CaCO_3$ is plotted in Figure 9.3 for both high and low A/V and 5 $mg \cdot L^{-1}$ Ca^{2+}.

Despite the high concentration of calcium, SR_{CaCO3} is only briefly higher than SR_{FeCO3} within the first 2 hours of both high and low A/V experiments. Illustrating the data in this way clearly suggests that the system will become saturated for $FeCO_3$ much faster than $CaCO_3$. Theoretically, when $FeCO_3$ precipitates it will consume CO_3^{2-} and reduce the SR of $CaCO_3$ in parallel with $FeCO_3$ as observed previously [84]. This would suggest that it would not be possible for $CaCO_3$ to form. Despite this, diffraction data and EDX analysis in Sections 8.4 and 8.5 indicated that there was approximately a 50 to 64% uptake of calcium in the $Fe_xCa_yCO_3$ corrosion product that formed by the end of the experiments.

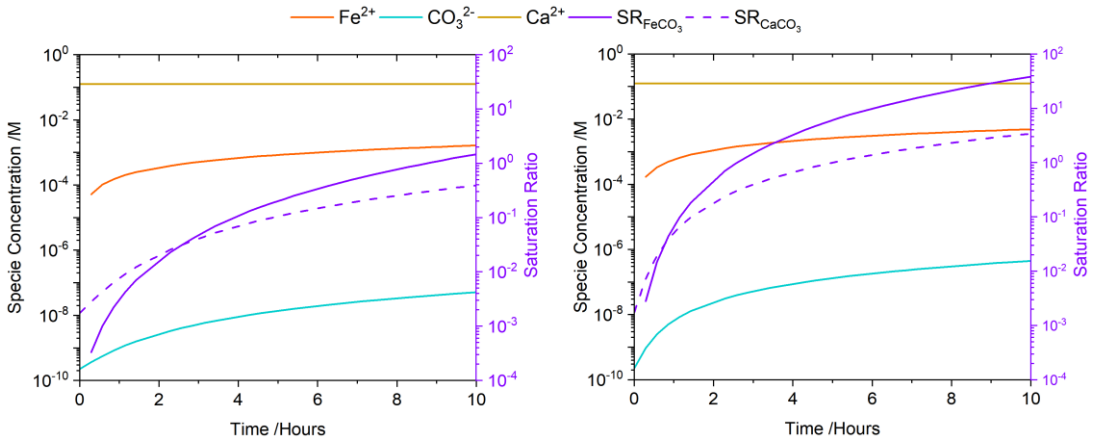

Figure 9.3: Effects of Fe^{2+} flux from corrosion on bulk chemistry and saturation of $FeCO_3$ and $CaCO_3$ in a CO_2 saturated solution at 80 °C, 5.5 bar pCO_2 with 5 $g \cdot L^{-1}$ Ca^{2+}. Low A/V ratio (left) and high A/V ratio (right)

The results suggest that uptake of calcium is not simply a function of bulk species concentrations or directly related to saturation of $FeCO_3$ and $CaCO_3$ as will be discussed later. Another observation from Figure 9.3 is that unlike higher initial pH systems, the dominant reactant is the cation (Ca^{2+} and Fe^{2+}) which is available in much higher concentrations than CO_3^{2-} and allows the carbonate to precipitate even at lower pH.

9.2.3 Effects of Bulk Chemistry on Surface Chemistry

The primary assumption of Figure 9.3 is that the system is homogenously mixed where in reality the stagnancy of the system will result in significant concentration gradients between the bulk and surface electrolyte. Numerous authors have reported on the importance of surface chemistry [25, 26, 67, 161-163] in determining accumulation rates of corrosion products. Even in well mixed and flowing systems the boundary layer adjacent to the surface will have different chemical properties to the bulk [120]. In the present system, a significant layer of porous Fe_3C is first exposed after ferrite depletion as shown in Chapter 6. The Fe_3C matrix creates tortuous pathways that electroactive species must diffuse through to exchange between the surface and bulk solution, this may further enhance the separation in surface and bulk chemistry [74, 75]. From a macroscopic perspective, the diffusion of surface species to the bulk depends on the concentrations already in the bulk.

Using a higher A/V ratio ensures higher levels of bulk Fe^{2+} much faster and will subsequently increase the surface concentrations when the system is in a steady state [71]. A simple depiction of this effect is highlighted in Figure 9.4.

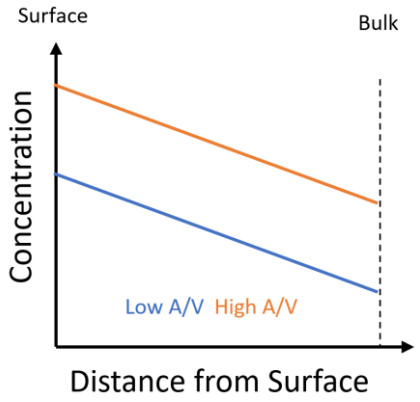

Figure 9.4: Simple depiction of the effects of bulk species concentrations on surface concentrations

9.3 $FeCO_3$ Precipitation

The result of much higher surface concentrations of Fe^{2+} is the supersaturation of $FeCO_3$, which leads to the nucleation and growth of $FeCO_3$ crystals either on or within the surface Fe_3C layer [74]. The way in which the crystal structures form for pure $FeCO_3$ was explored in Chapters 6 and 7.

9.3.1 Role of Fe_3C in Crystal Nucleation

In a flowing environment, surface roughness has been considered potentially detrimental to supersaturation of $FeCO_3$ [25] as the asperities increase mass transport through enhanced turbulence at the surface [161, 164]. Conversely, surface roughening can create sites of lower local surface energy which are more favourable for crystal nucleation [165]. De Yoreo and Vekilov [165] showed that crystal nucleation rates are strongly dependent on supersaturation and interfacial energy. In the current system, the absence of flow means that the increased surface roughening through exposure of Fe_3C will likely enhance nucleation rates through the decrease in local surface energy in addition to the increase in local supersaturation. The image in Figure 6.3(b) shows the early stages of $FeCO_3$ development with the crystals appearing to preferentially nucleate on exposed areas of Fe_3C instead of ferrite. The growth patterns depicted in Figure 8.16 also emanate out from areas of Fe_3C supporting the suggestion that Fe_3C provides a lower energy site for crystal nucleation.

Previous authors have also noted how Fe_3C provides anchoring of $FeCO_3$ to promote more adherent and tenacious layers [76, 166, 167]. At low A/V it is clear from the stages of crystal growth shown in Chapter 6 that almost all of the $FeCO_3$ forms within the exposed Fe_3C matrix. At higher A/V shown in Chapter 7, there is an apparent duplex $FeCO_3$ layer separated by the original surface boundary as imaged in Figure 7.13(b) and depicted in Figure 9.7. The lower layer grows within and is anchored to Fe_3C while the upper layer is purely $FeCO_3$. The observation of this type of duplex layer has also been made previously more commonly in the presence of calcium [102, 107, 113]. The EBSD images in Section 7.6 reveal that there is actually no separation in crystal growth at the original surface boundary and that the tightly packed surface crystals have grown out from nucleation sites within the Fe_3C matrix. Other authors have also noted how Fe_3C can act as a diffusion barrier to promote nucleation of $FeCO_3$ by increasing surface concentrations of Fe^{2+} therefore enhancing local supersaturation [74, 75, 168] though these investigations were typically in flowing environments. In summary, Fe_3C appears to promote crystal nucleation and growth by providing sites of lower surface energy for nucleation. It may also slow down diffusion of Fe^{2+}, enhancing local supersaturation of $FeCO_3$.

9.3.2 $FeCO_3$ Growth Behaviour within Fe_3C

Crolet et al. [28] identified four types of $FeCO_3$ formation within Fe_3C as shown in Figure 9.5 and categorised as either protective or unprotective. Only when $FeCO_3$ is able to form directly adjacent to the metal surface are the layers considered protective.

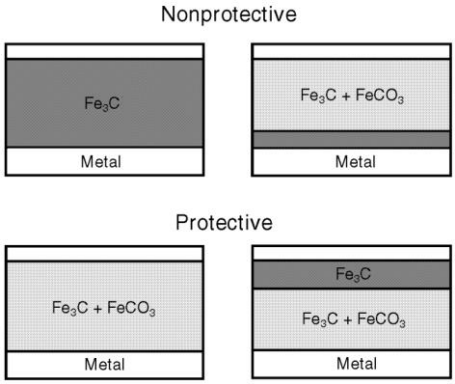

Figure 9.5: Morphologies observed for protective and unprotective corrosion layers from Crolet et al. [28]

Unprotective layers are said to occur when either no $FeCO_3$ forms at all, or when the $FeCO_3$ forms within the Fe_3C but detached from the substrate. In the current study, at low A/V Figure 7.13(a) appears to show that there is just enough Fe^{2+} in the system to displace that lost from the anodic dissolution with a similar volume of $FeCO_3$ and hence the $FeCO_3$ layer thickness is roughly equal to the steel penetration depth by the end of experiments. This is in line with the bottom left diagram from Crolet et al. [28] in Figure 9.5 and also depicted in Figure 9.6(c). Conversely at high A/V Figure 7.13(b) indicates that the increase in bulk Fe^{2+} has led to accumulation rates of $FeCO_3$ that are greater than the corrosion rate of the steel and a much thicker corrosion layer compared to steel penetration as depicted in Figure 9.7. This presents an additional case to those suggested by Crolet et al. [28].

Visual observations of the layer cross section in Chapter 6 suggest that the corrosion layer is porous when it forms within the Fe_3C network while in Chapter 7 the layer grown at high A/V is much more densely packed above the Fe_3C. Further, EBSD data in Chapter 7 revealed that crystallite size was generally reduced at low A/V with larger crystals forming at high A/V when able to grow out from the Fe_3C matrix.

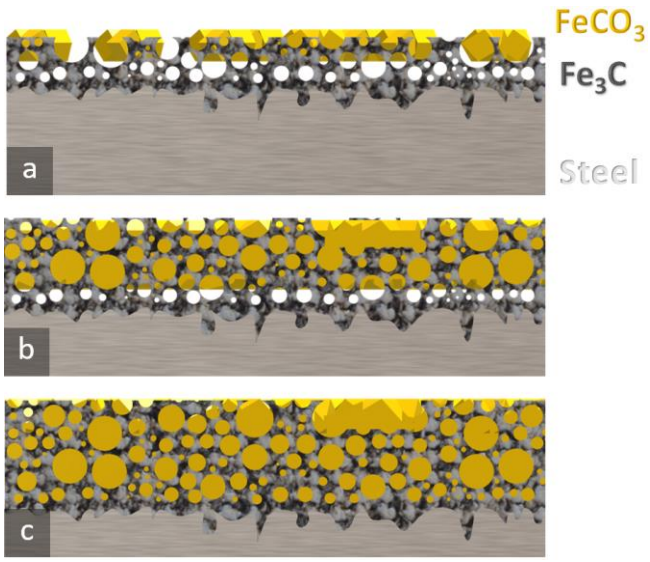

Figure 9.6: Proposed $FeCO_3$ growth behaviour at low A/V
(a) Initial nucleation of $FeCO_3$ (b) Formation of $FeCO_3$ barrier
(c) Void filling adjacent to surface

From the evidence in Chapters 6 and 7 it appears that while the tortuous pathways of the Fe_3C matrix can promote early nucleation of $FeCO_3$ it may also hinder full formation of an effective diffusion barrier.

This may be due to formation of smaller crystallites and the opportunity for increased porosity between the crystallites which is then slow to reduce. It is also possible that Fe_3C may provide a physical barrier to crystal agglomeration further inhibiting pore reduction.

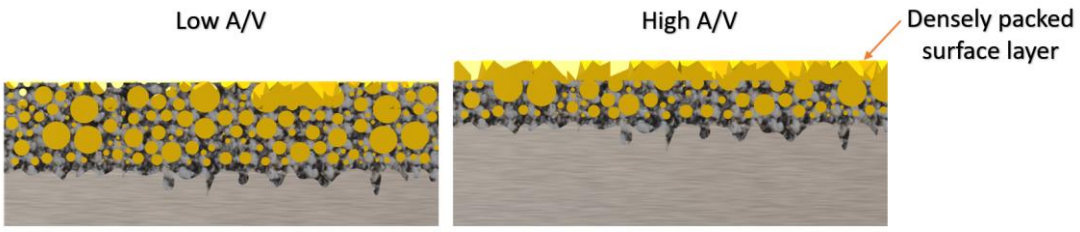

Figure 9.7: Comparison of $FeCO_3$ layers formed at high and low A/V

9.4 Evolution of Interfacial Properties Over Time

Implementation of the impedance models derived in Chapter 6 in combination with LPR and OCP measurement allowed significant detail to be obtained on the properties of the corrosion layers that formed over time at both high and low A/V and varying bulk calcium concentrations. Four key stages of the formation process were identified in Chapter 6 with the same trend observed across all experimental conditions tested throughout Chapters 6 to 8.

9.4.1 Stage 1 – Active Corrosion

In the early stages of experiments corrosion rates were extremely high (~12 $mm \cdot yr^{-1}$). This typically increased over the first 24 hours at low A/V irrespective of Ca^{2+} concentration. During the same time period the OCP value in the current work increased gradually before plateauing prior to corrosion product precipitation as highlighted in Figure 6.1, Figure 7.2, Figure 8.2 and Figure 8.5. During this time double layer capacitance (shown in Figure 8.10) also increased while charge transfer resistance (Figure 8.9) remained stable at low A/V. Previous authors have attributed increased corrosion rates over the course of an experiment to enhanced galvanic coupling as the net cathodic region of Fe_3C increases [169]. This corroborates EIS measurements which indicate an increases in active surface area during this stage, and SEM images of the cross section which show substantial Fe_3C at the surface after the first stage of corrosion. In the initial stage, the Nyquist plots for all experimental conditions (Figure 8.7(a)) indicated low frequency pseudo inductive (~0.2 Hz) and capacitive (~0.01 Hz) relaxation processes.

Experiments by Chen et al. [149] in an unbuffered solution at 60 °C and 0.8 bar pCO_2 also observed these phenomena at the same frequency ranges and proposed that the two processes were linked through the Fe(OH) adsorption mechanism. Research by Farelas et al. [146] at 80 °C, 0.54 bar pCO_2 and pH 6 only observed the pseudo inductive behaviour that occurs around 0.2 Hz and again attributed this to Fe(OH) adsorption. Conversely a study by Mora-Mendoza and Turgoose [73] conducted at room temperature and pressure using an RCE at 1000 RPM in a pH 3.8 solution observed only the low frequency capacitive response around 0.02 Hz with no inductive loop. They proposed the capacitive behaviour could be related to continuous precipitation and dissolution of an intermediary phase of $FeCO_3$.

The data in Figure 8.9 shows that unlike low A/V, at high A/V there is an immediate increase in R_{ct} across all calcium concentrations from the start of the experiment which is also evidenced in the LPR measurements in Figure 8.1 and Figure 8.4 (shown as a dip in R_p^{-1}). This may suggest that the larger A/V is causing an immediate build-up of Fe^{2+} at the surface as discussed in Section 9.2.3 that is significant enough to reduce the reaction kinetics, increasing R_{ct}. The mass loss results in Chapter 5, Figure 5.18 and electrochemical data in Chapter 8 also indicate that initial corrosion rates are higher in the absence of calcium which could lead to faster precipitation of corrosion products. The same observation was also made by Shamsa [30] using similar test conditions however it is still unclear what causes corrosion rate to decrease when calcium is present in the brine. The calculations in Table 5.4 suggest that the method of adding $CaCl_2$ while maintaining Cl^- content increases the ionic strength of the solution by as much as 24 %, though the pH change at this pressure is only 3.62 to 3.63. Nevertheless, future experiments should be conducted at fixed ionic strength to eliminate this as a potential cause.

9.4.2 Stage 2 – Nucleation and Growth of Corrosion Product

As shown in Figure 6.3 by the end of the first stage of the experiment at low A/V and no Ca^{2+}, $FeCO_3$ has nucleated on the surface of the steel. At this point R_{ct} and R_W begin increasing linearly while double layer capacitance decreases.

The result is a linear decrease in active surface area (Figure 8.11) proportional to the linear decrease in R_p^{-1} observed in LPR data. The linearity of the system response at this stage suggests a distribution of corrosion products across the surface, blocking active sites for reactions to take place. Figure 8.11 shows that the A/V ratio does not appear to significantly change the rate of decrease in active surface area in the linear region in the absence of calcium, only the induction time for this stage to start. Increasing calcium concentration does however appear to reduce rates of active site blocking at both high and low A/V. This observation was also made in Chapter 5 where it was shown in the electron image in Figure 5.20 that high calcium concentrations led to large clusters of smaller crystallites that poorly covered the surface.

Despite forming a corrosion product layer within the Fe_3C network, there are still significant voids between the $FeCO_3$ and the substrate steel as shown in Figure 6.5(a). This suggests the layer is not yet protective [28] and that the layer can continue to be undermined.

9.4.3 Stage 3 – Corrosion Layer Agglomeration and Thickening

As shown in the logarithmic plot of C_{dl} in Figure 8.10, active site blocking eventually transitions from a linear to logarithmic decay with the trend much more distinct at low calcium concentrations. Evidence from Figure 6.7 suggests that at this point the crystals that have formed at the surface have formed an almost continuous layer between the substrate and electrolyte. In the absence of calcium, this means the low frequency impedance response attributed to diffusion, starts to become significant, with R_W increasing concomitantly with R_{ct} as shown in Figure 6.7(a). The result is a rapid rise in impedance and a finite length diffusion profile in the low frequency region that increases as the layer thickness increases. Contrasting Figure 6.5(a) from stage 2 with the layer at Stage 3 (Figure 6.7(a)) suggests that the corrosion product layer is growing at a higher rate than it is being undermined and the Fe_3C void between the corrosion product layer and the substrate has become substantially filled. The effect of calcium at this stage is presented in Figure 8.7(c) which provides comparable impedance plots during stage 3 of corrosion layer development.

As discussed, the plot shows that at low calcium concentrations the impedance response is in a mixed kinetic and diffusion control with both R_{ct} and R_W comparable in magnitude. At high calcium concentrations the decay of C_{dl} is no longer clearly logarithmic. From Figure 8.7(c) it can be seen that the impedance response is also different and is dominated by the high frequency charge transfer loop. The above further reinforces the finding that calcium increases the heterogeneity of surface coverage and promotes nucleation and growth of smaller crystallites to decrease active area but slows down the formation of a diffusion barrier.

9.4.4 Stage 4 – Stabilisation of Corrosion Layer Thickness and Void Filling

In the final stage of the experiments, impedance magnitude, R_P^{-1} and OCP all stabilise or have a sudden transition in the rate of change as shown in Figure 6.1, Figure 7.1, Figure 8.1 and Figure 8.4. At high calcium concentration and low A/V this stage is not reached, suggesting that substantial active sites remain on the surface even after 7 days of testing. Across the other conditions, the final impedance response varies dramatically with no calcium high A/V and 5 $g \cdot L^{-1}$ high A/V being the two extreme cases. Focusing on the difference between $FeCO_3$ layers at high and low A/V explored in Chapter 7, the difference is that the impedance response at low A/V is dominated by charge transfer kinetics while high A/V is diffusion, presenting an almost semi-infinite Warburg response after just 58 hours (Figure 7.5). This effect is illustrated in the R_{ct} and R_W plots in Figure 7.8. Evaluation of the cross-sectional images in Figure 7.13 reveal that at the end of the experiment the corrosion product layer is much thinner at high A/V and while minimal pores exist close to the substrate surface the crystal growth above the Fe_3C boundary is highly compact. At low A/V the layer is much thicker but larger pores exist filled with smaller crystallites. This porosity evidently suggests a less effective diffusion barrier than that formed at high A/V with protection potentially provided by active site blocking. This difference in method of protection is also suggested in OCP measurements in Figure 7.2 which show that despite a much higher polarisation resistance at high A/V the final OCP is actually over 50 mV lower. Comparison of potentiodynamic sweeps in Figure 7.3 suggest that the anodic current is decreased at low A/V while the cathodic current is increased.

An explanation for this could be that at low A/V cathodic sites in the form of Fe_3C are still exposed at the surface while the ferrite regions are actually well covered. At high A/V the outer layer of $FeCO_3$ covers almost all of the available area for cathodic reactions but some voids may still exist under the layer that have not been filled.

In the presence of high concentrations of calcium, the clustering of crystallites evidently reduces the rate of substrate protection. However, after longer term exposure of up to 7 days at high A/V the system does eventually reach a stage 4 stabilisation as shown in Figure 8.4. Notably the system at this stage is dominated by charge transfer resistance much like the $FeCO_3$ system at low A/V. This layer is also extremely thick and porous as shown in Figure 8.14 and again it is evident that substrate protection is provided by active site blocking as opposed to the formation of an effective diffusion barrier. The active site blocking is expected to be due to $Fe_xCa_yCO_3$ however the local environment could also favour precipitation of other phases.

In the literature, Fe_3O_4 has been reported to form between the steel substrate and $FeCO_3$ layer [51]. The increased layer thickness at low A/V and high calcium concentration leads to R_{ct} being greater than R_W which has been attributed to continuous active site blocking at the surface due to undermining of the porous diffusion layer of corrosion products. It was also shown in Figure 7.3 that this reduced the anodic limiting current when compared to a sample with an effective diffusion layer (no calcium high A/V). One possibility is that continued separation of bulk and surface electrolyte by the corrosion layer may make local conditions favourable for precipitation of Fe_3O_4 which can form directly on anodic sites more easily when compared to the $FeCO_3$ and $Fe_xCa_yCO_3$ which preferentially nucleates on Fe_3C as discussed earlier. With the analytical techniques used, there were no obvious signs of Fe_3O_4 however more targeted analysis of the ferrite interface could be used in future.

9.5 Co-precipitation and Ca/Fe Interactions – Effects on Crystal Growth

The next section of the discussion takes a closer look at the formation of mixed $Fe_xCa_yCO_3$ that form in the presence of bulk Ca^{2+} ions. Particular focus is on the high calcium conditions (5 $g \cdot L^{-1}$ Ca^{2+}) where the composition is close to x=y=0.5.

9.5.1 Analysis of Crystallite Properties from Powder Diffraction Data

A number of previous authors have reported on the effects of calcium incorporation on $FeCO_3$ [31, 52, 102] in which the lattice can become strained due to the differences in atomic radii [103]. Powder diffraction (XRD) can provide insights in understanding lattice strain and crystallite size. When a crystal is strained, the d-spacings vary. A macroscopic strain changes the interplanar spacing giving rise to a shift in the average position of the diffraction peak while microscopic strains give a distribution of d-spacings which broaden the peak [127]. It is possible to use peak broadening to estimate crystallite size (t_{cry}) based on the Scherrer equation:

$$t_{cry} = \frac{K\lambda \sec\theta}{\beta} \tag{9.2}$$

Where β is the difference between the observed and instrumental broadening:

$$\beta = \beta_{obs} - \beta_{inst} \tag{9.3}$$

Both β_{obs} and β_{isnt} are measured based on the peak full width at half maximum (FWHM) of a peak, approximately equal to $2\delta\theta$ from Figure 9.8. The value of β_{isnt} can be obtained from a standard sample.

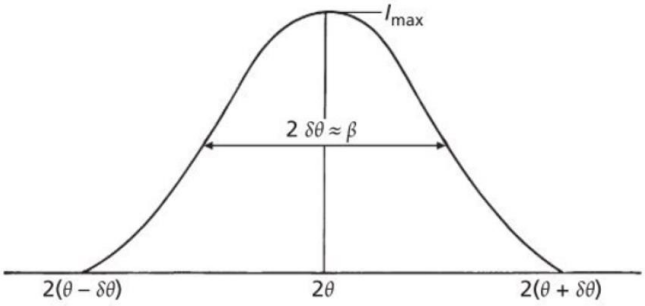

Figure 9.8: Schematic diagram of a broadened Bragg peak due to a finite crystal thickness [137]

It should be noted here that crystal strain can also have an effect on peak broadening and would require analysis of multiple peak profiles to produce a Williamson Hall plot to solve the following equation:

$$\beta \cdot \cos\theta = \frac{K\lambda}{t_{cry}} + 4 \cdot strain \cdot \sin\theta \tag{9.4}$$

Where $\beta\cos\theta$ is plotted on the y axis and $\sin\theta$ on the x in order to obtain t_{cry} from the y intercept and strain from the gradient. As discussed in Sections 5.5.4 and 5.5.5 it is evident from EDX analysis that there is variation in calcium content through the layers which would also give a distribution in peak position due to the shift in d-spacing from calcium incorporation.

Importantly, peak broadening was at a maximum when the average composition of the layer was roughly halfway between $FeCO_3$ and $CaCO_3$. This was verified by the electron images in Figure 8.12 which showed large clusters of smaller crystallites when the composition of the layer was roughly $Fe_{0.5}Ca_{0.5}CO_3$. It can also be hypothesised that crystallite strain would be at a maximum at this condition as the shift in d-spacing from either pure $FeCO_3$ or $CaCO_3$ is at a maximum. A study by Matamoros-Veloza suggested that increased crystallite strain can create instability in the crystal structure promoting early dissolution and breakdown of the $Fe_xCa_yCO_3$ corrosion product layer when compared to $FeCO_3$ [103].

9.5.2 Kinetics of Carbonate Growth

In Section 9.2.3 it was highlighted that saturation for $FeCO_3$ would be much higher than $CaCO_3$ even at 5 $g \cdot L^{-1}$ bulk Ca^{2+} concentration, particularly at the surface which is the source of Fe^{2+} ions. Despite this, under these conditions the corrosion products comprised of almost equal amounts of Fe and Ca. Although $FeCO_3$ has a lower solubility than $CaCO_3$ it has been shown that $CaCO_3$ has much faster kinetics of crystal growth. Alsaiari et al. [95] observed greater amounts of $CaCO_3$ precipitation in a well-controlled solution super-saturated with both $FeCO_3$ and $CaCO_3$. This was attributed to the higher water loss rate of Ca^{2+} compared to Fe^{2+} (see Figure 3.18) which allows Ca^{2+} to lose its water molecules more easily to attach to CO_3^-. Tomson and Johnson [29] also discuss this in their work on precipitation kinetics, highlighting that waters saturated with respect to $CaCO_3$ are often greatly supersaturated with respect to $FeCO_3$ owing to the much faster precipitation kinetics of $CaCO_3$. Both Herzog et al [82] and di Lorenzo [87] noted how Fe^{2+} can also reduce the growth rate of $CaCO_3$ with increasing bulk Fe^{2+} decreasing growth rates. This could further accentuate discrepancies in corrosion layer formation at different A/V ratios. If the solution chemistry is conducive to formation of $CaCO_3$, a higher A/V and subsequently higher bulk Fe^{2+} could be detrimental to fast formation of a protective carbonate layer.

9.5.3 Crystallite Poisoning by Impurity Ca/Fe

In terms of crystal growth, it is well known that Fe can inhibit Calcite formation [81-85, 87, 121]. Research by Meyer et al. [81] found that amongst 34 organic and inorganic impurities, Fe^{2+} had the greatest inhibitory effect on calcite growth. They proposed blocking of growth steps by adsorbed Fe^{2+} as the mechanism. de Leeuw [85] also proposed a mechanism of growth site blocking due to Fe^{2+} incorporation into calcite which showed how Fe incorporation at calcite crystal steps can initially be thermodynamically favourable before eventually decorating the crystal step and inhibiting further growth.

Herzog et al. [82] also observed $FeCO_3$ to have precipitated on the surface of $CacO_3$ crystals, blocking growth sites. Another study by Langerak [84] suggested that the observed inhibitory effect of Fe on their studies was attributed to the competition for CO_3^{2-} with precipitation of $FeCO_3$ leading to a reduction of the saturation for $CaCO_3$ although a later study by di Lorenzo [87] did not find any such effects in the pre nucleation stage. Regardless of the mechanism, it is well understood that Fe^{2+} can cause suppression and even complete termination of $CaCO_3$ crystal growth. In the current system, this could be the cause of decreased crystallite size as nucleation of new crystals becomes more favourable than continued growth of crystals that have become decorated with impurity Ca or Fe.

The value of reducing A/V ratio in the current experiments was that the complex relationship between the relative SR of $CaCO_3$ and $FeCO_3$ was elucidated more clearly by reducing the kinetics of crystal growth as evaluated in Section 8.6. This also shifted the average stoichiometry of the corrosion product layer to become calcium rich ($Fe_{0.36}Ca_{0.64}CO_3$) and caused distinctive crystal growth patterns to be observed as shown in Figure 8.17. This crystal poisoning effect appears to be present in the layers shown in Figure 8.18 and Figure 8.19 where the outer edge of each crystal layer is gradually more Fe rich before a sudden termination and the start of a new layer again rich in Ca. Electron diffraction confirmed that these bands where $Fe_xCa_yCO_3$ of varying lattice spacing. The findings would help to explain the morphology of layers formed in the presence of calcium where much smaller crystallites form larger structures.

Crystal growth appears to become limited by the inhibitory effects of both Fe and Ca in one another's crystal lattice, but nucleation of further crystallites is promoted on the surface.

Another potential explanation for the growth patterns is that Fe is actually continually diffusing through the lattice from the substrate after the crystal structures have already formed, thus enriching the outer edges of each crystallite.

The phenomena could explain why the growth patterns were only observed over longer term experiments, or it could simply be a fact that very specific conditions are required for this to occur. Figure 9.9 shows the lattice structure for $FeCO_3$ and $CaCO_3$ on the [010] zone axis, illustrating how Fe can diffuse through the structure.

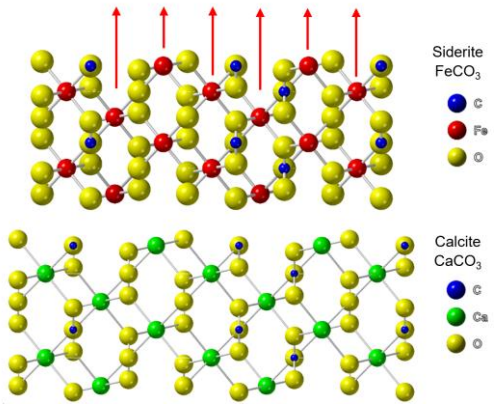

Figure 9.9: Lattice structure of Siderite and Calcite on [010] zone axis

Regardless of Fe enrichment process, TEM and STEM images of the growth structure (Figure 8.20) revealed nano-porosity at the interface between each crystal step as well as at the interface between the carbonate and Fe_3C. This could be detrimental to the integrity of the layer, compromising its protectiveness as a diffusion barrier or reducing its stability if environmental conditions change.

9.6 Effects of Crystal Growth Behaviour on Substrate Protection

9.6.1 Separation of Corrosion Layer from Substrate

Dugstad [26] noted that when accumulation rates of $FeCO_3$ are slow compared to corrosion rate, that the corrosion layer can become undermined creating a separation between the substrate and corrosion layer as shown in Figure 9.10(b) and similar to that identified by Crolet et al. [28] in Figure 9.5.

Dugstad also found that optimum protection was afforded when $FeCO_3$ grew directly onto the substrate as shown in Figure 9.10(c). $FeCO_3$ growth at low A/V in Chapter 6 initially resembled Figure 9.10(b). This could be a consequence of preferential nucleation of $FeCO_3$ on Fe_3C as discussed in Section 9.4.2, resulting in a void between the substrate and corrosion layer. Alternatively this could be an artifact of continued undermining of the layer as proposed by Dugstad.

The apparent layer undermining appeared to continue until eventually the $FeCO_3$ layer thickness and coverage was able to reduce corrosion rates and allow corrosion products to fill the majority of void spaces. It is possible that this was accelerated by the stagnancy and limited volume of the solution and that continuous flow could promote further corrosion layer undermining. van Hunnik et al. [71] related the expected protectiveness of $FeCO_3$ to scaling tendency based on local and bulk saturation as well as temperature, stating that protective layers could form more easily at 80 °C, requiring a pH of at least 6 to form at 40 °C. The complexity in the current system is that the solution is continuously evolving due to the finite volume and so both bulk and local scaling tendency varies throughout the experiment. This is evidenced by the variation in A/V ratio leading to different corrosion layer structures.

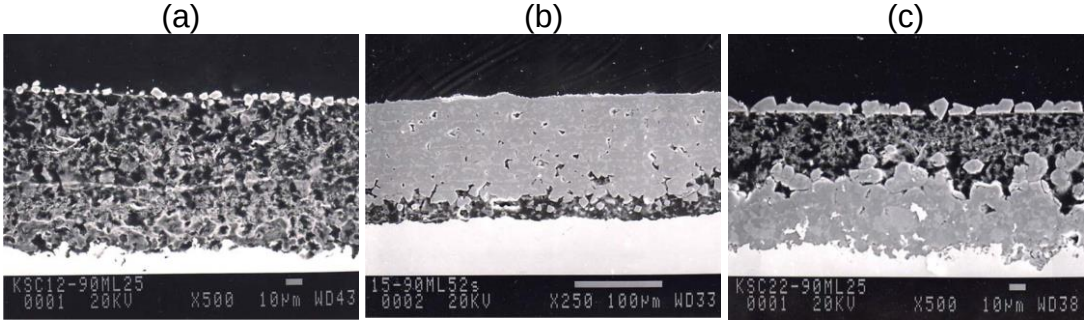

Figure 9.10: Corrosion films formed under various bulk conditions [26] (a) 40 °C and SR_{FeCO3} <40 (b) 40 °C and SR_{FeCO3} >40 (c) 80 °C and SR_{FeCO3} <10

9.6.2 Diffusion Barrier vs Active Site Blocking

Based on surface analysis and impedance measurements, it appears that corrosion layers in the current system only create an effective diffusion barrier when sufficient bulk Fe^{2+} allows for surface growth of $FeCO_3$ outside of the Fe_3C network when the crystals are able to form a tightly packed aggregate layer.

Reducing bulk Fe^{2+} by lowering A/V ratio or adding calcium to the brine appeared to inhibit the formation of a tightly packed layer by either limiting surface growth of crystals or by the clustering effect in the case of calcium. This appears to enhance porosity of the layer and promote the cathodic reaction due to the exposure of Fe_3C [169]. Protectiveness is eventually provided by greater resistance to charge transfer – likely caused by dramatic changes in chemistry at the surface, enabling further active site blocking that reduces the anodic reaction. This site blocking could simply be from $Fe_xCa_yCO_3$ or potentially another compound such as Fe_3O_4 [51].

9.6.3 Effects on Localised Corrosion

A crucial element in determining the effectiveness of the corrosion layer is the ability to prevent localised attack, particularly after corrosion layer formation.

It was alluded to in the previous section that the greater dispersion in the charge transfer response of $FeCO_3$ layers formed at high A/V could suggest greater heterogeneity of the layer which could promote localised corrosion. Despite this, profilometry in Section 8.7 did not suggest that A/V ratio had any effect on localised corrosion in the absence of calcium.

The most significant localised corrosion was observed at high calcium concentration, particularly at high A/V. Morphologically the crystal structures that formed under these conditions (Figure 8.12) where large clusters described previously with the average composition of $Fe_xCa_yCO_3$ close to x=y=0.5. At low A/V the average composition was more calcium rich (y=0.63) and the structure was noticeably less rounded in Figure 8.12, while XRD in Figure 8.13 indicated that peak broadening also significantly reduced compared to the high A/V layer.

All of this information suggests that the localised corrosion characteristics are driven by the morphology of the layer, with more rounded clusters of smaller crystallites providing more heterogeneous coverage, leaving voids between separate clusters, exposing cathodic Fe_3C sites leading to local attack as depicted in Figure 9.11. With clustering morphology appearing to peak at an average stoichiometry of $Fe_{0.5}Ca_{0.5}CO_3$, this appears to be a worse case composition for localised corrosion in the current environment.

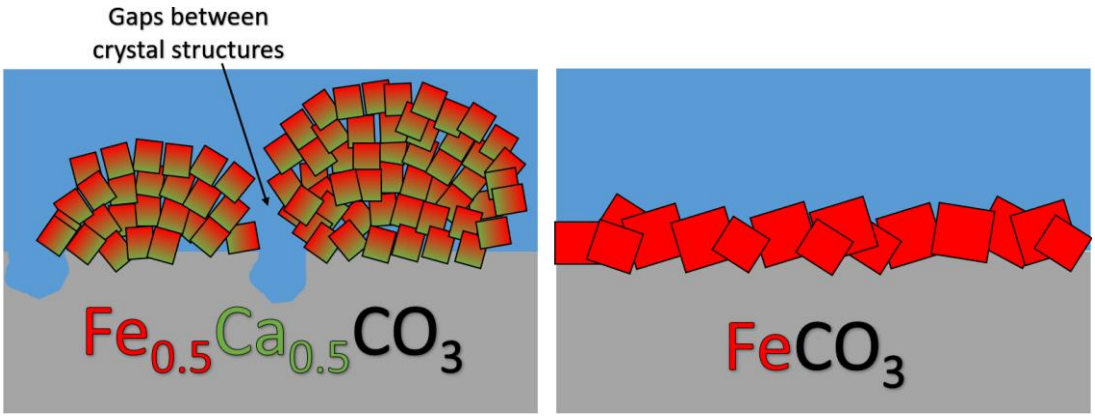

Figure 9.11: Proposed mechanism for enhanced localised corrosion due to morphological changes from Ca^{2+} incorporation into corrosion products (left) Large crystallite clusters formed when corrosion product is $Fe_{0.5}Ca_{0.5}CO_3$ (right) homogenous layer of $FeCO_3$ crystals in absence of Ca^{2+}

9.7 The Influence of Experimental Limitations on the Observed Protectiveness of Corrosion Products

All of the above analysis has led to clear conclusions on the overall perceived protectiveness of different corrosion layers in the current study. Varying A/V ratio has been a useful tool in understanding the how layer formation affects performance of the layer as a diffusion barrier. More generally, this study has proven that A/V ratio can change the resultant layer that forms. In the absence of calcium, a higher A/V ratio appeared to improve the layer performance by creating a more effective diffusion barrier without a detrimental effect on localised corrosion. However, in the presence of calcium, high A/V increased localised corrosion by pushing the average composition of the layer closer to $Fe_{0.5}Ca_{0.5}CO_3$. Many studies in the literature omit the reporting of A/V ratio and the general observation of how the system evolves over the course of the experiment is also limited. This study shows that an A/V ratio should be selected that is representative of the real-world system that is being simulated. In elevated pressure applications it is not always practical to select a low A/V ratio due to the confines of the pressure vessel, particularly at elevated temperature when water loading becomes restricted. The use of smaller material specimens is also not always practical for *ex situ* surface analysis. In these cases the researcher must take caution in their observations and consider how non representative experimental conditions could affect their results.

A systematic approach to A/V ratio selection could be to conduct an independence study whereby A/V ratio is gradually reduced until any effect on overall corrosion rate is negligible as depicted graphically in Figure 9.12. This could provide a cost effective compromise to large volume experiments whilst still providing reasonably accurate data.

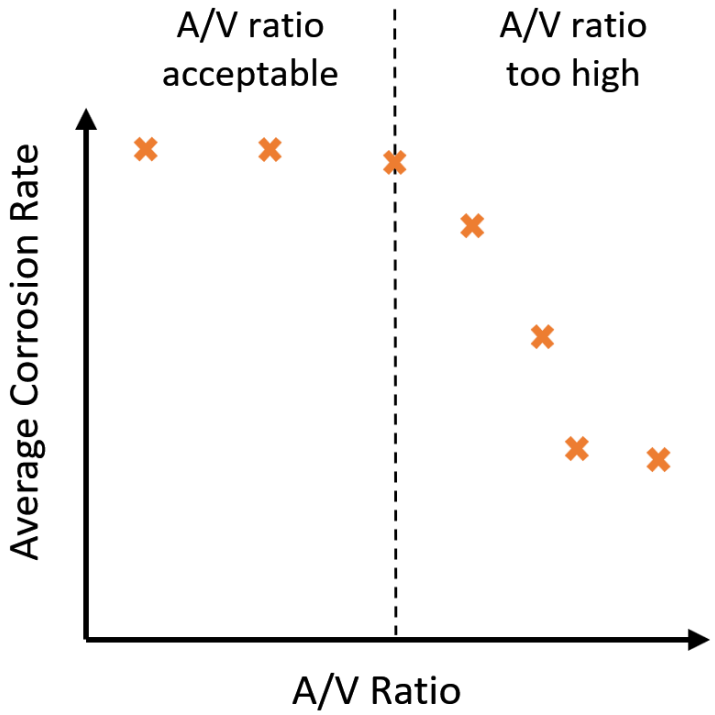

Figure 9.12: Depiction of A/V ratio independence study to identify suitable A/V ratio for a given set of experimental conditions in corrosion testing

The above suggestions further reiterate the need for caution when drawing conclusions from laboratory scale experiments, particularly when developing novel techniques for corrosion prevention such as through the use of naturally protective corrosion products. Field conditions can vary greatly even within the same system and are often not well defined. A robust and extensive experimental approach is therefore required to confidently translate the true performance of corrosion products from laboratory scale experiments to the field.

Chapter 10
Conclusions and Future Work

10.1 Conclusions

The conclusions from the project have been broken down into the key observations from each of the results chapters, using the analysis in the discussions from Chapter 9.

10.1.1 Conclusions from Chapter 5 – Experimental Design

In Chapter 5, chemical equilibrium equations were used to assess the effects of system parameters such as temperature, pressure and pH on the CO_2 speciation and saturation for $FeCO_3$ and $CaCO_3$. The model was also used to determine the sensitivity of a CO_2 system to the flux of Fe^{2+} ions for anodic dissolution of steel. The main findings from this analysis were that system sensitivity to Fe^{2+} increased with decreasing pCO_2 and pH. In addition to this analysis, existing experimental procedures for brine preparation were evaluated to identify a suitable set of industry relevant test conditions. The assessment identified several limitations of existing CO_2 charging methods such as poor control over pCO_2 resulting in variation in perceived corrosion rates from gravimetric analysis and variation in the properties of the corrosion products that form. To resolve this issue, a two-stage solution transfer and charging method was employed in conjunction with more precise pressure measurement and regulation during heat up. The pCO_2 was also increased to 5.5 bar to enhance corrosion product formation.

In the second part of Chapter 5 a set of preliminary 3 day mass loss experiments were conducted using the new design of experiments. The experiments utilised two area-to-volume (A/V) ratios (10.5 and 41.4 $cm^2 \cdot L^{-1}$) and three bulk Ca^{2+} concentrations (0, 1000 and 5000 $mg \cdot L^{-1}$). Gravimetric analysis showed that A/V ratio dramatically decreased average corrosion rate and increased corrosion product mass. Calcium was shown to increase average corrosion rate at high A/V and decrease it at low A/V. Surface analysis revealed that the likely cause of this was that both increasing calcium and decreasing A/V ratio delayed the formation of protective corrosion layers.

10.1.2 Conclusions from Chapter 6 – Impedance Measurements

In Chapter 6 electrochemical techniques were employed to characterize the development of the corrosion layers from Chapter 5 as they are forming.

This initial study focused on $FeCO_3$ formation in the absence of calcium and at low A/V. The study utilised a combination of OCP, LPR and EIS data to track the development of the layer over time. The trends in OCP and reciprocal polarisation resistance (R_P^{-1}) which is analogous to corrosion rate, suggested four key stages in corrosion layer development. The interface was examined at each stage by repeat experiments that were terminated during each of the four stages. This analysis revealed that the four stages were as follows:

- Free corrosion and increase in active surface area.
- Nucleation and growth of $FeCO_3$ leading to reduction in active surface area.
- Convergence of $FeCO_3$ layer to produce a diffusion barrier with increasing thickness.
- Reduction of voids between substrate and $FeCO_3$ layer limiting active species concentrations and impeding further increase to the diffusion layer thickness.

The above information, along with Nyquist and Bode impedance plots were used to develop equivalent circuit models which in turn were fitted to the impedance data to obtain quantitative measurements of interfacial properties such as double layer capacitance (C_{dl}), charge transfer resistance (R_{ct}) and diffusion resistance (R_W).

10.1.3 Conclusions from Chapter 7 – Effects of A/V Ratio on $FeCO_3$

Chapter 7 extended the analysis approach adopted in Chapter 6 to make a detailed assessment on the effects of A/V ratio on $FeCO_3$ formation. LPR measurements showed that corrosion rates decreased much earlier and at a greater rate at high A/V, reaching a much lower final R_P^{-1}. Cross-sectional analysis revealed that the corrosion layer formed predominantly within the exposed Fe_3C matrix after ferrite depletion at low A/V while at high A/V the layer formed both within and above the Fe_3C. EBSD analysis confirmed that the surface crystals formed at high A/V originated from sites within the Fe_3C layer, growing out to form larger more compact crystal agglomerations on the surface.

This growth behaviour produced a much more effective diffusion barrier at high A/V, with impedance data presenting an almost semi-infinite diffusion profile.

Potentiodynamic sweeps revealed that the cathodic limiting current was supressed at high A/V due to the densely packed surface layer of $FeCO_3$, where Fe_3C was still exposed at low A/V. Conversely the limiting current of the anodic branch was lower at low A/V, suggesting that anodic sites were not as well protected under the $FeCO_3$ layer. Analysis of impedance parameters showed that dispersion of the charge transfer loop was greater at high A/V, this could indicate that heterogeneity exists in the layer at high A/V. This could make the layer more susceptible to localised corrosion.

10.1.4 Conclusions from Chapter 8 – Protectiveness of $Fe_xCa_yCO_3$

In Chapter 8 the effects of calcium incorporation into the corrosion layer were evaluated using various *ex situ* techniques as well as the electrochemical methods used in Chapters 6 and 7. LPR measurements confirmed the observations in Chapter 5 that calcium delayed the formation of a protective corrosion layer while a higher A/V ratio increased formation kinetics. A low A/V also resulted in significant areas of exposed Fe_3C still remaining at the surface even once corrosion rates had dropped. The only condition to provide an effective diffusion barrier was at high A/V in the absence of calcium, where R_W dominated the polarisation resistance. Both low A/V and high calcium concentration lead to much thicker layers of greater porosity with impedance dominated by charge transfer resistance, suggesting protectiveness relied on active site blocking at the anodic sites.

Ex situ cross sectional analysis revealed complex banded layer growth at high calcium concentration and low A/V, which was confirmed as $Fe_xCa_yCO_3$ of varying composition by STEM analysis. The banded growth pattern resulted in areas of nano porosity at the crystallite boundaries which could further decrease the stability of the layer. The banded growth was attributed to the particular set of test conditions which resulted in the primary cation alternating between Fe and Ca. Critically, calcium incorporation was the most significant contributor to increases in localised corrosion.

Plotting average localised corrosion depth against the absolute difference in x and y from $Fe_xCa_yCO_3$ showed that local attack was maximised when x and y were close, i.e. x=y=0.5. In agreement with the preliminary results in Chapter 5, when the average stoichiometry of the layer (measured by EDX and XRD) was close to $Fe_{0.5}Ca_{0.5}CO_3$ the carbonates formed globular clusters of smaller crystallites with poorer surface coverage as a result which promoted localised attack.

10.1.5 Summary of Key Finding

- In the demanding CO_2 environment explored in this work, corrosion layers form in a four stage process, heavily influenced by evolution of system chemistry at the surface.
- A/V ratio can alter the way in which corrosion layers form as well as the mechanism by which they provide protection to the substrate, both initially and longer term. A higher A/V can provide sufficient bulk Fe^{2+} for tightly packed surface layers to form outside of the exposed Fe_3C matrix.
- The presence of brine calcium can reduce initial free corrosion rates but delays the build-up of a protective corrosion layer by causing stunted crystal growth, reducing crystallite size.
- The reduction in crystallite size from calcium incorporation creates larger clusters of crystals that poorly cover the substrate leaving voids that promote localised corrosion, with the effect maximised when the average stoichiometry of the layer is $Fe_{0.5}Ca_{0.5}CO_3$.

10.2 Recommendations for Future Work

The research project has laid the foundations for a number of further studies to build on the understanding brought forward in the current work.

10.2.1 Electrolyte Analysis

The composition of the bulk solution has been shown to have a critical effect on the corrosion layer formation. *In situ* pH measurement would allow better prediction of the chemical environment and identify if a critical pH exists for nucleation of corrosion products. This would also help quantify the effects of A/V ratio on the chemical environment.

Sampling of the solution would also allow the bulk Fe^{2+} and Ca^{2+} to be measured to quantify saturation and to link bulk conditions to corrosion product composition.

10.2.2 Detailed *Ex situ* Characterisation of $FeCO_3$ at High A/V

The detailed analysis performed in Chapter 6 using intermediate experiments and cross-sectional analysis could be extended to the high A/V layer shown in Chapter 7. This would confirm at what stage the surface layer evolved in conjunction with how this impacted the impedance response.

10.2.3 Further Investigation on Active Site Blocking

During the analysis and discussion of impedance properties it was highlighted that both low A/V and calcium incorporation produced more porous diffusion layers where R_{ct} was the dominate resistance. A further study could take a closer look at the interface between the steel substrate underneath these porous layers to investigate if any other nano layers of corrosion product have formed such as Fe_3O_4.

10.2.4 Evaluation of Layer Stability

It was postulated that calcium incorporation and defects introduced due to the crystallite poisoning and re-nucleation effect could decrease the stability of the layer. This could be explored by dissolution tests where the bulk solution pH is reduced or bulk Fe^{2+} and Ca^{2+} are removed to under-saturate the solution.

10.2.5 Introduction of Hydrodynamics

Mass transport by hydrodynamic control could help improve the characterisation of the system. Well defined mass transport enables better prediction of bulk and surface conditions allowing more accurate estimation of surface saturation in relation to corrosion product accumulation. This would also improve the assessment of diffusion layer performance.

10.2.6 Exploring Kinetics and Adsorption Behaviour

Varying system pressure and temperature would allow further information on corrosion layer build rates and the long-term effect this has on corrosion layer performance. Additionally, the effects of partial pressure of CO_2 could be explored using EIS, particularly focusing on the adsorption profile better understand the anodic reaction.

References

1. Koch, G., et al. *International Measures of Prevention, Application and Economics of Corrosion Technology Study* [online]. Houston: NACE International, 2016. [Accessed 19 December 2018]. Available from: http://impact.nace.org/documents/Nace-International-Report.pdf.
2. Papavinasam, S. *Corrosion control in the oil and gas industry.* London: Elsevier, 2014.
3. Robertson, T., DeCola, E. and Pearson, L. *North Slope Spills Analysis* [online]. Alaska: Nuka Research and Planning Group, 2010. [Accessed 20 November 2018]. Available from: https://dec.alaska.gov/spar/ppr/response-resources/publications-conferences/nssa-reports/.
4. Kermani, M.B. and Morshed, A. Carbon Dioxide Corrosion in Oil and Gas Production—A Compendium. *Corrosion*, 2003, **59**(8), pp.659-683.
5. Guraieb, P. and Wang, Q. 18 - Corrosion and scale at high pressure high temperature. *In:* A.M. EL-SHERIK, ed. *Trends in Oil and Gas Corrosion Research and Technologies*. Boston: Woodhead Publishing, 2017, pp.431-451.
6. Bogaerts, W.F. Reference Electrodes for electrochemical measurements in high-temperature high-pressure aqueous environments—Review of potential corrections for 'external' reference systems. *Electrochimica Acta*, 2016, **212**, pp.102-112.
7. Danielson, M.J. The Construction and Thermodynamic Performance of an Ag-AgCI Reference Electrode for Use in High Temperature Aqueous Environments Containing H2 and H2S. *Corrosion*, 1979, **35**(5), pp.200-204.
8. Global CCS Institute. *CO2 Reuse Technologies* [online]. 2019. [Accessed 18 June 2019]. Available from: https://hub.globalccsinstitute.com/publications/accelerating-uptake-ccs-industrial-use-captured-carbon-dioxide/1-co2-reuse-technologies.
9. Barker, R., Hua, Y. and Neville, A. Internal corrosion of carbon steel pipelines for dense-phase CO2 transport in carbon capture and storage (CCS) – a review. *International Materials Reviews*, 2017, **62**(1), pp.1-31.
10. Hua, Y., Barker, R. and Neville, A. Comparison of corrosion behaviour for X-65 carbon steel in supercritical CO2-saturated water and water-saturated/unsaturated supercritical CO2. *The Journal of Supercritical Fluids*, 2015, **97**, pp.224-237.
11. Hua, Y., Shamsa, A., Barker, R. and Neville, A. Protectiveness, morphology and composition of corrosion products formed on carbon steel in the presence of Cl−, Ca2+ and Mg2+ in high pressure CO2 environments. *Applied Surface Science*, 2018, **455**, pp.667-682.
12. Johnsen, K., Holt, H., Helle, K. and Sollie, O.K. Mapping of potential HSE issues related to large-scale capture, transport and storage of CO2. *DNV Report for Petroleumstilsynet*, 2009.
13. Julião, A. *Carbon gas storage cavern is the best way to obtain clean energy from a fossil fuel* [online]. 2019. [Accessed 14 February 2019]. Available from: https://phys.org/news/2019-02-carbon-gas-storage-cavern-energy.html.

14. Choi, Y.-S., Young, D., Nešić, S. and Gray, L.G.S. Wellbore integrity and corrosion of carbon steel in CO2 geologic storage environments: A literature review. *International Journal of Greenhouse Gas Control*, 2013, **16**, pp.S70-S77.
15. Advanced Resources International. *Optimization of CO2 storage in CO2 enhanced oil recovery projects* [online]. Department of Energy & Climate Change (DECC), Office of Carbon Capture & Storage, 2010. [Accessed 04 June 2019]. Available from: https://assets.publishing.service.gov.uk/government/uploads/system/uploads/attachment_data/file/47992/1006-optimization-of-co2-storage-in-co2-enhanced-oil-re.pdf.
16. Office of Fossil Energy. *Enhanced Oil Recovery* [online]. 2019. [Accessed]. Available from: https://www.energy.gov/fe/science-innovation/oil-gas-research/enhanced-oil-recovery.
17. Moritis, G. Special Report: EOR/Heavy Oil Survey: CO2 miscible, steam, dominate enhanced oil processes. *Oil & Gas Journal*, 2010, **104**(17), pp.37-57.
18. Laumb, J.D., et al. Corrosion and Failure Assessment for CO2 EOR and Associated Storage in the Weyburn Field. *Energy Procedia*, 2017, **114**, pp.5173-5181.
19. Kapusta, S.D. and Canter, S.C. *Corrosion control in CO2 enhanced oil recovery.* United States: NACE International, Houston, TX (United States), 1994.
20. British Geological Survey. *Geothermal energy | Renewables and energy security | British Geological Survey (BGS)* [online]. 2019. [Accessed 23 May]. Available from: https://www.bgs.ac.uk/research/energy/geothermal/.
21. Williams, Q. *Why is the earth's core so hot? And how do scientists measure its temperature?* [online]. 2019. [Accessed 23 May]. Available from: https://www.scientificamerican.com/article/why-is-the-earths-core-so/.
22. Nogara, J. and Zarrouk, S.J. Corrosion in geothermal environment: Part 1: Fluids and their impact. *Renewable and Sustainable Energy Reviews*, 2018, **82**, pp.1333-1346.
23. Mundhenk, N., et al. Electrochemical study of the corrosion of different alloys exposed to deaerated 80°C geothermal brines containing CO2. *Corrosion Science*, 2014, **84**, pp.180-188.
24. Zhu, S.D., et al. Failure analysis of P110 tubing string in the ultra-deep oil well. *Engineering Failure Analysis*, 2011, **18**(3), pp.950-962.
25. Barker, R., Burkle, D., Charpentier, T., Thompson, H. and Neville, A. A review of iron carbonate (FeCO3) formation in the oil and gas industry. *Corrosion Science*, 2018, **142**, pp.312-341.
26. Dugstad, A. Fundamental Aspects of CO2 Metal Loss Corrosion - Part 1: Mechanism. *In: CORROSION 2006*, 12-16 March 2006, San Diego, California. NACE International, 2006, p.18.
27. Nešić, S. Key issues related to modelling of internal corrosion of oil and gas pipelines – A review. *Corrosion Science*, 2007, **49**(12), pp.4308-4338.
28. Crolet, J.L., Thevenot, N. and Nesic, S. Role of Conductive Corrosion Products in the Protectiveness of Corrosion Layers. *Corrosion*, 1998, **54**(3), pp.194-203.

29. Tomson, M.B. and Johnson, M.L. How Ferrous Carbonate Kinetics Impacts Oilfield Corrosion. *In: SPE International Symposium on Oilfield Chemistry*, 1991/1/1/, Anaheim, California. Society of Petroleum Engineers, 1991, p.8.
30. Shamsa, A. *Corrosion Product Growth Kinetics/Characteristics and Inhibitor Performance in CO2 Environments*. PhD thesis, University of Leeds, 2019.
31. Mansoori, H., Young, D., Brown, B. and Singer, M. Influence of calcium and magnesium ions on CO2 corrosion of carbon steel in oil and gas production systems - A review. *Journal of Natural Gas Science and Engineering*, 2018, **59**, pp.287-296.
32. Al Kindi, M., et al. Substrate Protection with Corrosion Scales: Can We Depend on Iron Carbonate? *ACS Applied Materials & Interfaces*, 2021, **13**(48), pp.58193-58200.
33. LaQue, F.L. A Critical Look at Salt Spray Tests. *Mater. Methods*, 1952, **35**(2), pp.77-18.
34. McCafferty, E. *Introduction to corrosion science.* New York: Springer, 2010.
35. Revie, R.W. and Uhlig, H.H. *Corrosion and corrosion control : an introduction to corrosion science and engineering.* 4th ed. Hoboken, N.J.: J. Wiley, 2008.
36. Völker, E., Inchauspe, C.G. and Calvo, E.J. Scanning electrochemical microscopy measurement of ferrous ion fluxes during localized corrosion of steel. *Electrochemistry Communications*, 2006, **8**(1), pp.179-183.
37. Stansbury, E.E. and Buchanan, R.A. *Fundamentals of Electrochemical Corrosion* [online]. Ohio: ASM International, 2000. [Accessed 4 January 2019]. Available from: https://app.knovel.com/hotlink/toc/id:kpFEC0000L/fundamentals-electrochemical/fundamentals-electrochemical.
38. Bockris, J.O.m., Devanathan, M.A.V., Müller, K. and Butler, J.A.V. On the structure of charged interfaces. *Proceedings of the Royal Society of London. Series A. Mathematical and Physical Sciences*, 1963, **274**(1356), pp.55-79.
39. Fenton, J.M. *Basic Concepts in Electrochemistry* [online]. Connecticut: University of Connecticut, 2004. [Accessed 7 January 2019]. Available from: http://www.engr.uconn.edu/~jmfent/CHEG320_electrochemistry%20lectures.pdf.
40. Kahyarian, A. and Nešić, S. A New Narrative for CO2 Corrosion of Mild Steel. *Journal of The Electrochemical Society*, 2019, **166**(11), pp.C3048-C3063.
41. De Waard, C. and Milliams, D.E. Carbonic Acid Corrosion of Steel. *Corrosion*, 1975, **31**(5), pp.177-181.
42. Bockris, J.O.M., Drazic, D. and Despic, A.R. The electrode kinetics of the deposition and dissolution of iron. *Electrochimica Acta*, 1961, **4**(2), pp.325-361.
43. Nešić, S., Thevenot, N., Crolet, J.L. and Drazic, D. Electrochemical Properties of Iron Dissolution in the Presence of CO2 - Basics Revisited. *In: CORROSION 96*, 24-29 March 1996, Denver, Colorado. NACE International, 1996, p.23.

44. De Marco, R., Jiang, Z.-T., Pejcic, B. and Poinen, E. An In Situ Synchrotron Radiation Grazing Incidence X-Ray Diffraction Study of Carbon Dioxide Corrosion. *Journal of The Electrochemical Society*, 2005, **152**(10), pp.B389-B392.
45. Tanupabrungsun, T., Young, D., Brown, B. and Nešić, S. Construction And Verification of Pourbaix Diagrams For CO2 Corrosion of Mild Steel Valid Up to 250°C. *In: CORROSION 2012*, 11-15 March 2012, Salt Lake City, Utah. NACE International, 2012, p.16.
46. Sato, J., Kobayashi, M., Kato, H., Miyazaki, T. and Kakihana, M. Hydrothermal synthesis of magnetite particles with uncommon crystal facets. *Journal of Asian Ceramic Societies*, 2014, **2**(3), pp.258-262.
47. Barker, R., et al. Iron carbonate formation kinetics onto corroding and pre-filmed carbon steel surfaces in carbon dioxide corrosion environments. *Applied Surface Science*, 2019, **469**, pp.135-145.
48. Andritsos, N., Karabelas, A.J. and Koutsoukos, P.G. Morphology and Structure of CaCO3 Scale Layers Formed under Isothermal Flow Conditions. *Langmuir*, 1997, **13**(10), pp.2873-2879.
49. Webmineral. *Mineralogy Database* [online]. 2019. [Accessed 26 June]. Available from: http://www.webmineral.com/.
50. Chan, E.W.L. *Magnetite and its galvanic effect on the corrosion of carbon steel under carbon dioxide environments*. Doctor of Philosophy thesis, Curtin University, 2011.
51. De Motte, R., et al. A study by electrochemical impedance spectroscopy and surface analysis of corrosion product layers formed during CO2 corrosion of low alloy steel. *Corrosion Science*, 2020, **172**, p.108666.
52. Shamsa, A., et al. The role of Ca2+ ions on Ca/Fe carbonate products on X65 carbon steel in CO2 corrosion environments at 80 and 150 °C. *Corrosion Science*, 2019, **156**, pp.58-70.
53. Hua, Y., et al. The formation of FeCO3 and Fe3O4 on carbon steel and their protective capabilities against CO2 corrosion at elevated temperature and pressure. *Corrosion Science*, 2019, **157**, pp.392-405.
54. Schikorr, G. Über die Reaktionen zwischen Eisen, Seinen Hydroxyden und Wasser. *Zeitschrift für Elektrochemie und angewandte physikalische Chemie*, 1929, **35**(2), pp.65-70.
55. Antoshchak, I.M. and Gnyp, I.P. Equipment and method for autoclave corrosion-mechanical and electrochemical investigations. *Materials Science*, 2000, **36**(3), pp.392-400.
56. Gamry. *Two, Three and Four Electrode Experiments* [online]. 2022. [Accessed 1st March]. Available from: https://www.gamry.com/application-notes/instrumentation/two-three-four-electrode-experiments/.
57. Stern, M. and Geary, A.L. Electrochemical Polarization: I . A Theoretical Analysis of the Shape of Polarization Curves. *Journal of The Electrochemical Society*, 1957, **104**(1), pp.56-63.
58. Orazem, M.E. and Tribollet, B. *Electrochemical impedance spectroscopy.* 2nd ed. John Wiley & Sons, 2017.
59. Lasia, A. *Electrochemical impedance spectroscopy and its applications.* New York: Springer, 2020.
60. Hirschorn, B., et al. Determination of effective capacitance and film thickness from constant-phase-element parameters. *Electrochimica Acta*, 2010, **55**(21), pp.6218-6227.

61. Vivier, V. and Orazem, M.E. Impedance Analysis of Electrochemical Systems. *Chemical Reviews*, 2022.
62. Randles, J.E.B. Kinetics of rapid electrode reactions. *Discussions of the Faraday Society*, 1947, **1**(0), pp.11-19.
63. Orazem, M.E. and Tribollet, B. An integrated approach to electrochemical impedance spectroscopy. *Electrochimica Acta*, 2008, **53**(25), pp.7360-7366.
64. Sun, W., Nešić, S. and Woollam, R.C. The effect of temperature and ionic strength on iron carbonate (FeCO3) solubility limit. *Corrosion Science*, 2009, **51**(6), pp.1273-1276.
65. Videm, K. and Dugstad, A. Film covered corrosion, film breakdown and pitting attack of carbon steels in aqueous CO 2 environments. *In: Corrosion 88*, March 21-25 1988, St. Louis, MO. NACE, 1988.
66. Tanupabrungsun, T., Brown, B. and Nešić, S. Effect of pH on CO2 Corrosion of Mild Steel at Elevated Temperatures. *In: CORROSION 2013*, 17-21 March 2013, Orlando, Florida. NACE International, 2013, p.11.
67. De Motte, R., et al. Near surface pH measurements in aqueous CO2 corrosion. *Electrochimica Acta*, 2018, **290**, pp.605-615.
68. ASTM International. ASTM NACE / ASTM G31-21. *Standard Guide for Laboratory Immersion Corrosion Testing of Metals*. ASTM G31-21, West Conshohocken, PA: ASTM International, 2021.
69. ---. ASTM G111-21A. *Standard Guide for Corrosion Tests in High Temperature or High Pressire Environment, or Both*. ASTM International, 2021.
70. Sun, W. and Nešić, S. Kinetics of Corrosion Layer Formation: Part 1—Iron Carbonate Layers in Carbon Dioxide Corrosion. *Corrosion*, 2008, **64**(4), pp.334-346.
71. Van Hunnik, E., Hendriksen, E.L.J.A. and Pots, B.F.M. The Formation of Protective FeCO3 Corrosion Product Layers in CO2 Corrosion. *In: CORROSION 96*, NACE-96006, 1996.
72. Nesic, S., Lee, J. and Ruzic, V. A Mechanistic Model of Iron Carbonate Film Growth and the Effect on CO2 Corrosion of Mild Steel. *In: CORROSION 2002*, NACE-02237, 2002.
73. Mora-Mendoza, J.L. and Turgoose, S. Fe3C influence on the corrosion rate of mild steel in aqueous CO2 systems under turbulent flow conditions. *Corrosion Science*, 2002, **44**(6), pp.1223-1246.
74. Farelas, F., Brown, B. and Nešić, S. Iron Carbide and its Influence on the Formation of Protective Iron Carbonate in CO2 Corrosion of Mild Steel. *In: CORROSION 2013*, 17-21 March 2013, Orlando, Florida. NACE International, 2013, p.15.
75. Ieamsupapong, S., Brown, B., Singer, M. and Nešić, S. Effect of Solution PH on Corrosion Product Layer Formation in a Controlled Water Chemistry System. *In: CORROSION 2017*, 26-30 March 2017, New Orleans, Louisiana, USA. NACE International, 2017, p.13.
76. Ueda, M. and Takabe, H. Effect of Environmental Factor and Microstructure on Morphology of Corrosion Products in CO2 Environments. *In: CORROSION 99*, 1999/1/1/, San Antonio, Texas. NACE International, 1999, p.16.
77. Han, J., Carey, J.W. and Zhang, J. Effect of sodium chloride on corrosion of mild steel in CO2-saturated brines. *Journal of Applied Electrochemistry*, 2011, **41**(6), pp.741-749.

78. Romanek, C.S., et al. Inorganic synthesis of Fe–Ca–Mg carbonates at low temperature. *Geochimica et Cosmochimica Acta*, 2009, **73**(18), pp.5361-5376.
79. Davidson, P.M., Symmes, G.H., Cohen, B.A., Reeder, R.J. and Lindsley, D.H. Synthesis of the new compound CaFe(CO3)2 and experimental constraints on the (Ca,Fe)CO3 join. *Geochimica et Cosmochimica Acta*, 1993, **57**(23), pp.5105-5109.
80. Chai, L. and Navrotsky, A. Synthesis, characterization, and energetics of solid solution along the dolomite-ankerite join, and implications for the stability of ordered CaFe(CO3)2. *American Mineralogist*, 1996, **81**(9-10), pp.1141-1147.
81. Meyer, H.J. The influence of impurities on the growth rate of calcite. *Journal of Crystal Growth*, 1984, **66**(3), pp.639-646.
82. Herzog, R.E., Shi, Q., Patil, J.N. and Katz, J.L. Magnetic water treatment: the effect of iron on calcium carbonate nucleation and growth. *Langmuir*, 1989, **5**(3), pp.861-867.
83. Wada, N., Yamashita, K. and Umegaki, T. Effects of divalent cations upon nucleation, growth and transformation of calcium carbonate polymorphs under conditions of double diffusion. *Journal of Crystal Growth*, 1995, **148**(3), pp.297-304.
84. Langerak, E.P.A.V., Beekmans, M.M.H., Beun, J.J., Hamelers, H.V.M. and Lettinga, G. Influence of phosphate and iron on the extent of calcium carbonate precipitation during anaerobic digestion. *Journal of Chemical Technology & Biotechnology*, 1999, **74**(11), pp.1030-1036.
85. de Leeuw, N.H. Molecular Dynamics Simulations of the Growth Inhibiting Effect of Fe2+, Mg2+, Cd2+, and Sr2+ on Calcite Crystal Growth. *The Journal of Physical Chemistry B*, 2002, **106**(20), pp.5241-5249.
86. Mejri, W., Ben Salah, I. and Tlili, M.M. Speciation of Fe(II) and Fe(III) effect on CaCO3 crystallization. *Crystal Research and Technology*, 2015, **50**(3), pp.236-243.
87. Di Lorenzo, F., Burgos-Cara, A., Ruiz-Agudo, E., Putnis, C.V. and Prieto, M. Effect of ferrous iron on the nucleation and growth of CaCO3 in slightly basic aqueous solutions. *CrystEngComm*, 2017, **19**(3), pp.447-460.
88. Korchef, A. Effect of Iron Ions on the Crystal Growth Kinetics and Microstructure of Calcium Carbonate. *Crystal Growth & Design*, 2019, **19**(12), pp.6893-6902.
89. Wajon, J.E., Ho, G.-E. and Murphy, P.J. Rate of precipitation of ferrous iron and formation of mixed iron-calcium carbonates by naturally occurring carbonate materials. *Water Research*, 1985, **19**(7), pp.831-837.
90. Alsaiari, H.A., Yean, S., Tomson, M.B. and Kan, A.T. Iron Calcium Carbonate: Precipitation Interaction. *In: SPE International Oilfield Scale Conference*, 28/29 May 2008, Aberdeen, UK. Society of Petroleum Engineers, 2008, p.16.
91. Alsaiari, H.A., Zhang, N., Work, S., Kan, A.T. and Tomson, M.B. A New Correlation to Predict the Stoichiometry of Mixed Scale: Iron-Calcium Carbonate. *In: SPE International Conference on Oilfield Scale*, 2012/1/1/, Aberdeen, UK. Society of Petroleum Engineers, 2012, p.15.

92. Alsaiari, H.A. *Effect of calcium (II) and iron (II) on the precipitation of calcium carbonate and iron carbonate solid solutions and on scale inhibitors retention*. Doctor of Philosophy thesis, Rice University, 2012.
93. Alsaiari, H.A., Kan, A. and Tomson, M. Effect of Calcium and Iron (II) Ions on the Precipitation of Calcium Carbonate and Ferrous Carbonate. *SPE Journal*, 2010, **15**(02), pp.294-300.
94. Alsaiari, H.A., Kan, A.T. and Tomson, M.B. Constant Composition Study Of Crystal Growth Of Mixed Calcium-Ferrous Carbonate Salt. *In: CORROSION 2010*, 14-18 March, San Antonio, Texas. NACE International, 2010, p.12.
95. Alsaiari, H.A., Kan, A.T. and Tomson, M.B. Molar Ratio of Ca2+ to Fe2+ in the Supersaturated Solution of Iron Carbonate and Calcium Carbonate and in the Precipitate: Relation and Interpretation. *In: SPE International Symposium on Oilfield Chemistry*, 20-22 April 2009, The Woodlands. Texas. Society of Petroleum Engineers, 2009, p.18.
96. Eriksrud, E. and Sontvedt, T. Effect of Flow on CO2 Corrosion Rates in Real and Synthetic Formation Waters. *In: Corrosion 83*, April 18-22, Anaheim, CA. NACE, 1983.
97. Wu, S.L., et al. Characterization of the surface film formed from carbon dioxide corrosion on N80 steel. *Materials Letters*, 2004, **58**(6), pp.1076-1081.
98. Cui, Z.D., Wu, S.L., Zhu, S.L. and Yang, X.J. Study on corrosion properties of pipelines in simulated produced water saturated with supercritical CO2. *Applied Surface Science*, 2006, **252**(6), pp.2368-2374.
99. Zhang, G., Lu, M., Chai, C. and Wu, Y. Effect of HCO_3^- concentration on CO_2 corrosion in oil and gas fields. *Journal of University of Science and Technology Beijing, Mineral, Metallurgy, Material*, 2006, **13**(1), pp.44-49.
100. Gao, K., et al. Mechanical properties of CO2 corrosion product scales and their relationship to corrosion rates. *Corrosion Science*, 2008, **50**(10), pp.2796-2803.
101. Bai, H., Wang, Y., Ma, Y., Zhang, Q. and Zhang, N. Effect of CO_2 Partial Pressure on the Corrosion Behavior of J55 Carbon Steel in 30% Crude Oil/Brine Mixture. *Materials (Basel, Switzerland)*, 2018, **11**(9).
102. Rizzo, R., Gupta, S., Rogowska, M. and Ambat, R. Corrosion of carbon steel under CO2 conditions: Effect of CaCO3 precipitation on the stability of the FeCO3 protective layer. *Corrosion Science*, 2020, **162**, p.108214.
103. Matamoros-Veloza, A., Barker, R., Vargas, S. and Neville, A. Iron Calcium Carbonate Instability: Structural Modification of Siderite Corrosion Films. *ACS Applied Materials & Interfaces*, 2020, **12**(43), pp.49237-49244.
104. Teng, H.H., Dove, P.M., Orme, C.A. and De Yoreo, J.J. Thermodynamics of Calcite Growth: Baseline for Understanding Biomineral Formation. *Science*, 1998, **282**(5389), pp.724-727.
105. Prieto, C., Mansoori, H., Brown, B., Singer, M. and Young, D. Application of Scratch Testing for the Assessment of the Adherent Properties of Scales and CO2 Corrosion Product Layers and their Relation to Corrosion. *Corrosion Science*, 2021, **190**, p.109625.
106. Zhao, G.-x., Lu, X.-h., Xiang, J.-m. and Han, Y. Formation Characteristic of CO2 Corrosion Product Layer of P110 Steel

Investigated by SEM and Electrochemical Techniques. *Journal of Iron and Steel Research, International*, 2009, **16**(4), pp.89-94.

107. Ding, C., Gao, K.-w. and Chen, C.-f. Effect of Ca2+ on CO2 corrosion properties of X65 pipeline steel. *International Journal of Minerals, Metallurgy and Materials*, 2009, **16**(6), pp.661-666.
108. Jia, Z., Du, C., Liu, Z., Gao, J. and Li, X. Effect of calcium ions on CO2 corrosion of 3Cr low-alloy steel. *Acta Metallurgica Sinica*, 2011, **24**(5), pp.373-380.
109. Esmaeely, S.N., Choi, Y.-S., Young, D. and Nešić, S. Effect of Calcium on the Formation and Protectiveness of Iron Carbonate Layer in CO2 Corrosion. *In: CORROSION 2013*, 2013/3/17/, Orlando, Florida. NACE International, 2013, p.13.
110. Tavares, L.M., Costa, E.M.d., Andrade, J.J.d.O., Hubler, R. and Huet, B. Effect of calcium carbonate on low carbon steel corrosion behavior in saline CO2 high pressure environments. *Applied Surface Science*, 2015, **359**, pp.143-152.
111. Wang, B., Xu, L., Liu, G. and Lu, M. Corrosion behavior and mechanism of 3Cr steel in CO2 environment with various Ca2+ concentration. *Corrosion Science*, 2018, **136**, pp.210-220.
112. Mansoori, H., Young, D., Brown, B., Nesic, S. and Singer, M. Effect of CaCO3-saturated solution on CO2 corrosion of mild steel explored in a system with controlled water chemistry and well-defined mass transfer conditions. *Corrosion Science*, 2019, **158**, p.108078.
113. Mansoori, H., Brown, B., Young, D., Nešić, S. and Singer, M. Effect of FexCayCO3 and CaCO3 Scales on the CO2 Corrosion of Mild Steel. *Corrosion Journal*, 2019, **75**(12), pp.1434-1449.
114. Jiang, X., Zheng, Y.G., Qu, D.R. and Ke, W. Effect of calcium ions on pitting corrosion and inhibition performance in CO2 corrosion of N80 steel. *Corrosion Science*, 2006, **48**(10), pp.3091-3108.
115. Ren, C.Q., Wang, X., Liu, L., Yang, H.E. and Xian, N. Lab and field investigations on localized corrosion of casing. *Materials and Corrosion*, 2012, **63**(2), pp.168-172.
116. Esmaeely, S.N., Young, D., Brown, B. and Nešić, S. Effect of Incorporation of Calcium into Iron Carbonate Protective Layers in CO2 Corrosion of Mild Steel. *Corrosion*, 2017, **73**(3), pp.238-246.
117. Zhang, G.A. and Cheng, Y.F. Localized corrosion of carbon steel in a CO2-saturated oilfield formation water. *Electrochimica Acta*, 2011, **56**(3), pp.1676-1685.
118. Parkhurst, D.L. and Appelo, C. Description of input and examples for PHREEQC version 3—a computer program for speciation, batch-reaction, one-dimensional transport, and inverse geochemical calculations. *US geological survey techniques and methods*, 2013, **6**(A43), p.497.
119. Plummer, N., Jones, B.F. and Truesdell, A.H. *WATEQF; a FORTRAN IV version of WATEQ : a computer program for calculating chemical equilibrium of natural waters*. Water-Resources Investigations Report, 76-13. 1976.
120. Nordsveen, M., Nešić, S., Nyborg, R. and Stangeland, A. A Mechanistic Model for Carbon Dioxide Corrosion of Mild Steel in the Presence of Protective Iron Carbonate Films—Part 1: Theory and Verification. *Corrosion,* 2003, **59**(5), pp.443-456.

121. Alsaiari, H.A., Yean, S., Tomson, M.B. and Kan, A.T. Iron (II)-Calcium Carbonate: Precipitation Interaction. *In: SPE International Oilfield Scale Conference*, 28/29 May 2008, Aberdeen, UK. Society of Petroleum Engineers, 2008, p.16.
122. Plummer, L.N. and Busenberg, E. The solubilities of calcite, aragonite and vaterite in CO2-H2O solutions between 0 and 90°C, and an evaluation of the aqueous model for the system CaCO3-CO2-H2O. *Geochimica et Cosmochimica Acta*, 1982, **46**(6), pp.1011-1040.
123. Esmaeely, S.N., Choi, Y.-S., Young, D. and Nešić, S. Effect of Calcium on the Formation and Protectiveness of Iron Carbonate Layer in CO2 Corrosion. *Corrosion*, 2013, **69**(9), pp.912-920.
124. Vallejo Vitaller, A., Angst, U.M. and Elsener, B. A setup for electrochemical corrosion testing at elevated temperature and pressure. *Measurement*, 2020, **155**, p.107537.
125. Barcher, C.S., Omar. *Potentiostat Circuit Diagram and Working Principles | Ossila* [online]. 2022. [Accessed 15 May]. Available from: https://www.ossila.com/pages/potentiostat-application-notes.
126. ASTM International. ASTM G1-03. *Standard practice for preparing, cleaning and evaluating corrosion test specimens*. West Conshohocken, PA: ASTM International, 2017.
127. Dinnebier, R.E. and Billinge, S.J. *Powder diffraction: theory and practice.* Royal society of chemistry, 2008.
128. Oddo, J.E. and Tomson, M.B. Simplified Calculation of CACO3 Saturation at High Temperatures and Pressures in Brine Solutions. *Journal of Petroleum Technology*, 1982, **34**(07), pp.1583-1590.
129. Kharaka, Y.K., Gunter, W.D., Perkins, E.H. and DeBraal, J.D. Geochemical Modeling of Water—Rock Interactions Using SOLMINEQ.88. *In: Chemical Modeling of Aqueous Systems II*. American Chemical Society, 1990, pp.117-127.
130. Palmer, D.A. and Van Eldik, R. The chemistry of metal carbonato and carbon dioxide complexes. *Chemical Reviews*, 1983, **83**(6), pp.651-731.
131. Li, D. and Duan, Z. The speciation equilibrium coupling with phase equilibrium in the H2O–CO2–NaCl system from 0 to 250 °C, from 0 to 1000 bar, and from 0 to 5 molality of NaCl. *Chemical Geology*, 2007, **244**(3), pp.730-751.
132. Duan, Z., Sun, R., Zhu, C. and Chou, I.M. An improved model for the calculation of CO2 solubility in aqueous solutions containing Na+, K+, Ca2+, Mg2+, Cl−, and SO42−. *Marine Chemistry*, 2006, **98**(2), pp.131-139.
133. Wang, X., Conway, W., Burns, R., McCann, N. and Maeder, M. Comprehensive Study of the Hydration and Dehydration Reactions of Carbon Dioxide in Aqueous Solution. *The Journal of Physical Chemistry A*, 2010, **114**(4), pp.1734-1740.
134. Duan, Z. and Li, D. Coupled phase and aqueous species equilibrium of the H2O–CO2–NaCl–CaCO3 system from 0 to 250°C, 1 to 1000bar with NaCl concentrations up to saturation of halite. *Geochimica et Cosmochimica Acta*, 2008, **72**(20), pp.5128-5145.
135. Marshall, W.L. and Franck, E.U. Ion product of water substance, 0–1000 °C, 1–10,000 bars New International Formulation and its background. *Journal of Physical and Chemical Reference Data*, 1981, **10**(2), pp.295-304.

136. Corr Instruments. Q0823. *UltraDeg ORP and pH Probes for High Pressures and/or High Temperatures - Instruction Manual*. San Antonio, TX: Corr Instruments, LLC, 2017.
137. Hammond, C. *The basics of crystallography and diffraction.* International Union of Crystallography monographs on crystallography ; 21. Fourth edition. ed. Oxford: Oxford University Press, 2015.
138. Epelboin, I. and Keddam, M. Faradaic Impedances: Diffusion Impedance and Reaction Impedance. *Journal of The Electrochemical Society*, 1970, **117**(8), p.1052.
139. Bechet, B., Epelboin, I. and Keddam, M. New data from impedance measurements concerning the anodic dissolution of iron in acidic sulphuric media. *Journal of Electroanalytical Chemistry and Interfacial Electrochemistry*, 1977, **76**(1), pp.129-134.
140. Keddam, M., Mottos, O.R. and Takenouti, H. Reaction Model for Iron Dissolution Studied by Electrode Impedance: I . Experimental Results and Reaction Model. *Journal of The Electrochemical Society*, 1981, **128**(2), pp.257-266.
141. Keddam, M., Mattos, O.R. and Takenouti, H. Reaction Model for Iron Dissolution Studied by Electrode Impedance: II . Determination of the Reaction Model. *Journal of The Electrochemical Society*, 1981, **128**(2), pp.266-274.
142. Barcia, O.E. and Mattos, O.R. The role of chloride and sulphate anions in the iron dissolution mechanism studied by impedance measurements. *Electrochimica Acta*, 1990, **35**(6), pp.1003-1009.
143. Li, P., Tan, T.C. and Lee, J.Y. Impedance spectra of the anodic dissolution of mild steel in sulfuric acid. *Corrosion Science*, 1996, **38**(11), pp.1935-1955.
144. Zhang, G., Chen, C., Lu, M., Chai, C. and Wu, Y. Evaluation of inhibition efficiency of an imidazoline derivative in CO2-containing aqueous solution. *Materials Chemistry and Physics*, 2007, **105**(2), pp.331-340.
145. Zhang, G.A. and Cheng, Y.F. On the fundamentals of electrochemical corrosion of X65 steel in CO2-containing formation water in the presence of acetic acid in petroleum production. *Corrosion Science*, 2009, **51**(1), pp.87-94.
146. Farelas, F., Galicia, M., Brown, B., Nešić, S. and Castaneda, H. Evolution of dissolution processes at the interface of carbon steel corroding in a CO2 environment studied by EIS. *Corrosion Science*, 2010, **52**(2), pp.509-517.
147. Almeida, T.C., Mattos, O.R., Bandeira, M.C.E. and Moreira, R.M. The Effect of High Partial Pressure of CO2 on the Corrosion Mechanism of Carbon Steel in H2O-CO2 Systems. *In: CORROSION 2018*, NACE-2018-11623, 2018.
148. Li, S., Zeng, Z., Harris, M.A., Sánchez, L.J. and Cong, H. CO2 Corrosion of Low Carbon Steel Under the Joint Effects of Time-Temperature-Salt Concentration. *Frontiers in Materials*, 2019, **6**.
149. Chen, J., Wang, X., Ma, H., Huo, Z. and Wang, Y. Experimental Investigation on Corrosion Behavior of X80 Pipeline Steel under Carbon Dioxide Aqueous Conditions. *ACS Omega*, 2022, **7**(7), pp.6142-6150.

150. Wang, C., et al. Anti-corrosion characteristics of FeCO3 and FexCayMgzCO3 scales on carbon steel in high-PT CO2 environments. *Chemical Engineering Journal*, 2022, **431**, p.133484.
151. Boukamp, B.A. A Linear Kronig-Kramers Transform Test for Immittance Data Validation. *Journal of The Electrochemical Society*, 1995, **142**(6), p.1885.
152. Barsoukov, E. and Macdonald, J.R. *Impedance spectroscopy : theory, experiment, and applications.* Second edition / edited by Evgenij Barsoukov, J. Ross Macdonald. ed. Hoboken, N.J: Wiley-Interscience, 2005.
153. Brug, G.J., van den Eeden, A.L.G., Sluyters-Rehbach, M. and Sluyters, J.H. The analysis of electrode impedances complicated by the presence of a constant phase element. *Journal of Electroanalytical Chemistry and Interfacial Electrochemistry*, 1984, **176**(1), pp.275-295.
154. Devos, O., Gabrielli, C. and Tribollet, B. Simultaneous EIS and in situ microscope observation on a partially blocked electrode application to scale electrodeposition. *Electrochimica Acta*, 2006, **51**(8), pp.1413-1422.
155. Oldham, K.B. and Zoski, C.G. Chapter 2 Mass Transport to Electrodes. *In:* C.H. BAMFORD and R.G. COMPTON, eds. *Comprehensive Chemical Kinetics*. Elsevier, 1986, pp.79-143.
156. Nguyen, T.Q. and Breitkopf, C. Determination of Diffusion Coefficients Using Impedance Spectroscopy Data. *Journal of The Electrochemical Society*, 2018, **165**(14), pp.E826-E831.
157. Boukamp, B.A. Derivation of a Distribution Function of Relaxation Times for the (fractal) Finite Length Warburg. *Electrochimica Acta*, 2017, **252**, pp.154-163.
158. Cruz-Manzo, S. and Greenwood, P. Frequency Transition from Diffusion to Capacitive Response in the Blocked-Diffusion Warburg Impedance for EIS Analysis in Modern Batteries. *Journal of The Electrochemical Society*, 2020, **167**(14), p.140507.
159. Gamry. *Gamry Simplex Fit- Algorithm Details Gamry Instruments* [online]. 2023. [Accessed]. Available from: https://www.gamry.com/application-notes/software-scripting/simplex-fit-algorithm/.
160. Gao, M., Pang, X. and Gao, K. The growth mechanism of CO2 corrosion product films. *Corrosion Science*, 2011, **53**(2), pp.557-568.
161. Al-Khateeb, M., Barker, R., Neville, A. and Thompson, H.M. The Effect of Surface Roughness on Diffusion and Chemical Reaction Controlled Limiting Currents on a Rotating Cylinder Electrode in Deaerated Solutions with and Without CO2. *Corrosion*, 2018, **74**(9), pp.971-983.
162. Suhor, M.F., Mohamed, M.F., Nor, A.M., Singer, M. and Nesic, S. Corrosion Of Mild Steel In High CO2 Environment: Effect Of The Feco3 Layer. *In: CORROSION 2012*, NACE-2012-1434, 2012.
163. Tlili, M.M., Benamor, M., Gabrielli, C., Perrot, H. and Tribollet, B. Influence of the Interfacial pH on Electrochemical CaCO3 Precipitation. *Journal of The Electrochemical Society*, 2003, **150**(11), p.C765.
164. Dawson, D.A. and Trass, O. Mass transfer at rough surfaces. *International Journal of Heat and Mass Transfer*, 1972, **15**(7), pp.1317-1336.

165. De Yoreo, J.J. and Vekilov, P.G. Principles of Crystal Nucleation and Growth. *Reviews in Mineralogy and Geochemistry*, 2003, **54**(1), pp.57-93.
166. Ueda, M. and Ikeda, A. Effect of Microstructure and Cr Content in Steel on CO2 Corrosion. *In: CORROSION 96*, NACE-96013, 1996.
167. Palacios, C.A. and Shadley, J.R. Characteristics of Corrosion Scales on Steels in a CO2-Saturated NaCl Brine. *Corrosion*, 1991, **47**(2), pp.122-127.
168. Bonaventura, M.D., Brown, B., Nesic, S. and Singer, M. Removal of Iron Carbide in Turbulent Flow Conditions and Influence on Iron Carbonate Formation in Aqueous CO2 Corrosion of Mild Steel. *In: CORROSION 2020*, NACE-2020-15148, 2020.
169. Owen, J., Ropital, F., Joshi, G.R., Kittel, J. and Barker, R. Galvanic effects induced by siderite and cementite surface layers on carbon steel in aqueous CO2 environments. *Corrosion Science*, 2022, **209**, p.110762.